

**Crystal Structure, Phase Behaviour and Kinetics  
Associated with the Crystallisation of Octadecane,  
Hexadecane, and Mixtures Thereof**

**Xue Tang**

Submitted in accordance with the requirements for the degree of

DOCTOR OF PHILOSOPHY

The University of Leeds  
School of Chemical and Process Engineering  
Institute of Particle Science and Engineering

January 2017

The candidate confirms that the work submitted is her own and that appropriate credit has been given where reference has been made to the work of others.

This copy has been supplied on the understanding that it is copyright material and that no quotation from the thesis may be published without proper acknowledgement.

The right of Xue Tang to be identified as Author of this work has been asserted by her in accordance with the Copyright, Designs and Patents Act 1988.

## **Acknowledgements**

*I would like to greatly thank my supervisors, Prof Kevin Roberts and Dr Xiaojun Lai, not only for their instruction and supervision but also for the encouragement and supports in spirit, which helped throughout this PhD study.*

*Thanks to my colleges in the Institute of particle science from University of Leeds; In particular, Dr Diana Camacho, who has been working together for the Infineum Ltd., for always sharing her knowledge and experience to me and kind support; Tom Turner and Ian Rosbottom for their help with applications for synchrotron beamtime and the time spending during synchrotron experiments; Boyang Zou, for encouragement, supports and accompany in the hardest writing time. Guilherme Calligaris for his help with X-ray diffraction refinement. Pablo, David, Guangyi, Qi, Mo and Jonathan for providing a comfort study environment and interesting discussions.*

*Finally, I would like to express my sincerely thanks to my mum, sister and brother. It would not be possible to finish this PhD without their supports and lots of love.*

## Abstract

There is an ever-increasing use of sustainable, bio-derived feedstocks in fuel oils including hydrogenated vegetable oil (HVO) from agricultural or recycled sources. HVO fuels consist of a narrow alkane distribution mainly octadecane (C18) and hexadecane (C16). Such fuels crystallise easily, which can lead to vehicle failures in cold weather conditions. This thesis examines the interplay between crystallisation kinetics, crystal structure and phase behaviour using model C18/C16 alkane mixtures.

Computational systematic search modelling in combination with high resolution synchrotron X-ray powder data yields its crystallographic structure for C18 and C16 together with their volume thermal expansion coefficients:  $4.39 \pm (1.94) \times 10^{-4} \text{ } ^\circ\text{C}^{-1}$  and  $4.17 \pm (2.48) \times 10^{-4} \text{ } ^\circ\text{C}^{-1}$ . Morphological analysis of C18 crystals reveals a plate-like morphology dominated by the {001} habit plane with smaller side faces (depending upon supersaturation).

Analysis of C18/C16 binary phase diagram reveals five single phases (liquid,  $R_1$ ,  $M_{dcp}$ ,  $O_p$  and  $T_{18}$ ) and five three-phase-equilibrium invariants (eutectic and peritectic at high temperature, eutectoid and peritectoid at low temperature). Kinetic studies reveal the crossover behaviour of the  $R_1$  existed in a transient to metastable to stable phase, which the stability is affected by both composition and alkane chain length.

Studies of the ternary C18/C16/kerosene system reveal a variety of different structures with compositions close to that of its pure components forming solid-solution in triclinic structures, whilst high relative fractions result in its formation of multiple phases (triclinic and two higher symmetry structures). Rotator induced crystallisation observed in melt phase crystallisation is also formed in solution crystallisation but only for C18/C16 mixtures with its metastability depending on the composition.

Solubility studies reveal the closest to the ideal condition with highest solubility in n-dodecane followed by kerosene and toluene respectively. Calculated activity coefficients reflect the non-identical phase formation in the solution phase with higher deviations for C18 molar compositions of  $x=0.1$ ,  $0.5$ - $0.7$ . Solvents type is not found to have any significant effect on its solid for structure behaviour for C18/C16 mixtures.

Crystallisation of C18/C16 mixtures for most compositions in the three solvents are found to be mediated by progressive nucleation mechanism. Cases of instantaneous nucleation are also seen in particularly compositions with higher C18 concentration. Progressive nucleation reveals well correlated

with wider metastable zone width and concomitant larger interfacial tension ( $1.33-1.64 \frac{mJ}{m^2}$ ). Higher solubility is found to accelerate the instantaneous nucleation by increasing effective solute concentration, whilst inhibit the progressive nucleation by causing larger interfacial tension.

## Table of Contents

<b>Acknowledgements</b> .....	<b>iii</b>
<b>Abstract</b> .....	<b>iv</b>
<b>Table of Contents</b> .....	<b>vi</b>
<b>List of Tables</b> .....	<b>x</b>
<b>List of Figures</b> .....	<b>xiv</b>
<b>Chapter 1 Introduction</b> .....	<b>1</b>
1.1 Industrial Background .....	2
1.2 Research Aims and Objectives .....	4
1.3 Project Management .....	6
1.4 Report Structure.....	6
<b>Chapter 2 Crystallisation Science</b> .....	<b>8</b>
2.1 Introduction .....	9
2.2 Crystals and their Structures .....	9
2.2.1 Crystallography .....	9
2.2.2 Planes and Miller Indices .....	11
2.2.3 Crystal Chemistry and Polymorphism .....	12
2.2.4 Crystal Morphology .....	12
2.3 Phase Equilibria .....	13
2.3.1 The Phase Rule .....	13
2.3.2 Two Component Phase Diagram .....	13
2.4 Solutions, Solubility and Supersaturation.....	15
2.4.1 Melts, Solutions and Solubility.....	15
2.5 Crystallisation Kinetics .....	19
2.5.1 Nucleation .....	19
2.5.2 Methods to assess nucleation kinetics using the poly- thermal method .....	23
2.6 Crystallisation Characteristic Techniques.....	27
2.6.1 Differential scanning calorimetry (DSC) .....	27
2.6.2 X-rays and Diffraction.....	28
2.6.3 Powder X-ray diffraction (PXRD).....	32
2.6.4 Synchrotron Radiation.....	33
2.7 Conclusions.....	34
<b>Chapter 3. Normal Alkanes Crystallographic Structures, Thermodynamic and Crystallisation Properties</b> .....	<b>35</b>
3.1 Introduction .....	36

3.2	Normal Alkane Configuration and Structures .....	36
3.2.1	Configuration.....	36
3.2.2	Phase structures .....	37
3.3	Structural Behaviour of Mixtures of n-alkanes Homologues.....	40
3.4	Solubility and Crystallisation Kinetics and Morphology .....	42
3.5	Conclusions.....	43
<b>Chapter 4</b>	<b>Materials and Methods .....</b>	<b>44</b>
4.1	Introduction .....	45
4.2	Materials.....	45
4.2.1	Supplied Chemicals and Solvents.....	45
4.2.2	Binary Mixture Sample Preparation.....	46
4.3	Experimental Methodology.....	46
4.3.1	DSC Thermal Analysis .....	46
4.3.2	Powder X-ray Diffraction .....	49
4.3.3	Turbidimetric Measurements.....	52
4.3.4	Morphology Determination .....	57
4.3.5	Data analysis.....	58
4.3.6	Conclusions.....	62
<b>Chapter 5</b>	<b>Structure and Morphologies Properties of Octadecane and Hexadecane.....</b>	<b>64</b>
5.1	Introduction .....	65
5.2	Octadecane (C18).....	65
5.2.1	Unit Cell Parameter Determination.....	65
5.2.2	Structure Refinement .....	67
5.2.3	Thermal Expansion .....	74
5.2.4	Morphological Analysis .....	80
5.3	Hexadecane .....	85
5.3.1	Structure Refinement .....	86
5.3.2	Thermal Expansion .....	89
5.4	Discussions.....	92
5.5	Conclusions.....	93
<b>Chapter 6</b>	<b>Phase Behaviour and Crystallisation Kinetics in Octadecane and Hexadecane Binary System.....</b>	<b>95</b>
6.1	Introduction .....	96
6.2	Thermal Analysis.....	97
6.2.1	Influence of Heating/Cooling Rates.....	97

6.2.2	Temperature and Enthalpy Determination of Phase Transitions.....	102
6.2.3	Crossover Observation from Transient to Metastable to Stable Phase of R <sub>1</sub> .....	108
6.3	Phase Identification from PXRD Analysis.....	111
6.3.1	Disordered Phase at High Temperature Region (HT) .....	111
6.3.2	Intermediate Ordered Crystalline Phases in the Low-Temperature Region (LT).....	114
6.3.3	Variable Temperature XRD Analysis.....	118
6.4	Equilibrium Binary Phase Diagram of Octadecane and Hexadecane .....	124
6.5	Structural Analysis for Binary Mixture Formation by Rapid Quenching.....	127
6.6	Nucleation Kinetic Assessment Using the KBHR Approach.....	130
6.7	Conclusions.....	134
<b>Chapter 7</b>	<b>In-situ High Resolution XRD Studies of Phase Behaviour of the Octadecane, Hexadecane and Kerosene Solution Ternary System .....</b>	<b>135</b>
7.1	Introduction .....	136
7.2	Isothermal Analysis at LT (- 40°C) .....	136
7.2.1	LT Phase Behaviour as a Function of Composition .....	136
7.2.2	Structure Refinement .....	143
7.3	In-situ Dynamic Diffraction from Poly-thermal Crystallisation....	147
7.3.1	Pure Octadecane and Hexadecane .....	147
7.3.2	Octadecane and Hexadecane Mixtures .....	151
7.4	Ternary Phase Diagram of C18/C16/Kerosene (308 g/l).....	162
7.5	Conclusions.....	164
<b>Chapter 8</b>	<b>Solubility of Octadecane and Hexadecane Mixtures as a Function of Solution Environment.....</b>	<b>165</b>
8.1	Introduction .....	166
8.2	Results Using the Poly-thermal Method .....	166
8.3	Saturation Temperature .....	181
8.4	Van't Hoff Analysis .....	183
8.5	Conclusions.....	191
<b>Chapter 9</b>	<b>Nucleation Kinetics and Mechanism of Octadecane and Hexadecane Mixtures as a Function of Solution Environment .....</b>	<b>192</b>
9.1	Introduction .....	193

9.2 Metastable Zone Width (MSZW) .....	193
9.3 Nucleation Mechanism and Kinetic Assessment.....	194
9.4 Discussion.....	206
9.5 Conclusions.....	209
<b>Chapter 10 Conclusions and Future Work .....</b>	<b>210</b>
10.1 Conclusions of this Study .....	211
10.2 Review of Aims and Objectives.....	214
10.3 Suggestions for Future Work.....	214
<b>List of References .....</b>	<b>217</b>
<b>List of Symbols .....</b>	<b>224</b>
<b>List of Abbreviation.....</b>	<b>226</b>
<b>Appendix A .....</b>	<b>227</b>
<b>Appendix B .....</b>	<b>230</b>
<b>Appendix C .....</b>	<b>231</b>

## List of Tables

<b>Table 4.1 Properties of C16 and C18 chemicals and solvents used in this research.....</b>	<b>45</b>
<b>Table 4.2 Composition information of Kerosene as supplied by Infineum Ltd.....</b>	<b>46</b>
<b>Table 4.3 Melting temperatures and enthalpies of reference sample of Indium at different heating rates .....</b>	<b>47</b>
<b>Table 5.1 Lattice parameters of C18 at low temperature (-40 °C) together with the <math>R_{wp}</math> value determined from “Pawley fit” refinement by Topas. ....</b>	<b>66</b>
<b>Table 5.2 Parameters employed in the systematic search for trial packing motifs for the triclinic phase of C18.....</b>	<b>67</b>
<b>Table 5.3 Summary of results of the systematic search for trial packing motifs for the triclinic phase of C18.....</b>	<b>68</b>
<b>Table 5.4 Fractional coordinates of carbon atoms of C18 at -40 °C and relative isotropic displacement parameters in the asymmetric unit of triclinic structure after Rietveld refinement.....</b>	<b>70</b>
<b>Table 5.5 Fractional coordinates of carbon atoms of C18 at room temperature and relative isotropic displacement parameters in the asymmetric unit of triclinic structure after Rietveld refinement.....</b>	<b>70</b>
<b>Table 5.6 Crystallographic data of C18 from the best-fit Rietveld refinement at different temperature together with detailed information from single crystal structure from Nyburg. In quotation is the calculated reduce cell obtained from Avogadro [107] programme according to Niggli theory. ....</b>	<b>71</b>
<b>Table 5.7 List of thirteen groups of zone axis with their representative planes (<math>hkl</math>) and respective inter-planer d spacing.....</b>	<b>82</b>
<b>Table 5.8 List of pair-wise planes matching the internal angel from experimental crystals at <math>\sigma = 0.036, T = 12.2</math> °C. The potential solutions of the morphological planes are presented with the best solution highlighted. Planes designated are shown in Figure 5.9 (a).....</b>	<b>83</b>
<b>Table 5.9 List of pair-wise planes matching the internal angel from experimental crystals <math>\sigma = 0.045, T = 12.1</math> °C. The unique potential solution is presented of the morphological predication. Planes designated are shown in Figure 5.9 (b). ....</b>	<b>83</b>
<b>Table 5.10 Fractional coordinates of carbon atoms of C16 at -40 °C and relative isotropic displacement parameters in the asymmetric unit of triclinic structure after Rietveld refinement.....</b>	<b>88</b>

<b>Table 5.11 Fractional coordinates of carbon atoms of C16 at 0 °C and relative isotropic displacement parameters in the asymmetric unit of triclinic structure after Rietveld refinement.....</b>	<b>88</b>
<b>Table 5.12 Crystallographic data of C16 from the best-fit Rietveld refinement at different temperature together with detailed information from lab PXRD crystal structure from Me ´tivaud. In quotation is the calculated reduce cell obtained from Avogadro programme according to Niggli theory .....</b>	<b>89</b>
<b>Table 6.1 Phase transition temperatures and enthalpies of C16 from two cycle sequences and three fresh sample repeats. The negligible values of standard deviation (Std) show the consistent repeatability of the DSC measurements.....</b>	<b>97</b>
<b>Table 6.2 Averaged temperatures of crystallisation (<math>T_c</math>) and melting (<math>T_m</math>) with their standard deviations as a function of cooling/heating rates. The resultant MSZW as obtained from <math>T_m-T_c</math> was also presented. ....</b>	<b>101</b>
<b>Table 6.3 Onset, Peak and Endpoints as integrated from the solid to liquid transitions and resultant heat enthalpy for 21 samples of binary mixtures. E and P represent to eutectic and peritectic invariants, respectively. ....</b>	<b>107</b>
<b>Table 6.4 Peak points of solid-solid phase transitions for compositions from 0.05C18 to 0.85C18 at LT; E☆ represents eutectoid invariant; P☆ represents peritectoid invariant. ....</b>	<b>108</b>
<b>Table 6.5 Unit cell parameters of <math>R_1</math> from C16/C18 mixture obtained from STOE© and refined by TOPAS [87].....</b>	<b>113</b>
<b>Table 6.6 Literature determined unit parameters of <math>R_1</math> .....</b>	<b>113</b>
<b>Table 6.7 Unit cell parameters determined from XRD patterns collected by X'pert and Pawley refinement using TOPAS software. ....</b>	<b>117</b>
<b>Table 6.8: Best linear fitting for <math>\ln q</math> vs <math>\ln uc</math> results with corresponding nucleation mechanism for C16, C18 and binary mixture 0.4C18. Values obtained from non-linear fitting of <math>\ln q</math> vs <math>uc</math> are listed for sample of C16 and C18 crystallising in a PN nucleation mechanism. ....</b>	<b>133</b>
<b>Table 7.1 Unit cell parameters of C18/C16 mixtures crystallising from kerosene at - 40°C .....</b>	<b>142</b>
<b>Table 7.2 Crystallographic data of C16 crystalline formed from Kerosene obtained from Rietveld refinement using Topas software .....</b>	<b>145</b>
<b>Table 7.3 Crystallographic data of C18 crystalline formed from Kerosene obtained from Rietveld refinement using Topas software .....</b>	<b>146</b>

<b>Table 7.4 Comparison results (lattice parameters and <math>R_{wp}</math>, <math>R_p</math> values ) between <math>M_{dcp}</math> and <math>O_p</math> as applied to fit X1 phase by “Pawley fit” for three samples at the early stage of crystallisation of composition 0.3C18, 0.4C18 and 0.5 C18 in kerosene solution (308 g/l).</b> .....	<b>160</b>
<b>Table 8.1 Average temperatures of crystallisation <math>T_c</math> and dissolution <math>T_{diss}</math> as a function of cooling rate and binary mixture composition of C18/C16 in n-dodecane solution at concentrations of 192, 231, 269, 308 g/l. STD: standard deviation of the measured <math>T_c</math> and <math>T_{diss}</math> from 5 recycles of repeats.</b> .....	<b>168</b>
<b>Table 8.2 Average temperatures of crystallisation <math>T_c</math> and dissolution <math>T_{diss}</math> as a function of cooling rate and binary mixture composition of C18/C16 in kerosene solution at concentrations of 231, 269, 308, 350 g/l. STD: standard deviation of the measured <math>T_c</math> and <math>T_{diss}</math> from 5 recycles of repeats.</b> .....	<b>170</b>
<b>Table 8.3 Average temperatures of crystallisation <math>T_c</math> and dissolution <math>T_{diss}</math> as a function of cooling rate and binary mixture composition of C18/C16 in toluene solution at concentrations of 300, 350, 400, 350 g/l. STD: standard deviation of the measured <math>T_c</math> and <math>T_{diss}</math> from 5 recycles of repeats.</b> .....	<b>173</b>
<b>Table 8.4 Solubility (<math>T_e</math>) and supersolubility (<math>T_c</math>, <math>lim</math>) data of C18/C16 mixtures in n-dodecane solvent, together with the calculated equilibrium MSZW (<math>\Delta T</math>) at each concentration. std: standard deviation from five recycles of repeats.</b> .....	<b>176</b>
<b>Table 8.5 Solubility (<math>T_e</math>) and supersolubility (<math>T_c</math>, <math>lim</math>) data of C18/C16 mixtures in kerosene solvent, together with the calculated equilibrium MSZW (<math>\Delta T</math>) at each concentration. Std: standard deviation from five recycles of repeats.</b> .....	<b>177</b>
<b>Table 8.6 Solubility (<math>T_e</math>) and supersolubility (<math>T_c</math>, <math>lim</math>) data of C18/C16 mixtures in toluene solvent, together with the calculated equilibrium MSZW (<math>\Delta T</math>) at each concentration. std: standard deviation from five recycles of repeats.</b> .....	<b>178</b>
<b>Table 8.7 Thermodynamic parameters derived from the Van’t Hoff plots for C18/C16 mixtures in three solvents of n-dodecane, kerosene and toluene with high correlation <math>R^2 &gt; 0.97</math> from a linear fit of <math>\ln x</math> versus <math>1/T</math> except for mixture component of 0.4C18 in kerosene with <math>R^2 = 0.79</math>. Activity coefficient (<math>\gamma</math>)</b> .....	<b>187</b>
<b>Table 9.1 (a-c) Relative critical undercooling (<math>uc</math>) as a function of cooling rate (<math>q</math>) and solution concentration of eleven compositions of C16/C18 mixture crystallising from three solvents: (a) n-Dodecane, (b) Kerosene and (c) Toluene.</b> .....	<b>195</b>

<b>Table 9.2 Parameters derived from the KBHR approach from C16/C18 mixtures crystallising from a solution of n-dodecane: slope from <math>\ln q</math> vs. <math>\ln uc</math> plots with indicated nucleation mechanism and correlation <math>R^2</math> values; parameters (<math>a_1, a_2</math> and <math>\ln q_0</math>) as obtained from fitting equation of <math>\ln q</math> vs. <math>uc</math> according to Equation (2.26) and correlation <math>R^2</math> values. ....</b>	<b>199</b>
<b>Table 9.3 Parameters derived from the KBHR approach from C16/C18 mixtures crystallising from solution of kerosene: slope from <math>\ln q</math> vs. <math>\ln uc</math> plots with indicated nucleation mechanism and correlation R square values; parameters (<math>a_1, a_2</math> and <math>\ln q_0</math>) as obtained from fitting equation of <math>\ln q</math> vs. <math>uc</math> according to Equation (2.26) and correlation R square values. ....</b>	<b>201</b>
<b>Table 9.4 Parameters derived from the KBHR approach from C16/C18 mixtures crystallising from solution of toluene: slope from <math>\ln q</math> vs. <math>\ln uc</math> plots with indicated nucleation mechanism and correlation R square values; parameters (<math>a_1, a_2</math> and <math>\ln q_0</math>) as obtained from fitting equation of <math>\ln q</math> vs. <math>uc</math> according to Equation (2.26) and correlation R square values. ....</b>	<b>202</b>
<b>Table 9.5 Interfacial tension, critical radius and number of molecules for nucleation of C16/C18 mixtures in n-dodecane solution .....</b>	<b>204</b>
<b>Table 9.6 Interfacial tension, critical radius and number of molecules for nucleation of C16/C18 mixtures in toluene solution .....</b>	<b>204</b>
<b>Table 9.7 Interfacial tension, critical radius and number of molecules for nucleation of C16/C18 mixtures in kerosene solution .....</b>	<b>205</b>
<b>Table 9.8 Previous studied data of interfacial tension of normal alkanes and their mixtures .....</b>	<b>206</b>
<b>Table 9.9 Interfacial tension values with mixture compositions are the most PN controlled components (large slope number from the rule of three fitting) in three model solvents. Unit of <math>\gamma</math> is <math>mJm^2</math>.....</b>	<b>208</b>

## List of Figures

Figure 1.3 The wax crystal morphology for n-alkane crystallised from diesel fuel into plate-like crystals [10].....	4
Figure 1.4 Thesis delivery plan route .....	5
Figure 1.5 Schematic of the report layout.....	7
Figure 2.1: A representative unit cell with crystallographic axes (x, y, and z) and lattice parameters (a, b, c, $\alpha$ , $\beta$ , $\gamma$ ) [11].....	9
Figure 2.2: Representation of seven possible crystal unit cells [13].....	10
Figure 2.3: The fourteen possible space lattice called Bravais Lattices [14] .....	10
Figure 2.4: Representation of planes together with their Miller indices for a cubic cell [15] .....	11
Figure 2.5: Simple two-component phase diagram with temperature versus composition (T-X): (a) Solid solution type; (b) Eutectic mixture. ....	14
Figure 2.6: A representation of solubility and supersolubility curves with the three regions include: labile, metastable and stable [13]. ....	19
Figure 2.7: Nucleation classification [13].....	20
Figure 2.8: Scheme shows the bimolecular addition process [13].....	20
Figure 2.9: Free energy change corresponding to a critical nucleus size [13] .....	21
Figure 2.11: Schematic of a modern x-ray tube [33]. ....	29
Figure 2.12: X-ray spectrum of $K_{\alpha}$ and $K_{\beta}$ and the $K_{\alpha 1}$ and $K_{\alpha 2}$ . ....	30
Figure 2.13: Illustration of the superposition of two waves in constructive interference (Right) and destructive interference (left). [ <a href="https://en.wikipedia.org/wiki/Interference_(wave_propagation)">https://en.wikipedia.org/wiki/Interference_(wave_propagation)</a> )] .....	31
Figure 2.14: Diffraction of x-rays from crystal planes [35]. ....	32
Figure 3.1 Representative diagrams of molecular arrangements in the triclinic (a), monoclinic (b) and orthorhombic structures (c).[47] .....	37
Figure 3.2: Chain length dependent phase diagram of transition temperatures with respect to even alkane chain number from (n=14 to 24) corresponding to the L-R-T transitions [54]. ....	39
Figure 3.3: DSC traces from heating and cooling processes of even number alkanes of $C_{20}H_{42}$ , $C_{22}H_{46}$ , $C_{24}H_{50}$ and odd number alkane of $C_{23}H_{48}$ . [55] .....	40

Figure 4.1: Differential Scanning Calorimeter (DSC) from Mettler Toledo®.....	46
Figure 4.2: Powder diffractometer with high resolution transmission mode from STOE®.....	49
Figure 4.3: Phillips X'Pert Pro MPD diffractometer with a cold stage sample environment.....	50
Figure 4.4: Experimental layout of I11 beamline showing the five arms for MAC detectors mounted on the 2 $\theta$ circle, the sample in capillary mounted on a rotational stage, beam pipe and the PSD detector mounted on $\delta$ circle [86]. .....	51
Figure 4.5: Apparatus of the Avantium Crystal 16® [www.crystallizationsystems.com/pharma/crystal16/].....	52
Figure 4.6: Poly-thermal profile for temperature and transmission against the time for measuring the cloud and clear points of the solution.....	54
Figure 4.7: A turbidity result of a solution through a poly-thermal process. ....	55
Figure 4.8: Plots of T <sub>diss</sub> and T <sub>c</sub> as a function of cooling rate (q). The best linear fitting for each plot was listed with the equation as y=ax +b and the fitting accuracy factor R square.....	56
Figure 4.9: Equilibrium solubility/supersolubility curves for C18 in dodecane solution. The points were obtained from the extrapolation of the linear fitting from T <sub>diss</sub> and T <sub>c</sub> as a function of cooling rates from each concentration. The fitting curves are fitted by the polynomial equation in order 2. ....	57
Figure 4.10: In-situ growth microscopic cell: a) whole set up with Olympus BX51 optical microscopic. b) Enlargement of growth cell. Individual parts are 1) Sample cuvette cell. 2) Glass window area. 3) Crystal morphology observation area. 4) QImaging/QICAM camera. 5) Huber Ministat 125 circulation bath.....	58
Figure 4.11: Van't Hoff plot with the ideal and experimental solubility. The best fitting linear line for each was fitted by the equation as y=ax+b.....	61
Figure 5.1 High resolution synchrotron XRD pattern of C18 at -40 °C collected on beamline of I11, DLS. Together with the indexation (hkl) of the most important reflections. The resultant lattice parameters are given in Table 5.1. ....	66
Figure 5.2 Rietveld refinement of C18 in the range of 5 to 34° 2 $\theta$ with $\lambda = 0.825678 \text{ \AA}$ with different scale of amplified according to the intensity of the reflection peaks. Observed (o), calculated (—), difference (—) and positions of calculated reflections (I). ....	69

Figure 5.3 Packing of the C18 unit cell along with c-axis (a) and b-axis (b).....	73
Figure 5.4 In-situ SPXD patterns for pure C18 collected from 21.21 °C to -40.17 °C with 2 °C intervals during cooling process at 1.67 °C /min. ....	75
Figure 5.5 Diffraction pattern of C18 at the onset of crystallisation shows a large broad amorphous content. This is also observed within diffraction pattern prior to crystallisation in a liquid state. ....	75
Figure 5.6 Low angle (00L) diffraction patterns collected from the early stage of crystallisation (21.21 °C and 15.6 °C) and the bottom temperature at -40 °C. ....	76
Figure 5.7 The enlargement of typical reflection peaks, as position shift not standardised from thermal effects: (a) twisted (b) converged (c) splitting.....	78
Figure 5.8 Unit cell parameters (a, b c axis and $\alpha$ , $\beta$ , $\gamma$ angels) obtained from “Pawley fit” using TOPAS software are plotted as a function of temperature for C18.....	79
Figure 5.9 Volume of C18 unit cell obtained from “Pawley fit” using TOPAS software are plotted as a function of temperature. ....	79
Figure 5.10 Experimental morphology pictures of C18 in supersaturated n-dodecane solutions with three different supersaturations: $\sigma = 0.036$ , $T = 12.2$ °C (a); $\sigma = 0.045$ , $T = 12.1$ °C (b); $\sigma = 0.08$ , $T = 11.7$ °C (c).....	81
Figure 5.11 BFDH morphology prediction (left hand) with Miller indices obtained from the best solutions according to the experimental morphology (right hand) in three different supersaturation (a) $\sigma = 0.036$ , $T = 12.2$ °C (b) $\sigma = 0.045$ , $T = 12.1$ °C (c) $\sigma = 0.08$ , $T = 11.7$ °C.....	84
Figure 5.12 High resolution synchrotron XRD pattern of C16 at -40 °C collected on I11 of Diamond Light Source. Together with the indexation results of the high-intensity reflections.....	85
Figure 5.13 Rietveld refinement of C16 in the range of 5 to 34° 2 $\theta$ with $\lambda = 0.825678$ Å with different scale of amplified according to the intensity of the reflection peaks. Observed (o), calculated (–), difference (–) and positions of calculated reflections (l). ....	86
Figure 5.14 Packing of C16 unit cell along c-axis (a) and b-axis (b).....	87
Figure 5.15 In-situ SPXD patterns for pure C16 collected from 13.72 °C to -40 °C with 2 °C intervals during cooling process at 1.67 °C/min.....	90
Figure 5.16 Unit cell parameters (a, b c axis and $\alpha$ , $\beta$ , $\gamma$ angels) obtained from “Pawley fit” using Topas software are plotted as a function temperature for C16.....	91

Figure 5.17 Volume of C16 unit cell obtained from “Pawley fit” using TOPAS software are plotted as a function temperature.....	91
Figure 6.1: DSC curves plotted with normalised heat flow versus sample temperature from C16 collected at various heating/cooling rates .....	98
Figure 6.2: DSC curves plotted with scaled normalisation heat flow versus sample temperature from 0.4C18 collected at various heating/cooling rates. ....	99
Figure 6.3: Plots of onset/peak points of crystallisation/melting temperatures and their standard deviations versus cooling/heating rates. a) Pure C16, b) 0.4C18 and c) Pure C18...	102
Figure 6.4: DSC thermograms towards heating for C16/C18 binary mixtures from 21 compositions collected from -20°C to 30°C. The two equilibrium invariants (Eutectic and Peritectic) with compositions having an identical onset melting point at HT region are shown with dashed lines. The LT region phase transitions are enlarged as shown in Figure 6.5. ....	105
Figure 6.5: Enlarged thermograms from - 20°C to 15°C for compositions from 0.05C18 to 0.7C18 representing the solid-solid phase transitions at LT region. The two equilibrium invariants (Eutectoid and Peritectoid) with compositions having identical transition temperature at LT region are shown with dashed lines. ....	106
Figure 6.6: DSC traces from two cycles (red and black lines) of heating/cooling processes at 1°C/min within a temperature range of 23°C to 30°C with phase transition peaks from exothermic (upper side) and endothermic (downside) reactions. The non-repeatable exothermic peaks from two cycles towards cooling are indicative of a transient state of the rotator phase state with C18 (a) and 0.98C18 (b). ....	109
Figure 6.7: DSC curves of binary mixtures of 0.8C18, 0.85C18, 0.9C18 and 0.95C18 from two cycles heating/cooling processes at 1°C/min from 2 to 30°C with phase transition peaks from exothermic (upper side) and endothermic (downside) reactions. Identical thermal traces from two cycles measurements indicating the state of rotator phase is stabilised and no longer a transient state.....	110
Figure 6.8: Example of “Pawley fit” of sample 0.3C18 from experimentally collected XRD scan at 5°C; determined background; calculated reflection pattern from the determined unit cell; the difference between the experimental and calculated data is also shown. ....	113
Figure 6.9: XRD patterns collected at - 30°C of C16/C18 binary mixtures with two theta range from 15 to 30° at a wavelength of 1.54 angstrom:♦ T (P-1, Z=1), ♣ MdcP (Aa, Z=4) and ♥ Op (Pca21, Z=4. ....	115

- Figure 6.10: Example illustrating the difference between pure solid solution Op or M<sub>dcp</sub> and the mixture phases of both for mixture samples collected at - 30°C ..... 116
- Figure 6.11: Example of multiple phases “Pawley fit” of sample 0.1C18 from experimental data collected at - 30°C; determined background; Calculated reflection pattern from the determined unit cell of T16 and M<sub>dcp</sub>; Difference between the experimental and calculation data is also shown..... 116
- Figure 6.12: Temperature dependent PXRD collected from X’Pert for C18/C16 binary with molar composition x= 0.05, 0.1, 0.15, 0.2, 0.3, 0.4, 0.45, 0.5, 0.6, 0.7 and 0.8 of C18. Symbols: ♦ T (P<sub>1</sub>, Z=1), • R<sub>1</sub> (F<sub>mmm</sub>, Z=4), ♣ M<sub>dcp</sub> (A<sub>a</sub>, Z=4) and ♥ Op (P<sub>ca21</sub>, Z=4).. 124
- Figure 6.13: Experimental determined binary phase diagram of C16/C18 mixtures as a function of composition and temperature towards heating processes. Phase transition temperatures are determined by DSC represented by symbols of □ (Solid-liquid), □ (liquid-solid) and ○ (solid-solid). Structural evolution was determined from PXRD: ♦ T (P-1, Z=1), • R<sub>1</sub> (F<sub>mmm</sub>, Z=4), ♣ M<sub>dcp</sub> (A<sub>a</sub>, Z=4) and ♥ O<sub>p</sub> (P<sub>ca21</sub>, Z=4). In between of the adjacent monophasic phases are bi-phasic solid phases: Liquid+R<sub>1</sub>, T<sub>16</sub>+R<sub>1</sub>, T<sub>18</sub>+R<sub>1</sub>, M<sub>dcp</sub>+R<sub>1</sub>, O<sub>p</sub>+R<sub>1</sub>, M<sub>dcp</sub>+T<sub>16</sub>, M<sub>dcp</sub>+O<sub>p</sub> and O<sub>p</sub>+T<sub>18</sub>. Three-phase-equilibrium invariants are represented by dash line ( - ). ..... 126
- Figure 6.14: Collected XRD patterns for mixed samples of 0.3C18, 0.5C18 and 0.7C18 as crashed cooled to - 30°C from R<sub>1</sub> phase at HT; (a) low angle and (b) high angle reflections..... 128
- Figure 6.15: XRD patterns in q vector of sample 0.3C18 collected both at - 30°C from diffractometers of Expert and STOE with respect to the equilibrium and crash cooling crystallisation. (a) Low angles and (b) high angle reflections. ♣ M<sub>dcp</sub> (A<sub>a</sub>, Z=4); ♦ T (P-1, Z=1) ..... 129
- Figure 6.16: Nucleation mechanism assessment plot of *lnq vs lnuc* for a) C16, b) 0.4C18 and c) C18 in melt phase crystallisation ..... 131
- Figure 6.17: *lnq vs uc* for C16 with the best non-linear fit according to PN mechanism expression from KBHR for a) C16 and b) C18. .... 132
- Figure 7.1: Stack plot of high resolution XRD (MAC detector) with  $\lambda = 0.82568^\circ$  at - 40°C for C18/C16 mixtures crystallising from kerosene; selected “low angles” with  $2\theta$  from 1 to 10° and “high angles” with  $2\theta$  from 20 to 32°. Single triclinic phase with low angles reflections indexed; the low angles region for mixtures of 0.3C18, 0.4C18 and 0.5C18 presenting multiple phases are enlarged and shown in Figure 7.3..... 138

Figure 7.2: Set of (00L) peaks at low angle range for mixture samples crystallising from kerosene with molar compositions of $x= 0.3, 0.4$ and $0.5$ ) C18 in C16. Multiple phases were detected in all three samples, i.e. triclinic (T) and unknown phases (X1 and X2). .....	139
Figure 7.3: Stack XRD plot in $q$ vector of 0.5C18 with the melt crystallisation crash cooling process at $- 30^{\circ}\text{C}$ collected using STOE lab diffractometer and 0.5C18 with kerosene crystallisation at $- 40^{\circ}\text{C}$ collected using high resolution synchrotron beamline. Selected reflections from the low angles ( $q$ from $0.21$ to $1.89 \text{ \AA}$ ) and high angles ( $q$ from $3.2$ to $5.3 \text{ \AA}$ ) regions.....	140
Figure 7.4: High resolution synchrotron XRD pattern of C16 in Kerosene at $-40^{\circ}\text{C}$ collected on beamline I11 from Diamond Light Source. Low-intensity peaks are scaled up from $2\theta$ of $15$ to $40^{\circ}$ . .....	143
Figure 7.5: Rietveld refinement of C16 crystalline formed from Kerosene in the range of $5$ to $35^{\circ} 2\theta$ with $\lambda = 0.825678 \text{ \AA}$ with different scale of amplification according to the intensity of the reflection peaks. Observed ( $o$ ), calculated ( $-$ ), difference ( $-$ ) and positions of calculated reflections ( $!$ ).....	144
Figure 7.6: Rietveld refinement of C18 crystalline formed from Kerosene in the range of $5$ to $35^{\circ} 2\theta$ with $\lambda = 0.825678 \text{ \AA}$ with different scale of amplification according to the intensity of the reflection peaks. Observed ( $o$ ), calculated ( $-$ ), difference ( $-$ ) and positions of calculated reflections ( $!$ ).....	144
Figure 7.7: In-situ SPXD patterns for C18/Kerosene collected from the onset of crystallisation at $- 1.29^{\circ}\text{C}$ to a limited low temperature at $- 40.21^{\circ}\text{C}$ at $2^{\circ}\text{C}$ intervals during cooling at $1.67^{\circ}\text{C /min}$ .....	147
Figure 7.8: In-situ SPXD patterns for C16/Kerosene collected from the onset of crystallisation at $- 10.97^{\circ}\text{C}$ to a limited low temperature at $- 40.11^{\circ}\text{C}$ with $2^{\circ}\text{C}$ intervals during cooling at $1.67^{\circ}\text{C /min}$ .....	148
Figure 7.9: Unit cell parameters ( $a, b, c$ axis and $\alpha, \beta, \gamma$ angels) obtained from “Pawley fit” using Topas software are plotted as a function temperature for C18 in kerosene .....	149
Figure 7.10: Volume of C18 in kerosene unit cell obtained from “Pawley fit” using Topas software are plotted as a function temperature .....	149
Figure 7.11: Unit cell parameters ( $a, b, c$ axis and $\alpha, \beta, \gamma$ angels) obtained from “Pawley fit” using Topas software are plotted as a function of temperature for C16 in kerosene .....	150
Figure 7.12: Volume of C16 in kerosene unit cell obtained from “Pawley fit” using TOPAS software are plotted as a function of temperature.....	150

Figure 7.13: In-situ SPXD patterns for 0.1 C18 in kerosene (308 g/l) collected from - 16.55 to - 40.10°C at 2°C intervals during cooling crystallisation at 1.67°C /min .....	152
Figure 7.14: Stack plot in 2θ of 2 to 15° of early stage crystallisation from -14.65 to -18.45°C showing phase transition with reflection peak position changed from R (•) to T (◆). .....	152
Figure 7.15: In-situ SPXD patterns for 0.3C18 in kerosene (308 g/l) collected from - 12.82°C to - 40.11°C with 2°C intervals during cooling crystallisation at 1.67°C /min. Symbol of ♣ represents for M <sub>dcp</sub> structure; ◆: Triclinic structure. ....	153
Figure 7.16: Stack plot in 2θ (11 to 15°) of 0.3C18 in kerosene early stage crystallisation from - 14.68 to - 22.42°C showing phase transition with reflection peak position changed from R <sub>1</sub> (•) to M <sub>dcp</sub> (♣). .....	154
Figure 7.17: A comparison of “Pawley fit” of M <sub>dcp</sub> and O <sub>p</sub> lattice parameters to simulate XRD pattern of 0.3C18 in kerosene at - 20.42°C. Scaled peaks have shown the main difference. ....	155
Figure 7.18: In-situ SPXD patterns for 0.4C18 in kerosene (308 g/l) collected from - 12.88 to - 40.04°C with 2°C intervals during cooling crystallisation at 1.67°C /min. Scaled insert figure shows the appearance of the (X2) phase at - 24.19°C. Symbol ◆ represents the triclinic structure. ....	156
Figure 7.19: Stack plot in 2θ (11 to 13°) of 0.4 C18 in kerosene at early stage crystallisation from - 12.88 to - 18.59°C showing the phase transition with reflection peak position changed from R <sub>1</sub> (•) to O <sub>p</sub> (♥). .....	156
Figure 7.20: A comparison of “Pawley fit” of M <sub>dcp</sub> and O <sub>p</sub> lattice parameters to simulate XRD pattern of 0.4C18 in kerosene at - 20.42°C at the early stage of crystallisation. Scaled peaks have shown the main difference. ....	157
Figure 7.21: In-situ SPXD patterns for 0.5C18 in kerosene (308 g/l) collected from - 10.80 to - 40.11°C with 2°C intervals during cooling crystallisation at 1.67°C /min. Scaled inserted figure shows the appearance of the (X2) phase at - 25.92°C. The symbol ◆ represents the triclinic structure. ....	158
Figure 7.22: Stack plot in 2θ (10 to 14°) of 0.5C18 in kerosene at early stage crystallisation from - 10.82 to - 16.48°C showing phase transition with reflection peak position changed from R <sub>1</sub> (•) to O <sub>p</sub> (♥). ....	159
Figure 7.23: The comparison of “Pawley fit” of M <sub>dcp</sub> and O <sub>p</sub> lattice parameters to simulate XRD pattern of 0.5C18 in kerosene at - 16.48°C at the early stage of crystallisation. Scaled peaks have shown the main difference. ....	160

Figure 7.24: In-situ SPXD patterns for pure 0.7C18 in kerosene collected from - 5.18°C to - 40.15°C with 2°C intervals during cooling crystallisation at 1.67°C /min. ....	161
Figure 7.25: In-situ SPXD patterns for pure 0.9C18 in kerosene solution collected from - 1.38°C to - 40.19°C with 2°C intervals during cooling crystallisation at 1.67°C/min. ....	162
Figure 7.26: The structural revolution of C18 and C16 mixtures in kerosene solution (308 g/l) as a function of composition and temperature. Solid lines represent the phase boundary of first ordered crystalline, the boundary for the disordered R phase presented with a dash line. ....	163
Figure 8.1: Crystallisation ( $T_c$ ) and dissolution ( $T_{diss}$ ) temperatures as a function of heating/cooling rate ( $q$ ) for C18/C16 mixtures (eleven compositions varied in 10% molar concentration of C18) in toluene at a concentration of 300 g/l. Error bars are presented with standard deviation from five recycles of repeats.....	167
Figure 8.2: Solubility-supersolubility curves for samples of C16, C18 and equimolar composition of both 0.5C18. Determined from extrapolation of the poly-thermal data from four concentrations (300, 350, 400 and 450 g/l).....	179
Figure 8.3: Solubility-supersolubility curves for binary mixture samples a) 0.2C18 and b) 0.3C18 in n-dodecane solution determined from extrapolation of poly-thermal data from four concentrations (192, 231, 269 and 380 g/l).....	180
Figure 8.4: Equilibrium saturation temperature patterns as a function of C18/C16 mixture composition in three solvents of (a) n-dodecane with four concentrations of (192, 231, 269 and 308 g/l); (b) kerosene (231, 269, 308 and 350 g/l) and (c) toluene (300, 350, 400 and 450 g/l).....	181
Figure 8.5: Patterns of equilibrium saturation temperatures ( $T_e$ ) as a function of C18/C16 mixture composition in three representative solvents: n-dodecane, kerosene (at concentration of 308 g/l) and toluene (350 g/l). The corresponding structural phases are presented as obtained from in-situ synchrotron X-ray diffraction analysis of C18/C16/kerosene in Chapter 7 (Figure 7.26). ....	183
Figure 8.6: Solubility plots applied with Van's Hoff model for C18/C16 mixtures in n-dodecane. Experimental solubility data derived by extrapolation of $T_{diss}$ - $q$ lines at each concentration. ....	184
Figure 8.7: Solubility plots applied with Van's Hoff's model for C18/C16 mixtures in kerosene. Experimental solubility data derived by extrapolation of $T_{diss}$ - $q$ lines at each concentration. ....	184

<b>Figure 8.8: Solubility plots applied with using Van's Hoff model for C18/C16 mixtures in toluene. Experimental solubility data was derived by extrapolation of <math>T_{diss}</math>-q lines at each concentration. ....</b>	<b>185</b>
<b>Figure 8.9: Van't Hoff ideality plots for C18/C16 binary mixtures in three solvents of n-dodecane, kerosene and toluene. a) Pure C16. b) Pure C18. c) The equimolar composition of 0.5C18. The ideal solubility was calculated according to the enthalpy of fusion of each composition as provided by DSC measurements in Chapter 6. ....</b>	<b>186</b>
<b>Figure 8.10: Activity coefficient (<math>\gamma</math>) patterns as a function of C18/C16 mixture compositions in three representative solvents: n-dodecane, kerosene at concentration of 308 g/l and 350 g/l in toluene. Resultant structural phases are also presented as obtained from in-situ synchrotron X-ray diffraction analysis of C18/C16/kerosene in Chapter 7.....</b>	<b>188</b>
<b>Figure 8.11: <math>\Delta H_{diss}</math> (a) and <math>\Delta S_{diss}</math> (b) patterns as a function of C18/C16 mixture compositions in three representative solvents: n-dodecane, kerosene at concentration of 308 g/l and 350 g/l in toluene. Resultant structural phases are also presented as obtained from in-situ synchrotron X-ray diffraction analysis of C18/C16/kerosene in Chapter 7.....</b>	<b>190</b>
<b>Figure 9.1: Equilibrium MSZW patterns as a function of composition for C18/C16 binary mixtures in three solvents of n-dodecane (308 g/l), kerosene (380 g/l) and toluene (350 g/l). Resultant structural phases are also presented as obtained from in-situ synchrotron X-ray diffraction analysis of C18/C16/kerosene in Chapter 7.....</b>	<b>194</b>
<b>Figure 9.2: Plots <math>\ln q</math> vs. <math>\ln uc</math> for equi-molar 0.5C18 mixture component in toluene solvent at concentrations of a) 300 g/l. b) 350 g/l. c) 400 g/l. d) 450 g/l. Together with the best linear fit and correlation <math>R^2</math> values. Data points obtained using the poly-thermal method as provided in Chapter 8. ....</b>	<b>198</b>
<b>Figure 9.3: Nucleation mechanism, represented by the slope of <math>\ln q</math> vs. <math>\ln uc</math> according to the "rule of three", for C18/C16 mixtures in three solvents of n-dodecane (308 g/l), kerosene (308 g/l) and toluene (350 g/l). ....</b>	<b>207</b>
<b>Figure 10.1: The integrated SAXS raw data for pure C18 during a poly-thermal cooling crystallisation process at a 0.1°C/min cooling rate, the figure is plotted in scattering counts as a function of q range (<math>\text{\AA}^{-1}</math>) and cooling time (mins).....</b>	<b>216</b>

## Chapter 1 Introduction

*Summary:*

*A general description of the background and motivation of this work will be first introduced. Followed by the defined research question and objectives and how these could be accomplished by a brief delivery plan. Finally, management of this project and an outline of the thesis structure will be given.*

## 1.1 Industrial Background

Increasing concerns with the shortage of feedstock availability of non-renewable petroleum product and greenhouse emissions have caused increasing demand for a search for alternative energy sources. Fuels derived from biomass lipids such as vegetable oils and animal fats have received increasing attention [1, 2]. Different conversion processes of triglycerides (vegetable or animal fats) using different bio-feedstocks will yield fuels with different compositions and properties. The most dominant of these bio-fuels is biodiesel which is defined as a Fatty Acid Methyl Ester (FAME) obtained by a trans-esterification process of triglycerides with alcohol (**Figure 1.1**) [3].

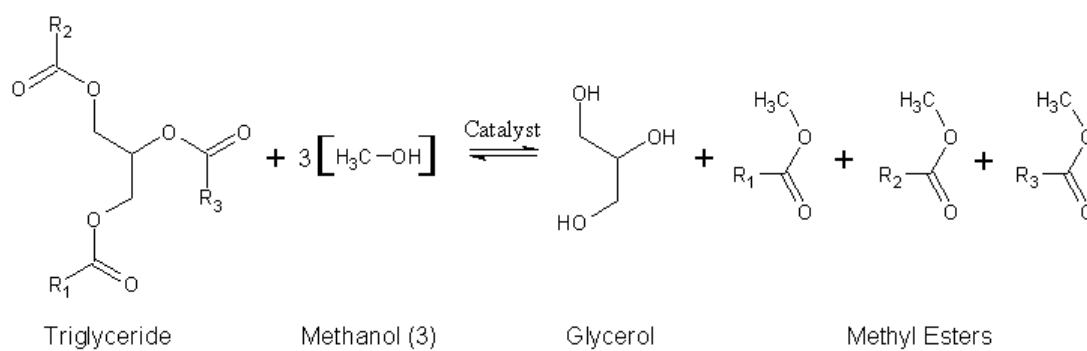


**Figure 1.1 Chemical reactions of trans-esterification process of triglyceride to methyl esters [4].**

Alternatively, hydrotreatment of vegetable oil (HVO) [5] is another way to produce “renewable diesel fuels” used as a blending component for petrodiesel fuels having a similar composition to petrodiesel with a very high cetane number (80-100) and great fuel properties. Typically, the products of HVO fuels are mixtures of hydrocarbons (n-alkanes) and by-products are propane, water, CO and CO<sub>2</sub>. The advantages of the HVO often referred as the second generation of biodiesel, are its compatibility with diesel and the flexibility of feedstock. A series of complicated chemical reactions were induced during the conversion process given in **Figure 1.2**. First of all, the unsaturated double bonds in triglycerides were hydrogenated with hydrogen. After that, the removal of oxygen, n-alkanes with an even carbon chain parity, i.e. octadecane (C18) and hexadecane (C16) could be obtained as the main components of the HVO fuels [6].

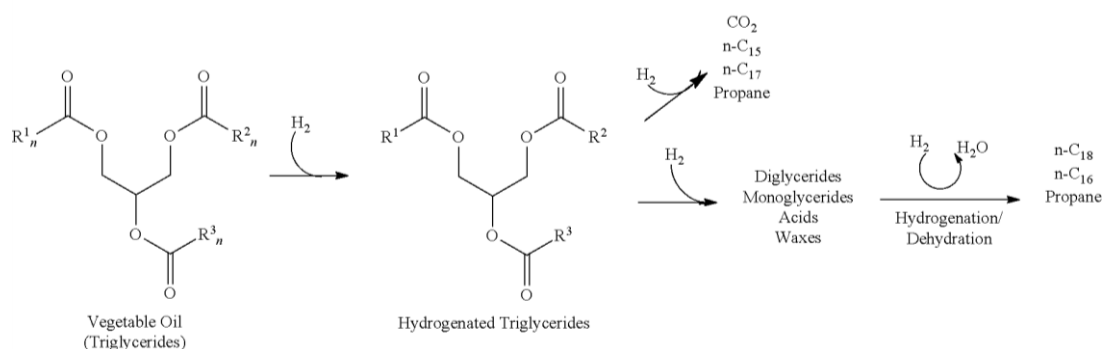


**Figure 1.2 Scheme for hydrogenation reactions of triglycerides to normal alkanes [7].**

Technologically, the cold flow properties of the hydrocarbon fuels like HVO and diesel are undesirable due to the high crystallisation temperatures of long chain compounds. The high molecular weight alkanes become saturated during cooling, which precipitates and acts as a nucleus for further crystallisation. Due to the interactions between the methylene groups in the chains rather than the slow-growing end groups, diesel fuel crystallises as plate-like crystals. At low temperatures, the flat plate-like wax crystals (Figure 1.3) form and melt together which can block the filters causing the low operability of vehicles in cold climate regions. The studies on additives to modify crystal shape and crystallisation temperature on the mixture of diesel fuel have been investigated for many years. Conventional additives can partly destabilise the fast-growing faces of these wax crystals and produce more compact habits in which the crystals are usually needle-like in shape and much reduced in size [8, 9]. However, the consequence of variance distribution of carbon number blending with this HVO into the traditional diesel has altered the crystallisation mechanism of this “new” fuel which means there is a necessity for the development of novel additives. A few attempts have been made to determine the structure of isolated petroleum waxes and to understand the nature of crystallisation when mixed back into dewaxed oil or solvent in known proportions. The mechanism of additive action has been explained in terms of crystal formation. However, the knowledge of the composition of HVO (mainly C18 and C16) in terms of its crystallisation behaviour as a mixture of diesel is inadequate. No attempt appears to have been made to understand the changes that occur in the lattice structure of this new fuel when they are forming gels and also the effects of the nature of the solvents.

To be able to cope with new and changing demands from the economic sector, it is vital that an overall understanding of the crystallisation behaviour of these fuels associated with their structure, morphology, solubility and kinetic behaviour is studied. As a result of that, this research aims to understand the crystallisation of model C18/C16 alkane mixtures through examination of their melt and solution states.

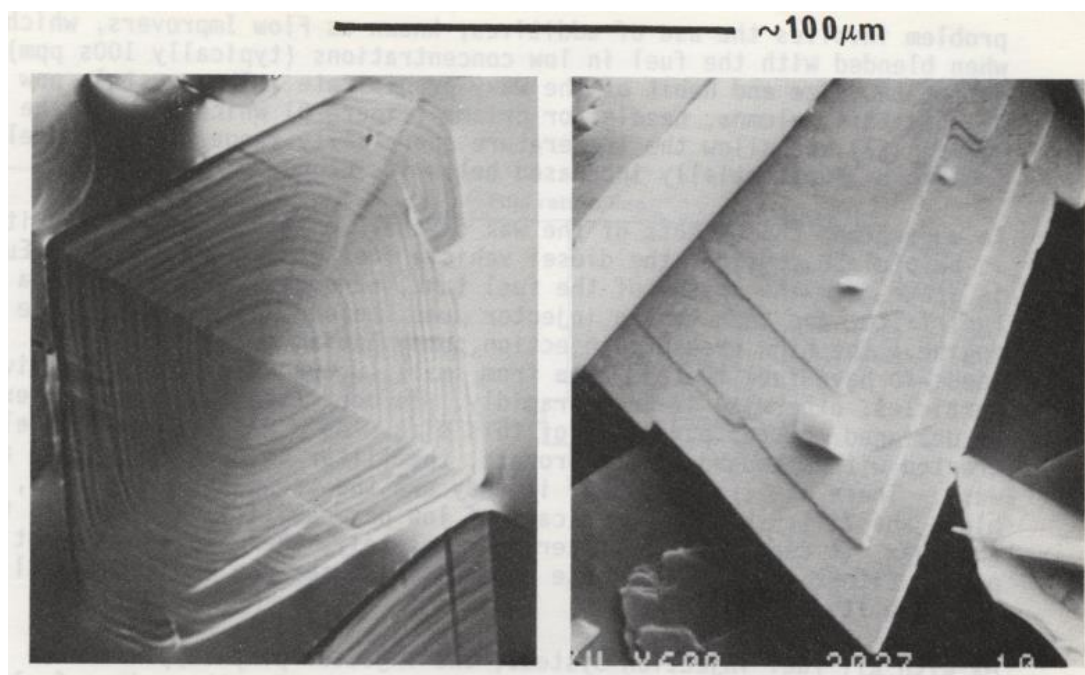


**Figure 1.3 The wax crystal morphology for n-alkane crystallised from diesel fuel into plate-like crystals [10].**

## **1.2 Research Aims and Objectives**

As a result of these issues, this project aims to understand the interplay between crystallisation kinetics, crystal structure and phase behaviour in biofuels derived from HVO feedstock solutions, notably the octadecane (C18) and hexadecane (C16) mixtures. The question underlying this PhD research is:

How does the addition of C18/C16 binary mixtures influence the crystallisation of diesel fuel and how does this relate to the structural properties of the crystals.

This research can be delivered through the following objectives:

- Determine the phase diagram and corresponding crystal structures of binary mixtures of C18/C16 measured as a function of composition for both in melt and solutions.
- Establish the solubility and solution ideality in representative model solvents, i.e. dodecane, toluene and kerosene.
- Characterise the nucleation and growth kinetics of binary mixtures of C18/C16 measured as a function of solvent and composition.
- Study the morphologies and growth rates of C16/C18 mixtures as a function of supersaturation in representative solvents, i.e. n-dodecane, toluene and kerosene.
- Apply the characterisation methods developed in the above studies into blended diesel & biodiesel fuel systems.

To accomplish these objectives, a delivery plan for this PhD work has been developed as outlined below:

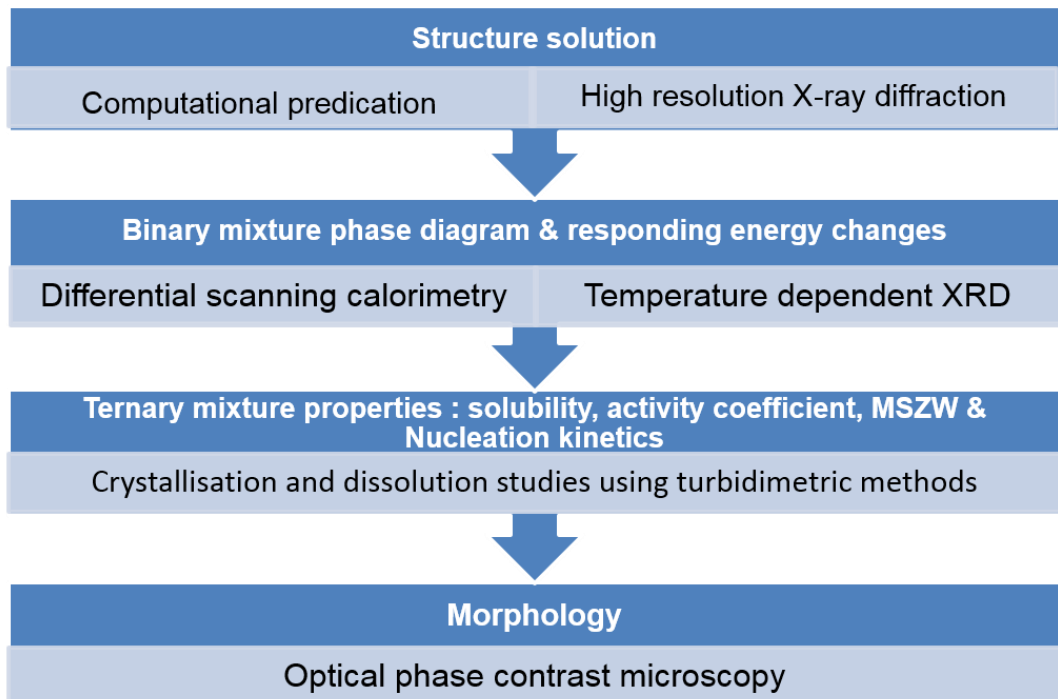


**Figure 1.4 Thesis delivery plan route**

### **1.3 Project Management**

This research project is supported by industrial sponsorship from Infineum UK Ltd. The majority of the research work has been carried out at the Institute of Particle Science and Engineering at the University of Leeds. This research work was carried out under the supervision of Professor Kevin Roberts and supported by Dr Xiaojun Lai from the University of Leeds. My supervisor from our industrial partners was Dr Ken Lewtas, and Dr Iain More and Prof Peter Dowding from Infineum UK Ltd.

The structure prediction of octadecane carried out in Chapter 5 was carried out in collaboration with Dr Robert Hammond from the University of Leeds and Prof Jim Kaduk from American Crystallography Association (ACA) Summer School provided training in crystal structure analysing methods. Development of the poly-thermal technique for analysing solubility and crystallisation kinetics in Chapters 8 and 9 was carried out in collaboration with Dr Diana Camacho-Corzo from the University of Leeds. The collection and analysis of crystallisation data in toluene solvent were supported by a supervised MEng student Mr Peter Lloyd Kaskiewicz.

The high resolution X-ray diffraction data using a STOE diffractometer was collected with the help of Dr Peter Hutchins (Infineum) and was carried out in the Organic Chemistry Laboratory of University of College London (UCL). The synchrotron high resolution X-ray diffraction at beamline I11 was carried out with Dr Peter Hutchins and I11 beamline scientist Chiu Tang.

### **1.4 Report Structure**

This report is divided into ten chapters as listed in Figure 1.3. Following this introduction, Chapter 1 will be the literature review summarised in two chapters. Chapter 2 will be a review of basic knowledge about crystallisation science, crystallisation in solution phase and characteristic methods theory. Chapter 3 will describe the previous study of crystallisation science of n-alkanes. Chapter 4 will be an overview of materials and methods including the materials, equipment and methodologies.

The results and discussion of this study will be divided into five chapters from Chapter 5 to Chapter 9 around the research of C18/C16 binary mixtures crystallisation behaviour in different crystallisation environments using various techniques. The Conclusions and Recommendations for Future Work will be given in the final chapter, Chapter 10.

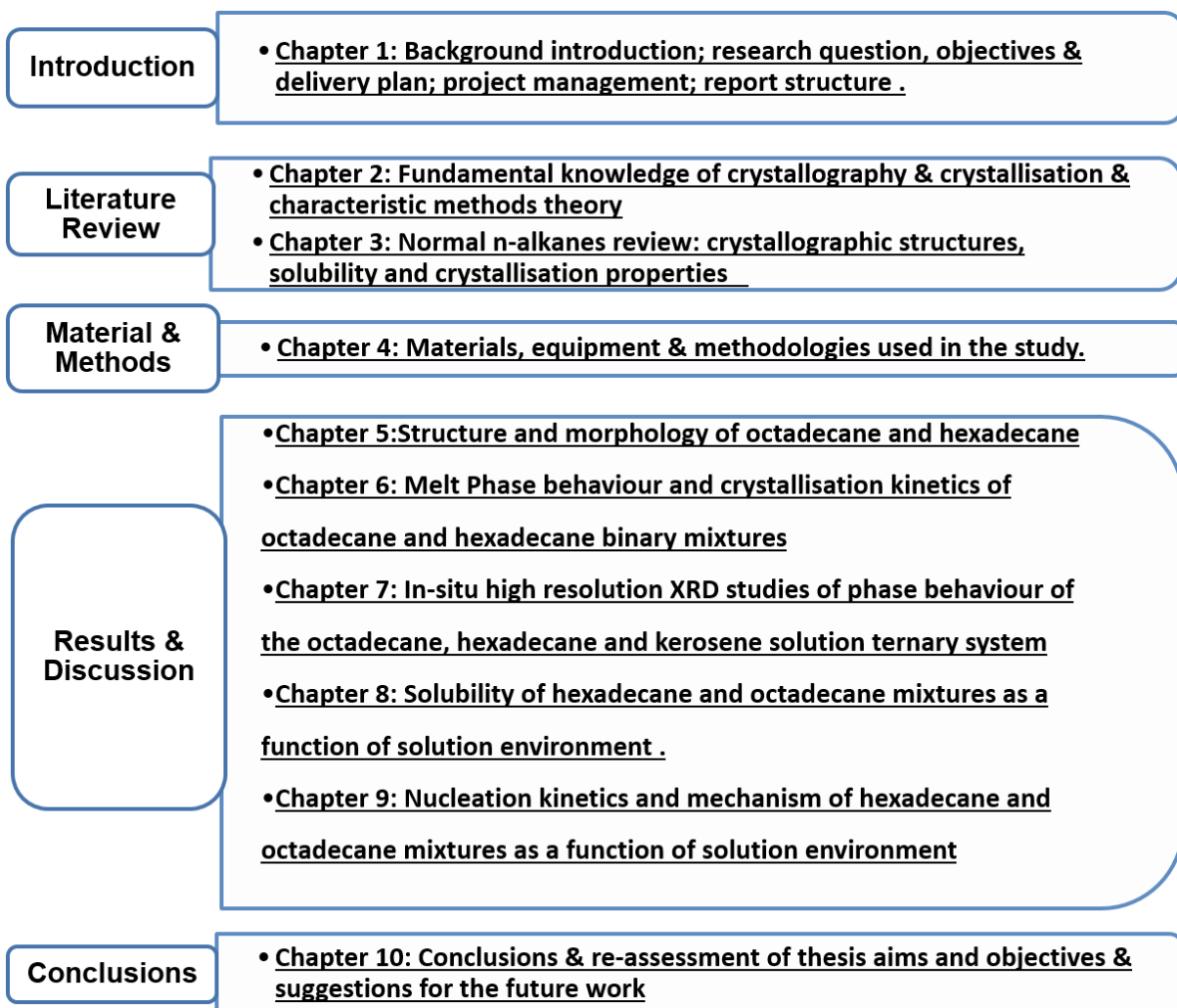


Figure 1.5 Schematic of the report layout

## Chapter 2 Crystallisation Science

*Summary:*

*Reviews the fundamental knowledge of crystallisation science from crystal chemistry, crystallography, morphology, phase equilibria, solubility and nucleation. Together with a review of the theory of characteristic techniques as employed in this research.*

## 2.1 Introduction

This chapter will introduce the fundamental knowledge of crystallisation science from crystal chemistry and crystallography to solution solubility and nucleation kinetics. In addition, the theory of characteristic techniques will be reviewed at the end of this chapter.

## 2.2 Crystals and their Structures

### 2.2.1 Crystallography

Crystals are referred to as three-dimensional repeating patterns of the ordered arrangement of motifs, i.e. atoms, ions or molecules. For the purpose of simplification, the motifs in the crystal are imagined by the points with an identical environment in a 3-dimensional pattern which is known as a lattice. Within it, the smallest repeat is a parallelepiped defined as the unit cell. In Figure 2.1, a 3-dimensional unit cell is described as in crystallographic coordinate axes ( $x$ ,  $y$ , and  $z$ ). The lengths of unit cells parallel to the reference axes are ( $a$ ,  $b$ ,  $c$ ) together with the interaxial angles which are ( $\alpha$ ,  $\beta$ ,  $\gamma$ ) these are the six lattice parameters [11].

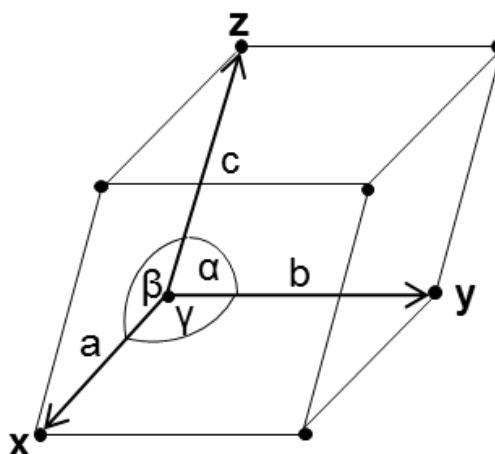


**Figure 2.1: A representative unit cell with crystallographic axes ( $x$ ,  $y$ , and  $z$ ) and lattice parameters ( $a$ ,  $b$ ,  $c$ ,  $\alpha$ ,  $\beta$ ,  $\gamma$ ) [11].**

In order to describe the periodicity of crystals, one other element besides the lattice repetition is used, which is symmetry. Most crystals can show some degree of symmetry in appearance and this can be used to classify the

crystals. For the entire unit cell, there are four types of macroscopic symmetry elements: rotation axes, mirror planes, inversion centre, rotation-inversion axes. On one hand, microscopic symmetry is usually used to describe the arrangement of the atomic or molecular positions [12]. While some crystals may have more than one symmetry element, for instance, cubic unit cells, others may have none [13].

In total, there are 32 possible symmetry elements which can be combined in the crystalline bodies as mentioned above. These so called 32 point groups can be classified into seven crystal systems including cubic, tetragonal, orthorhombic, rhombohedral, hexagonal, monoclinic, and triclinic as shown in Figure 2.2.

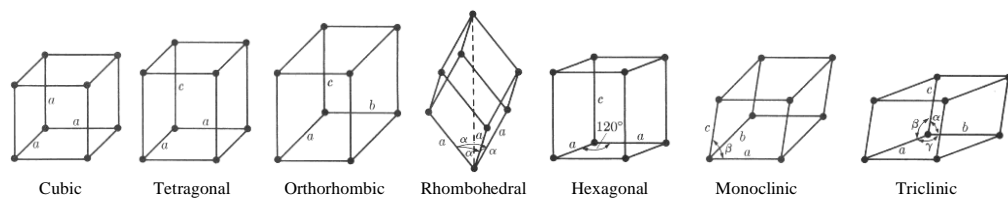


**Figure 2.2: Representation of seven possible crystal unit cells [13]**

Due to the identical environment of the space lattices in a crystal, there are 14 different space lattices, known as “Bravais Lattice” based on the seven crystal systems as shown in Figure 2.3.

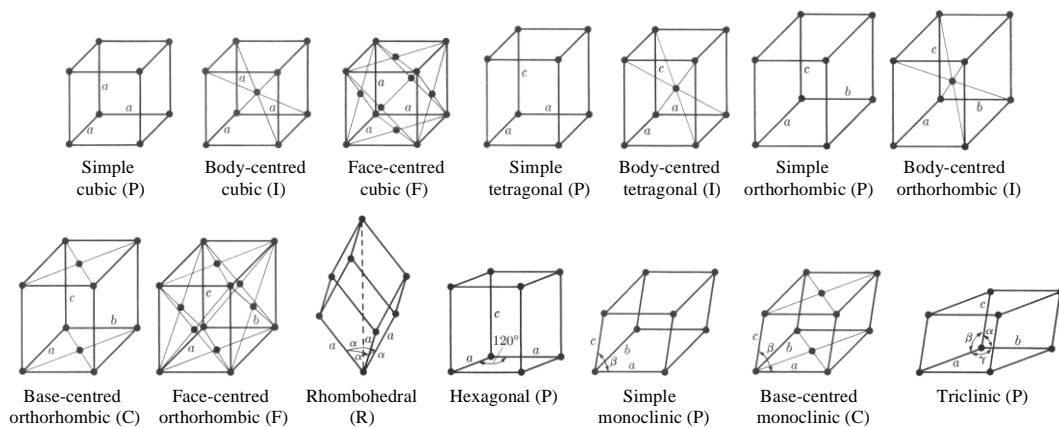


**Figure 2.3: The fourteen possible space lattice called Bravais Lattices [14]**

### 2.2.2 Planes and Miller Indices

Crystallographic planes are described by a set of indices referred to as Miller indices. The crystallographic axes in the plane are fractional intercepts. The reciprocals of the intercepts are defined as  $(h, k, l)$  values in the Miller indices. An example of a plane with assigned Miller indices  $(100)$  is shown in Figure 2.4. The plane has an intercept on the x-axis which is equal to one, the surface is parallel to the y-axis and z-axis with infinity intercepts. Therefore the resultant fractional intercepts are  $(1, \infty, \infty)$  and with regarded Miller indices are  $(1, 0, 0)$ .

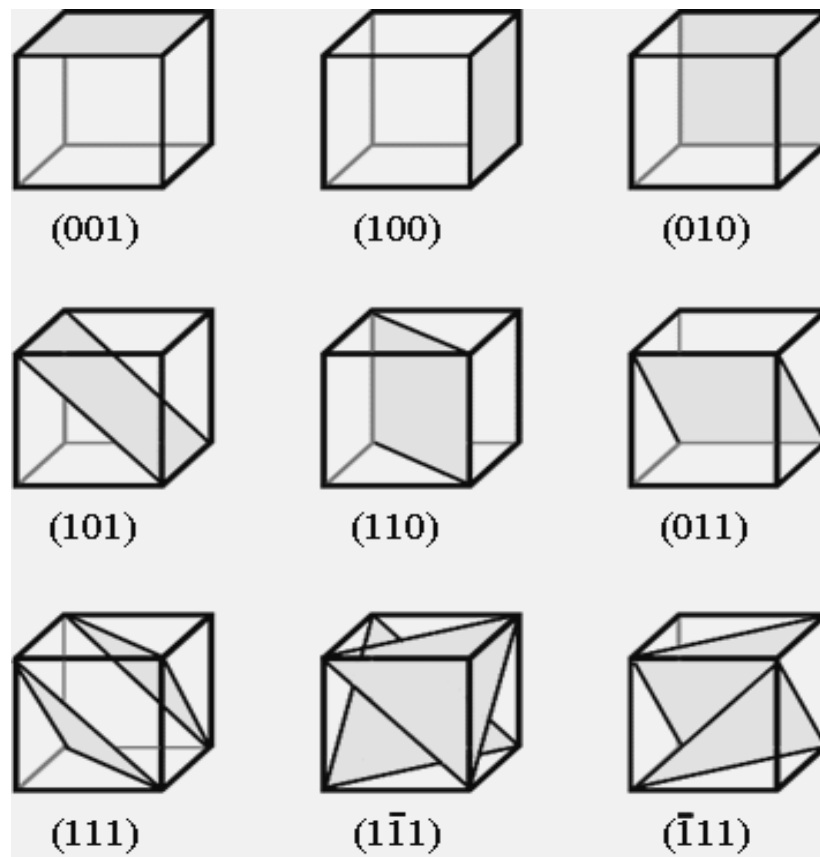


Figure 2.4: Representation of planes together with their Miller indices for a cubic cell [15]

### **2.2.3 Crystal Chemistry and Polymorphism**

The chemistry of a crystal is subject to forces acting between its molecules or particles along with their physical properties, such as size, shape and rotational capacity, all of which affect the crystal structure. Intermolecular bonding plays a key role in the properties of a crystal, with both strong (hydrogen and ionic bonds) and weak (Van der Waals and dipole-dipole interactions) as well as short (Van der Waals and hydrogen bonds) and long (dipole-dipole and ionic bonds) range interactions between molecules having a great effect on mechanical and thermal properties. Organic solids are held together by relatively weak forces, therefore the intensity of these interactions has an effect on the structure itself, with the isotropic behaviour leading to the lowest possible bond length as the molecules maximise the bonding strength.

Polymorphism is defined as a solid material existing in multiple forms of structural crystalline, referred to as polymorphs, which are chemically identical but with varied physicochemical properties, i.e. solubility, thermodynamic properties, conductivity and thermal expansion. Polymorphs with different lattice parameters are normally environmentally dependent on factors such as temperature, solvent nature and the effect of impurities. A different degree of stability is associated with different polymorphs referred as a metastable form (least stable) which is crystallised first according to Ostwald's rule. While the stability of the metastable phase can be varied from seconds to longer-lived, the transition of polymorphs including the metastable form of organic material is highly relative to the change of intermolecular interactions with resultant packing and conformational differences.

### **2.2.4 Crystal Morphology**

The external shape of a crystal defines the crystal morphology and habit. Different crystal faces have different growth rates and relative orientation due to different functional group attachment energy. This is in relation to the strength of the intermolecular interactions in specific crystallographic directions in directing growth rates.

The final crystalline shape of the particle is the slowest growing face. Overall, the growth rate of crystal faces depends on the structure, impurity supersaturation and solvent type [16]. Crystal morphology is particularly important to the fuel and biofuel industry using additives and impurities to inhibit the growth of specific faces and modify the plate-like crystals to needle-like and improve the flowability.

## 2.3 Phase Equilibria

### 2.3.1 The Phase Rule

A phase is a homogeneous part of a system with identical physical nature. Any system comprising multiple phases is defined as a heterogeneous system. The thermodynamic equilibrium follows Gibb's phase rule,  $F = C - P + 2$  where  $F$  is the number of freedom degrees,  $C$  is the number of components and  $P$  is the number of phases. The main variables which can affect the phase number in a system are temperature, pressure or concentrations. Without changing the number of phases, however, one or more variables can be independently changed, the number is defined as degrees of freedom in a phase diagram. Whilst the number of components in a system is chemically dependent and is always fixed.

An example of a one-component system of water, ice and vapour, as three phases are in equilibrium with  $C=1$ ,  $P=3$  and  $F=0$ . Therefore, no variables can be changed without phase transformation and the system will be defined as invariant.

### 2.3.2 Two Component Phase Diagram

A phase diagram showing conditions at which thermodynamically distinct phases can exist at equilibrium in the system with certain variables such as temperature, concentration and pressure. For normal crystallisation processes, the main attention will be on the temperature and component concentration effects. Thus the phase changes can be represented on a temperature-composition (T-X) diagram at constant pressure. The phase rule is therefore reduced to  $F=C-P+1$ . Simple types of two-component solid phase in eutectic and solid solution are given in **Figure 2.5** to illustrate that information can be obtained from a phase diagram.

A solid solution is two phases behaving like a homogeneous liquid solution with complete miscibility in the solid phase (**Figure 2.5a**).  $T_A$  and  $T_B$  are the

melting point of the single components of A and B, respectively. All compositions of the two mixtures have melting temperatures between  $T_A$  and  $T_B$ , notably as a temperature range rather than a point. The onset point of melting is the liquidus point, defined at the beginning of liquid formation, and whereas the end point is the last solid which becomes liquid and is defined as the solidus point. In between the liquidus and solidus points are solid and liquid mixtures. For example point O, denotes a liquid of composition C in equilibrium with a solid solution of composition D. To determine the amount of solid and liquid existing at this point, the lever rule can be applied by measuring the distances of OC, OD, and CD: mass of solid (with composition D) =  $[x/(x + y)]$ , while the mass of liquid (with composition C) =  $[y/(x + y)]$ .

Another extreme condition is one where the two mixed solids are entirely insoluble, which is called the eutectic system and this is shown in **Figure 2.5b**. The temperatures above the liquidus line of the two components are completely soluble liquid while at the temperature below the solidus line they are a mixture of crystals A and B. The melting temperatures of all the compositions are reduced and the onset points are identical at the eutectic temperature  $T_E$ . The eutectic point (E) can be distinguished as the only composition of mixture components where melting occurs immediately at one point. The system is invariant, in which three phases of liquid, crystal A and B are in equilibrium with  $C=2$ ,  $P=3$  and  $F=0$  according to the reduced phase rule.

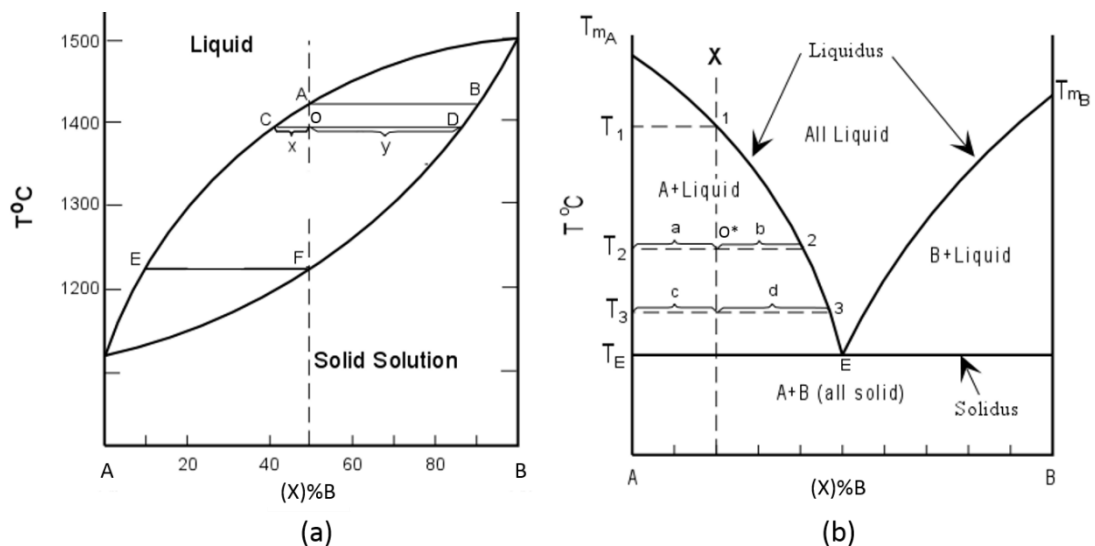


**Figure 2.5: Simple two-component phase diagram with temperature versus composition (T-X): (a) Solid solution type; (b) Eutectic mixture.**

## 2.4 Solutions, Solubility and Supersaturation

### 2.4.1 Melts, Solutions and Solubility

A solution is a homogeneous mixture of two or more components including gaseous, liquid and solid. It is conventionally known as solvents and solutions within a liquid solution. Strictly, a liquid phase that is close to its freezing point should be referred to as a melt phase, this also includes multiple substances that are homogeneously mixed in liquid and will crystallise out at different temperatures towards a cooling process. A solution is formed which involves the solute separating into ions or molecules, and each ion or molecule is surrounded by molecules of solvent, the interaction between the solute particles and the solvent molecules is called solvation. The enthalpy change in solution during dissolution will first involve internal energy to break the intermolecular bonds between solvent-solvent and solute-solute interaction respectively. In addition, energy will be released when new bonds are formed between solute-solvent molecules [13].

When excess solid is mixed with a solvent at a constant temperature, the solid will dissolve until equilibrium is established. The composition of this saturated solution is the equilibrium solubility at that temperature. The solubility of a substance fundamentally depends on the physical and chemical properties of the solute and solvent, i.e. particle size. In common, the solubility of a solution will increase with increasing temperature. A disconnected point of the solubility curve indicates the phase transition point as well [17].

### 2.3.2 Ideal and Non-ideal Solutions

An ideal solution is in terms of the molecular interaction from solute-solvent molecules being the same as the solute-solute and solvent-solvent molecules in the solution [13]. Even though the critical ideal solution is unrealistic, this definition can still be used as a reference of the ideality of a solvent. For an ideal solution, the solubility can be calculated by Van't Hoff's equation:

$$\ln x = \frac{\Delta H_f}{R} \left[ \frac{1}{T_f} - \frac{1}{T} \right]$$

(2.1)

where,

$x$  is the mole fraction of the solute in the solution,

$T$  is the solution temperature (K),

$T_f$  is the melting temperature of the solute (K),

$\Delta H_f$  is the molar enthalpy of melting of the solute ( $\text{J mol}^{-1}$ ),

$R$  is the gas constant ( $\text{J mol}^{-1} \text{K}^{-1}$ ).

The solubility of an ideal solution at any temperature can be calculated by the known melting temperature and the enthalpy of fusion. However, this solubility curve is not related to any specific solution. Since  $\Delta H_f$  is equal to  $T_f$  multiple  $\Delta S_f$  which is the entropy of fusion. The Van't Hoff equation can be substituted into:

$$\ln x = -\frac{\Delta H_f}{RT} + \frac{\Delta S_f}{R} \quad (2.2)$$

In addition, a plot of  $\ln x$  versus  $\frac{1}{T}$  for ideal and experimental solubility provides a useful tool of how the system behaves with respect to the solute and the solvent. As the slope of this plot should be the value of  $-\frac{\Delta H_f}{R}$  for the ideal solution, otherwise the solution shows non-ideality. In this case, the change in enthalpy and entropy of the mixing solution have to be taken into account. Equation (2.2) should be changed as:

$$\ln x = -\frac{\Delta H_{diss}}{RT} + \frac{\Delta S_{diss}}{R} \quad (2.3)$$

where  $\Delta H_{diss}$  and  $\Delta S_{diss}$  are the molar enthalpy and entropy of dissolution of solute.

Also, in the mixing process, the Gibbs free energy can be approached with the entropy and enthalpy changed in the dissolution as:

$$\Delta G = \Delta H - T\Delta S \quad (2.4)$$

For an ideal solution, the Gibbs free energy of mixing two liquids can be assumed as:

$$\Delta G = RT \ln a \quad (2.5)$$

where,  $a$  is the mole fraction of one component in the ideal solution. The enthalpy change for an ideal solution is zero, thus from Equation (2.4), the entropy change during the mixing is:

$$S = -R \ln a \quad (2.6)$$

The activity coefficient ( $\gamma$ ) is a concept to describe the offset of real solution behaviour with the ideal one. For example, the free energy change for a non-ideal solution can be modified by the appropriate activity coefficient as ( $\gamma x$ ). In other words:

$$a = \gamma x \quad (2.7)$$

$$\gamma = \frac{a}{x} \quad (2.8)$$

The activity coefficient ( $\gamma$ ) can be obtained from Equation (2.1) applying the Van't Hoff equation as:

$$\ln(x\gamma) = \frac{\Delta H_f}{R} \left[ \frac{1}{T_f} - \frac{1}{T} \right] \quad (2.9)$$

### 2.3.3 Supersaturation

A solution could actually dissolve more material than the normal solubility as measured in an equilibrium condition. This is known as supersaturation which is the driving force of crystallisation which could be achieved from changes in solubility of the solution in two different ways, by cooling or by solvent evaporation, as shown in **Figure 2.6**, at a temperature of  $T_A$ , concentration of the solution is under the solubility curve which means the solution is under-saturated. If the change in the solution is either cooling down to  $T_B$  or increasing the concentration to  $C_B$ , it will be just saturated. Further, going to the point of  $T_C$  or  $C_C$ , the concentration of solution exceeds the equilibrium solubility tending to supersaturation.

The supersaturation can be described in terms of concentration driving force:

$$\Delta C = C - C_e \quad (2.10)$$

Where:  $C$  is the solution concentration at a specific temperature and  $C_e$  is the concentration at equilibrium with that temperature. From a thermodynamic point of view, it can be expressed using the supersaturation ratio in Equation (2.11), which is commonly expressed as a relative supersaturation ratio (2.12).

$$S = \frac{C}{C_e} \quad (2.11)$$

$$\frac{\Delta C}{C_e} = S - 1 \quad (2.12)$$

The state of supersaturation is an essential stage to form the nucleation in order to start the crystallisation process. To classify supersaturated solution in which the primary nucleation could occur, Oswald [18] introduced the labile region and metastable region in which spontaneous crystallisation happens or not respectively. Under the solubility curve, the stable zone which is

unsaturated where the crystallisation is impossible. The significance of MSZ and the experimental method to measure the MSZW will be introduced in the following section.

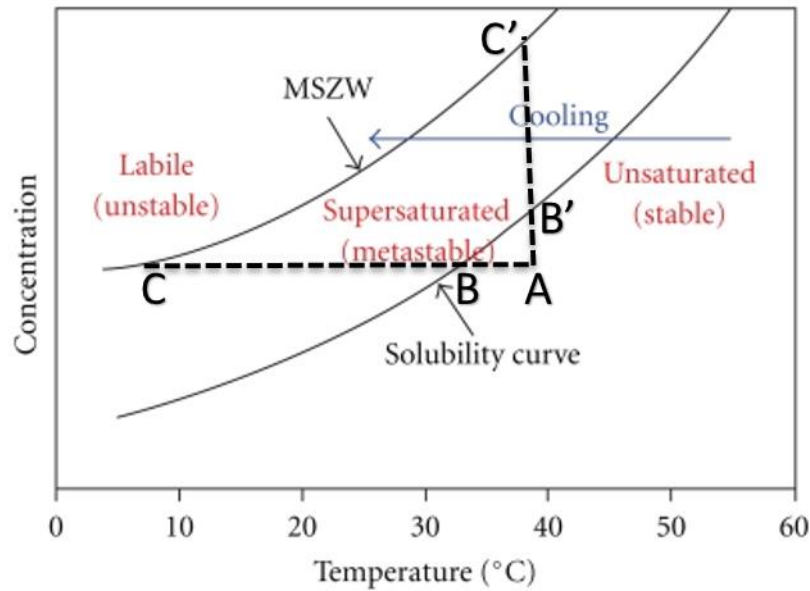


**Figure 2.6: A representation of solubility and supersolubility curves with the three regions include: labile, metastable and stable [13].**

## 2.5 Crystallisation Kinetics

### 2.5.1 Nucleation

The supersaturation condition of a solution is not sufficient to form crystals; it must begin with some mini solid bodies, i.e. embryos, nuclei or seeds that act as the centre of crystallisation [13].

Nucleation is defined as the process where solute molecules aggregate to form clusters or nuclei and start to grow after overcoming the energy barrier of cluster stability. This process is classically divided into two stages: primary and secondary nucleation which can be distinguished by the presence of crystalline or seed crystal. Furthermore, the primary nucleation can be split into homogeneous and heterogeneous nucleation. The first one is spontaneous nucleation whereas the later one is nucleation induced by other substances.

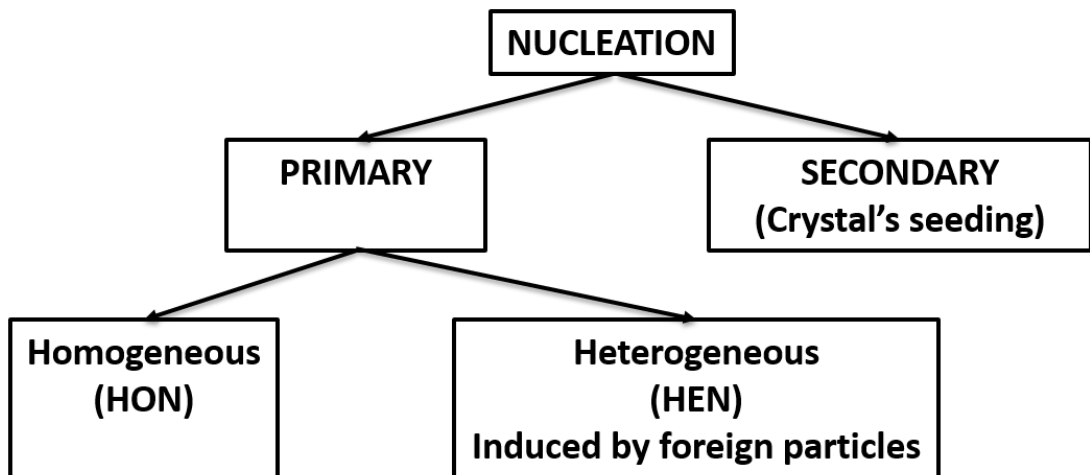


Figure 2.7: Nucleation classification [13]

### 2.5.1.1 Homogeneous nucleation

Solute molecules in the supersaturation coagulate to form a cluster which has the tendency to re-dissolve back into the solution. If enough molecules come together to form an embryo where lattices start to form and reach the critical cluster size can be called a nucleus which is likely to form additional bimolecules into it to make it stable like the scheme in Figure 2.8.

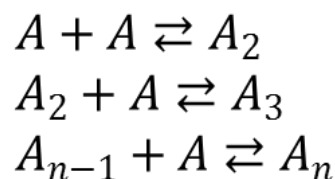


Figure 2.8: Scheme shows the bimolecular addition process [13]

The critical nucleus is going to perform either a crystal lattice, which is going to be a macromolecular crystal or a liquid state with no order lattice structure. This is better illustrated by the classical theory of free energy in Figure 2.9. The overall change in free energy ( $\Delta G$ ) during nucleation is illustrated by Equations (2.13) and (2.14).

$$\Delta G = \Delta G_S + \Delta G_V \tag{2.13}$$

$$\Delta G = 4\pi r^2 \gamma + \frac{4}{3} \pi r^3 \Delta G_V \tag{2.14}$$

$\Delta G$  is equal to the sum of the surface and volume free energy of  $\Delta G_S$  and  $\Delta G_V$  respectively.  $\Delta G_S$  increases with new solid phase per unit surface area and  $\Delta G_V$ , which is the volume free energy.  $\gamma$  is the interfacial tension between the crystal and the surrounding liquid interphase.  $\Delta G_S$  is dependent on a magnitude of  $r^2$  which is the radius of the sphere and  $\Delta G_V$  is  $r^3$  dependence.

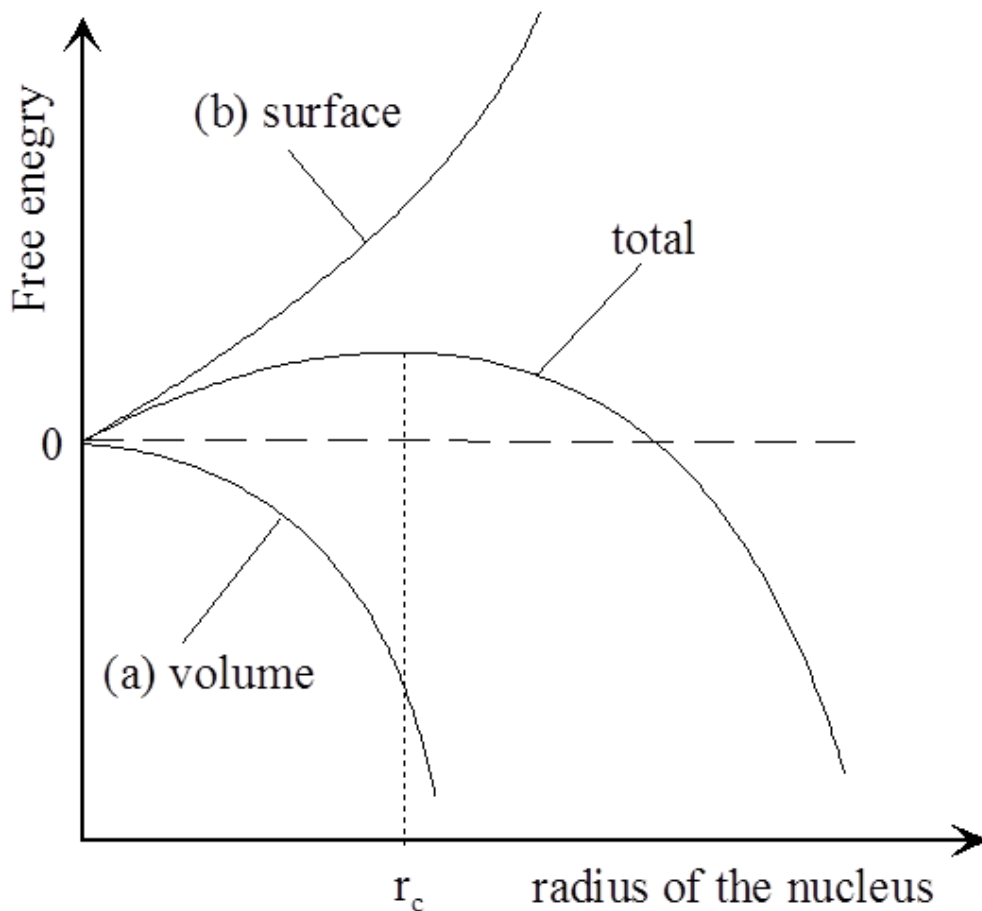


Figure 2.9: Free energy change corresponding to a critical nucleus size [13]

As the opposite effect on the surface and volume given in **Figure 2.9**, the total excess of free energy can attain maximum value at the critical radius ( $r_c$ ). The tendency of a newborn nucleus depends on its radius size and should result in a reduction of total free energy. A nucleus prefers to dissolve to achieve the reduction of free energy if the nucleus is smaller than  $r_c$ , as the free energy is decreasing with the reducing of radius size. Conversely, for a nucleus larger than  $r_c$ , the growing of a nucleus can result in a decrease of free energy, therefore, the nucleus will prefer to grow and become stable. The critical radius of nucleus assumed as a 3-D sphere can be calculated based on the equation below,

$$r_c = \frac{2\gamma\omega}{kT\ln(1 + \sigma)} \quad (2.15)$$

Where  $\gamma$  is the surface energy,  $\omega$  is the molecular volume,  $k$  is the Boltzmann constant,  $\sigma$  is the supersaturation. Thus, the radius of the nucleus is decreased with the increase of supersaturation which means the high supersaturation will make the nucleation easier due to a smaller size being needed. The nucleation rate e.g. the number of nuclei formed by unit time by unit volume can be expressed:

$$J = k_j \exp\left[-\frac{16\pi\gamma^3 v_0^2}{3k^3 T^3 (\ln S)^2}\right] \quad (2.16)$$

Parameter of  $k_j$  can be related to attachment frequency of monomers to the nucleus ( $f^*$ ), concentration of nucleation sites ( $C_0$ ) and the zeldovich factor  $Z$  by expression (2.17). The attachment frequency of monomers is controlled by two factors from volume diffusion and interface transfer.

$$J = z f^* C_0 \exp\left(-\frac{W^*}{kT}\right) \quad (2.17)$$

### 2.5.1.2 Heterogeneous nucleation

Primary nucleation may also be initiated by suspended particles of foreign substances, and this mechanism is generally known as heterogeneous nucleation (HEN) [1, 14]. Foreign particles provide a surface for nucleation, decreasing the interfacial tensions to be overcome for nucleation to occur. Thus, the nucleation work decreases and nucleation rates drastically increase. The homogeneous nucleation interfacial tension  $\gamma$  is related to the effective heterogeneous interfacial tension  $\gamma_{eff}$  by  $\gamma_{eff} = \psi \times \gamma$ . Where the activity factor  $\psi$  ranges between 0 and 1 and is associated with the contact angle between the nucleus and the heterogeneous particle.

### 2.5.2 Methods to assess nucleation kinetics using the polythermal method

The characteristics of the crystallisation process are not only related to the chemical property of the solution, it also depends on the kinetics which is related to the MSZW as the driving force of the process. As discussed in the previous section, from **Figure 2.6** it can be seen that the metastable zone is the region between the equilibrium solubility curve and the supersaturation curve. The supersaturation is determined by the concentration driving force as in Equation (2.16) [19]:

$$\Delta C = C - C_e \quad (2.16)$$

where, supersaturation is ( $\Delta c$ ),  $C$  solution's concentration and  $C_e$  solution's equilibrium concentration. The MSZW which is the maximum supersaturation is a useful parameter as it can be related to the nucleation rate,  $J$ , from the empirical law through Equation (2.17):

$$J = k(\Delta c_{max})^n \quad (2.17)$$

where:  $k$  is the nucleation constant,  $n$  is the nucleation order. As the supersaturation ( $\Delta c$ ) can be related to the supercooling ( $\Delta T$ ) defined in Equation (2.18) through Equation 2.19:

$$\Delta T = T_e - T \quad (2.18)$$

$$\Delta c = \left( \frac{dc_0}{dT} \right) \Delta T \quad (2.19)$$

where  $dc_0/dT$   $dc$  is the slope of the solubility curve at the given temperature  $T$ , and combination of Equations (2.17) and (2.19) gives the following relationship:

$$J = k_n \left( \left( \frac{dc_0}{dT} \right) \Delta T \right)^n \quad (2.20)$$

$T$  is induction time or MSZW can be influenced by a crystallisation environment, i.e. solution temperature [20], impurities [21] and stirring rate [22]. Moreover, the cooling rate has shown the most relative factor discovered by Bonnin [23] in crystallisation MSZW and thus can be referred as  $\Delta T_{max}$ . According to Nyvlt's equation, it suggests that there is a linear relationship between cooling rate ( $q$ ) and critical undercooling ( $\Delta T_{max}$ ). A poly-thermal method to determine the MSZW by a known concentration solution at a specified cooling rate according to Nyvlt approach is introduced in the following section.

Nyvlt [24] and Nielsen [25] assumed that at the early stage of nucleation, the rate of nucleation changes to the same as that of supersaturation rate by cooling which can be expressed as:

$$J = \varepsilon \left( \frac{dc_0}{dT} \right) q \quad (2.21)$$

Where  $q$  is the cooling rate at supersaturation, connect with the empirical law in Equation (2.19):

$$\varepsilon \left( \frac{dc_0}{dT} \right) q = k_n \left( \left( \frac{dc_0}{dT} \right) \Delta T \right)^n \quad (2.22)$$

By taking the logarithms of this equation we can obtain the linear relationship of cooling rate ( $q$ ) and supercooling ( $\Delta T_c$ ) with a slope which is the nucleation order ( $n$ ).

$$\log q = (n - 1) \log \frac{dC_e}{dT} - \log \varepsilon + \log K_n + n \log \Delta T_c \quad (2.23)$$

From the poly-thermal method, a solution under cooling control at a stable cooling and heating rate is used to increase the temperature to the solution to detect the dissolution temperature. Similarly, the crystallisation temperature was detected when cooling this temperature to form the crystals. From Equation (2.18) the maximum undercooling can be taken to be equal to the temperature of dissolution minus the crystallisation temperature.

Later on, Kubota [26] suggested that the measured critical undercooling related to the equipment sensitivity on the onset point of crystal formed. He then assumed the MSZW from experimental measurements are from the onset point where the nucleus accumulated to some extent. By this assumption,  $\ln q$  and  $\ln \Delta T_c$  is still in a linear relationship. Over recent decades, Sangwal [27] employed classical theory to derive a linear relationship from  $1/(\Delta T_c)^2$  and  $\ln q$ .

More recently, Kolmogorov-Johnson-Mehl-Avrami (KJMA) takes account of the initial fraction of crystallised volume or the number of nucleated crystallites [28]. Based on this, the Kaschiev, Borissova, Hammond and Roberts (KBHR) [29, 30] approach allows from a poly-thermal data, which can determine the important kinetic parameters, gives an insight understanding of nucleation and growth process. It also differs two nucleation mechanisms from instantaneous (IN) that all crystals would form once such super-cooling has been reached notably as  $C_0$  (the initial concentration) and progressive nucleation (PN) that crystals are continuously forming during the cooling process [31].

KBHR employed the dependence of critical undercooling ( $u_c$ ) on cooling rate with linear relationship in  $\ln$ - $\ln$  co-ordinates which revealed the nucleation mechanism from IN or PN within the inequalities of  $u_c$  were smaller than 0.1 and  $au_c$  being smaller than 1, where  $a$  is the dimensionless molecular latent heat of crystallisation, shown in Equation (2.26), where:  $\lambda$  – is the molecular latent heat of crystallisation,  $k$  – Boltzmann constant. A slope of  $\ln u_c$ - $\ln q$  is larger than three indicating a PN mechanism, while a slope is smaller than three indicating an IN ruled nucleation. Critical undercooling  $u_c$  can be determined:

$$\Delta T = T_e - T \tag{2.24}$$

Relative critical undercooling ( $u_c$ ) which is a dimensionless parameter can be further determined:

$$u_c = \frac{\Delta T}{T_e} \quad (2.25)$$

$$a = \frac{\lambda}{kT_e} \quad (2.26)$$

For the cases of PN, critical undercooling and the cooling rate can be correlated with  $\ln q$  with non-linear least squares fit from Equation (2.27).

$$\ln q = \ln q_0 + a_1 \ln u_c - \frac{a_2}{(1 - u_c)u_c^2} \quad (2.27)$$

Where:  $a_1 = 3$ ,  $a_2 = b$  and  $q_0$  is given by Equations (2.28) and (2.29):

$$b = \frac{k_n v_o^2 \gamma_{eff}^3}{kT_e \lambda^2} \quad (2.28)$$

Where:  $k_n$  – nucleus shape factor,  $v_o$  – volume occupied by a solute molecule in the crystal,  $\gamma_{eff}$  – nucleus effective interfacial tension.

$$q_0 = \frac{VK_j T_e}{N2b} \quad (2.29)$$

Where:  $V$  – volume of solution,  $K_j$  – nucleation rate constant.

Crystal growth related to  $a_1$ ,  $a_2$  is proportional or equal to  $b$  and  $q_0$  is subject to both nucleation and growth parameters.

This method also allows for the determination of the critical radius of the nucleus ( $r_c$ ) as well as the number of molecules within that nucleus ( $i_c$ ), shown by Equations (2.30) and (2.31), respectively.

$$r_c = \frac{2\gamma_{eff} v_o}{\lambda u} \quad (2.30)$$

$$i_c = \frac{2bkT_e}{\lambda u^3} \quad (2.31)$$

## 2.6 Crystallisation Characteristic Techniques

### 2.6.1 Differential scanning calorimetry (DSC)

Phase transformation and/or chemical reactions are mostly accompanied by changes in enthalpy. DSC is a thermo-analytical technique used for phase change observation and the associated energetic changes.

The principle of DSC can be regarded as the measurement of the heat difference between the sample and one reference placed in the same situation as a function of temperature. The instrument can detect the temperature difference between the sample and reference during heating or cooling and converts this through calibrating the amount of heat added to, or removed from, the sample at the sample temperature to compensate for the temperature difference.

The typical result of one experiment is represented by a curve of heat flux as a function of temperature as shown in **Figure 2.10**. Peaks having two different directions can be achieved as the positive and negative peak regarding the exothermic and endothermic reactions in the sample during the experiment. In the evaluation window, the data regarding melting and crystallisation temperatures and the corresponding heat of fusion can be evaluated by the selection of the peak area. Need to be noted, only a pure sample gives a sharp peak, while an impure sample would show a broader peak, an indefinite start and a blunt maximum.

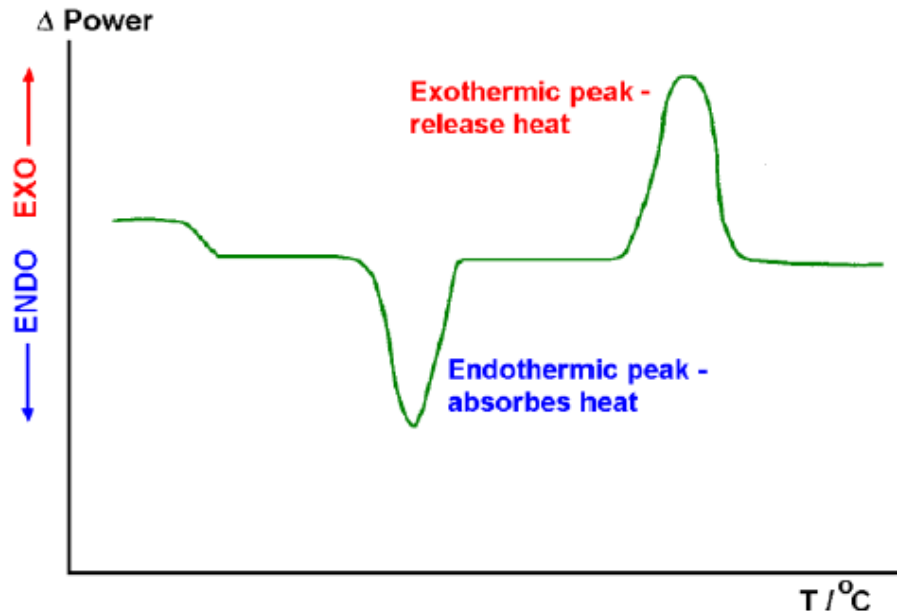


Figure 2.10: Typical DSC curve: heat flow as a function of temperature [32]

## 2.6.2 X-rays and Diffraction

X-radiation, known as X-ray, is a form of electromagnetic radiation having a wavelength ( $\lambda$ ) in the range of  $10^{-2}$  to  $10^2$  nanometres and energies around  $200 \text{ eV}$  to  $10^6 \text{ eV}$ . The energy of each quantum,  $E$  is related to its frequency  $\nu$  in Equation (2.31). Since  $\lambda$  is related to the frequency and the speed of the light, thus the wavelength of the x-ray can be given by the energy as shown in Equation (2.32).

$$E = h\nu \tag{2.31}$$

$$\lambda = \frac{hc}{E} \tag{2.32}$$

### 2.6.2.1 X-ray tube

X-rays are generated from a tube, as shown in **Figure 2.11**, which consists of two metal targets enclosed in a vacuum tube. A large amount of electric current will be passed through the cathode which is made of a tungsten filament and heated to produce a source of the electron beam. The high electrical potentials between the cathode and the anode pull electrons from the cathode and accelerate towards the anode. The interaction of the electrons in the anode results in the emission of a continuous Bremsstrahlung spectrum and also characteristic X-rays from the target material. Beryllium is used for the window as it transmits X-rays well resulting in an increase in the intensity of the beam source.

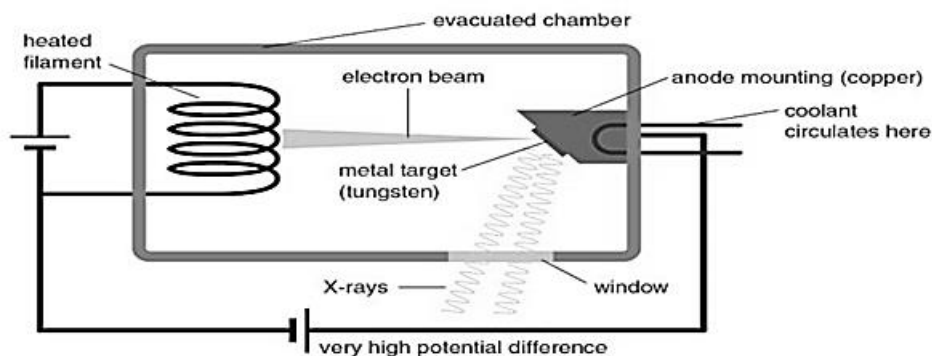


**Figure 2.11: Schematic of a modern x-ray tube [33].**

### 2.6.2.2 Filters and Monochromators

A typical x-ray spectrum is shown in **Figure 2.12**. It consists several components including the continuous spectrum represented by the high background and the characteristic lines nominated by the sharp peaks. These characteristic lines are useful in normal diffraction work, namely  $K\alpha$  and  $K\beta$ . The  $K\alpha$  X-rays on the right hand are amplified to resolve the two close wavelengths of  $K\alpha_1$  and  $K\alpha_2$  components.

The most diffraction experiments require an X-ray radiation which is monochromatic or as close as possible. The intensity of the undesirable lines ( $K\beta$ ) can be effectively reduced by passing through a filter made up of materials having absorption edge in between of  $K\alpha$  and  $K\beta$  wavelength of the

target metal. For example, a nickel filter can be used for copper, and zirconium for molybdenum.

Modern diffractometers, alternately use a single-crystal monochromator to diffract the selected radiation to achieve a narrower wavelength distribution, graphite and silicon are commonly used. The principle of monochromator obeys the Bragg's law, with a particular lattice spacing of the monochromatic crystal, differing wavelengths radiation are diffracted at different angles.

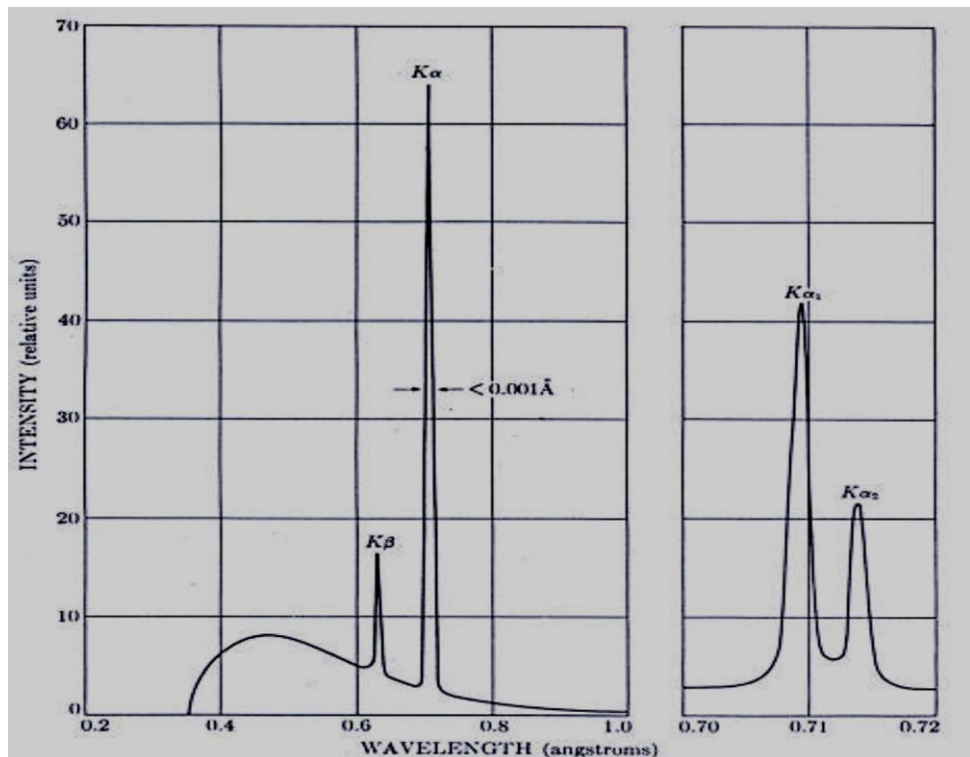


Figure 2.12: X-ray spectrum of  $K_{\alpha}$  and  $K_{\beta}$  and the  $K_{\alpha 1}$  and  $K_{\alpha 2}$ .

### 2.6.2.3 Diffraction

When two waves are in the same space, they can either be constructive interference or destructive interference due to the two waves being in phase or anti-phase respectively. For example, in **Figure 2.13**, if two waves having the same frequency and amplitude are in phase, the resultant wave showed the same frequency but twice their amplitude. Whereas if the two waves are in the same frequency and amplitude but are out of phase then the resultant wave is completely zero amplitude.

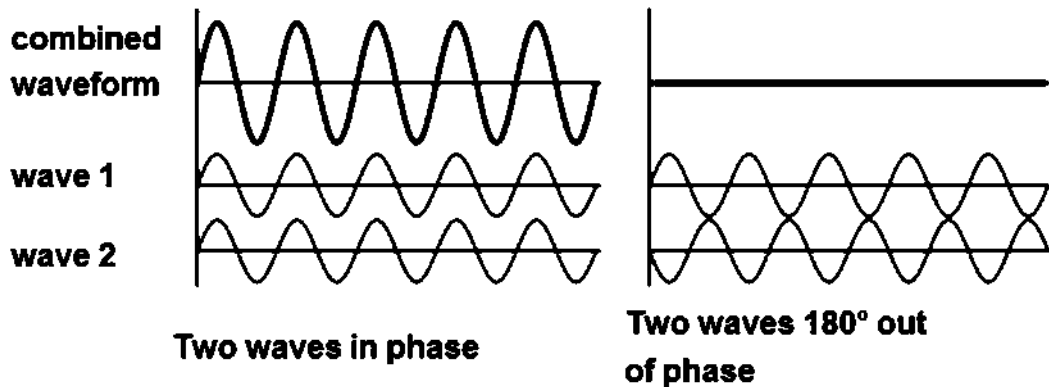


Figure 2.13: Illustration of the superposition of two waves in constructive interference (Right) and destructive interference (left). [\[https://en.wikipedia.org/wiki/Interference\\_\(wave\\_propagation\)\]](https://en.wikipedia.org/wiki/Interference_(wave_propagation))

The incident radiation is absorbed and then re-emitted in a different direction which is known as scattering. Interference is the superposition of two or more of these scattered waves, producing a resultant wave that is the sum of the overlapping wave contributions. Diffraction is constructive interference of more than one scattered wave. There is no real physical difference between constructive interference and diffraction [34].

#### 2.6.2.4 Bragg's Law

As mentioned previously, scattering waves from many of atoms can interfere and be constructive waves, then we can get the specific directions of these diffracted waves. Bragg's law relates these directions with the wavelength of incident X-rays and the spacing of the atomic planes.

In order for the waves to interfere constructively, the difference in the travel path must be equal to integer multiples of the wavelength. When this constructive interference occurs, a diffracted beam of X-rays will leave the crystal at an angle equal to that of the incident beam. To illustrate this feature, consider the schematic diagram given in **Figure 2.14**. In this, we see a crystal with crystal lattice planar distances  $d$ , where the path length difference between the ray paths ABC and A'B'C' is an integer multiple of the wavelength, constructive interference will occur for a combination of that specific wavelength, crystal lattice planar spacing and angle of incidence ( $\theta$ ). Each

rational plane of atoms in a crystal will undergo diffraction at a single, unique angle for X-rays of a fixed wavelength.

The general relationship between the wavelength of the incident X-rays, angle of incidence and spacing between the crystal lattice planes of atoms is known as Bragg's Law,

$$n\lambda = 2d\sin\theta \quad (2.33)$$

Where  $n$  (an integer) is the "order" of reflection,  $\lambda$  is the wavelength of the incident X-rays,  $d$  is the inter-planar spacing of the crystal and  $\theta$  is the angle of incidence.

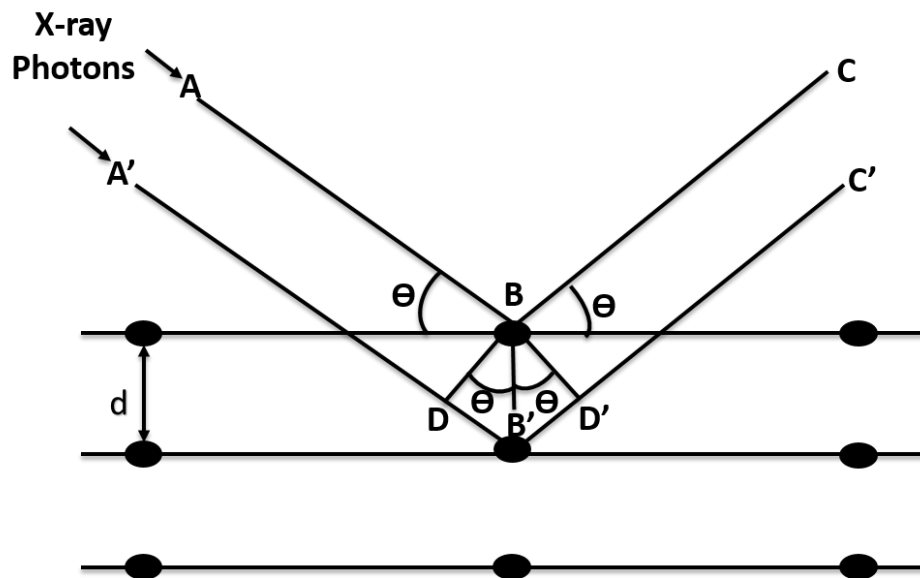


Figure 2.14: Diffraction of x-rays from crystal planes [35].

### 2.6.3 Powder X-ray diffraction (PXRD)

Powder samples of many small crystallites, which are randomly oriented scattered by monochromatic X-rays. The pattern is plotted by peak intensity versus measuring the angle of two theta. Each peak intensity is accounting from all the scattering intensities of atoms a specific set of planes at the certain detect angle that satisfies Bragg law. Two common modes of PXRD are used as reflection mode and transmission mode depending on the geometry of rig set-up.

At the condition of failure growing large single crystal, a good quality of PXRD pattern can be utilised for structure solution by Rietveld refinement. The

structural parameters are refined to minimise the difference from calculated intensity and collected intensities by a least-squares refinement. The quality of the fitting is normally qualified by R factors including  $R_{wp}$  which is the weighted R-factor. The lower of this values can be regarded as the small difference.  $R_{exp}$  is the statically expected value. Another important factor is  $\chi_2 (gof)$ , referred as  $R_{wp}/R_{exp}$  which is ideally equal to one.

Pawley method entitled Unit-cell refinement from powder diffraction scans to refine cell parameters from the whole pattern providing a starting point for the application of Rietveld refinement. In the Pawley method, diffraction profiles could be fitted with only the following parameters:

- $I(hkl)$ : Intensity of each reflection with indices hkl;
- A,B,C,D,E,F: Unit cell metric tensor parameters;
- $2\theta_{zero}$ : Instrumental zero error;
- U, V, W: Peak width parameters.

Many of the parameters are identical to those used in a Rietveld refinement program, but the significant difference is the intensity of the peaks is calculated from the structure factors,  $F(hkl)$ , which are themselves calculated from the parameters of the model structure.

#### 2.6.4 Synchrotron Radiation

Studies using laboratory X-ray sources are with drawbacks with beam divergence, limited angular resolution or long scan time. All of these factors will result in issues, such as the error peak positions, shape and intensities, which will challenge the structure determination especially using powder diffraction data. In the case of normal alkanes with low-symmetry structures crystallising in plate-like crystals, which tend to twin around the long chain c-axis, are essentially needed to be examined by powerful synchrotron radiation.

Current work has enabled the use of synchrotron radiation to accomplish structure determination with benefit high polarised beam, wide angular and high resolution. The instrumentation factors are straightforward to correct with standard values all well set-up. In addition, the high flux photon energy of such beamline enabled the in-situ crystallisation to be undertaken with seconds scale scanning time, especially in a solution environment with high background.

## **2.7 Conclusions**

This chapter has reviewed the fundamental knowledge on crystallisation science. The crystal structure was initially introduced by defining the lattice and unit cell parameters, then the directions and planes of crystals, followed by the symmetry and defined crystal systems. Subsequently, the introduction of solution science, including concepts of the solution, solubility, ideality calculation in a thermodynamic way and solution supersaturation, which is the metastable zone width. In the end, the process after supersaturation solution, which is the crystallisation driving force of nucleation, was introduced. Here, the homogenous nucleation was highlighted and the poly-thermal method used to determine the MSZW was described with nucleation assessment methods which is the theory employed for the studies in Chapter 9.

## **Chapter 3. Normal Alkanes Crystallographic Structures, Thermodynamic and Crystallisation Properties**

### *Summary:*

*This chapter will present the review of studies for normal alkanes and their homologue mixtures in terms of structure, thermodynamics and crystallisation kinetics and morphology.*

### **3.1 Introduction**

Normal alkanes have been intensively studied for decades, not only because they are important from the scientific point of view as a base unit for more complex polymers, lipids and membranes, but they are also the common contributor materials in life with diesel fuels. Previous studies regarding the structural behaviour and rich polymorphic nature of the normal alkanes will be reviewed. Much attention has been given to the mixture phases as the most common existence condition over the last 10 years. Therefore, a general summary of literature studies of solubility and crystallisation kinetics is also provided.

Some previously published review papers need to be noted. For example, Mnyukh [36], in 1960, presented the early studies of n-alkanes configuration and structures. Based on a large number of publications Turner [37], in 1971, wrote a review paper regarding the phase transition studies of pure n-alkanes and their mixtures. A comprehensive review paper including the work on thermodynamic properties, structural behaviour and crystallisation of single and mixed alkanes was published by Dirand in 2002 [38].

### **3.2 Normal Alkane Configuration and Structures**

#### **3.2.1 Configuration**

The most stable configuration for the chain of carbon and hydrogen atoms is a flat zigzag arrangement known as the all-trans type, whereas the molecular chain can be hindered to rotate along the main carbon axis with resultant conformational defects [36].

In the stable all-trans configuration, the closely packed molecular chains are aligned to the c-axis referred to as the long spacing of the crystalline. Therefore, it is useful to verify chain lengths and packing arrangements for pure component and also provide impurity checks for homologue preference [39]. Ideally, the c-axis length should be linearly increased as a function of chain length. Otherwise, disordering or phase transition might occur.

### 3.2.2 Phase structures

The earliest crystallographic studies of alkanes started from the work of Muller [40] using the powder X-ray diffraction (PXRD) method, and Broadhurst [41] summarised that almost all the present pure n-alkanes could be crystallised in three crystal structures (triclinic, orthorhombic and monoclinic). Craig, in 1994 [42] confirmed the unit cell parameters using high resolution synchrotron PXRD within homologue series from  $C_{13}H_{28}$  to  $C_{60}H_{122}$  of even and odd alkanes. The polymorphic behaviour of even alkanes has been observed as increasing the carbon number along with raising structural symmetry from triclinic (P-1) for  $[12 \leq \text{even number} \leq 26]$  to monoclinic ( $P2_1/a$ ) for  $[28 \leq \text{even number} \leq 36]$  to orthorhombic ( $Pca2_1$ ) for ( $C_{36}H_{74}$ ,  $C_{46}H_{94}$ ,  $C_{50}H_{102}$  and  $C_{60}H_{122}$ ). Polytypic orthorhombic ( $Pbca$ ) unit cells have been found in  $C_{38}H_{78}$ ,  $C_{40}H_{82}$  and  $C_{44}H_{90}$ . Odd alkanes were confirmed as having the  $Pbcm$  orthorhombic structure. **Figure 3.1** shows the representative diagrams of molecular arrangements in the triclinic (a), monoclinic (b) and orthorhombic structures (c). Apart from these all-trans configurations, fully ordered phases, end-gauche defects packing phase also appears as reported from authors [43-46] who determined a modification crystalline phase of  $C_{25}H_{52}$  with monoclinic A-face-centre unit cells ( $Aa$ ) based on an orthorhombic sub-cell.

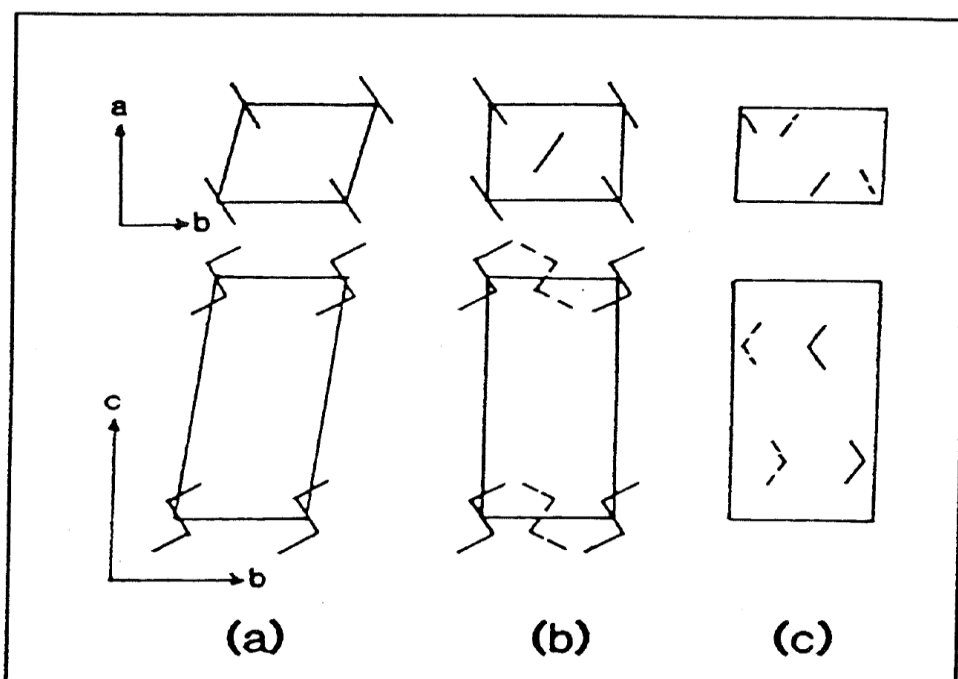


**Figure 3.1** Representative diagrams of molecular arrangements in the triclinic (a), monoclinic (b) and orthorhombic structures (c).[47]

Rotator phases are one of the typical phases in crystals, which have a long-range positional order in three dimensions without having a long-range order in the rotational degree of freedom of the molecule along its long axis [48]. The rotator phases are present between the liquid phase and the low temperature ordered crystal phase, giving a weakly ordered crystalline phase. Unlike the fully crystalline phases, the rotator phases are characterised by relatively significant changes in their structural constants as a function of temperature. The rotator phases of alkanes are representative of all weakly ordered phases where the interaction energies are weak and a large number of phases can occur related to subtle entropic effects which are insignificant when the interaction terms in the free energy are strong.

In summary of previous studies [49-51], five rotator phases have been identified. The RII phase has molecules that are untilted with respect to the layers, which are self-packed in a hexagonal lattice with a tri-layer stacking sequence, which is also denoted as rhombohedral (RH). Also, the RI phase is untilted but contains a rectangular distorted hexagonal lattice and bi-layer stacking sequence, which is also referred to as face centred orthorhombic (FCO). Furthermore, the RIII and RIV phases are tilted triclinic and tilted monoclinic, respectively. From work performed by Sirota et al. [48], a fifth phase was characterised, RV, which is the tilted version of RI. When any combination of the rotator phases occurs, the order with respect to decreasing temperature is R<sub>IV</sub>-R<sub>III</sub>-R<sub>II</sub>-R<sub>I</sub>-R<sub>V</sub>.

For even number alkanes, Denivolo [50] and Sirota [52] pointed out that,  $n=22, 24$  and  $26$  exhibits a phase transition between liquid (L) and rotator phase (R<sub>2</sub>) which can be observed by either heating or cooling processes. For lower  $n$  of  $C_{20}H_{42}$ , the rotator phase only appears in decreasing temperature as a metastable phase prior to the transformation from liquid to triclinic. At last, the rotator phase is not observable from the XRD experiment in  $C_{18}H_{38}$  or  $C_{16}H_{34}$ . Moreover, Sirota [53, 54] suggested that the rotator phase even occurs in crystallisation of  $C_{18}H_{38}$  and  $C_{16}H_{34}$  as a transient metastable phase observed from in-situ synchrotron X-ray diffraction on crystallisation of the supercooled melt. The stability of the rotator phase associated with alkane chain length is explained as a crossover from stable to long-lived metastability, and to transient metastability as shown in **Figure 3.2**.

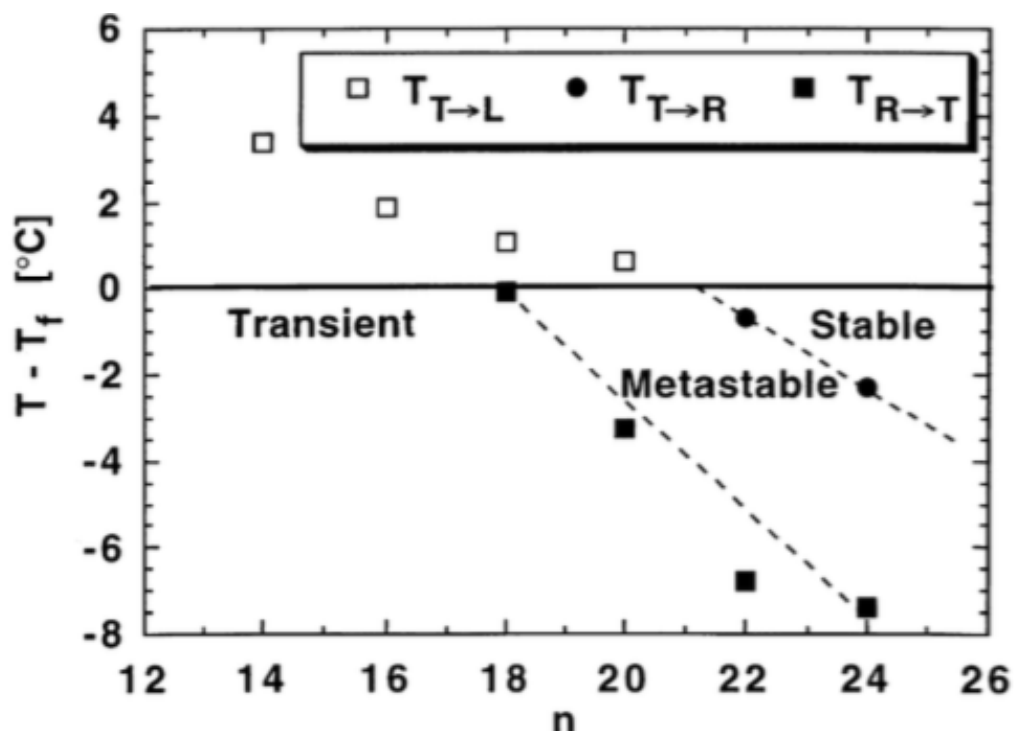


**Figure 3.2:** Chain length dependent phase diagram of transition temperatures with respect to even alkane chain number from ( $n=14$  to  $24$ ) corresponding to the L-R-T transitions [54].

Meanwhile, thermal analysis of  $n$ -alkanes by DSC from Srivastava [55] showed consistent observations. The rotator phase was observed with an additional thermal peak corresponding to L-R transition and its stability depends on the chain length and even-odd structural nature, as illustrated in **Figure 3.3**. A solid-solid phase transitional peak can be observed in the thermal plot towards either heating or cooling in longer  $n$  alkane  $C_{24}H_{50}$  while it only exists as a small exothermic peak towards cooling of  $C_{22}H_{46}$ . For  $C_{20}H_{42}$ , it only exists for a short period presented as an incomplete peak shape. The odd number alkane of  $C_{23}H_{48}$  showed the rotator phase both from cooling and heating processes involved with two transitional peaks referring to the liquid to rotator phase and rotator phase to ordered crystalline, respectively.

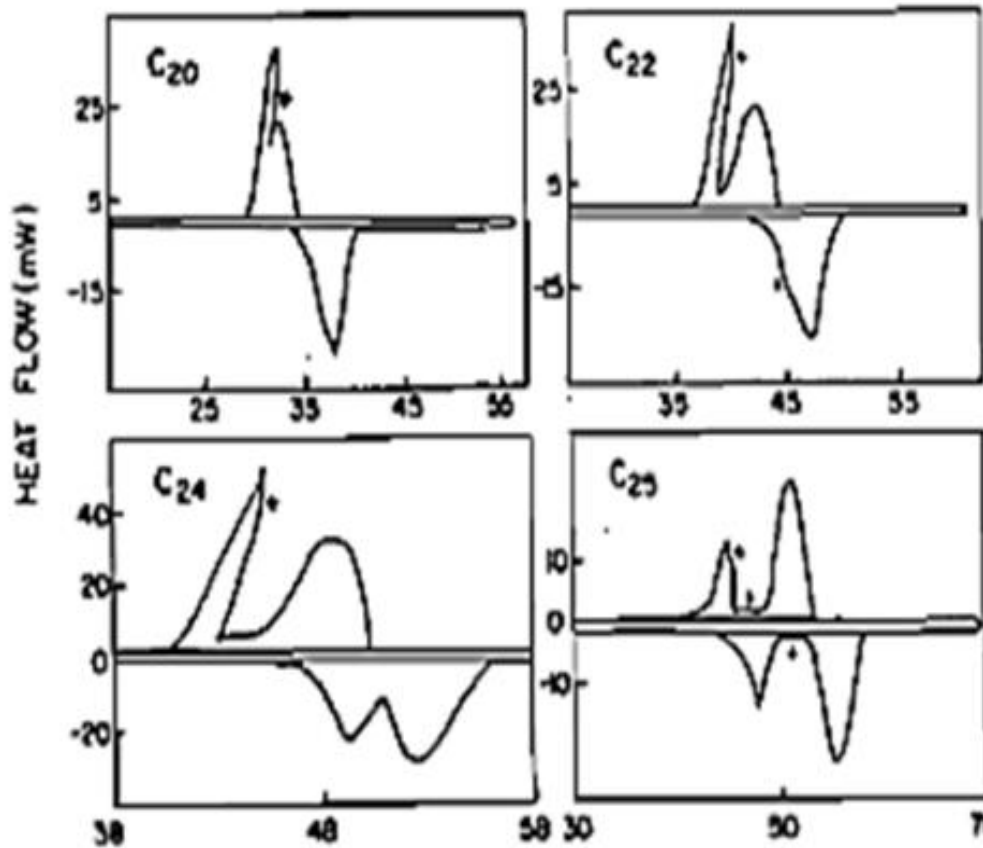


Figure 3.3: DSC traces from heating and cooling processes of even number alkanes of  $C_{20}H_{42}$ ,  $C_{22}H_{46}$ ,  $C_{24}H_{50}$  and odd number alkane of  $C_{23}H_{48}$ . [55]

### 3.3 Structural Behaviour of Mixtures of n-alkanes Homologues

N-alkane mixtures are subject to thermodynamic rules which govern phase stability, miscibility, molecular size and phase equilibria with respect to the mixtures. For binary mixtures, the miscibility in the solid phase is influenced by the carbon number difference and odd-even effect. That means when the carbon number difference is larger than five, the homologues tend to segregate in the solid phase to form lamellae composed of single homologues, as summarised by Kravchenko [56], which can be used to differentiate the nature of mixing type from continuous solid solution, eutectic type or immiscible solid. Solid solution can only be formed if the solid phase displays the same crystal structure and space group. In other words, the

intermediate solid solution of the mixture components will be present if their Gibbs free energies are lower than those of the pure components.

Binary mixtures between homologous have been significantly studied as a function of compositions and temperatures to reveal the complex polymorphic behaviour [57, 58]. Early studies were the work from Piper et al., Kravchenko [56], Smith, and Mazee [59] Luth [60], who employed a combination of calorimetry and x-ray methods on homologues alkanes. They proposed a continuous solid solution in the high temperature (HT) region and various behaviour in a low temperature (LT) region with three orthorhombic intermediate phases. Structure solution by a single crystal method was used to determine the high temperature solid solution ( $\beta_0$ ) and the dominant low temperature phase ( $\beta''$ ) by Gerson [61] from the C24-C26 mixture. The HT temperature  $\beta_0$  is a disordered phase with isostructure to the  $R_1$  ( $F_{mmm}$ ,  $Z=4$ )[62, 63] which always exists in odd number alkanes. The " $\beta$ " at LT is an ordered crystalline with an orthorhombic ( $B_{b21m}$ ,  $Z=4$ ) structure. However, in the following study on C24/C26 mixtures from Achour-Boudjema [64], some disagreed diffraction peaks from the  $B_{b21m}$  structure were found. More phases at low temperature were distinguished by Rajabalee [65] corresponding to the crystalline structures with defects in binary systems, i.e.  $O_i$  ( $P_{cam}$ ,  $Z=4$ ) which was the first observed for C23 by Smith,  $O_{dci}$  ( $P_{nam}$ ,  $Z=4$ ) which was determined by Nozaki [66] for C23,  $M_{dci}(A_a)$  from C27 which was determined by Rajabalee [67, 68] and  $O_p(P_{ca21})$  which can be obtained from longer chain alkane of C36 with unit cell determined by Teare [69] and Craig [42].

Phase transitions are not easy to detect between these intermediate solid solution phases as their structures are closely similar and have a long c-axis which demands a detectable low angle diffractometer. Also, the correlated energy change is expected to be small and is not easy to measure using thermal analysis. Nevertheless, the  $M_{dci}$  structure specialises in the peak split nature of the diffraction lines due to the monoclinic symmetry of  $A_a$ . Moreover, the decreased intensity of 00L reflections can be caused by an increase in end-gauche defects (gt) as the intensities of the 00L reflections reflect the degree of order of the methyl layer.

### 3.4 Solubility and Crystallisation Kinetics and Morphology

The solubility of pure normal alkane in organic solvents was found to decrease with the increased  $C_n$  number from the studies of Domanska and Rolinska [70] for C20, C24, C26 and C28 in pure light hydrocarbons. Provost [71] observed the consistent behaviour of C23, C25, C26 and C28 in C7 which has a different nature of the solvent, i.e. linear, aromatic and cyclic solvents with respect to heptane, toluene and methylcyclohexane. He also concluded that the solvent nature has no obvious influence on the solute solubility. Gerson [72] measured the saturation temperature which was increased as in longer chain length of n-alkanes between C18 to C23, indicating a lower solubility. Low temperatures from odd number alkanes compared with the one from the even n-alkanes relative to their chain length suggests that the triclinic stable phase dissolved at higher temperatures upon heating due to the intermolecular force being lower in the packing of the orthorhombic cell. The saturation temperature difference between even and odd alkanes becomes less pronounced as chain length increases. This converging behaviour shows the end group  $CH_3$  decreases the role of intermolecular force. Both enthalpy and entropy of dissolution from C18 to C23 are approximately in the linear trend without any difference from even-odd structural effects.

Binary mixtures of n-alkane homologues ( $\Delta C_n=1$  or 2) in a light solvent, which is a ternary system has been studied regarding structural behaviour, solubility and nucleation kinetics. Early studies from Luth with C20/C22 in n-dodecane solution suggested that three phases of orthorhombic, are exhibited within the structure of the even-even binary mixtures when the percentage of the longer homologues exceeds 60%. Such behaviour is not evident in similar mixtures crystallised from the melt [73]. It is suggested that the different phases correspond to microcrystalline segments within the wax mixture induced into the high and low temperature orthorhombic states. Previously a ternary system of C26/C28 in C7 was carried out by Provost [71, 74]  $C_n/C_n'$  ( $\Delta=1$  or 2) in light solvent, intermediate solid solution of the two  $C_n$  as a single pseudo component ( $\beta''$ ) which is isostructural to the orthorhombic intermediate solid solution in the C26/C28.

Nucleation kinetics [75-77] and interfacial tension [78] were measured which is the resistance (undercooling) to crystal nucleation under near equilibrium conditions originating mainly from the crystal-melt interfacial tension. Taggart [77] examined nucleation kinetics associated with the melt phase crystallisation of n-alkanes in the range of C13 to C32 and their mixtures using differential thermal analysis (DSC) presenting the kinetically metastable zone

widths (MSZW) on crystallisation form, the melt was found to reflect alkane structure and chain length dependence.

Previously studies on measurements of interfacial tension from liquid of n-alkanes [78], solutions of C20 and homologue mixtures (C18 to C22) in dodecane [79], C22 in n-dodecane solution with variation in solution concentrations from molar fraction of 10%, 15% and 20% [80], both homogeneous nucleation and heterogeneous nucleation mechanism were observed from C24 in dodecane [81].

Surface freezing was detected as a phenomenon that an ordered layer at the surface of disordered liquid observable in chain alkane [82, 83] at temperatures up to 3°C above the freezing point in the layer are hexagonally packed from C16 to C50.

Crystal morphology [84, 85] studies of n-alkanes are with dominant faces of {001}, however, it is limited with its less contrast from the solvent environment due to the single crystal observation and instrumentation for collection of the micrographs.

### **3.5 Conclusions**

This chapter presented a literature review from the configuration and packing and structures within normal alkanes, this included the disordered rotator phase. Mixed alkanes could have an essential effect on the polymorphic behaviour which is reviewed and addressed on even homologue phase diagrams. Solubility and crystallisation kinetics and morphological properties which are essential to the study were also reviewed.

## **Chapter 4**

### **Materials and Methods**

*Summary:*

*Detailed information about the materials and sample preparation methods used in this thesis is provide. Followed by the equipment set-up and the methodologies for the experimental work and related data analysis.*

## 4.1 Introduction

This chapter covers the methodology used in the analysis of this research. Here, information about the chemicals and solvents as used in the following experimental methods is explained first. The focus will be the experimental methods with a variety of techniques and data processing.

Thermal analysis is first employed to examine the binary mixtures of octadecane and hexadecane in melt phase crystallisation. Powder X-ray diffraction is utilised to determine the phase behaviour and structural information within different mixture compositions and crystallisation environments. Solubility and nucleation kinetic studies, as a function of solvents and compositions, are also carried out utilising the turbidimetric technique with a poly-thermal method. Finally, an optical microscopic with an in-situ growth cell is used to determine crystal morphology behaviour.

## 4.2 Materials

### 4.2.1 Supplied Chemicals and Solvents

Chemical mixtures of n-hexadecane (C16) and n-octadecane (C18) were studied as the major compounds in HVO fuels. Three different solvents were selected to simulate the hydrocarbon fuels environment: normal alkane (n-dodecane), aromatic (toluene) and a mixture of the two former cases (kerosene). Detailed information about these materials is listed in **Table 4.1**. Kerosene was supplied by Infineum Ltd. with the compositions provided in

### Table 4.2.

**Table 4.1** Properties of C16 and C18 chemicals and solvents used in this research

Chemical Name	Formula	Synonym	Purity	Density g/mL at 25 °C	MW g/mol	Supplier
n-Hexadecane	C <sub>16</sub> H <sub>34</sub>	C16	≥99%	0.773	226.44	Sigma-Aldrich
n-Octadecane	C <sub>18</sub> H <sub>38</sub>	C18	99%	0.777	254.49	Sigma-Aldrich
n-dodecane	C <sub>12</sub> H <sub>26</sub>	C12	99%	0.750	170.33	Sigma-Aldrich
Toluene	C <sub>7</sub> H <sub>8</sub>	N.A.	99%	0.865	92.14	Sigma-Aldrich
Kerosene	N.A.	N.A.	99%	0.815	167.90	Infineum Ltd.

**Table 4.2** Composition information of Kerosene as supplied by Infineum Ltd.

<b>Molecular Type</b>	<b>% wt</b>
Paraffins	39.33
Naphthenes	42.41
Alkyl benzenes	7.62
Benzocycloparaffins	6.79
Naphthalenes	3.43
Biphenyls/acenaphthenes	0.27
Fluorenes	0.15
Phenanthrenes	0.00

### 4.2.2 Binary Mixture Sample Preparation

Binary mixed samples of C18 and C16 were prepared by weighing each one according to the appropriate mole ratios. A shaker with the temperature being controlled by a water bath was then used to prepare homogeneous mixing liquids as heated up above the melting point.

## 4.3 Experimental Methodology

### 4.3.1 DSC Thermal Analysis

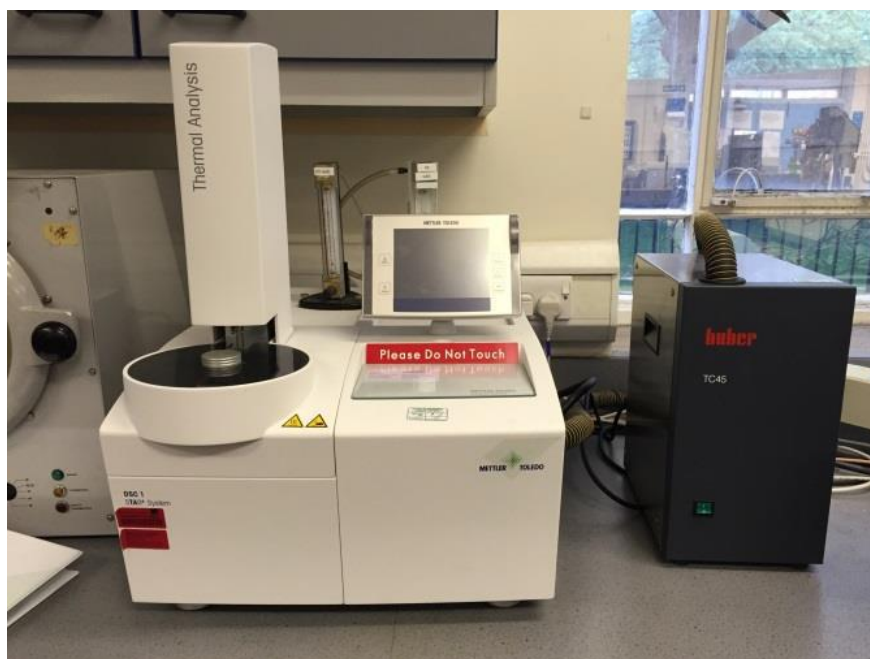


**Figure 4.1:** Differential Scanning Calorimeter (DSC) from Mettler Toledo®

Calorimetric measurements were carried out to determine phase transition temperatures and associated heat fusion enthalpy changes using a conventional DSC (Mettler Toledo<sup>®</sup> DSC 1) running in a high purity nitrogen atmosphere as seen in **Figure 4.1**. The instrument consists of two crucibles sitting on their own sensor where the reference sample and the experimental sample respectively, are placed. A computer monitors the temperature and regulates the heat flow throughout the programme which is defined in advance.

Samples (3 to 5 mg) were initially hermetically sealed into Al-40  $\mu$ l standard pans and run by a pre-programmed poly-thermal heating/cooling process in a temperature range that allows measurements of all phase transitions. For each composition of binary melts, three fresh samples were prepared and examined over two sequences of heating and cooling cycles to ensure accuracy and stability. The peaks, observed from the DSC curves, corresponding to solid/solid and solid/liquid transitions were then evaluated by the STAR<sup>e</sup> software purchased from Mettler Ltd.

#### 4.3.1.1 Calibration

Calibration and adjustment were achieved referencing samples of In and Zn. Tau lag adjustment was performed to calibrate the error of melting point as increasing heating rate could cause thermal inertia arising from the heat capacities and thermal resistances. **Table 4.3** lists the melting temperatures and enthalpies of reference material Indium after calibration and adjustment at three different heating rates of 5, 10 and 20 °C/min.

**Table 4.3** Melting temperatures and enthalpies of reference sample of Indium at different heating rates

Heating Rate °C/min	Onset °C	Peak °C	End °C	$\Delta$ H J/g
5	156.41	156.76	157.96	-28.3
10	156.64	156.95	158.6	-28.21
20	156.26	157.08	160.24	-27.98

#### **4.3.1.2 Measurements**

##### **Temperature and enthalpy determination**

Binary phase diagram determination was carried out on 21 binary mixture samples varying from the molar ratio ( $x$ ) of C18 in the mixture. Thermal data from liquid-solid and solid-solid phase transitions were examined from the heating process to avoid a supercooling effect. A relatively slow heating rate of 1°C/min was employed to ensure approximate thermodynamic equilibrium conditions.

The temperature ranges determined were then explored by temperature-dependent powder X-ray diffraction analysis in order to characterise the structural evolution and to confirm the temperatures of these transformations.

##### **Nucleation kinetics determination**

Samples of single components of C18 and C16 and their binary solid solution at a composition of 0.4C18 were selected to carry out further nucleation kinetics studies. The exothermic and endothermic peak temperatures from these samples were determined by poly-thermal cooling and heating processes using five heating/cooling rates (0.25, 0.5, 1.0, 3.2, 5.0 °C/min) and four heating/cooling rates (0.25, 0.5, 1.0, 3.2 °C/min) for single and binary samples, respectively.

### 4.3.2 Powder X-ray Diffraction

The crystallographic studies were carried out in three different facilities to achieve various tasks.

#### 4.3.2.1 Lab source: High resolution XRD with transmission geometry

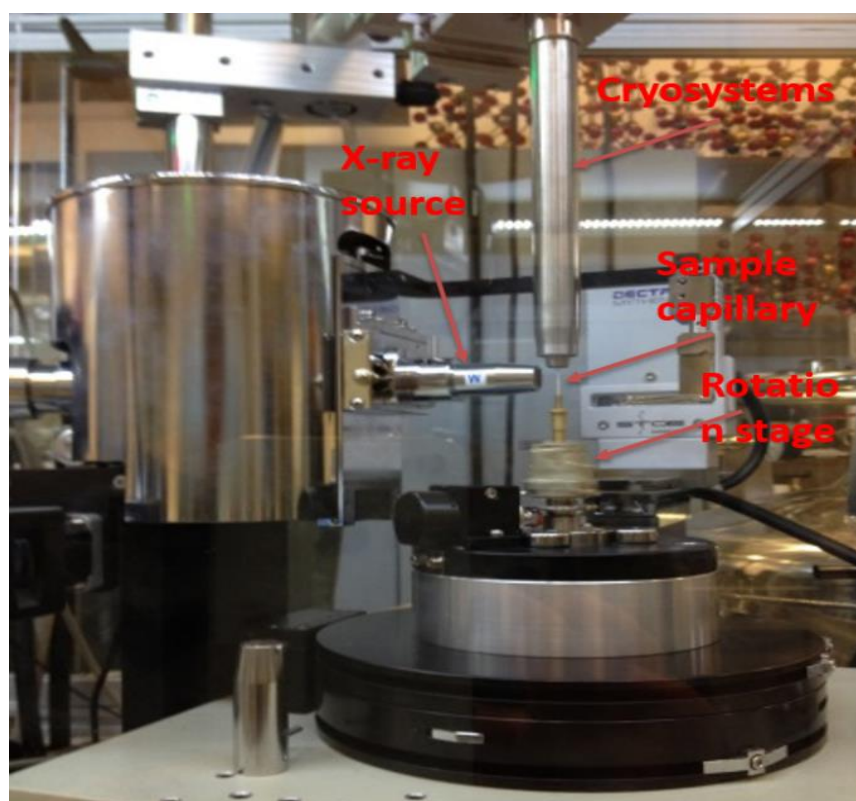


**Figure 4.2:** Powder diffractometer with high resolution transmission mode from STOE<sup>®</sup>.

Isothermal experiments accomplished using a high resolution STOE STADI-P with transmission geometry (**Figure 4.2**) and a pure Cu  $K\alpha_1$  radiation with  $\lambda=1.54056 \text{ \AA}$  by a Ge (111) monochromator with generator energy of 40 Kev, 30 mA. XRD patterns were collected by a PSD (position sensitive detector) with scanning range from 0 to  $80.0^\circ$  in  $2\theta$  range with a step size of  $0.495^\circ$ . Samples (C16, 0.3 C18, 0.5 C18, 0.7 C18 and C18) were prepared in a borosilicate glass capillary with 0.7 mm diameter and mounted on a rotation sample stage equipped with cryosteam (Oxford Cryosystems Ltd) cooling by liquid nitrogen. This transmission cell with sample stage rationing in 360 degrees would reduce the texture/preferred orientation of the crystals.

Two patterns were collected during the cooling process. One was in the HT region, just below the melting point by slowly cooling from room temperature at 1°C/min, and a step time of 25 s/s was used. Followed by crash cooling to the LT region at -30°C, where another one was collected with a scan speed 90 s/s.

#### 4.3.2.2 Lab source: Temperature dependent PXRD with reflection mode

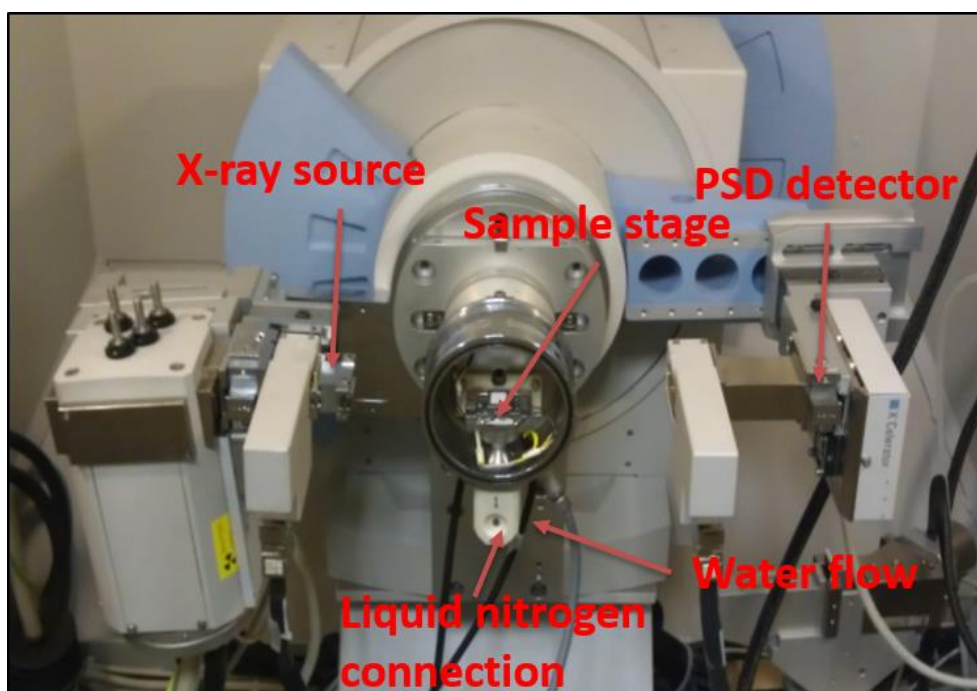


**Figure 4.3:** Phillips X'Pert Pro MPD diffractometer with a cold stage sample environment

Temperature dependent XRD experiments were carried out on the Philips X'Pert Pro MPD with reflection geometry for the purpose of phase identification for binary C18/C16 mixtures. The diffractometer has a stationary, centrally placed, X-ray tube with (para-focusing) line focus and (parallel beam) point focus (**Figure 4.3**) using Cu  $K\alpha$  radiation with  $\lambda=1.54 \text{ \AA}$  wavelength source at a power of 40 Kev, 40 mA. A nickel filter was inserted to remove  $K\beta$  from X-ray lines, no monochromatic is installed to remove  $K\alpha_2$ .

15 binary mixture samples referred to the determination of the binary phase diagram and were examined with compositions of C16, 0.05C18, 0.1C18, 0.2C18, 0.25C18, 0.3C18, 0.4C18, 0.4C18, 0.5C18, 0.6C18, 0.65C18, 0.7C18, 0.8C18, 0.9C18 and C18. Pre-melted liquid samples were held in the sample holder with a rectangular dimension of approximately  $2 \text{ cm} \times 2 \text{ cm} \times 2$

cm at 40°C until equilibrium condition was reached and then the sample was cooled down to -30°C at a cooling rate of 10°C/min. XRD patterns were collected at the selected temperatures according to the thermal analysis from LT to HT at a heating rate of 2°C/min with a step size of 0.07° over 5 to 40° in  $2\theta$ . A cold sample stage facilitated with liquid nitrogen was applied for cooling crystallisation purposes. All measurements were computer controlled and pre-programmed for the purpose of running consecutively.

#### 4.3.2.3 Synchrotron: High resolution X-ray Powder Diffraction

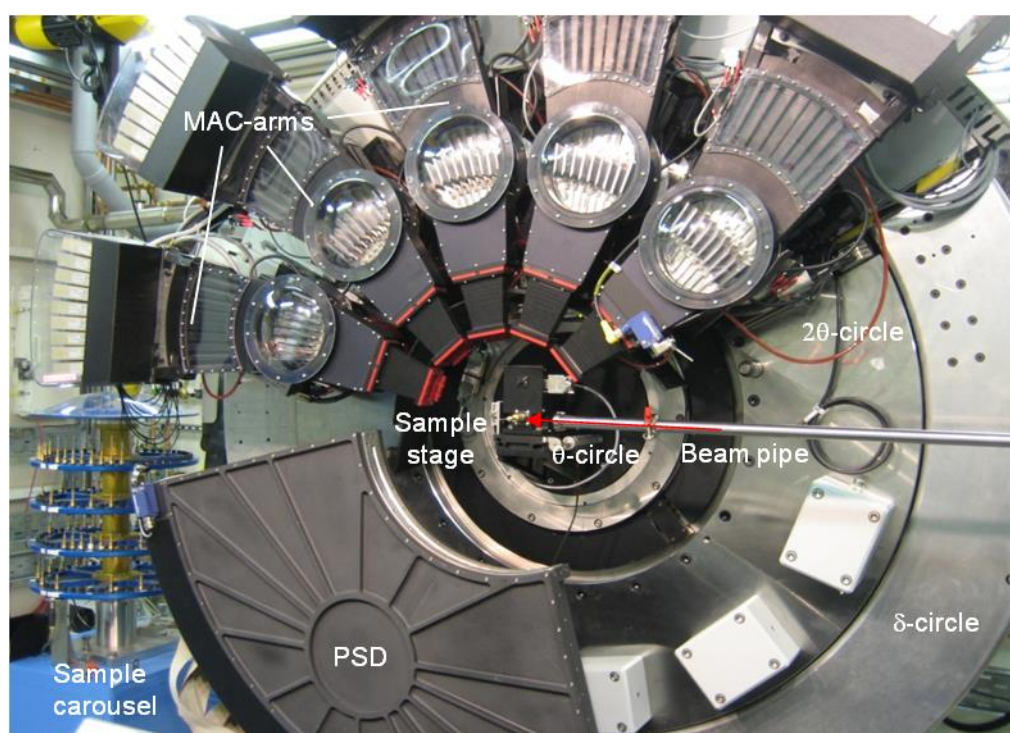


**Figure 4.4:** Experimental layout of I11 beamline showing the five arms for MAC detectors mounted on the  $2\theta$  circle, the sample in capillary mounted on a rotational stage, beam pipe and the PSD detector mounted on  $\delta$  circle [86].

Time-resolved and high resolution powder diffraction data were collected at beamline I11 from Diamond Light Source (DLS) in the UK. The monochromatic incident beam was calibrated using a high-quality Si powder standard. Cooling was controlled by an Oxford Instruments CryojetHT®. Heating was provided by a water bath. Samples in liquid phase were introduced into a 0.7 mm borosilicate glass capillary and sealed with a flame mounted on brass holders and spun at 1250 r.p.m during the data collection.

A fast position sensitive detector (PSD) of  $\lambda=0.82578 \text{ \AA}$  using Mythen-2 Si modules with a 90 degree aperture was used to collect diffraction data (a few seconds per pattern) during a cooling crystallisation process from 40 to  $-40^{\circ}\text{C}$  at a cooling rate of  $1.5^{\circ}\text{C}/\text{min}$  with a binned step size of  $0.004^{\circ}$ . At the end of cooling, at  $-40^{\circ}\text{C}$ , five MAC (multi-analysing crystal) detectors covering a full  $2\theta$  scan range from  $0 - 150^{\circ}$  degrees were used to collect high-quality data for half an hour using an incident wavelength of  $0.825678 \text{ \AA}$ . The data was subsequently binned in  $0.001^{\circ}$  steps and summed to a single PXRD pattern.

### 4.3.3 Turbidimetric Measurements

A turbidimetric technique to measure crystallisation experiments using the Avantium<sup>®</sup> Crystal 16 System which contains multiple small scale reactors which allow 1 ml vial solution measurements.

#### 4.3.3.1 Avantium Crystal 16<sup>®</sup>



**Figure 4.5:** Apparatus of the Avantium Crystal 16<sup>®</sup>  
[[www.crystallizationsystems.com/pharma/crystal16/](http://www.crystallizationsystems.com/pharma/crystal16/)]

Avantium Crystal 16 is a multiple variable temperature reactors at its 1 mL scale and applies the turbidimetric technique to detect the cloudy and clear points of a solution associated with crystallisation and dissolution phenomenon. As seen in **Figure 4.5**, this automatic crystallisation equipment can hold 16 ( $4 \times 4$ ) standard HPLC vials. It has 4 parallel units containing 4 individually heated aluminium reactor blocks. Each unit can be heated and cooled by a specific programme (heating rate from 0 to  $20^{\circ}\text{C}/\text{min}$  and a temperature range of  $-15$  to  $100^{\circ}\text{C}$ ).

Crystallisation and dissolution temperatures were analysed according to the solution turbidity profile as the temperature at which the transmission falls from 100% to 0% due to the precipitation or the transmission increasing to 100% from 0% meaning the dissolution of the solids.

#### **4.3.3.2 Calibration test for Avantium Crystal 16**

As there is no temperature probe inserted into the solution in the 1 ml vial, it is essential to test the difference between the actual temperatures obtained from Crystal 16 and the real values.

The calibration was carried out using vials with fresh solvent as employed in this experiment and placed into the unit blocks. A programme was set up on the Crystal 16 to cool down the solutions to certain temperatures of 10°C, -5°C, -10°C (within experimental range). A FLUKE 50 series portable digital thermometer was placed directly into the solutions to measure the real time temperature over several repetitions. The resultant difference is negligible within our temperature range measurements which confirmed the sensitivity and accuracy of Crystal 16.

#### **4.3.3.3 Sample preparation**

11 binary mixed samples of differing molar ratios varying from 10% of C18 in each C16/C18 samples were first prepared. For each composition of the C16/C18 mixture solution in four concentrations (192, 231, 269, 308 g/l), (231, 269, 308, 350 g/l) and (300, 350, 400, 450 g/l) for solvents of dodecane, kerosene and toluene respectively. The homogeneously mixed solutions were then induced to the 1 ml scale transparent vials with mini magnetic stirrers.

#### **4.3.3.4 A poly-thermal method**

A poly-thermal heating segment was programmed to 1 ml scale solution to detect the onset temperature of dissolution and crystallisation by a heating up and cooling down the process. In this experiment, the heating cycle was first increased to 40°C above the expected dissolution temperature and then decreased down to -15°C which is the lowest temperature of Crystal 16. Similarly, the crystallisation temperature of the sample needed to be above this limitation which is detectable. Additionally, constant holding was applied

to the top/bottom temperature for half an hour to ensure complete homogenization. The four heating/cooling rates used were 0.25, 1, 2 and 3.2°C/min for all three solvents with 5 sequences of cycle repeats to obtain good quality data. It needs to be noted that constant stirring was applied to all 1 ml vials at a speed of 300 r.p.m.

A typical profile as obtained from Crystal 16 using the poly-thermal method is displayed in **Figure 4.6** and **Figure 4.7** highlighting the detection of the onset of cloud point and clear point with associated temperatures of dissolution ( $T_{\text{diss}}$ ) and crystallisation ( $T_c$ ).

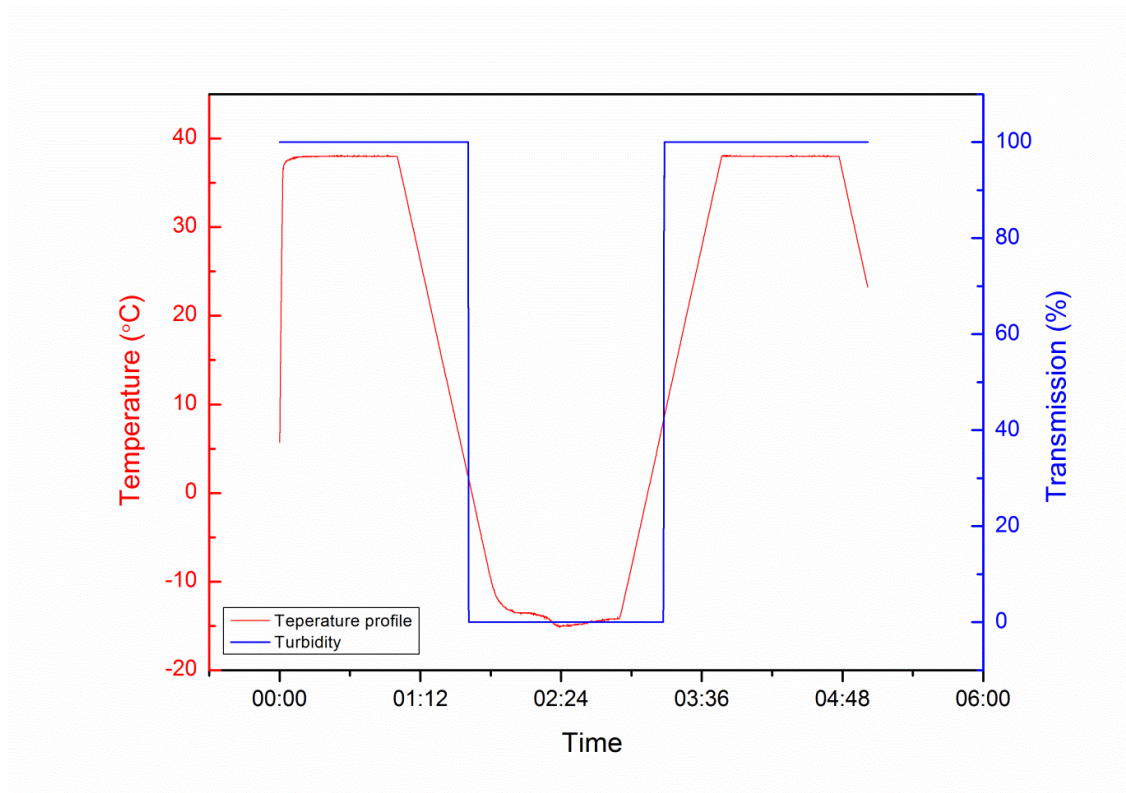


**Figure 4.6:** Poly-thermal profile for temperature and transmission against the time for measuring the cloud and clear points of the solution.

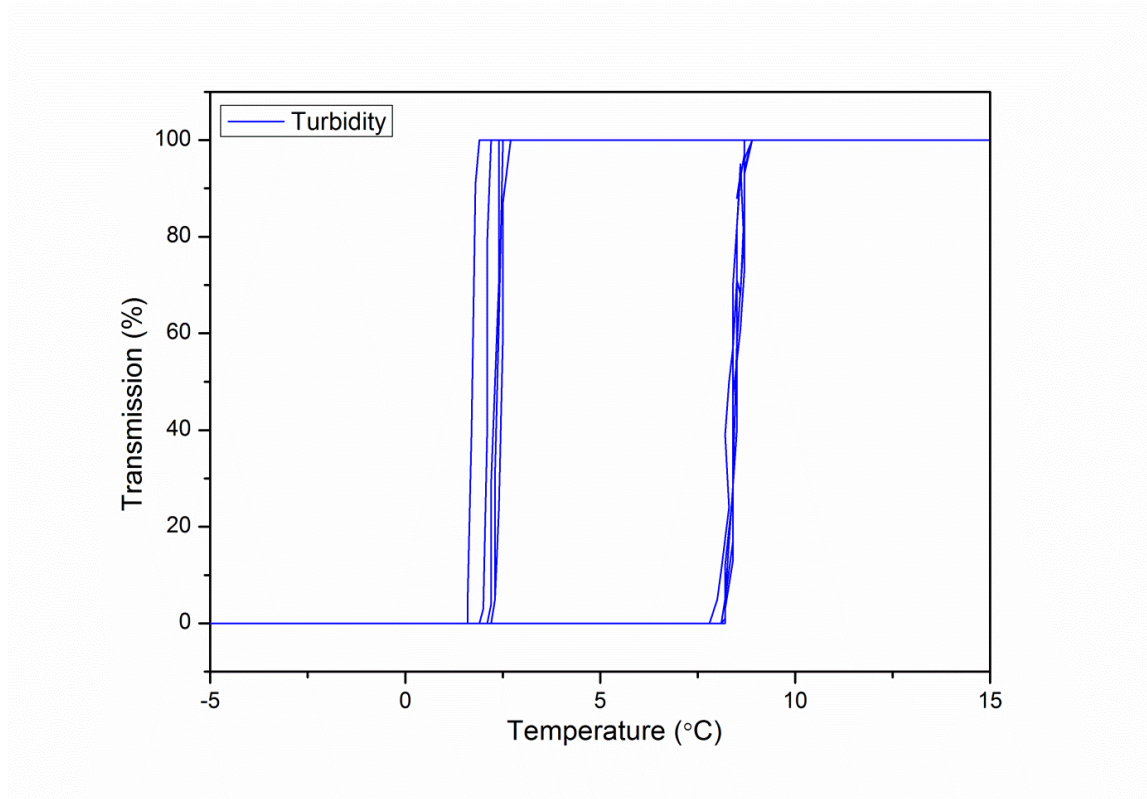


**Figure 4.7: A turbidity result of a solution through a poly-thermal process.**

#### 4.3.3.5 Processing raw data

The turbidimetric method was successfully used in all 3 solvents (n-dodecane, kerosene and toluene) to detect the cloudy points and clear points of each composition of C16/C18 mixtures with 4 different concentrations using 4 different cooling rates.

The resulting plotted average value of  $T_{\text{diss}}$  and  $T_c$  were obtained from five repeats of the heating/cooling processes as a function of cooling rates ( $q$ ). By fitting a straight line to these points, the MSZW as a function of cooling rate was obtained. By the extrapolation of the dissolution tendency and crystallisation tendency fitting linear lines to the cooling rate as 0 °C/min, the equilibrium saturation and supersaturation temperatures could be obtained respectively and solubility-supersolubility curves could be constructed. **Figure 4.8** shows an example of the plots and the fitting linear lines of MSZW as a function of cooling rate. **Figure 4.9** is an example of the solubility-supersolubility curve by plotting concentration against the extrapolated values of equilibrium saturation and supersaturation temperatures.

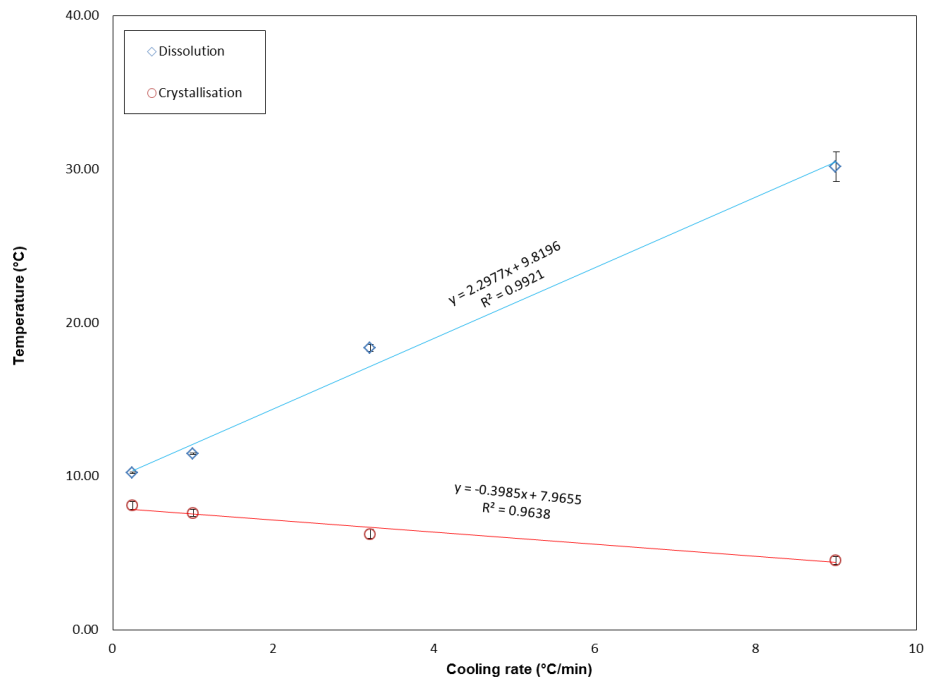


**Figure 4.8: Plots of T<sub>diss</sub> and T<sub>c</sub> as a function of cooling rate (q). The best linear fitting for each plot was listed with the equation as  $y=ax +b$  and the fitting accuracy factor R square.**

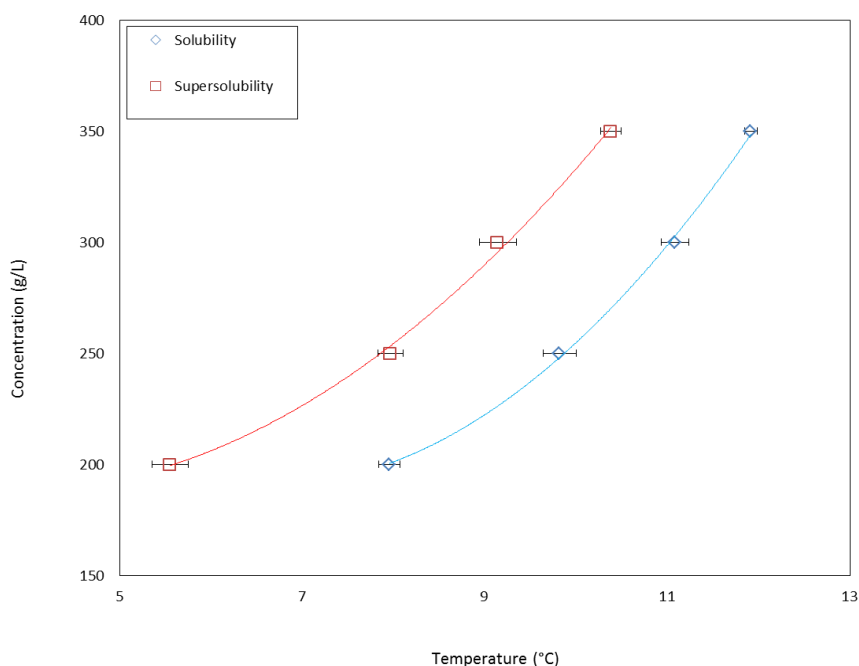


**Figure 4.9: Equilibrium solubility/supersolubility curves for C18 in dodecane solution. The points were obtained from the extrapolation of the linear fitting from  $T_{\text{diss}}$  and  $T_c$  as a function of cooling rates from each concentration. The fitting curves are fitted by the polynomial equation in order 2.**

#### 4.3.4 Morphology Determination

Single crystals of the thin plate-like alkanes were attempted to grow using an in-situ growth cell with temperature controlled by a water bath to reach certain supersaturation. The morphology was captured by an optical microscopic with a QImaging/QICAM camera. Detailed information for the set-up is explained in **Figure 4.10 (a and b)**.

A sample of C18 was prepared in a solution of n-dodecane with 400 g/l concentration and injected and sealed in a sample cuvette cell which was stabilised inside a glass window area. Circulating water would surround the cuvette cell to keep the temperature homogenous. A single crystal was obtained and captured by the camera within the observation area by moving to an appropriate position. The dimension of the growth is approximately around  $10\text{ cm} \times 12\text{ cm} \times 1.5\text{ cm}$  with a rectangular shape.

As the sample metastable zone width was determined from solubility and supersolubility measurements as introduced in section 4.3.3. Crystal

morphology was observed at 4 different supersaturation ratios of  $\sigma = 0.036$ ,  $T = 12.2\text{ }^{\circ}\text{C}$ ,  $\sigma = 0.045$ ,  $T = 12.1\text{ }^{\circ}\text{C}$  and  $\sigma = 0.08$ ,  $T = 11.7\text{ }^{\circ}\text{C}$ , within the MSZW from  $T_{diss} = 13\text{ }^{\circ}\text{C}$  to  $T_c = 11.7\text{ }^{\circ}\text{C}$ .

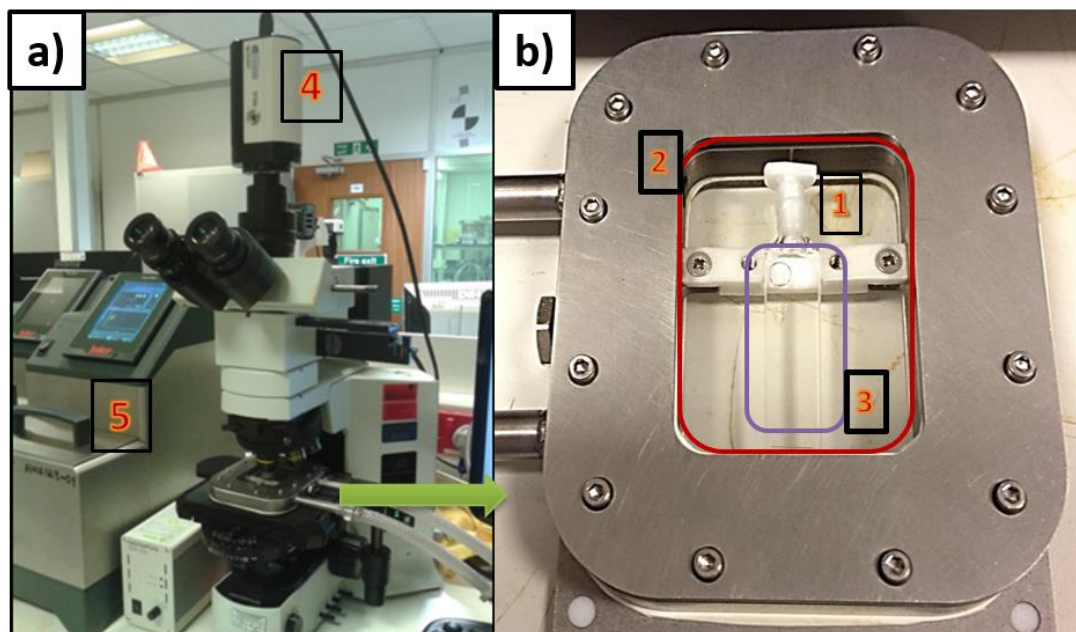


**Figure 4.10: In-situ growth microscopic cell: a) whole set up with Olympus BX51 optical microscope. b) Enlargement of growth cell. Individual parts are 1) Sample cuvette cell. 2) Glass window area. 3) Crystal morphology observation area. 4) QImaging/QICAM camera. 5) Huber Ministat 125 circulation bath.**

### 4.3.5 Data analysis

#### 4.3.5.1 Indexing and Pawley and Rietveld refinement

All PXRD data collected from three different diffractometers processing was carried out using an academic version of Topas5.0 [87]. The peak positions (initial 20 reflections) of high resolution XRD of C16 and C18 collected from I11 were indexed using LSI-Index with an indexing algorithm based on the iterative use of least squares [88].

The unit cell parameters were refined from peak positions of the experimental pattern by Pawley fitting [89]. For this, a pseudo-Voigt (PV) function was utilised to model the peak shape. The emission profile, background, instrument factors such as diffractometer radius and axial divergence were provided. Corrections were refined for zero-point, Lorentz-polarisation (LP) factor and absorption. In addition, phase level variables (Lorentzian crystallite

size, Gaussian microstrain, preferred orientation and anisotropic factor by spherical harmonics) were refined. The fitting factors ( $R_p$ ,  $R_{wp}$  and Gof) were generated to give an indication of the fitting from experimental and predicted.

The refined unit cell parameters were employed in the trial structure determination using a molecular modelling method. The profile parameters obtained were used as a reasonable starting point for Rietveld refinement to refine the structure of calculated to experimental data. To ensure sensible configuration, certain restraints were applied before refining the atomic coordinates. To keep the alkane chain configuration, bond distance of C-C and bond angle of C-C-C was restrained to regular dimension. The alkane chain was additionally restrained to be planar (flatten). Penalty weighting was applied to keep the carbon atoms in reasonable positions. Isotropic displacement parameters of carbon atoms and hydrogen atoms were also refined.

The refined structure was further viewed in the programme of Mercury [90] to examine all the atoms were in reasonable positions and attached to each other. Distances of each C-C and angles of C-C-C were calculated. Geometry optimisation was accomplished using Material Studio software with fixed unit cell parameters and space group. Finally, lattice energy was calculated using the Habit programme as implemented in Mercury.

TOPAS implements a normalised symmetrized spherical harmonics function. The expansion is simply a series that is a function hkl values. The series is normalised such that the maximum value of each component is one. Typically usage is preferred orientation correction or description of anisotropic line shapes.

#### **4.3.5.2 Applying molecular modelling techniques to structure determination**

The computational software of the Material Studio was initially employed to build up the molecular structure of the asymmetry unit and followed by energy optimisation using a Compass force field. Following this, a systematic search [91-94] was employed based on the grid search by motifs in a direct space for the appropriate unit cell to be used as a trial structure for Rietveld refinement. The motifs, which can be referred as searchers, check the possible configurations with rotations and translations to locate the trial structures. A truncated lattice is constructed based on reducing the radial cut-off distances, which is known as the pre-screen step. Only sensible structures will be used

by filtration of improbable cell arrangement. The sensible structures can be ranked using lattice energies or the goodness of fit [95] from simulated and observed powder X-ray data.

The lattice energy used for C18 in this study was the implicit hydrogen potential parameters in the Dreiding [96] Potential for methyl, C33, and methylene, C32, carbon atoms in the C18 chain.

#### 4.3.5.3 Thermal expansion calculation

The lattice parameters obtained from the “Pawley-fit” programme using TOPAS software with good residual factor  $R_{wp}$  were used to calculate the molecular volume thermal expansion coefficient [97] by Equations (4.1) and (4.2).

Strain ( $\epsilon$ ) caused by the thermal effect on the length ( $l$ ) can expressed by equation, the change in measured length ( $dl$ ):

$$\epsilon = \frac{dl}{l} \tag{4.1}$$

The thermal expansion coefficient ( $\alpha$ ) can be calculated from the change of strain and temperature ( $dT$ ):

$$\alpha = \frac{dl}{l} \frac{1}{dT} \tag{4.2}$$

#### 4.3.5.4 Solubility assessment by Van't Hoff plots and ideality calculation

As introduced previously in section 2.3.2, for an ideal solution, the solubility is no relation to the solvent and can be calculated by Equation 2.3 which is derived from the Van't Hoff Equation 2.4. The heat value of  $\Delta H_f$  and  $T_f$  used in this equation were provided by the results of DSC measurements towards a slow heating process for all the binary mixtures including pure C16 and C18. The equilibrium saturation temperature for each concentration was obtained from the solubility curve as the extrapolation of measured dissolution temperature to 0°C/min. As the mass concentration of each solution is known,

the solubility in the real condition is calculated by the mass concentration expressed as the mole fraction ( $x$ ) of solute with solvent.

Plot the logarithm of the solution molar fraction ( $\ln x$ ) against the reciprocal of the equilibrium saturation ( $1/T$ ) should be a linear relationship known as the Van't Hoff plots. For a specified concentration of the solution, by plotting the ideal solubility plot with the real one shows the deviation behaviour of this solution to the ideal mode shown in **Figure 4.11** presented as an example.

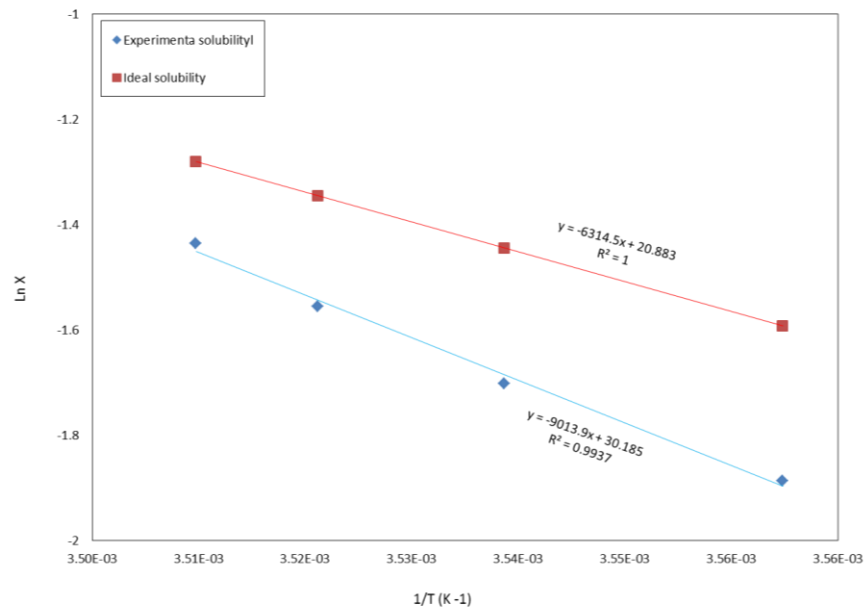


**Figure 4.11: Van't Hoff plot with the ideal and experimental solubility. The best fitting linear line for each was fitted by the equation as  $y=ax+b$ .**

The dissolution enthalpy and entropy can be estimated from the experimental Van't Hoff plots by the slope ( $a$ ) and intercept ( $b$ ) value from the best linear fitting equation. The deviation behaviour from real solution and the ideal solution can be estimated by the calculation of activity coefficient ( $\gamma$ ):

$$\gamma = \frac{x_{ideal}}{x_{real}} \tag{4.3}$$

Thus the ideality property of the solution can be accessed using the value of activity coefficient given by  $\gamma = 1$  is an ideal solution and  $\gamma < 1$  indicating that the solubility of the solution is higher than ideal concentrations. Whereas the

solution behaves non-ideally when  $\Upsilon > 1$  in which the solubility is lower than the ideal solution.

#### **4.3.5.5 Morphology analysis**

The single crystal morphologies of C18 grown in kerosene at three supersaturations were predicted and analysed by a recently published methodology. Crystallographic lattice parameters of C18 determined in section (5.22) were initially utilised to predict all the possible Miller indices using Bravais, Friedel, Donnay and Harker [98] (BFDH) approach by Material Studio. According to the BFDH law, the planes with larger lattice distance ( $d$ ) possess higher morphological importance with larger crystal facets which will appear as the final habit with lowest growth rates.

Zone axis is subsequently introduced to group the lattice planes into specified group axis  $[u\ v\ w]$ . The lattice planes in each zone axis having an equal projection on 2 dimensions of  $x, y$ -axis. The lowest order planes ( $h\ k\ l$ ) in each zone axis were pair-wised to each other which was input into the crystallographic information file (.cif) morphology simulation with the predominant (001) plane using Mercury software.

Finally, comparison of the internal angles of each prediction-projection from the experimental observation onto the simulated morphologies to obtain the potential solution pairs for the experimental pair. Then cross checking by correlating the pairs to match with each other can reduce the number of potentials.

#### **4.3.6 Conclusions**

Materials used in these experiments for the melt phase and solution phase studies were listed in terms of characteristic information and the quantities in different molar ratios. The thermal technique of DSC was employed as a routine to determine the phase transition temperatures and enthalpy in melt crystallisation analysis. Solubility and supersolubility measurements were successfully carried out by using the turbidimetric poly-thermal method using Crystal 16. The raw data process and analysis method were presented with example figures. Powder diffraction was carried out on three different instruments which were introduced and also included was the Topas software with relative setting parameters. The set-up of a crystal growth cell on a

microscope to observe the morphology of a single crystal of C18 as a representative alkane sample was also introduced.

## Chapter 5 Structure and Morphologies Properties of Octadecane and Hexadecane

### *Summary:*

*High-resolution powder X-ray diffraction data is collected from C18 and C16 for structure analysis in combination with computational prediction method. Thermal expansion analysis is also presented with lattice volume coefficients calculated. In addition, experimental morphological observations are indexed and predicted according to the determined structure.*

## 5.1 Introduction

This part of study serves as a start point for the analysis of octadecane (C18) and hexadecane (C16) system, which is essential to determine the structural and polymorphic behaviour of these two pure materials. The crystallography information for octadecane is available from early studies conducted from the years of 1948 to 1972 by means of the single crystal method at room temperature [40, 60, 99]. Hexadecane structure was determined from powder X-ray diffraction data by using laboratory source [100] in 2004. However, the structural behaviour of these two components is still not well defined as associated with temperatures, especially at lower temperatures.

In this study, high resolution synchrotron powder X-ray diffraction was essentially applied due to the low symmetry nature of these studied organic molecules. Here, we demonstrated the structure prediction by a computational systematic search method and the reliability to determine structure from powder data. In-situ XRD in real time crystallisation study was also applied to monitor the phase behaviour and thermal expansion properties. Additionally, to build up the insight of the structure, crystal morphology measurements were also carried out with predictions using the determined structure. This is particularly important for morphology modification as to make the crystals flowable in vehicle engines.

## 5.2 Octadecane (C18)

### 5.2.1 Unit Cell Parameter Determination

The low temperature (-40 °C) collected XRD pattern of C18 normalised from five multi-analysing crystal (MAC) detectors is detail presented in **Figure 5.1**, highlighting the sharp peak width and exceptional angular resolution by synchrotron radiation of Diamond light source (DLS). In addition, the indexation planes of the major reflections by TOPAS software [88] are provided in **Figure 5.1**. **Table 5.1** presents the resultant unit cell parameters and relative  $R_{wp}$  value obtained from “Pawley fit” [89] method by refining the indexing prediction to the diffraction pattern.

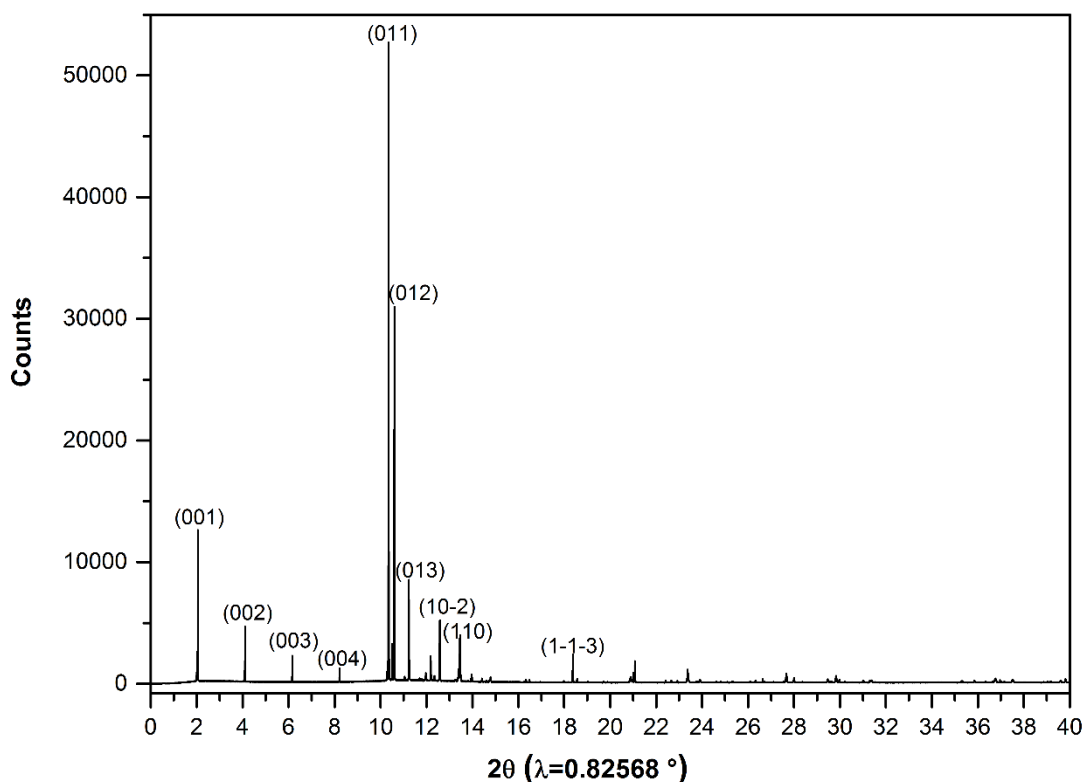


**Figure 5.1** High resolution synchrotron XRD pattern of C18 at -40 °C collected on beamline of I11, DLS. Together with the indexation (hkl) of the most important reflections. The resultant lattice parameters are given in Table 5.1.

**Table 5.1** Lattice parameters of C18 at low temperature (-40 °C) together with the  $R_{wp}$  value determined from “Pawley fit” refinement by Topas.

$a/\text{Å}$	4.225
$b/\text{Å}$	4.771
$c/\text{Å}$	23.49
$\alpha/^\circ$	78.988
$\beta/^\circ$	84.541
$\gamma/^\circ$	73.574
$V/\text{Å}^3$	445.386
$R_{wp}/\%$	4.7

## 5.2.2 Structure Refinement

According to the symmetry of triclinic lattice, an initial molecular model of the asymmetry molecule was generated with atomic positions and unit cell parameters which were just determined. The generated asymmetric molecular model is a start point for application of structure solution using a grid systematic search method.

### 5.2.2.1 Systematic search

The parameters selected for running the systematic search programme are given in **Table 5.2**. In this search, the asymmetric model was necessarily considered from only three rotational degrees of freedom in three directions, with the angular range of 0 to 360° in a step size of 5°. A distance cut-off criteria of 3.0 Å and lattice energy cut-off of -48 KJ/mol were also included at the initial pre-screening stage.

**Table 5.2 Parameters employed in the systematic search for trial packing motifs for the triclinic phase of C18.**

Search parameters	Range of values	Increment employed
Rotation about <i>a</i> axis (°)	0-360	5
Rotation about <i>b</i> axis (°)	0-360	5
Rotation about <i>c</i> axis (°)	0-360	5
<b>Control parameters</b>		
High lattice energy cut-off	-48 KJ/mol	
Short distance cut-off	3.0 Å	

**Table 5.3 Summary of results of the systematic search for trial packing motifs for the triclinic phase of C18.**

Total number of configurations tried	373248
Total number of failed configurations	373096
Failures on non-bonded distance criteria	279626
Failures on lattice energy criteria	93522
Failures on XRD fit criteria	93570
Failures on both energy and XRD fit criteria	93470
Successful configurations on energy	100
Successful configurations on XRD fit	52
Total number of successful configurations	152

The results after searching procedure for the best trial structure are presented in **Table 5.3**. This systematic search started with 373248 packing arrangements reduced significantly by distance criteria which were the pre-screen step. Overall, only 100 structures were accepted with lattice energy calculation and only 52 structures were accepted with XRD fit. It is worth noting that the best trial structure as ranked from the energy calculation was not consistent with the top one regarding XRD fit. For the purpose of comparison of different start points, both of the top ranked structures were further processed with further Rietveld refinement.

### 5.2.2.2 Rietveld refinement

The best trial structure based on lattice energy calculation could not fit the XRD data by Rietveld refinement under reasonable restraints as applied to bond length and angle. The successful fit was obtained with best trial structure regarding the XRD fit. The best fit plot from the structure after Rietveld refinement [101] by TOPAS software and energy optimisation by COMPASS force field [102] is given in **Figure 5.2**. The first reflection peaks of (001) and (002) showed highly asymmetry behaviour due to the extreme axial divergence at low angles and were excluded from the Rietveld refinement. The fractional coordinates of carbon atoms in the asymmetric unit are given in **Table 5.4**.

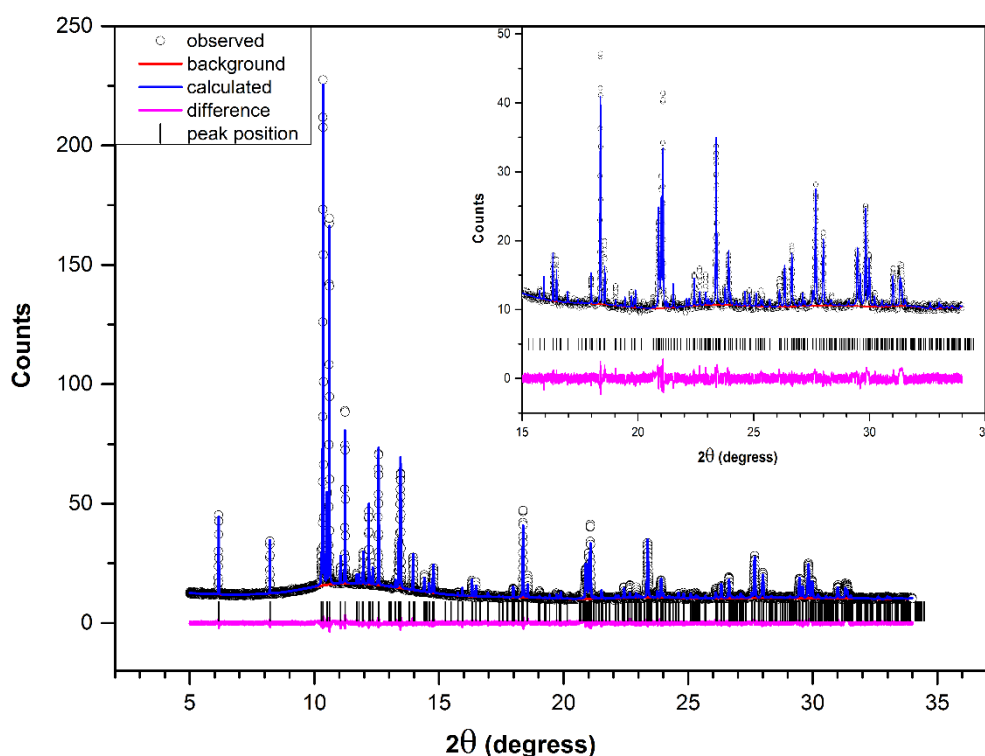


**Figure 5.2** Rietveld refinement of C18 in the range of 5 to 34° 2θ with  $\lambda = 0.825678 \text{ \AA}$  with different scale of amplified according to the intensity of the reflection peaks. Observed (o), calculated (—), difference (—) and positions of calculated reflections (!).

**Table 5.4 Fractional coordinates of carbon atoms of C18 at -40 °C and relative isotropic displacement parameters in the asymmetric unit of triclinic structure after Rietveld refinement**

	$x/\text{Å}$	$y/\text{Å}$	$z/\text{Å}$	$U_{\text{iso}}/\text{Å}$
<b>C1</b>	0.05359	-0.12679	0.02543	0.04433
<b>C2</b>	0.09368	-0.02148	0.08108	0.04433
<b>C3</b>	0.2245	-0.26938	0.1313	0.04433
<b>C4</b>	0.27581	-0.1623	0.18589	0.04433
<b>C5</b>	0.40724	-0.41286	0.23534	0.04433
<b>C6</b>	0.45808	-0.31021	0.29028	0.04433
<b>C7</b>	0.58972	-0.56203	0.33942	0.04433
<b>C8</b>	0.63741	-0.46003	0.3948	0.04433
<b>C9</b>	0.77068	-0.71543	0.44306	0.04433

**Table 5.5 Fractional coordinates of carbon atoms of C18 at room temperature and relative isotropic displacement parameters in the asymmetric unit of triclinic structure after Rietveld refinement**

	$x/\text{Å}$	$y/\text{Å}$	$z/\text{Å}$	$U_{\text{iso}}/\text{Å}$
<b>C1</b>	0.07497	-0.12629	0.02426	0.04433
<b>C2</b>	0.10943	-0.0207	0.08034	0.04433
<b>C3</b>	0.25925	-0.27321	0.12888	0.04433
<b>C4</b>	0.29316	-0.16745	0.18496	0.04433
<b>C5</b>	0.44269	-0.41976	0.23357	0.04433
<b>C6</b>	0.47539	-0.31369	0.28968	0.04433
<b>C7</b>	0.62451	-0.56584	0.33835	0.04433
<b>C8</b>	0.65578	-0.46042	0.39461	0.04433
<b>C9</b>	0.80496	-0.71433	0.44272	0.04433

For the purpose of comparison of structures from PXRD data and single crystal result from Nyburg [60], the XRD data at room temperature (RT) detected by a PSD detector with limited collection time was utilised to determine the structure by Rietveld refinement using the low-temperature structure from this work. The fractional coordinates of carbon atoms in the asymmetric unit are given in **Table 5.5**.

Furthermore, lattice energies were calculated using a programme called HABIT [103] applied with Williams Forcefield [104]. These calculations are listed in **Table 5.6** together with the associated molecular geometry information obtained from the Mercury with averaged bond angles of C-C-C

and bond length of C-C are also provided. Finally, the relative reduce cell [105] parameters were also calculated based on the theory of Niggli [106].

**Table 5.6 Crystallographic data of C18 from the best-fit Rietveld refinement at different temperature together with detailed information from single crystal structure from Nyburg. In quotation is the calculated reduce cell obtained from Avogadro [107] programme according to Niggli theory.**

	<b>This work -40 °C</b>	<b>This work RT</b>	<b>Nyburg_1972 RT</b>
<b>a/Å</b>	4.224 (4.224)	4.291 (4.291)	4.285 (4.285)
<b>b/Å</b>	4.771 (4.771)	4.826 (4.826)	4.82 (4.82)
<b>c/Å</b>	23.488 (23.056)	23.476 (23.065)	24.898 (23.068)
<b>α/°</b>	78.982 (90.700)	79.208 (91.067)	85.15 (91.102)
<b>β/°</b>	84.548 (92.199)	84.485 (92.017)	67.8 (92.081)
<b>γ/°</b>	73.600 (106.400)	72.562 (107.437)	72.7 (107.300)
<b>V/Å<sup>3</sup></b>	445.26	455.11	454.35
<b>C-C-C/°</b>	113.9	113.1	114.9
<b>C-C/ Å</b>	1.520	1.532	1.508
<b>R<sub>wp</sub>/%</b>	10.46	8.16	8
<b>R<sub>p</sub>/%</b>	6.79	4.99	8
<b>Gof (χ<sup>2</sup>)</b>	2.15	28.19	NA
<b>Number of reflections</b>	337	345	NA
<b>Number of independent parameters</b>	63	48	NA
<b>2θ range/°</b>	5-34	5-34	NA
<b>D<sub>c</sub>/ g cm<sup>-3</sup></b>	0.95	0.93	0.93
<b>Lattice energy/ KJ mol<sup>-1</sup></b>	-136	-134	-135

The final Rietveld refinement of C18 at -40 °C indicates a success of the solved structure as seen from **Figure 5.2** together with the relatively low value of  $R_{wp}$  and goodness fit value that close to the one from the simulation with a wide angular range of XRD data (**Table 5.6**). The packing of this structure as shown in **Figure 5.3** is sensible with molecular geometry and is in good agreement with literature with averaged C-C bond length of 1.520 Å and bond angle C-C-C of 113.9°. Moreover, it is proved by the low lattice energy (-136 KJ mol<sup>-1</sup>) indicating a high stability of this structure.

The determined room temperature (RT) structure of C18 from this work shows consistency with the low temperature structure as seen from the atomic positions (**Table 5.5**) and from the unit cell parameters (**Table 5.6**) except the expanding axis lengths which are caused by the thermal effect. It is worth noting that the  $R_{wp}$  value from Rietveld refinement of room temperature diffraction data is smaller than the fit at -40 °C but with poor value of goodness fit which is 28.19 rather than the more ideal case at LT which is closer to one. This is possibly due to the wider step size and shorter scanning time with resultant diffraction pattern having a reduced resolution with fewer variables can be refined. Hence, the insufficient resolution powder diffraction data would affect the structure determination to some extent.

From the comparison in **Table 5.6**, the molecular structures determined using PXRD and single XRD have shown close molecular volumes and minimum geometry difference at RT. Exceptions are found in Nyburg [60] configuration with a larger C-C-C bond angle (114.9°) and shorter bond length of C-C (1.508 Å). The lattice energy is nearly the same with the two structures, whereas the lattice parameters are quite different in terms of c axis length and  $\alpha$ ,  $\beta$  angles. In this case, the reduce cell calculation is applied to each lattice. As a result, the reduced cell from the structure determined in this work is in good agreement with the one determined by Nyburg at RT.

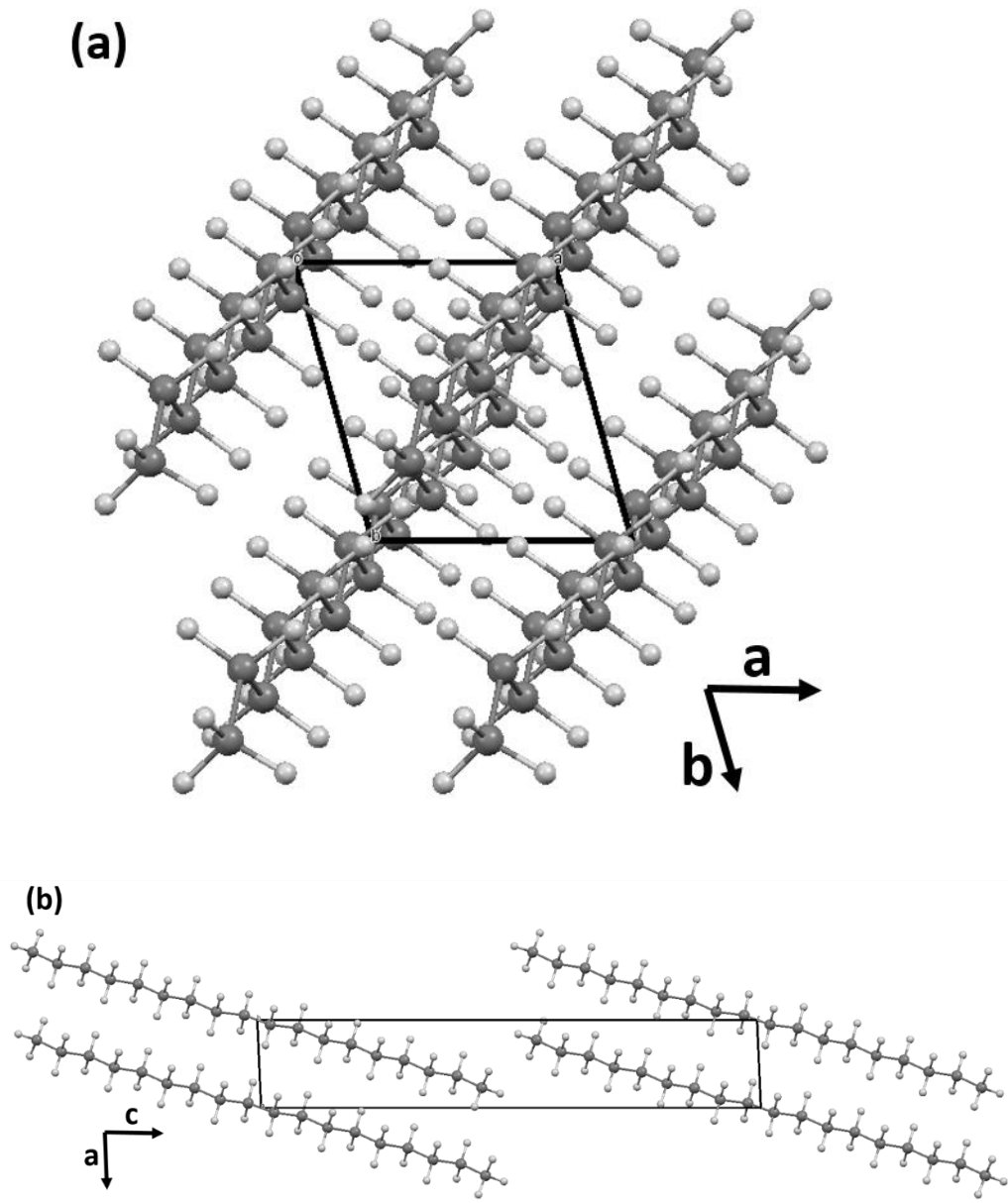


Figure 5.3 Packing of the C18 unit cell along with c-axis (a) and b-axis (b).

### 5.2.3 Thermal Expansion

An overview of crystallographic diffractions collected from in-situ SPXD (synchrotron powder X-ray diffraction) during continuous cooling from the early stage of solidification to the very low temperature at  $-40\text{ }^{\circ}\text{C}$  is shown in **Figure 5.4**. The polymorphic behaviour of C18 was not observable over the temperature range as discovered in this work. Preferred orientation character was clearly seen from high-intensity reflection planes of (011) and (012) at  $2\theta$  around  $10.5^{\circ}$ . Because of the wide angular range of the collected XRD patterns and a large amount of collection number as scanned with  $2\text{ }^{\circ}\text{C}$  intervals within a temperature range of  $20\text{ }^{\circ}\text{C}$  to  $-40\text{ }^{\circ}\text{C}$ , 30 plots in total are presented resulting that it is technically impossible to present all the information clearly. Hence, as highlighted, these parts with interests with respect to low angle (00L) reflections, amorphous content and thermally peak shift behaviour, are enlarged and presented in following Figures of 5.5, 5.6 and 5.7 (a-c).

High amorphous content represented by a large diffuse peak under diffraction peaks around  $2\theta$  of  $10.5^{\circ}$  exists at the beginning of crystallisation at  $23.04\text{ }^{\circ}\text{C}$  as shown in **Figure 5.5**. This could indicate the disordering packing exists at high temperature near the onset of crystallisation. Interestingly, the broad peak is observable even before crystallisation within the liquid phase. Due to the relatively d-spacing is approximately  $4.5\text{ \AA}$ , which is corresponding to the lateral interchain attraction. Interpretation can be made from this as the interchain interaction is actually formed prior to the solid formation [73]. The disordering behaviour can also be achieved as the diffraction patterns at low angles have shown splitting (00L) peaks at the early stage of crystallisation (**Figure 5.6**).

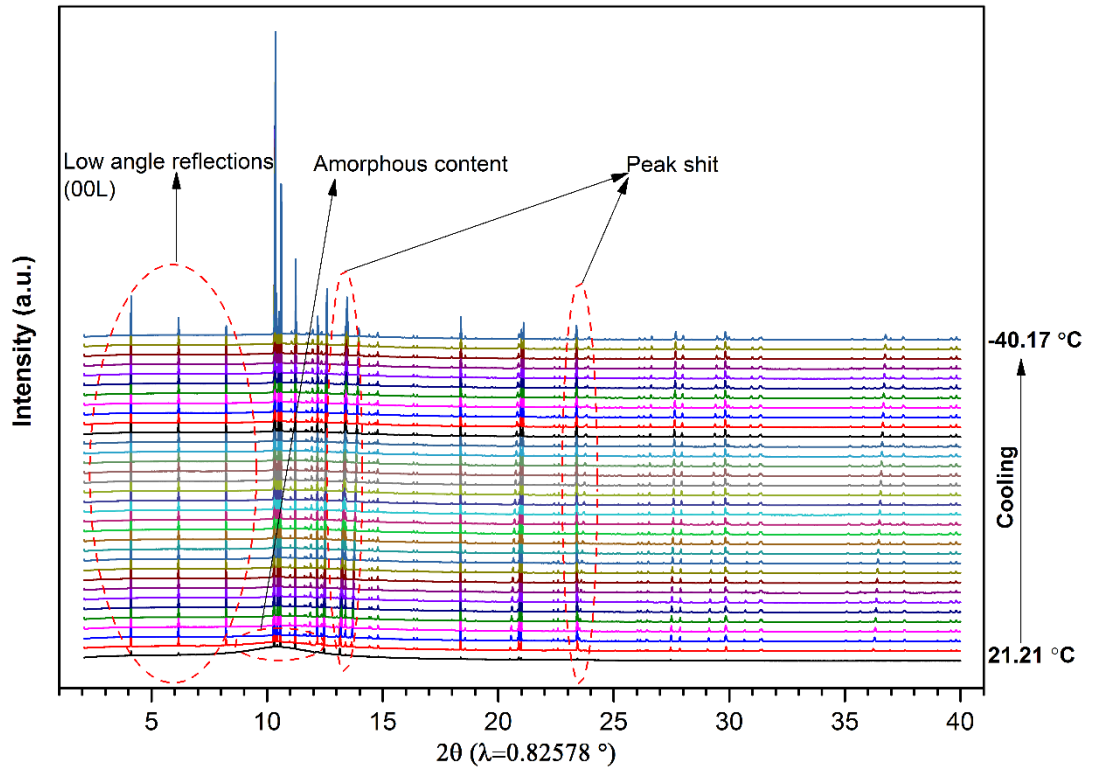


Figure 5.4 In-situ SPXD patterns for pure C18 collected from 21.21 °C to -40.17 °C with 2 °C intervals during cooling process at 1.67 °C /min.

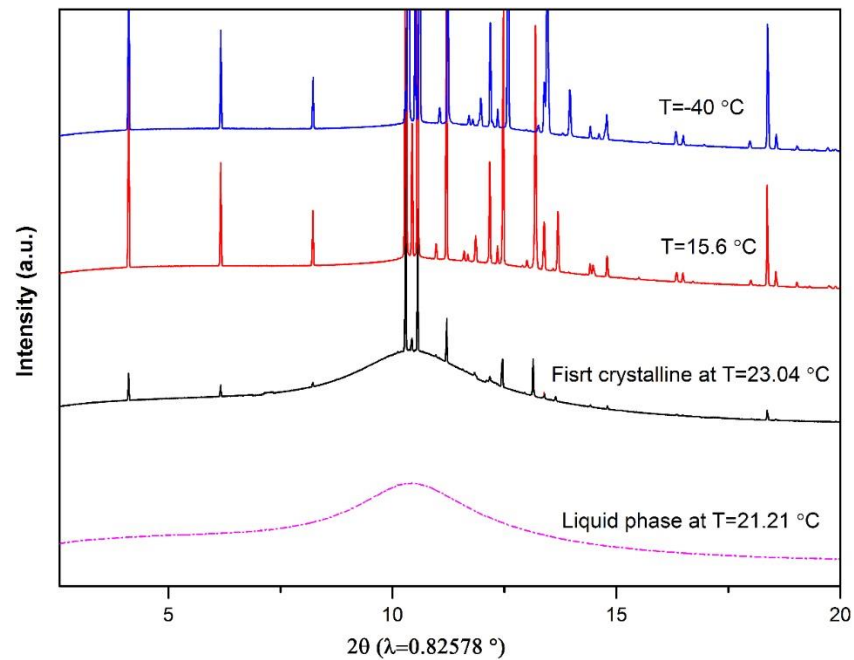
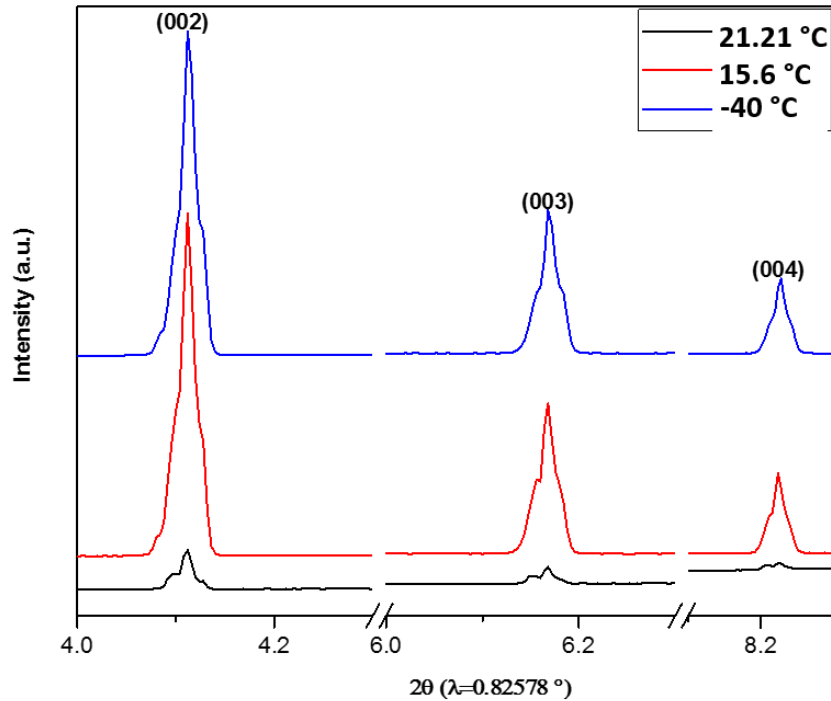
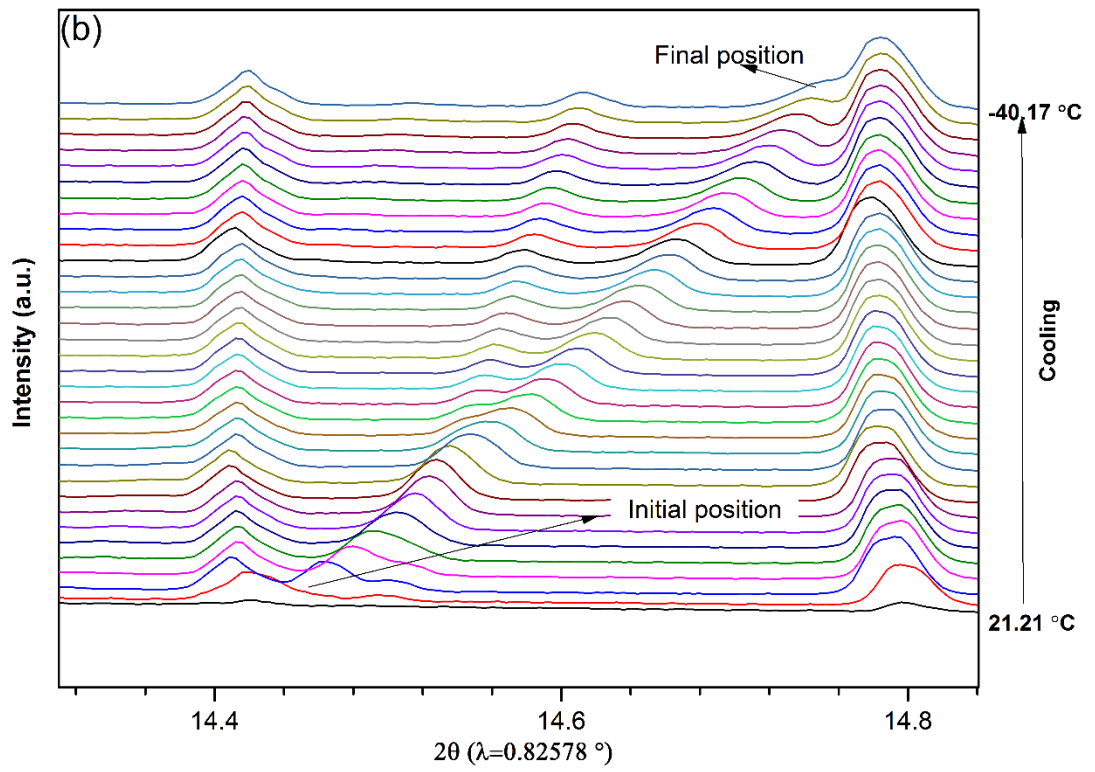
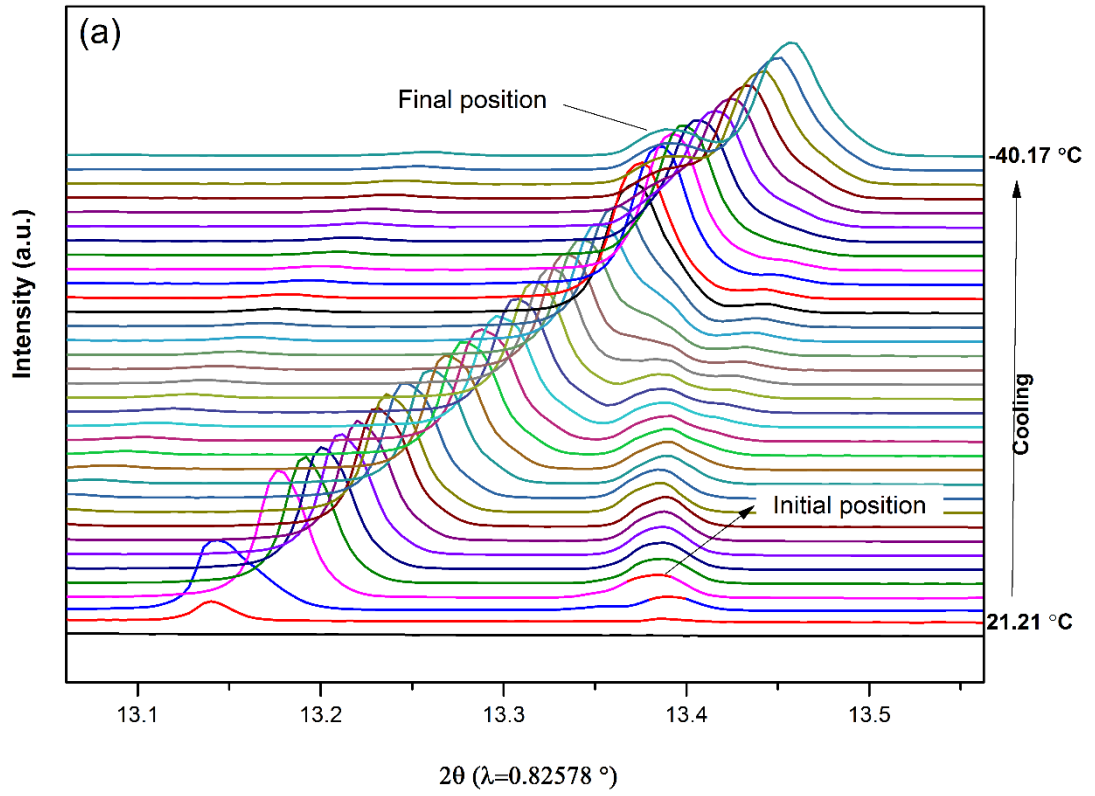


Figure 5.5 Diffraction pattern of C18 at the onset of crystallisation shows a large broad amorphous content. This is also observed within diffraction pattern prior to crystallisation in a liquid state.



**Figure 5.6** Low angle (00L) diffraction patterns collected from the early stage of crystallisation (21.21 °C and 15.6 °C) and the bottom temperature at -40 °C.

Thermal expansion properties of the fully ordered crystalline with decreasing temperature shows anisotropic behaviour as the peak shift is not standardised. It is larger for some reflections (e.g., (110)) than others (e.g., (002)). The enlargement of typical peak shifts are shown in **Figure 5.7 (a-c)** with the summarised main thermal effects of diffraction peaks shifts i.e. (a) low-intensity peak position twisted from higher angle to lower angle side from the nearest higher intensity peak; Two close peaks might be converged (b) or splitting behaviour from the broad peaks (c). These various changes within the reflections during cooling might result in different habit faces of crystal growth from various supersaturations.



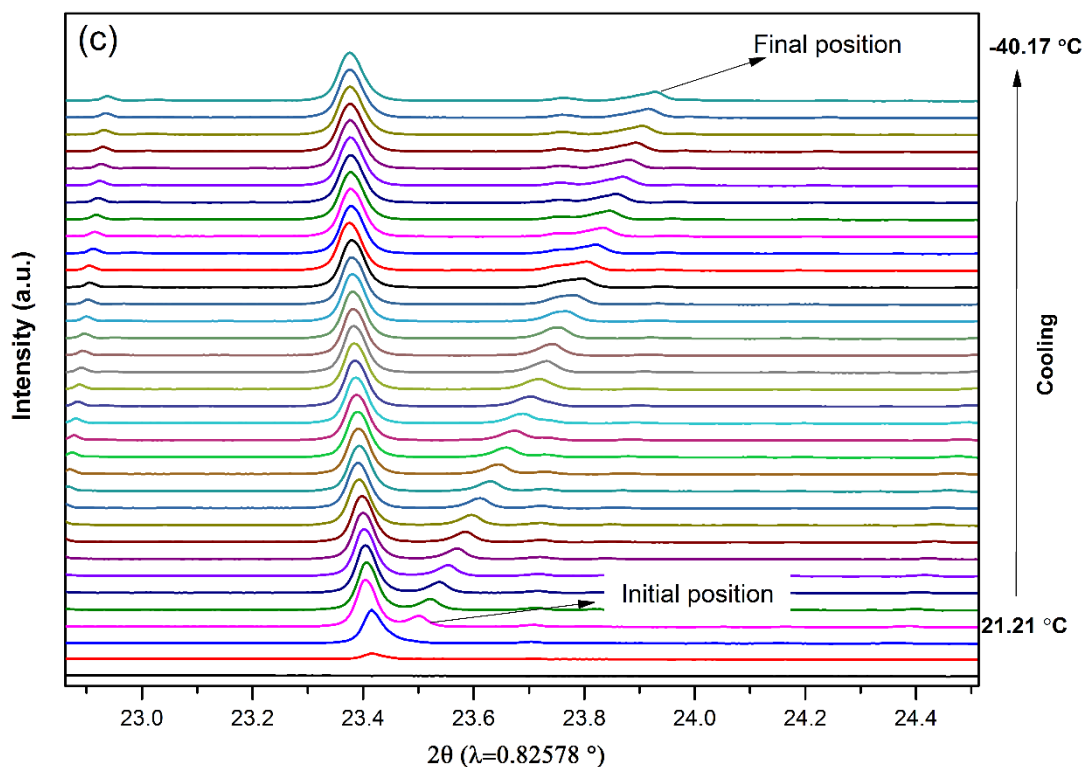


**Figure 5.7 The enlargement of typical reflection peaks, as position shift not standardised from thermal effects: (a) twisted (b) converged (c) splitting.**

Further inspection on thermal expansion properties was carried out with unit cell parameters determined to investigate the effects of each direction and the total volume of the lattice. The stack XRD patterns as a function of temperature were analysed with lattice parameters determined using “Pawley fit” by the programme of Topas by indexation of the unit cell determined in this work. The high quality of unit cell fitting was achieved with relatively low values of  $R_{wp}$  averaged at 4.09% ( $\pm 0.44$ ) and  $R_p$  averaged at 2.69% ( $\pm 0.23$ ). The resultant lattice parameters in six dimensions of unit cell plotted as a function of temperature are given in **Figure 5.8**. No significant change in volume of the unit cell was observed in this work, which again confirms that polymorphic behaviour or disorder phase did not exist. The thermal expansion coefficient of the volume of C18 triclinic cell over the temperature range -40 °C to 21 °C was calculated to be  $4.17 \pm (2.48) \times 10^{-4} \text{ } ^\circ\text{C}^{-1}$ .

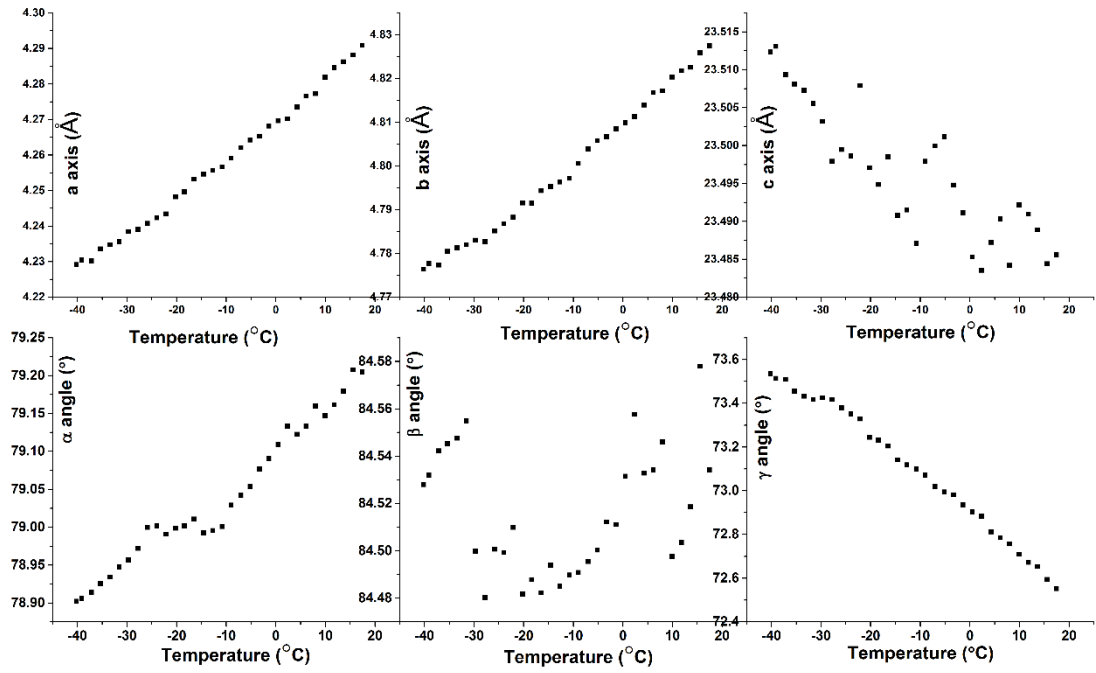


Figure 5.8 Unit cell parameters (a, b c axis and  $\alpha$ ,  $\beta$ ,  $\gamma$  angels) obtained from “Pawley fit” using TOPAS software are plotted as a function of temperature for C18.

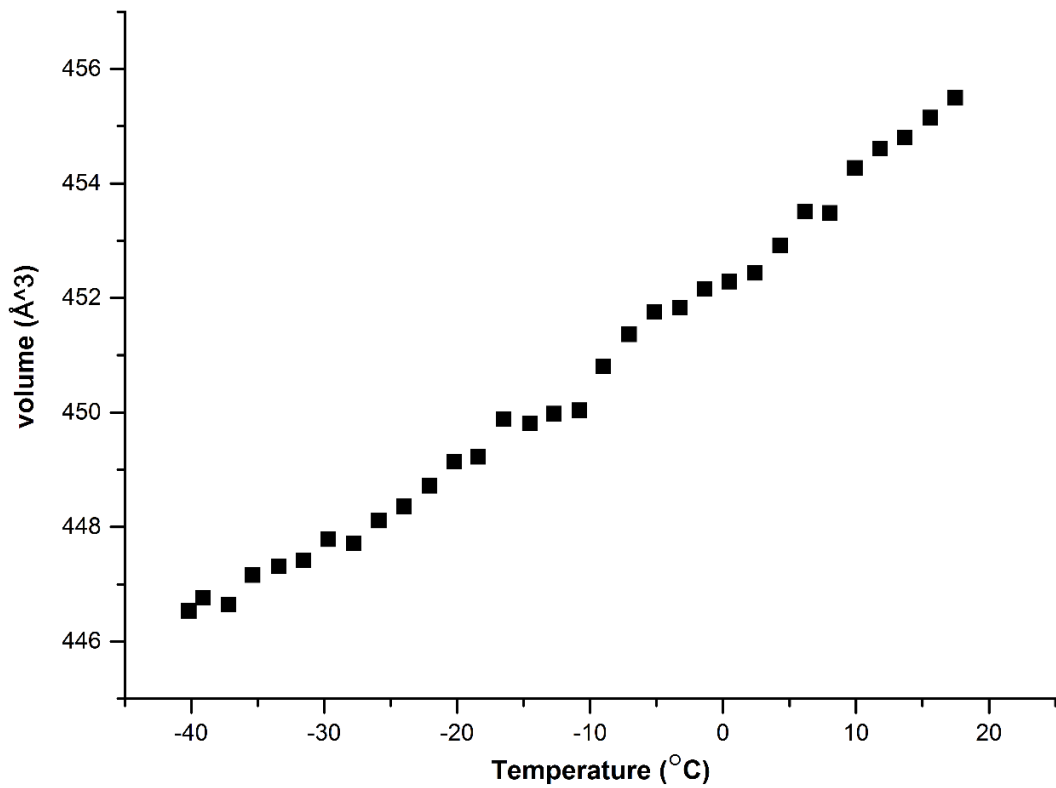


Figure 5.9 Volume of C18 unit cell obtained from “Pawley fit” using TOPAS software are plotted as a function of temperature.

As seen from **Figure 5.8**, the unit cell directions of a, b axis and  $\alpha$ ,  $\gamma$  angles have shown linear expansion as increasing temperatures from  $-40\text{ }^{\circ}\text{C}$  which can be regarded as the reference temperature. However, both c axis and  $\beta$  angle showed a negative increase trend and irregular behaviour at a high-temperature region near the onset of crystallisation. This can be explained due to the nature of low symmetry of triclinic unit cell, angles between each axis are with distinct thermal changes as a result of anisotropic behaviour. Totally, the lattice volume of C18 was thermally expanded positively in a near linear trend as a function of temperature (**Figure 5.9**).

As the thermal expansion of a certain lattice direction demonstrates how easy or difficult it is to thermally expand the plane, this can be related to the specific intermolecular interactions which run in that direction. This is seen from the c-axis is not thermally expanded but changes with disordering effects, which can be correlated to the relatively low angle peaks (OOL) are not shifting with temperature changes. By considering the splitting nature and higher amorphous content, it can be concluded the existence of disordering phenomenon from early stage crystallisation of C18 at high temperature region. Differentially, a and b axis thermally expanded regularly in a linear trend, as referred to the intermolecular attraction from the methylene groups along lamellae interchains, is stronger than the interaction between end methyl group along c-axis.

#### 5.2.4 Morphological Analysis

Crystal growth work had faced extreme difficulties, i.e. small MSZW, fast growth rate and difficult to observe faceted crystals with sufficient equilibrium time. Overall, morphology measurements of C18 crystallised in n-dodecane (400 g/l) solution as shown in **Figure 5.10**, typical [84, 108] n-alkane dominate face of  $\{001\}$  has been obtained in three different supersaturations of  $\sigma = 0.036$ ,  $T = 12.2\text{ }^{\circ}\text{C}$ ,  $\sigma = 0.045$ ,  $T = 12.1\text{ }^{\circ}\text{C}$  and  $\sigma = 0.08$ ,  $T = 11.7\text{ }^{\circ}\text{C}$ , within the MSZW from  $T_{diss} = 13\text{ }^{\circ}\text{C}$  to  $T_c = 11.7\text{ }^{\circ}\text{C}$ . At low supersaturation of  $\sigma = 0.036$ , hexagonal shape of the crystal suggests a hexagonal rotator phase  $R_2$  which is known as existing in longer chain of even alkanes prior to the inherent triclinic phase formation [48]. Shape collected at  $\sigma = 0.045$  is of an irregular polygon shape and the parallelogram shape of typical triclinic crystals were only observed at higher supersaturation of  $\sigma = 0.08$ . These morphologies

however are having non-identical smaller faces in comparison with the longer chain homologue alkane of n-docasane [109], even though the two components have identical triclinic structures (P-1). Hence, independent indexation for all these crystals were carried out by BFDH morphological predication utilising structure of C18 as just determined.

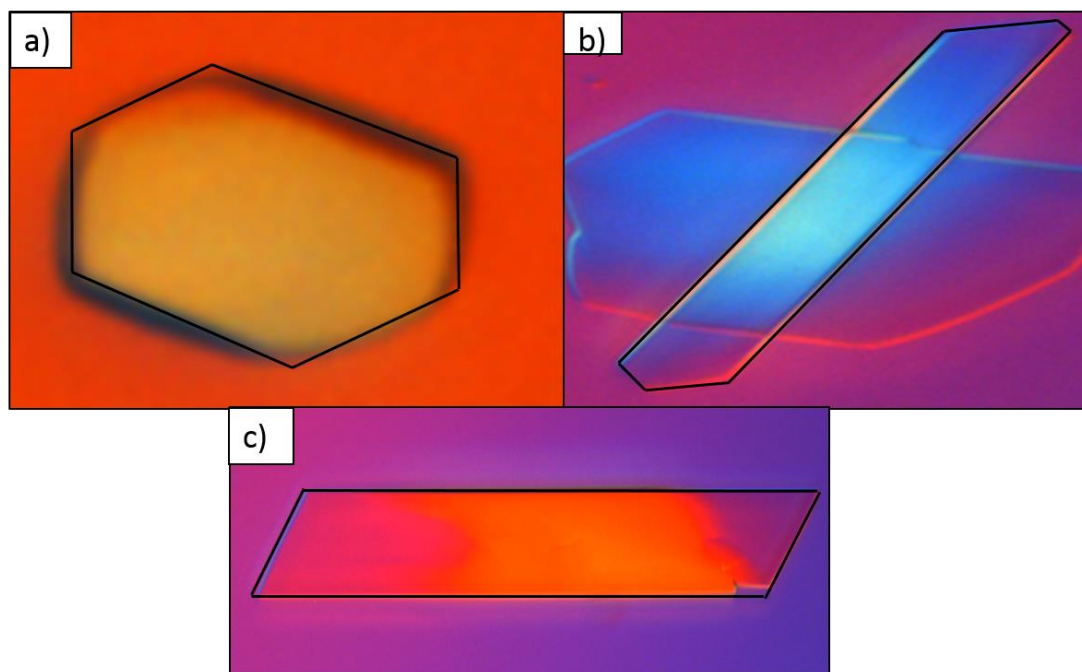


**Figure 5.10 Experimental morphology pictures of C18 in supersaturated n-dodecane solutions with three different supersaturations:  $\sigma = 0.036$ ,  $T = 12.2\text{ }^{\circ}\text{C}$  (a);  $\sigma = 0.045$ ,  $T = 12.1\text{ }^{\circ}\text{C}$  (b);  $\sigma = 0.08$ ,  $T = 11.7\text{ }^{\circ}\text{C}$  (c).**

From the analysis of BFDH prediction by the software of Material Studio, 100 morphological faces ( $hkl$ ) were revealed with their relative values of d spacing and distance to centre of the crystal. This includes the predominant face (001) as indexed for the largest facet area (73%) and the largest d spacing of ( $23.04\text{ \AA}$ ) which could be directly indexed to the largest face for each crystal. Other predications ( $hkl$ ) need further assessments to interpret the appropriate faces for experimental observation. According to the introduced methodology (4.3.5), the rest 99 uncertain planes were grouped into thirteen zones axis as listed in **Table 5.7**. Within each group, representatives ( $hkl$ ) are also presented with corresponding d spacing range. Full list table from BFDH is provided in Appendix A.

**Table 5.7 List of thirteen groups of zone axis with their representative planes (*hkl*) and respective inter-planer d spacing.**

Group	Zone axis [uvw]	Representative plane (hkl)	$d_{hkl}$
1	[010]	(010)	4.60
		(021)	2.28
		(031)	1.53
2	[100]	(100)	3.80
		(201)	1.96
		(302)	1.31
3	[110]	(110)	3.47
		(221)	1.77
4	[1-10]	(1-10)	2.59
		(1-11)	2.65
5	[120]	(120)	2.28
		(121)	2.32
6	[210]	(210)	1.97
		(211)	2.03
7	[1-20]	(1-20)	1.76
8	[2-10]	(2-10)	1.60
9	[130]	(130)	1.59
10	[230]	(230)	1.41
11	[310]	(310)	1.32
12	[321]	(321)	1.30
13	[1-31]	(1-31)	1.31

Pair-wise the thirteen (hkl) planes from zone axis analysis (**Table 5.7**), success pair candidates are listed in **Table 5.8 and 5.9** for supersaturation of  $\sigma = 0.036$  and  $\sigma = 0.045$  respectively with the correlated matching faces (A, B and C) according to designation of experimental crystal morphological faces as shown in **Figure 5.11 (a) and (b)**.

As cross-checked with each pair of (AB), (AC) and (BC), potential solutions of A, B and C for  $\sigma = 0.036$  are (010) (321) (2-10) and (130) (2-10) (321). The best solution is selected to be (010) (321) (2-10) due to the regarded “A” face of (130) with a shorter d spacing which indicates higher growth rate hence lower importance than the selected one of (010). At  $\sigma = 0.045$  the unique solution matching all the pairs is solution of (1-20) (100) (230) for the designate faces of A B and C. The resultant potential is a unique solution of (-110) (130) from the pair-wise analysis for the parallelogram shape at high supersaturation of  $\sigma = 0.08$

Regarding the potential solution faces of (hkl) and predominant face of (001), resultant morphological predictions are observed with a further modification of the perpendicular distances from the centre of the crystal to the edge of the faces, which gives the compatible length of each face to the experimental observation. Hence, **Figure 5.11** also compares the most likely morphology from prediction with the micrograph taken from experimental crystals at three different supersaturations and the respect Miller indices are given with the predictions.

**Table 5.8 List of pair-wise planes matching the internal angel from experimental crystals at  $\sigma = 0.036, T = 12.2$  °C. The potential solutions of the morphological planes are presented with the best solution highlighted. Planes designated are shown in Figure 5.9 (a).**

AB	AC	BC
(010) (2-10)	(010) (-100)	(010) (110)
(1-10) (310)	(1-10) (-1-20)	(100) (1-31)
(120) (1-31)	(010) (321)	(120) (310)
(130) (321)	(130) (2-10)	(2-10) (321)
Potential solutions		
A	C	B
(010)	(321)	(2-10)
(130)	(2-10)	(321)

**Table 5.9 List of pair-wise planes matching the internal angel from experimental crystals  $\sigma = 0.045, T = 12.1$  °C. The unique potential solution is presented of the morphological predication. Planes designated are shown in Figure 5.9 (b).**

AB	AC	BC
[1-20] [100]	[1-20] [230]	[230] [100]
[210] [2-10]	[310][1-31]	[1-20] [310]
[1-20] [130]		
Potential unique solution		
A	C	B
(1-20)	(230)	(100)

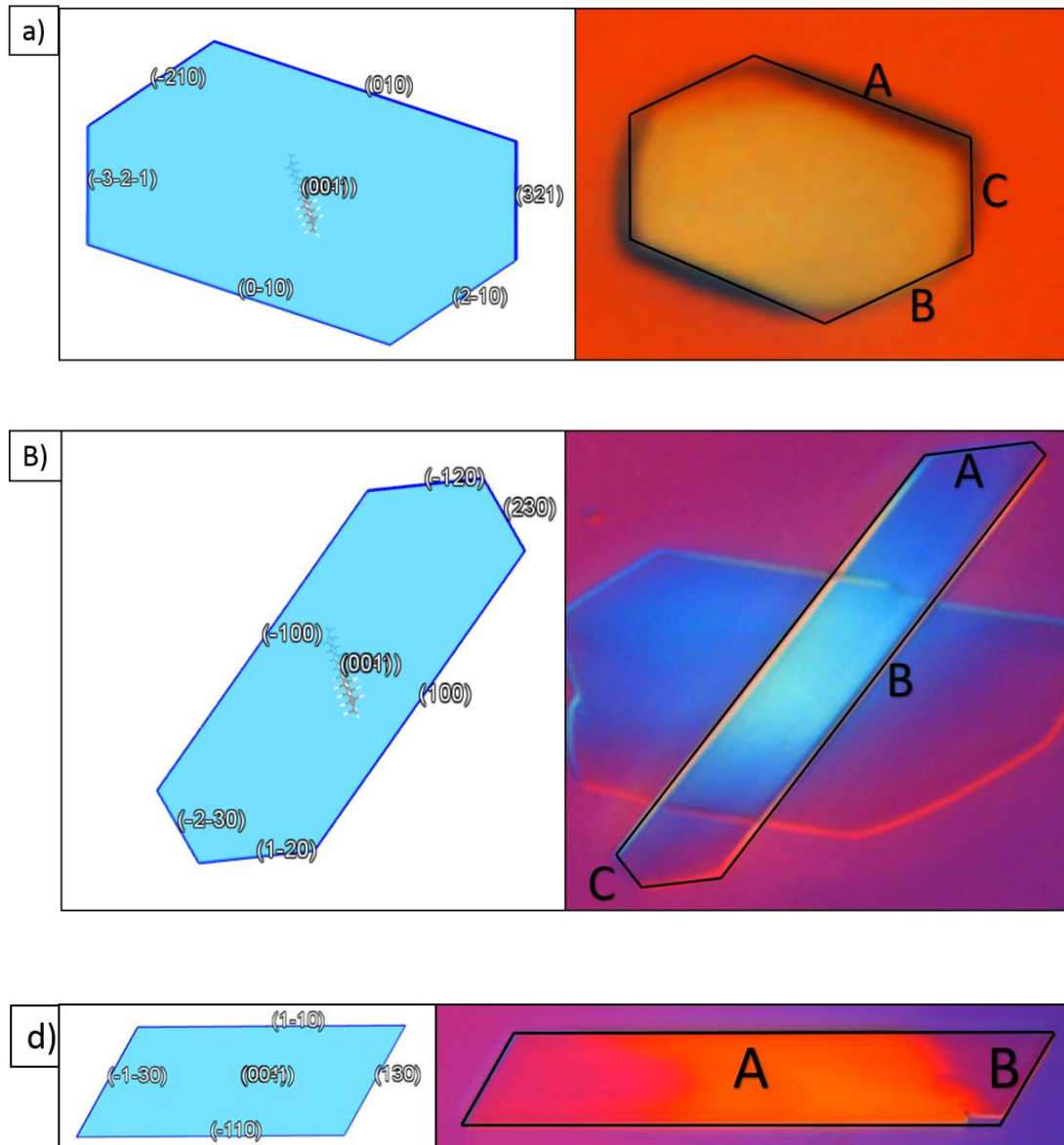


**Figure 5.11 BFDH morphology prediction (left hand) with Miller indices obtained from the best solutions according to the experimental morphology (right hand) in three different supersaturation (a)  $\sigma = 0.036, T = 12.2\text{ }^{\circ}\text{C}$  (b)  $\sigma = 0.045, T = 12.1\text{ }^{\circ}\text{C}$  (c)  $\sigma = 0.08, T = 11.7\text{ }^{\circ}\text{C}$**

### 5.3 Hexadecane

The presented structure of C16 at low temperature (-40 °C) was accomplished during the attendance in ACA crystallography school with help from Prof Jim Kaduk. The structure solution utilised indexation of the unit cell and Rietveld refinement by GSAS [110] software. Further Rietveld refinements using TOPAS software utilising the determined structure to experimental data both collected at 0 °C and -40 °C are presented and discussed in following section (5.3.1).

The low temperature (-40 °C) collected XRD pattern of C16 from the MAC detectors is detail presented in **Figure 5.12** with the indexation results of the major peaks.

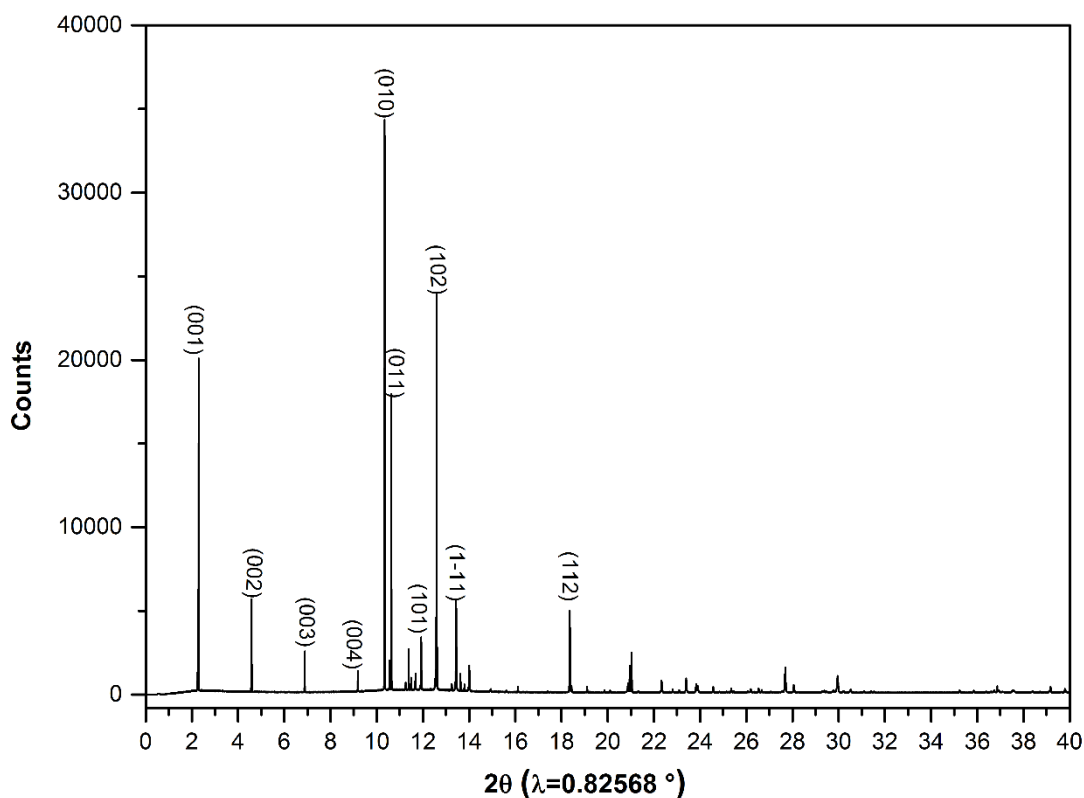


**Figure 5.12** High resolution synchrotron XRD pattern of C16 at -40 °C collected on I11 of Diamond Light Source. Together with the indexation results of the high-intensity reflections.

### 5.3.1 Structure Refinement

The final Rietveld refinement of C16 crystallised at -40 °C with the calculated and experimental observation of XRD patterns are shown in **Figure 5.13** representing the good agreement with the observed structure. The molecular structure and intermolecular packing along b-axis and c-axis are given in **Figure 5.14**. The refined structures for C16 at -40 °C and 0 °C with fractional coordinates of carbon atoms are given in Table 5.10 and 5.11. The respected crystallographic and fitting data are summarised in **Table 5.12**. Crystallographic cell dimension parameters of a, b and c are smaller than crystal determined just below crystallisation due to the thermal effects. Averaged C-C and C-H bond length is 1.531 ( $\pm 0.001$ ) Å and 1.098 ( $\pm 0.049$ ) Å. Averaged bond angles of C-C-C (110.4°) is consistent with structure published from Me´tivaud [100]. The H-H intermolecular contract between the adjacent chains is averaged at 2.624 (0.004) Å. C-C-C-C torsion angle is 175.0 ( $\pm 1.9$ ) ° which slightly deviates from the ideal 180° for the all-trans configuration.

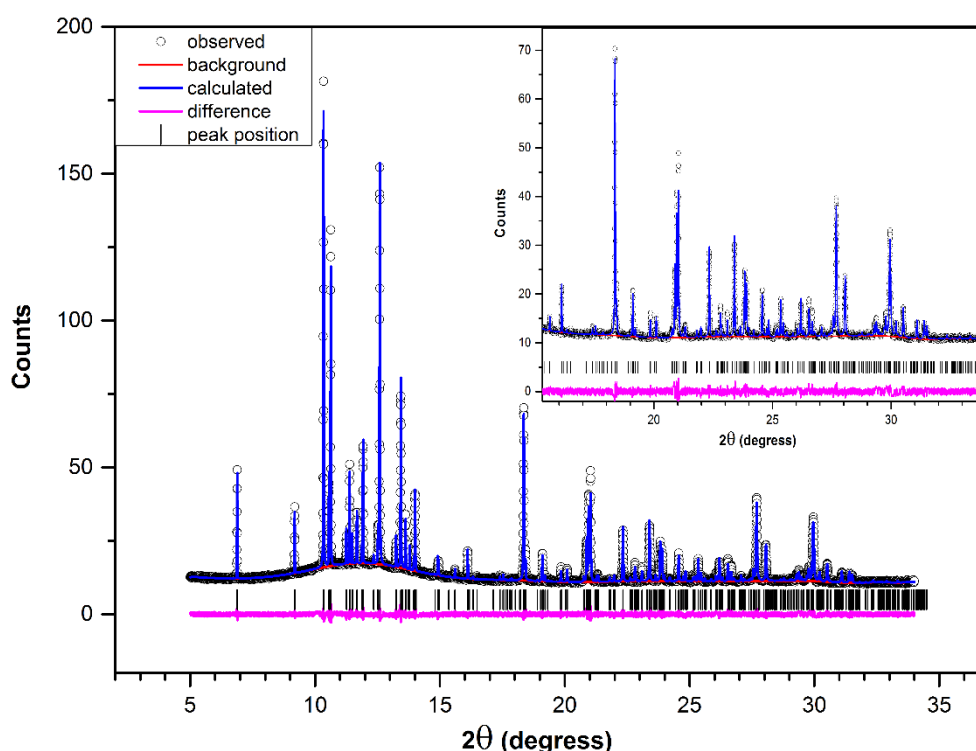


**Figure 5.13** Rietveld refinement of C16 in the range of 5 to 34°  $2\theta$  with  $\lambda = 0.825678$  Å with different scale of amplified according to the intensity of the reflection peaks. Observed (o), calculated (—), difference (—) and positions of calculated reflections (!).

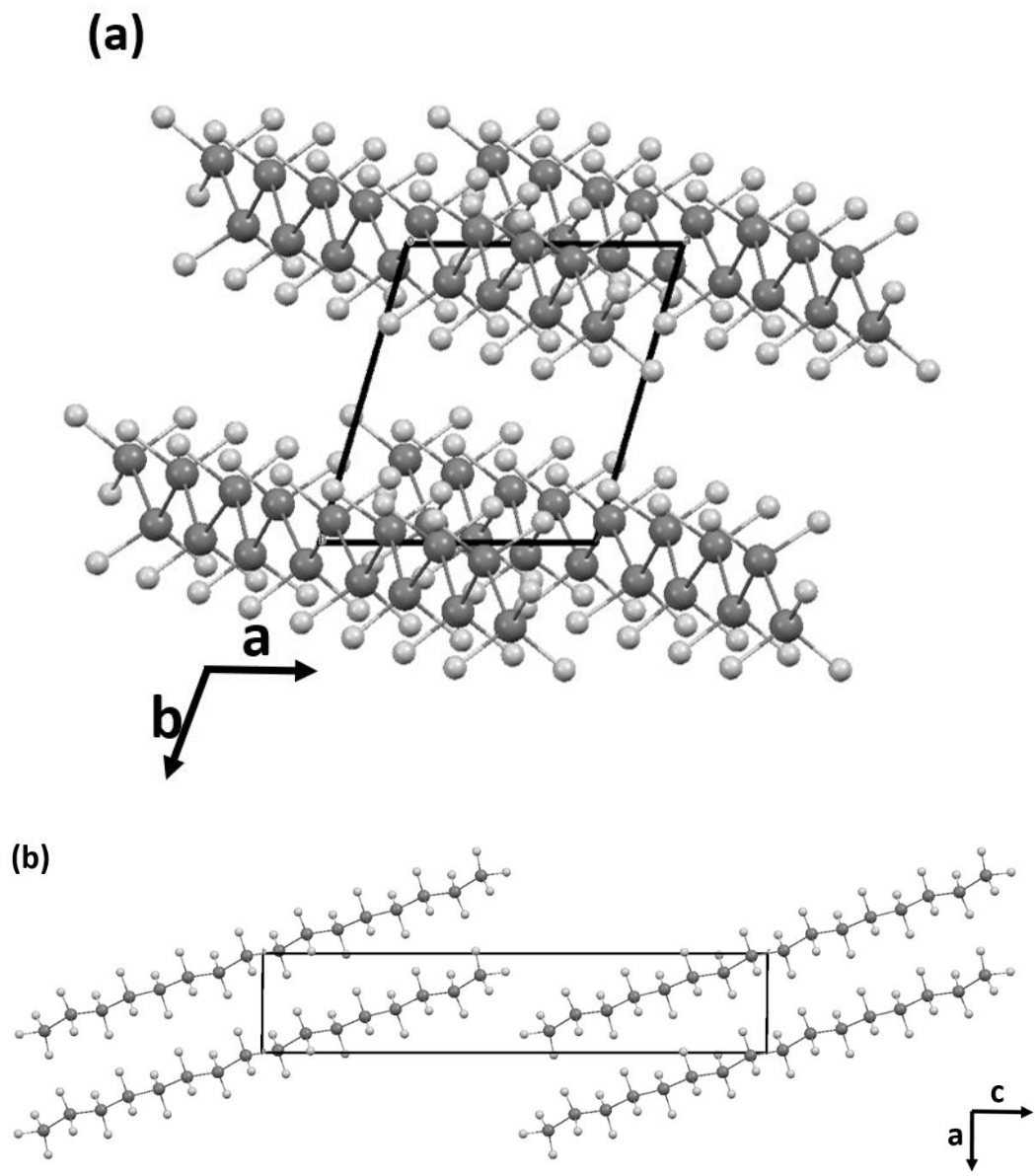


Figure 5.14 Packing of C16 unit cell along c-axis (a) and b-axis (b).

**Table 5.10 Fractional coordinates of carbon atoms of C16 at -40 °C and relative isotropic displacement parameters in the asymmetric unit of triclinic structure after Rietveld refinement**

	<b>x/Å</b>	<b>y/Å</b>	<b>z/Å</b>	<b>U<sub>iso</sub>/Å</b>
<b>C1</b>	0.7794	0.2782	-0.43106	0.0363
<b>C2</b>	0.6152	0.0605	-0.37914	0.0363
<b>C3</b>	0.5738	0.2294	-0.31776	0.0363
<b>C4</b>	0.4381	0.0119	-0.26388	0.0363
<b>C5</b>	0.3627	0.1715	-0.20354	0.0363
<b>C6</b>	0.2407	-0.0402	-0.14786	0.0363
<b>C7</b>	0.1925	0.1282	-0.08659	0.0363
<b>C8</b>	0.0269	-0.0735	-0.03191	0.0363

**Table 5.11 Fractional coordinates of carbon atoms of C16 at 0 °C and relative isotropic displacement parameters in the asymmetric unit of triclinic structure after Rietveld refinement**

	<b>x/Å</b>	<b>y/Å</b>	<b>z/Å</b>	<b>U<sub>iso</sub>/Å</b>
<b>C1</b>	0.77053	0.27413	-0.43126	0.0363
<b>C2</b>	0.61846	0.05715	-0.37841	0.0363
<b>C3</b>	0.57799	0.22708	-0.31671	0.0363
<b>C4</b>	0.42793	0.00849	-0.2633	0.0363
<b>C5</b>	0.38323	0.1785	-0.20196	0.0363
<b>C6</b>	0.23234	-0.03931	-0.14837	0.0363
<b>C7</b>	0.19309	0.13284	-0.08662	0.0363
<b>C8</b>	0.04317	-0.08246	-0.03318	0.0363

**Table 5.12 Crystallographic data of C16 from the best-fit Rietveld refinement at different temperature together with detailed information from lab PXRD crystal structure from Me´tivaud. In quotation is the calculated reduce cell obtained from Avogadro programme according to Niggli theory**

	<b>This work -40 °C</b>	<b>This work 0 °C</b>	<b>Me´tivaud 0 °C</b>
<b>a/Å</b>	4.229 (4.229)	4.276 (4.276)	4.270 (4.270)
<b>b/Å</b>	4.773 (4.773)	4.810 (4.809)	4.811 (4.811)
<b>c/Å</b>	20.623 (20.623)	20.640 (20.637)	22.345 (20.633)
<b>α/°</b>	90.789 (90.789)	91.085 (91.081)	84.541 (91.032)
<b>β/°</b>	90.297 (90.297)	90.155 (90.156)	67.428 (90.103)
<b>γ/°</b>	106.368 (106.368)	107.089 (107.088)	72.996 (107.004)
<b>V/Å<sup>3</sup></b>	399.32	405.791	405.211
<b>C-C-C/°</b>	110.4	108.882	113.12
<b>C-C/ Å</b>	1.531	1.539	1.532
<b>R<sub>wp</sub>/%</b>	10.08	5.96	8
<b>R<sub>p</sub>/%</b>	6.64	3.58	8
<b>Gof (χ<sup>2</sup>)</b>	2.16	19.61	NA
<b>Number of reflections</b>	304	308	NA
<b>Number of independent parameters</b>	63	82	NA
<b>2θ range/°</b>	5-34 (λ=0.82568°)	5-45 (λ=0.82578°)	3-60 (λ=1.56°)
<b>D<sub>c</sub>/ g cm<sup>-3</sup></b>	0.94	0.93	0.93

### 5.3.2 Thermal Expansion

As expected, thermal expansion properties of shorter chain homologue component of C16 are consistent with observations from C18. Analysis from in-situ crystallisation as shown in **Figure 5.15**, again, indicates isomorphism nature of C16 with the triclinic structure formed in the studied temperature range (13.7 °C to -40.1 °C). Low angle reflections (00L) were enhanced with peak intensities increased in relative to the rest reflections. The high content of amorphous was also observed from diffraction pattern at the onset of crystallisation around 2θ of 10.5°. Additionally, anisotropic peak shift behaviour is also similar to C18 reflections (**Figure 5.7**).

The resultant unit cell parameters as a function of temperature are plotted in **Figure 5.16** with the high quality of “Pawley fit” analysis indicated by low values of  $R_{wp}$  averaged at 6.82 % ( $\pm 0.44$ ) and  $R_p$  averaged at 4.18 % ( $\pm 0.27$ ). The thermal expansion coefficient of triclinic cell of C16 over temperature range  $-40\text{ }^{\circ}\text{C}$  to  $13.7\text{ }^{\circ}\text{C}$  was calculated to be  $(4.39 \pm 1.94) \times 10^{-4}\text{ }^{\circ}\text{C}^{-1}$  in volume. This value is very close to the triclinic cell from C18 of  $(4.17 \pm 2.48) \times 10^{-4}\text{ }^{\circ}\text{C}^{-1}$  which is a lower value of deviation from C16 indicating the disordering effects are reduced as the chain length decreases. This can also be reflected from **Figure 5.16** with the more regular linear trend of thermal expansion plots is observed from C16 unit cell especially the c-axis direction.

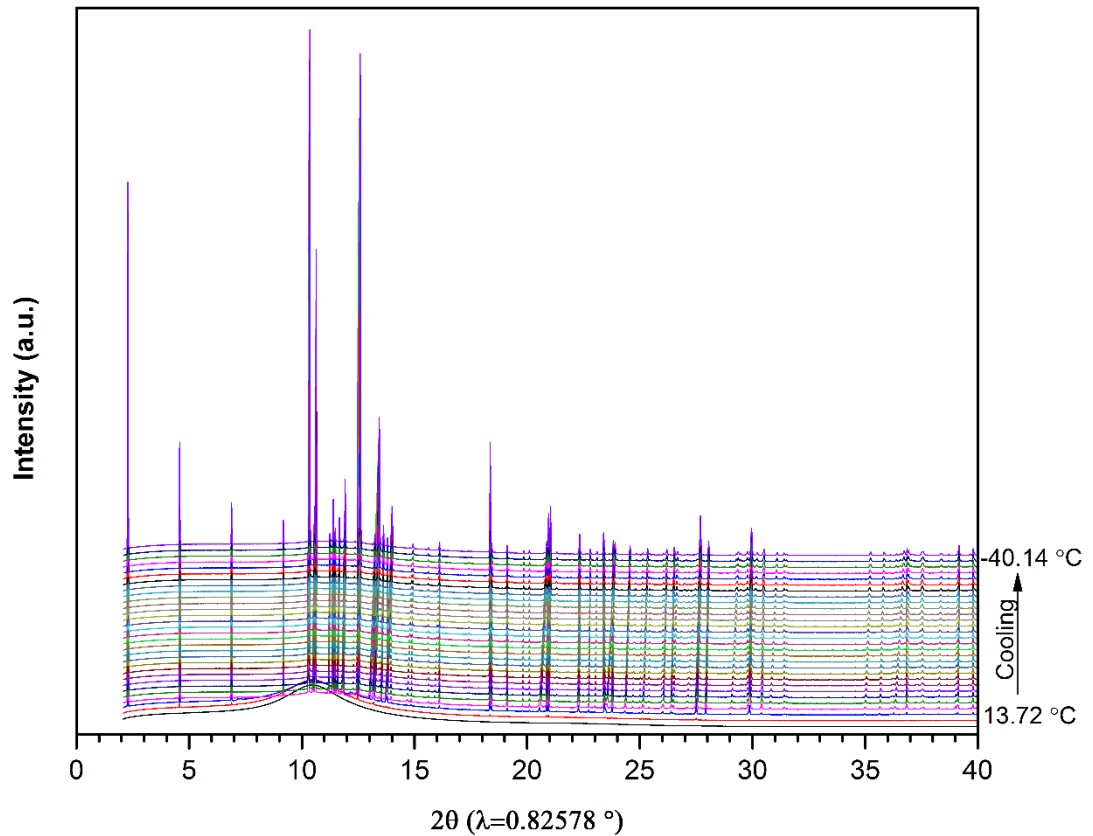


**Figure 5.15** In-situ SPXD patterns for pure C16 collected from  $13.72\text{ }^{\circ}\text{C}$  to  $-40\text{ }^{\circ}\text{C}$  with  $2\text{ }^{\circ}\text{C}$  intervals during cooling process at  $1.67\text{ }^{\circ}\text{C}/\text{min}$ .

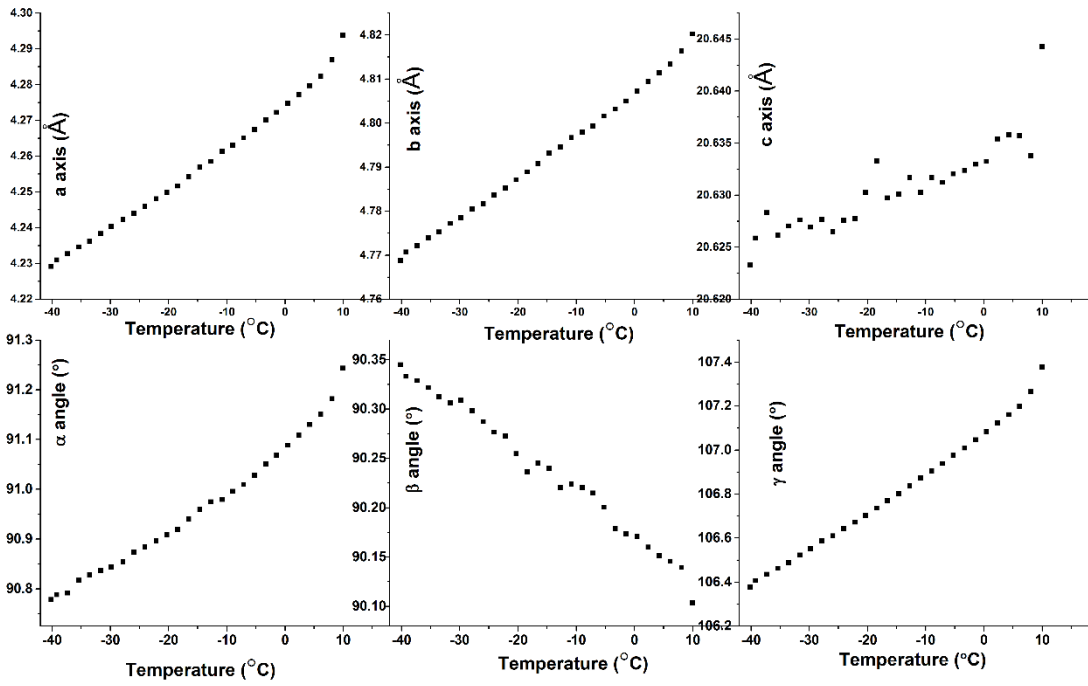


**Figure 5.16** Unit cell parameters (a, b c axis and  $\alpha$ ,  $\beta$ ,  $\gamma$  angels) obtained from “Pawley fit” using Topas software are plotted as a function temperature for C16

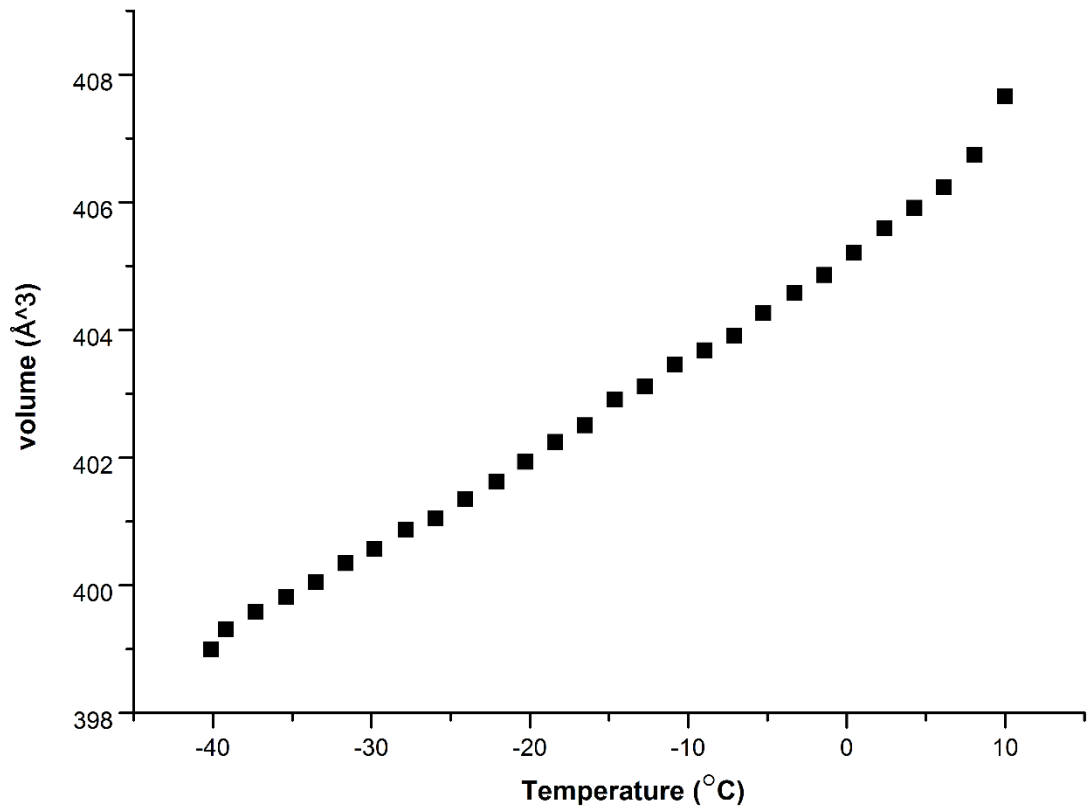


**Figure 5.17** Volume of C16 unit cell obtained from “Pawley fit” using TOPAS software are plotted as a function temperature.

## 5.4 Discussions

A reasonable trial structure indeed makes the refinement much easier and more sensible since the best configuration has been selected from a large number of possibilities in respect of both lattice energy and XRD fit. In this case, we have proved this point as only certain bond restraints and spherical harmonics corrections for preferred orientation and anisotropic factor had been applied during Rietveld refinement to determine the final structure. In other words, it has not been corrected far away from the beginning of the selected best trial structure obtained from the systematic search. The benefit of the lattice energy calculation is taken into account with the intermolecular bonding of both methylene and methyl groups with reasonable packing arrangement of the molecular configuration. Whereas for the Rietveld refinement, hydrogen positions which are not recognised might result in ideal simulation between the structure with experimental XRD data but unrealistic packing arrangement.

From both alkanes of C18 and C16, even though the good agreement is observed from the determined structures and literature work, the room temperature structures from the literature are not applicable to the low temperature data (-40 °C) collected with high resolution synchrotron XRD in MAC detector with minimum step size. This could be interpreted by the reason of thermal expansion effect with resultant more reflection peaks at -40 °C as seen from the dynamic diffraction plots in **Figure 5.7 (a-c)**.

It was known that the even alkane crystallising with triclinic structure with inverse centre symmetry rather than the orthorhombic structure with a mirror symmetry in odd number alkane is caused by the effect of end methyl group attractions [77]. However, it is weak with resultant c-axis not linearly thermal expanded but showing disordering especially happened at an early stage of crystallisation. The hypothesis can be made with surface molecules freezing first with end group packed ideally in the orthorhombic symmetry.

From the crystal growth studies of C18 carried out in this work together with the previous results of C22, it can be illustrated that the morphological behaviour of the even carbon number homologue molecule of C16 could be similar, to some extent, with irregular polygon or hexagonal shape crystals at lower supersaturation and parallelogram shape habits at high supersaturation solutions.

## 5.5 Conclusions

This chapter presents structure determination of C18 crystallised in melt phase at a low temperature of -40 °C and room temperature. Computational prediction systematic search in combination with high resolution synchrotron powder diffraction data are confirmed to be reliable to determine the structure as indicated by a good agreement with the single crystal method but with benefit in simple sample preparation.

The stack plots of time-resolved synchrotron X-ray diffraction reveals the polymorphic behaviour notably a rotator phase with positional disordering along the c-axis, is not observable from this study. Nevertheless, at the beginning of crystallisation, disordering effects are shown with low angle peaks splitting and high amorphous content represented by a broad peak at a d spacing of 4.5 Å. This is also observed even in liquid phase suggested by the existence of pre-ordering clusters prior to the solid formation due to the methylene group interaction between inter-chain molecules. The rotator phase is not detectable, which could stem from that the phase is not stable enough during the poly-thermal cooling process. The isothermal method can be used in the future study.

Thermal expansion coefficient in lattice volume of C18 ( $4.17 \pm 2.48 \times 10^{-4} \text{ } ^\circ\text{C}^{-1}$ ) and C16 ( $4.39 \pm 1.94 \times 10^{-4} \text{ } ^\circ\text{C}^{-1}$ ) crystals are with close values which were determined from unit cell parameters from the time-resolved XRD. Also, the anisotropic character of crystals is observed as the variable thermal expansion behaviour from different axial directions and angles.

Crystal growth studies of C18 carried out in three supersaturations ( $\sigma = 0.036, 0.045$  and  $0.08$ ) in n-dodecane solution reveal a plate-like morphology dominated by the {001} habit plane with smaller side faces changing with supersaturations. Morphological indexation of the observed crystals are predicted using BFDH in combination with zone axis method with faces the observed smaller faces (010) (321) (2-10) for  $\sigma = 0.036$ , (1-20) (230) (100) for  $\sigma = 0.045$ , (-110) (130) for  $\sigma = 0.08$ . Attachment of energy ( $E_{att}$ ) calculation is suggested to confirm these findings in future studies.

Hexadecane shows consistency with the homologue molecule of C18 in association with polymorphic behaviour and thermal expansion properties except for the reduced disordering effects along the c-axis. The structure determined only using Rietveld refinement shows good simulation with values of  $R_{wp}$  (0.01) and goodness fit (2.16). However, as the hydrogen positions could not be recognised in Rietveld refinement which is the same issue from

the previous study of Me´tivaud [100], lattice energy calculations need to be taken into account for future work by systematic search.

## **Chapter 6**

### **Phase Behaviour and Crystallisation Kinetics in Octadecane and Hexadecane Binary System**

*Summary:*

*This chapter characterises the binary system of octadecane (C18) and hexadecane (C16) in melt phase crystallisation carried out using a combination of energetic and structural analysis.*

## 6.1 Introduction

Following the structural and morphological studies of pure components of C18 and C16, this chapter will present results from the characterisation of C18/C16 binary mixtures in terms of their phase behaviour and kinetics.

Thermal analysis (DSC) is initially employed to study the heating/cooling rates effects on single and binary mixture components. Consequently, a relatively slow heating/cooling rate is employed to determine the temperature and enthalpy of phase transitions for 21 binary mixture samples. Additionally, a rotator phase is discovered from C18 during the cooling process. The stability of this phase is further studied using impurity compositions.

The phase transitions determined from the heating process are further discovered by powder X-ray diffraction (XRD). The evolution of the newborn phases from mixing of C18/C16 in high temperature (HT) and low temperature (LT) regions are first identified and characterised. Furthermore, structural behaviour as a function of temperature for each composition of mixtures is identified from the relative reflection peak positions using temperature dependent XRD. Hence, the overall equilibrium binary phase diagram of C18/C16 as a function of mixture compositions is presented with phase transition temperatures obtained from thermal analysis, and the phases involved during the temperature ranges determined are resolved through XRD analysis.

In comparison with equilibrium conditions, crash cooling effects on the formation phase of binary mixtures are also studied to indicate the importance of kinetics on the phase formation of binary mixtures. The kinetics are further studied by application of the “KBHR” approach (2.5.2) to access nucleation mechanisms and obtain important kinetic parameters.

## 6.2 Thermal Analysis

### 6.2.1 Influence of Heating/Cooling Rates

The effect of heating/cooling rates on solid-liquid phase transitions was investigated on three samples: pure components of C16 and C18 representing the triclinic phase; a binary mixture of 0.4C18 representing the solid solution rotator phase (R<sub>1</sub>). Quantitative measurements were performed using three individual samples and two cycles of repeats. The full-set data in terms of crystallisation and melting temperatures (onset, peak and end points) as evaluated and integrated from DSC curves are given in **Table 6.1** which illustrates the consistent repeatability from this experiment. For simplicity, DSC curves exclusive from the specialisation (exceptions would be expressed later) will just show one representative plot from all the repeats in the following figures of this chapter.

**Table 6.1 Phase transition temperatures and enthalpies of C16 from two cycle sequences and three fresh sample repeats. The negligible values of standard deviation (Std) show the consistent repeatability of the DSC measurements**

q (°C/min)	Crystallisation				Melting				Mszw (°C)
	Onset (°C)	Peak (°C)	End (°C)	ΔH (J/g)	Onset (°C)	Peak (°C)	End (°C)	ΔHm (J/g)	
0.25	15.85	16.39	15.65	207.64	17.99	18.60	18.98	-207.76	2.75
	15.90	16.41	15.66	207.69	17.99	18.61	18.99	-207.91	2.71
	16.07	16.52	15.85	202.33	17.96	18.66	18.95	-204.83	2.59
	16.05	16.49	15.83	204.03	17.95	18.74	18.94	-205.86	2.69
	16.05	16.67	15.85	204.98	17.92	18.52	18.87	-205.46	2.47
	16.02	16.64	15.81	205.03	17.93	18.46	18.88	-205.88	2.44
<b>Ave.</b>	<b>15.99</b>	<b>16.52</b>	<b>15.78</b>	<b>205.28</b>	<b>17.96</b>	<b>18.60</b>	<b>18.94</b>	<b>-206.28</b>	<b>2.61</b>
<b>Std.</b>	0.09	0.12	0.09	2.09	0.03	0.10	0.05	1.26	0.13
0.50	15.91	16.38	15.53	210.35	17.94	18.77	19.33	-211.28	2.86
	15.96	16.47	15.61	210.47	17.96	18.80	19.33	-211.96	2.84
	15.99	16.36	15.57	205.39	17.99	18.89	19.45	-208.23	2.90
	15.95	16.26	15.45	205.84	17.94	19.09	19.31	-206.05	3.14
	15.93	16.56	15.61	207.69	17.90	18.74	19.07	-207.77	2.81
	15.89	16.53	15.58	206.30	17.90	18.59	19.09	-208.21	2.70
<b>Ave</b>	<b>15.94</b>	<b>16.43</b>	<b>15.56</b>	<b>207.67</b>	<b>17.94</b>	<b>18.81</b>	<b>19.26</b>	<b>-208.92</b>	<b>2.88</b>
<b>Std.</b>	0.04	0.11	0.06	2.26	0.03	0.17	0.15	2.25	0.15
1.00	15.87	16.18	15.00	199.10	17.99	19.26	20.20	-199.76	3.39
	15.81	16.13	14.93	198.58	17.98	19.28	20.18	-199.52	3.47
	15.93	16.32	15.22	190.92	17.97	19.13	19.94	-191.44	3.20
	15.97	16.35	15.22	190.69	17.99	19.09	19.96	-191.82	3.12
	15.94	16.64	15.43	215.21	17.92	18.77	19.54	-214.63	2.83
	15.91	16.62	15.42	214.40	17.93	18.79	19.61	-214.53	2.88
<b>Ave.</b>	<b>15.91</b>	<b>16.37</b>	<b>15.20</b>	<b>201.48</b>	<b>17.96</b>	<b>19.05</b>	<b>19.91</b>	<b>-201.95</b>	<b>3.15</b>
<b>Std.</b>	0.06	0.22	0.21	10.93	0.03	0.22	0.28	10.42	0.26
3.20	15.75	15.78	13.86	209.49	17.65	19.46	21.14	-210.98	3.71
	15.73	15.73	13.86	209.31	17.63	19.63	21.15	-211.05	3.90
	15.72	15.59	13.99	190.72	17.70	19.42	20.82	-192.14	3.70

	15.67	15.81	14.09	190.22	17.70	19.42	20.79	-192.29	3.75
	15.68	15.89	13.86	199.87	17.61	19.44	21.17	-201.72	3.76
<b>Ave.</b>	<b>15.71</b>	<b>15.76</b>	<b>13.93</b>	<b>199.92</b>	<b>17.66</b>	<b>19.47</b>	<b>21.01</b>	<b>-201.64</b>	<b>3.76</b>
<b>Std.</b>	0.03	0.11	0.10	9.47	0.04	0.09	0.19	9.40	0.08
5.00	15.67	15.66	13.22	209.88	17.93	20.20	22.26	-212.41	4.53
	15.63	15.75	13.25	209.50	17.93	20.28	22.25	-211.89	4.65
	15.69	15.50	13.18	215.13	18.00	20.09	22.46	-215.88	4.40
	15.60	15.57	13.19	213.32	17.98	20.09	22.55	-216.28	4.49
	15.84	15.79	13.32	217.09	17.94	20.08	22.20	-218.53	4.24
	15.78	15.72	13.32	217.06	17.93	20.07	22.18	-218.60	4.29
<b>Ave.</b>	<b>15.70</b>	<b>15.67</b>	<b>13.25</b>	<b>213.66</b>	<b>17.95</b>	<b>20.14</b>	<b>22.32</b>	<b>-215.60</b>	<b>4.43</b>
<b>Std.</b>	0.09	0.11	0.06	3.38	0.03	0.09	0.15	2.90	0.15

A pure component example is shown in **Figure 6.1** with a set of DSC curves from sample C16 examined at 5 heating/cooling rates (0.25, 0.5, 1, 3.2 and 5 °C/min) with a temperature range from 10 to 24°C. A binary mixture sample of 0.4C18 is presented in **Figure 6.2** with 4 heating/cooling rates (0.25, 0.5, 1 and 3.2 °C/min) in the temperature range of 10 to 24°C.

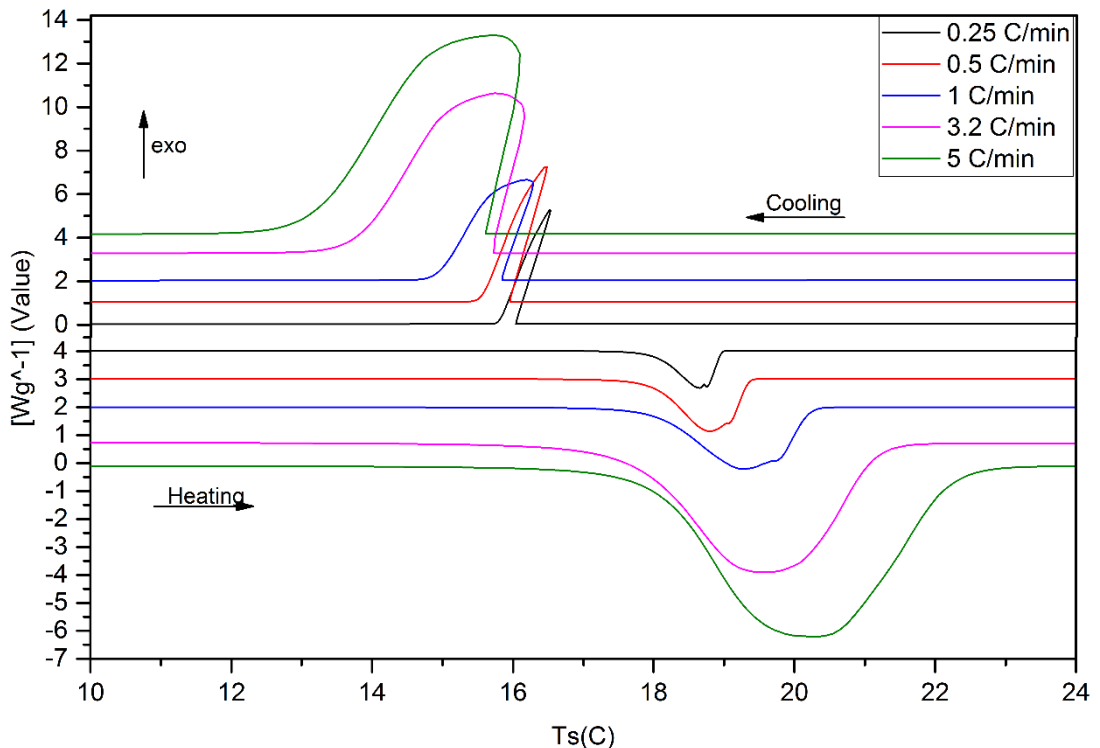


**Figure 6.1: DSC curves plotted with normalised heat flow versus sample temperature from C16 collected at various heating/cooling rates**

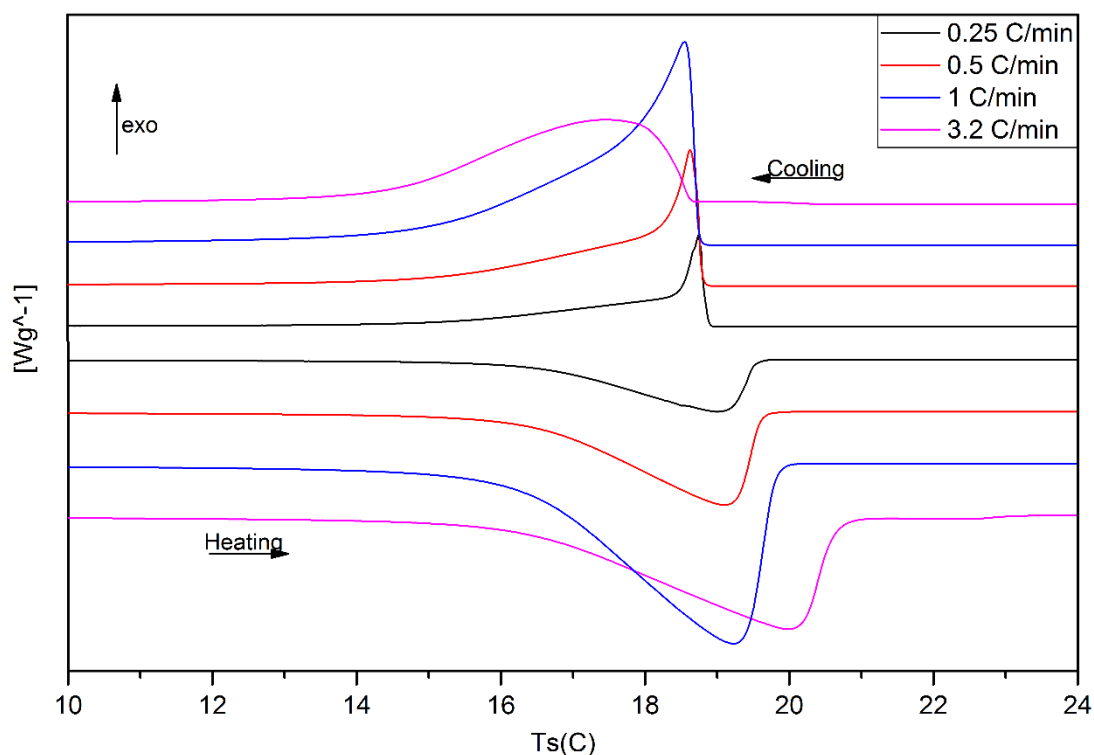


**Figure 6.2: DSC curves plotted with scaled normalisation heat flow versus sample temperature from 0.4C18 collected at various heating/cooling rates.**

From all the curves, there was only one major peak observed from either the cooling or heating process representing the crystallisation or melting of liquid-solid phase transition. While the shape of the transition peak was varied not only from the transition phenomenon referred to crystallisation or melting but also the scanning rate. Crystallisation usually occurred with a sharp onset in comparison with an indistinct start of melting phenomenon, even though for a high purity sample (C16 or C18). The broad shape of the melting peak can be explained by the nature of normal alkanes with a long chain of c-axis and lamella packing [36]. Nevertheless, increasing the heating/cooling rates, the shape of the peaks from both reactions became broader due to the larger temperature gradient inside the sample. Generally, from this study and previous work, a heating/cooling rate of 5°C/min can be defined as the limitation for normal alkanes that gives better resolution and results for thermal energetic measurements [111]. In addition, supercooling was obtained in pure samples, as seen in **Figure 6.1**, lower crystallisation temperature due to the involvement of the nucleation process and that the onset point was decreased

with increasing the cooling rate. The associated nucleation kinetics study will be further discussed. It should be noted that the triclinic phase formation of C16 or C18, involved an exothermic peak inclining to higher temperature direction along with the cooling process. This is because a large amount of energy can be released accompanied by a phase transition from liquid to triclinic crystalline which is densely packed and stabilised. This typical peak shape is always presented from a thermal analysis of normal alkanes once a triclinic phase crystallisation is comprised [55].

Regardless of the sharp exothermic peak shape observed from pure components with rapid phase transition reaction, both crystallisation and melting processes involved a large temperature range and a long period for the binary mixture sample of 0.4C18 as shown in **Figure 6.2**. The progression of the liquid phase to the solid phase for a mixture component happened gradually in a poly-thermal temperature range comprising diffusion from both solid-solid and solid-liquid phases to achieve equilibrium composition at the end point of cooling. Thus relatively slow cooling rates were essential such as 0.25, 0.5 and 1°C/min with the sharp onset of solidification following a long tail of wide temperature ranges as required for the diffusion process. Whereas the faster cooling rate of 3.2°C/min showed an arc-shaped exothermic peak that could give a different composition under equilibrium conditions. As a result, the data collected at 3.2°C/min was not appropriate for further nucleation kinetic assessment. Furthermore, adjacent melting and crystallisation points were detected implying a negligible supercooling was needed to overcome the energy barrier from nucleation. This distinct behaviour of the C18/C16 binary mixture can be explained by the formation of solid solution  $R_1$  which is a disordered rotator phase rather than the inherent triclinic structure, low energy involved from crystallisation which is demonstrated by the observation of a regular straight exothermic peak.

The onset point is taken to be the crystallisation temperature while for the melting process it is the peak point, due to the sharp onset peak only be observable from the crystallisation transaction. Averaged values of crystallisation ( $T_c$ ) and melting temperatures ( $T_m$ ) and resultant heat enthalpies and MSZWs with their standard deviations are listed in **Table 6.2** and plotted in **Figure 6.3 (a, b and c)** for C16, 0.4C18 and C18, respectively.

Linear line fitting was applied to all plots with correlation coefficients  $R^2$  that could indicate good fits for all three samples. Equilibrium  $T_m$  determined from these extrapolation lines back to the zero heating rate for sample C16, 0.4C18 and C18 were 18.63°C, 18.94°C and 28.28°C, respectively.

The dependence of  $T_c$  and  $T_m$  on cooling/heating rates was also demonstrated in **Figure 6.3 (a)** and **(b)** which both show flat  $T_c$ - $q$  and  $T_m$ - $q$  lines for sample C16 and C18 indicating the crystallisation process will be more thermodynamically controlled; while **(c)** shows a kinetic control on both cooling and heating rates for binary mixture 0.4C18. As seen in **Table 6.2**, MSZW and enthalpies as measured from these three components reflected the chain length and structural dependence. Small MSZWs and enthalpies were obtained from binary mixture 0.4C18 with a disordered rotator phase. For a single component of C16 and C18, the MSZW decreased with the increase in chain length. Meanwhile, the enthalpy of the triclinic phase formation was also increased.

**Table 6.2 Averaged temperatures of crystallisation ( $T_c$ ) and melting ( $T_m$ ) with their standard deviations as a function of cooling/heating rates. The resultant MSZW as obtained from  $T_m$ - $T_c$  was also presented.**

q(°C/min)	Crystallisation				Melting				MSZW (°C)
	$T_c$ (°C)	std	$\Delta H$ (J/g)	std	$T_m$ (°C)	std	$\Delta H_m$ (J/g)	std	
<b>C16</b>									
0.25	15.99	0.09	205.28	2.09	18.60	0.10	-206.28	1.26	2.61
0.5	15.94	0.04	207.67	2.26	18.81	0.17	-208.92	2.25	2.88
1	15.91	0.06	201.48	10.93	19.05	0.22	-201.95	10.42	3.15
3.2	15.71	0.03	199.92	9.47	19.47	0.09	-201.64	9.40	3.76
5	15.70	0.09	213.66	3.38	20.14	0.09	-215.60	2.90	4.43
<b>0.4C18</b>									
0.25	18.84	0.01	158.71	0.22	19.00	0.03	-156.93	1.24	0.16
0.5	18.79	0.02	144.90	0.35	19.10	0.01	-146.67	1.44	0.31
1	18.74	0.01	155.52	1.94	19.22	0.01	-153.80	0.20	0.48
<b>C18</b>									
0.25	26.66	0.01	208.85	9.21	28.27	0.11	-208.81	8.07	1.61
0.5	26.64	0.07	199.21	10.66	28.34	0.03	-202.95	11.79	1.71
1	26.52	0.12	210.51	2.73	28.71	0.14	-208.70	4.33	2.19
3.2	26.44	0.04	228.98	12.26	29.28	0.09	-231.45	11.83	2.84
5	26.21	0.19	215.00	1.20	29.66	0.22	-215.60	2.36	3.45

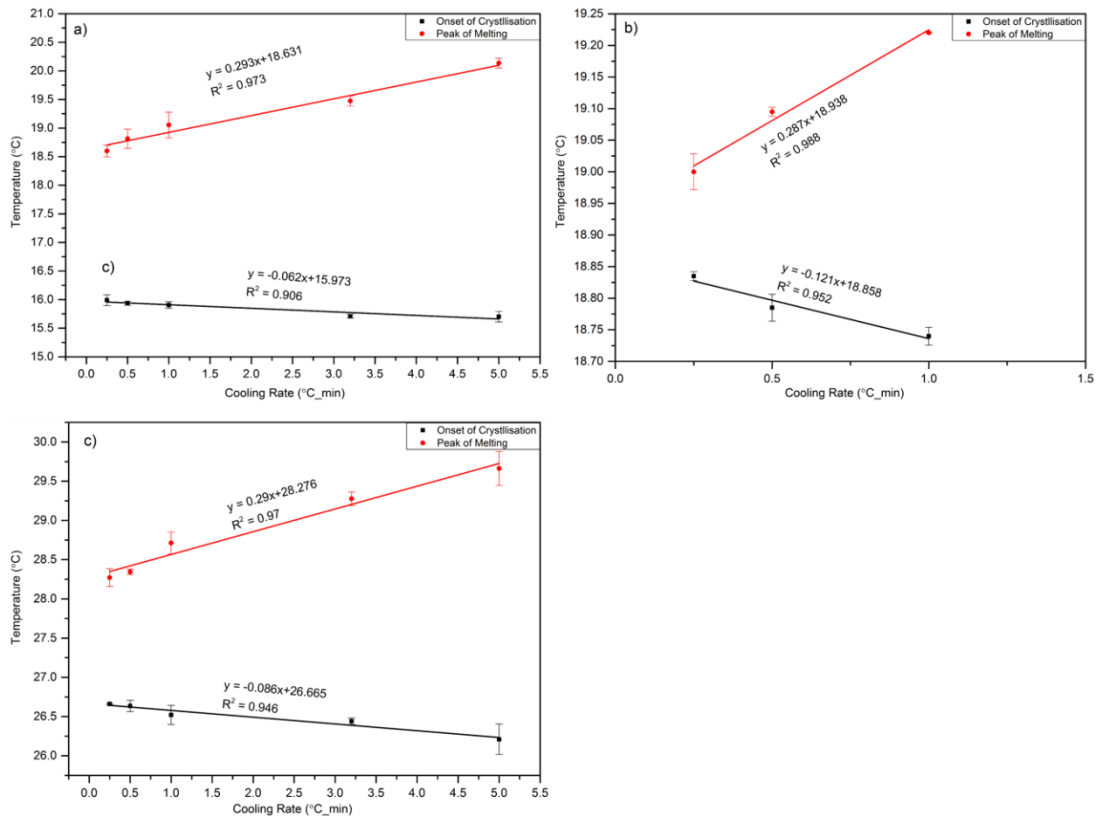


**Figure 6.3: Plots of onset/peak points of crystallisation/melting temperatures and their standard deviations versus cooling/heating rates. a) Pure C16, b) 0.4C18 and c) Pure C18.**

## 6.2.2 Temperature and Enthalpy Determination of Phase Transitions

To observe phase transition temperatures and enthalpies, 21 binary mixed samples were examined by calorimetric measurements of DSC. A set of thermograms of the mixed samples is shown in **Figure 6.4** from - 20 to 30°C at a heating rate of 1°C/min. The main large peak observed in the HT region for each composition is relative to the transition from solid to liquid referred to as the melting peak. Normal alkanes of C18 and C16 with carbon number differences smaller than four are expected [56] to be completely soluble in the solid phase which forms in a solid solution. However, multiple phases of solid solution could be detected across the overall mixture samples as the melt peak shape varied from compositions: samples rich in C16 or C18 were in sharp and high peaks, whereas samples having equalised percentage of both components were in broad and short peaks. Overall, two equilibrium invariants were observed with respect to eutectic reaction for compositions from

0.05C18 to 0.2C18 having the same onset point of melting at 16°C and for compositions from 0.8C18 and 0.85C18 notably by an extra peak observed at the melt peak shoulder indicating the existence of peritectic equilibrium invariant located around 26°C. It needs to be noted that 0.1C18 was found to be the eutectic composition due to the sharp melting peak that was comparable to the pure components whereas others always had broader peaks with a period of melting [112].

In addition, some relatively smaller peaks were observed at low temperatures (LT) with respect to the solid-solid phase transitions which is enlarged and shown in **Figure 6.5** for compositions from 0.05C18 to 0.7C18. The polymorphism transformation between the solid phase at HT and LT regions was accompanied by subtle packing and structural difference as a result of smaller energy changes. This would be the reason that the peak shape for the solid-solid phase transition at LT was not as sharp and regular as the solid to liquid phase transitions at HT. Melting transition occurred in a wide temperature range and was possibly due to the slow diffusion in the solid phase of the mass transfer from different compositions. Thus, the peak point instead of the onset was more appropriate to be taken as the transition temperature for the solid-solid phase transition. Two equilibrium invariants (eutectoid and peritectoid) were achieved located around - 10.5°C and - 13°C, respectively. In addition to the observation of three solid-solid phase transitions for sample 0.45C18, it can be concluded that the presence of discontinuous phase formation at LT. The outcome from our studies supports the idea from the latest work [113] of normal alkanes and against the earlier observation from Mazee [59] which proposed a single phase region at LT.

The integrated results of averaged values and their standard deviations are listed in **Table 6.3** and **Table 6.4** for transitions peaks observed from the HT and LT regions respectively. The onset, peak and end points of the solid to liquid phase transitions and resultant enthalpies are listed in **Table 6.3** for the determination of phase boundary for liquidus and solidus lines. The solidus points were the onset of melting transitions, therefore below the solidus line will be all solid phase. The liquidus temperatures were calculated using the "Shape factor" empirical method to determine the actual end temperatures of binary phase mixtures from DSC analysis [112]. For binary mixtures, the

melting phenomenon is no longer isothermal, so the peak width increases except the eutectic composition like 0.1C18 which has a lowest melting temperature (peak) and the liquidus point as shown in **Table 6.3**. These observed phase transitions would be further investigated by PXRD from the temperature range determined.

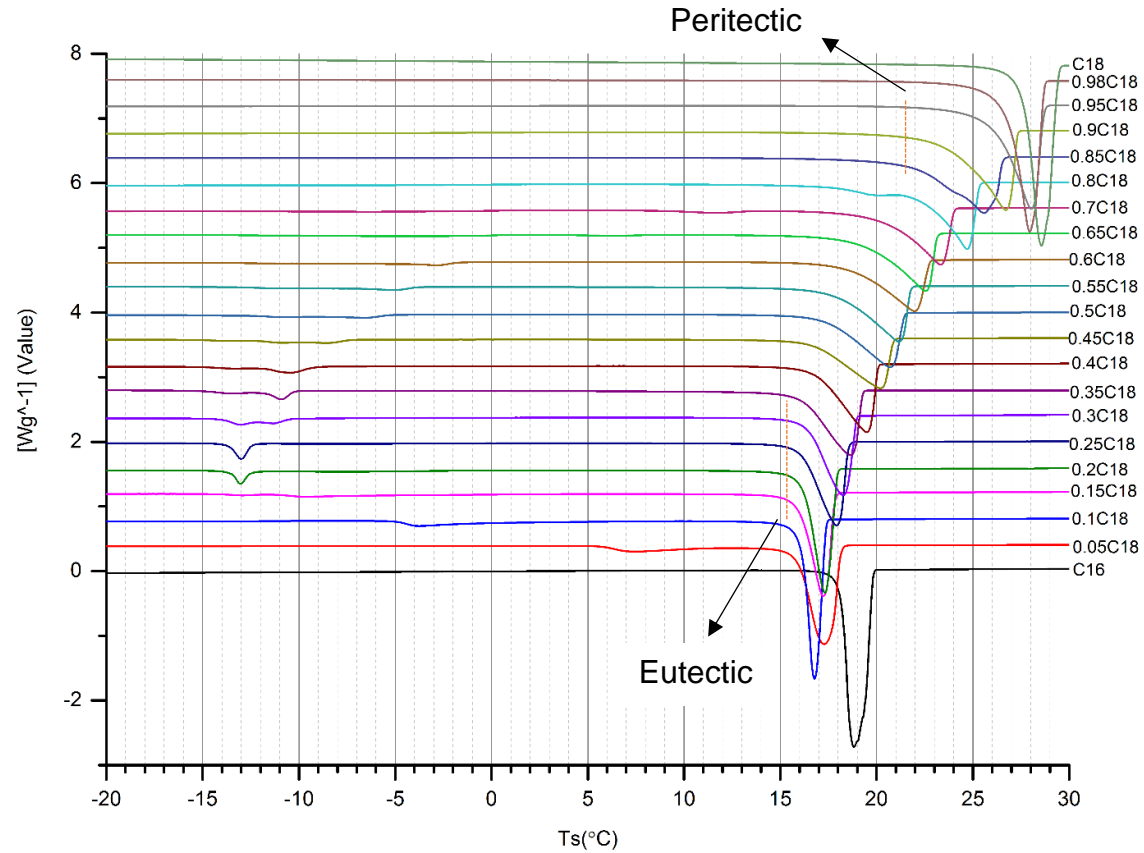


**Figure 6.4: DSC thermograms towards heating for C16/C18 binary mixtures from 21 compositions collected from -20 $^{\circ}\text{C}$  to 30 $^{\circ}\text{C}$ . The two equilibrium invariants (Eutectic and Peritectic) with compositions having an identical onset melting point at HT region are shown with dashed lines. The LT region phase transitions are enlarged as shown in Figure 6.5.**

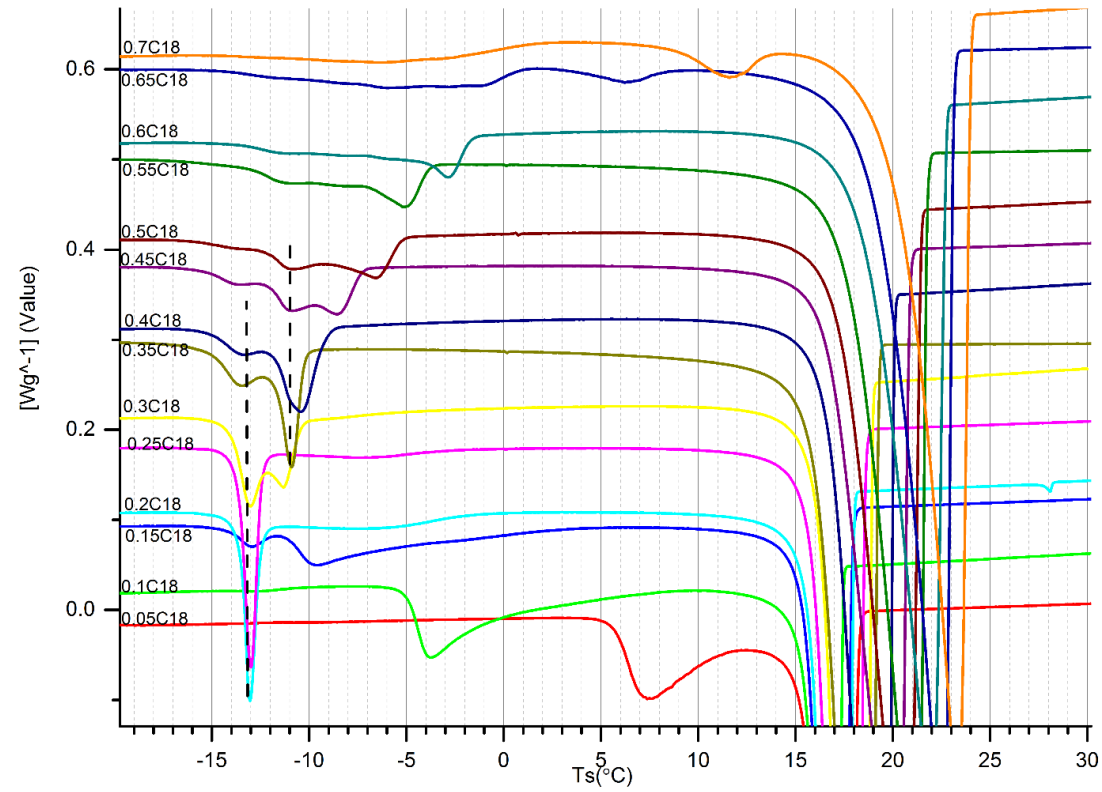


**Figure 6.5: Enlarged thermograms from - 20°C to 15°C for compositions from 0.05C18 to 0.7C18 representing the solid-solid phase transitions at LT region. The two equilibrium invariants (Eutectoid and Peritectoid) with compositions having identical transition temperature at LT region are shown with dashed lines.**

**Table 6.3 Onset, Peak and Endpoints as integrated from the solid to liquid transitions and resultant heat enthalpy for 21 samples of binary mixtures. E and P represent to eutectic and peritectic invariants, respectively.**

<i>X C18</i>	<i>Liquidus</i> °C	<i>Onset (Solidus)</i> °C		<i>Peak</i> °C		<i>End</i> °C		<i>Enthalpy</i> J/g	
0	18.52	17.96	±0.03	19.05	±0.22	19.91	±0.28	-201.95	±10.42
0.05	16.65	15.86 <sup>E</sup>	±0.01	17.22	±0.07	18.04	±0.10	-150.77	±1.01
0.1	16.07	16.07 <sup>E</sup>	±0.01	16.79	±0.02	17.46	±0.11	-140.15	±4.07
0.15	16.51	15.89 <sup>E</sup>	±0.04	17.31	±0.08	17.90	±0.12	-133.62	±4.83
0.2	16.59	16.17	±0.02	17.35	±0.03	17.98	±0.02	-149.24	±4.25
0.25	17.19	15.97	±0.02	18.01	±0.08	18.58	±0.06	-139.97	±0.27
0.3	17.50	16.28	±0.02	18.26	±0.01	18.90	±0.07	-143.06	±3.15
0.35	17.84	16.02	±0.05	18.68	±0.01	19.23	±0.03	-145.87	±10.47
0.4	18.68	16.65	±0.09	19.47	±0.03	20.08	±0.06	-141.82	±1.26
0.45	19.39	16.49	±0.04	20.10	±0.05	20.78	±0.08	-138.16	±1.06
0.5	20.02	17.30	±0.05	20.67	±0.05	21.42	±0.01	-137.11	±2.22
0.55	20.35	17.88	±0.02	21.17	±0.01	21.75	±0.01	-152.13	±13.07
0.6	21.33	18.66	±0.04	21.99	±0.01	22.72	±0.02	-140.32	±4.19
0.65	21.76	19.39	±0.07	22.56	±0.02	23.16	±0.04	-154.88	±9.27
0.7	22.62	20.49	±0.09	23.36	±0.03	24.02	±0.03	-143.62	±1.83
0.8	23.96	22.28	±0.08	24.69 <sup>P</sup>	±0.03	25.36	±0.04	-178.23	±1.75
0.85	25.16	22.59	±0.05	25.58 <sup>P</sup>	±0.01	26.55	±0.01	-171.98	±3.33
0.9	25.94 <sup>P</sup>	24.01	±0.02	26.76	±0.04	27.34	±0.02	-191.56	±4.02
0.95	27.07	26.01	±0.03	27.90	±0.06	28.46	±0.06	-189.64	±6.04
0.98	27.29	26.73	±0.03	27.98	±0.03	28.69	±0.03	-208.33	±2.20
1	28.04	27.70	±0.07	28.71	±0.14	29.43	±0.13	-208.7	±4.33

**Table 6.4 Peak points of solid-solid phase transitions for compositions from 0.05C18 to 0.85C18 at LT; E☆ represents eutectoid invariant; P☆ represents peritectoid invariant.**

<i>X C18</i>	<i>Oder-R</i> °C		<i>S-S</i> °C		<i>T<sub>E</sub></i> °C		<i>S-S</i> °C	
0.05	7.41	±0.07						
0.1	-3.60	±0.20						
0.15	-9.67	±0.09			-12.99 <sup>E☆</sup>	±0.07		
0.2					-13.03 <sup>E☆</sup>	±0.01		
0.25					-12.97 <sup>E☆</sup>	±0.02		
0.3	-11.37	±0.06			-13.01 <sup>E☆</sup>	±0.02		
0.35					-10.94 <sup>P☆</sup>	±0.04	-13.46	±0.02
0.4					-10.37 <sup>P☆</sup>	±0.11	-13.29	±0.03
0.45	-8.55	±0.01			-10.83 <sup>P☆</sup>	±0.02	-13.45	±0.06
0.5	-6.58	±0.06			-10.79 <sup>P☆</sup>	±0.07	-12.75	±0.24
0.55	-5.05	±0.03			-10.62 <sup>P☆</sup>	±0.55		
0.6	-2.86	±0.04	-5.93	±0.14				
0.65	6.43	±0.14	-1.26	±0.04			-5.19	±0.32
0.7	11.54	±0.07						
0.8	20.18	±0.04						
0.85	24.72	±0.19						

### 6.2.3 Crossover Observation from Transient to Metastable to Stable Phase of R<sub>1</sub>

As previously mentioned the repeatability from two cycles of the heating/cooling processes, the exceptional observation was found for C18 with second cooling differing from the first one which involved a solid phase transaction. As seen in **Figure 6.6(a)**, the second cycle of cooling had an overlapping exothermic twin peak. The minor one was for phase transition from isotropic liquid crystallised into a low energy phase with a small half shaped peak. However, the solid phase formed was not stable and directly transferred into a triclinic phase with a sharp peak and typical tilt which is evidence of the high energy triclinic phase formation. A similar observation was also found for 0.98C18 as shown in **Figure 6.6(b)**, the different behaviour in two cycles of crystallisation indicating a solid-solid transition represented by the additional exothermic peak in an integrated shape.

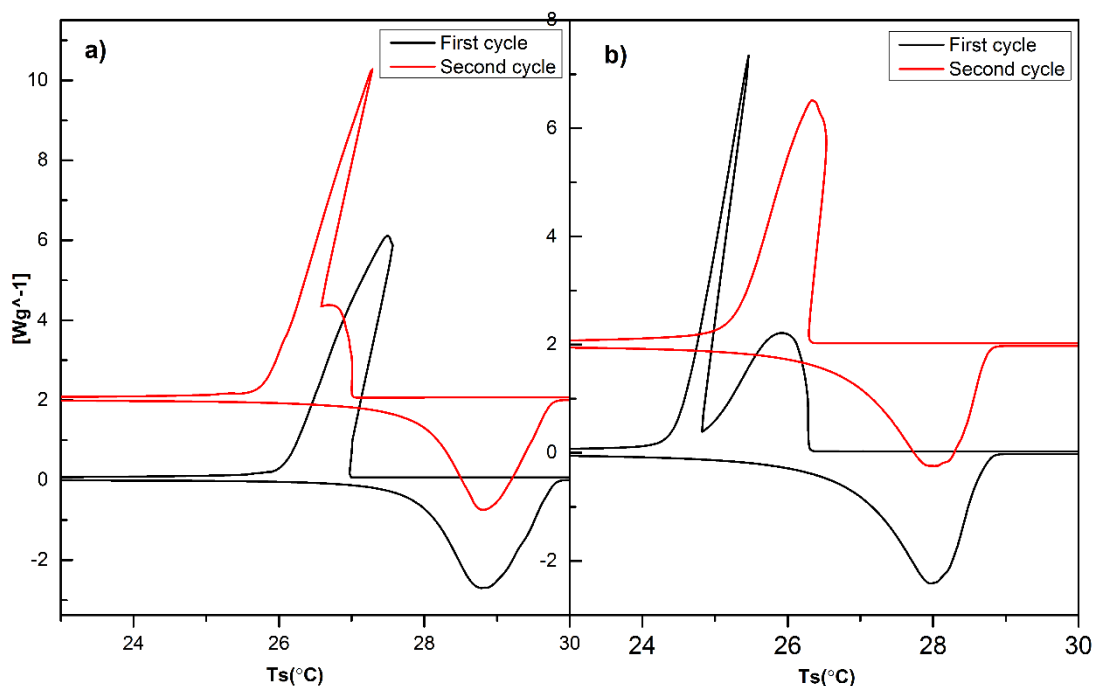


**Figure 6.6: DSC traces from two cycles (red and black lines) of heating/cooling processes at  $1^{\circ}C/min$  within a temperature range of  $23^{\circ}C$  to  $30^{\circ}C$  with phase transition peaks from exothermic (upper side) and endothermic (downside) reactions. The non-repeatable exothermic peaks from two cycles towards cooling are indicative of a transient state of the rotator phase state with C18 (a) and 0.98C18 (b).**

Since the rotator phase formation could be the essential role of the nucleation kinetics mechanism [53, 54], increasing the amount of impurity of C16 in C18 from 0.95C18 to 0.8C18 was performed with two cycles of heating/cooling as shown in **Figure 6.7**. Nevertheless, the non-repeatable behaviour of two cycles of cooling from the rotator phase transition observed from C18 and 0.98C18 (Figure 6.6), the rotator phase appeared to be a metastable phase which could be detected from both cycles of cooling as increasing the amount of impurity to 0.95C18. A small melting peak of this rotator phase could be observed represented by a shoulder for 0.85C18, while a small fully shaped peak for 0.8C18 turned out to be a stable phase seen in **Figure 6.7**.

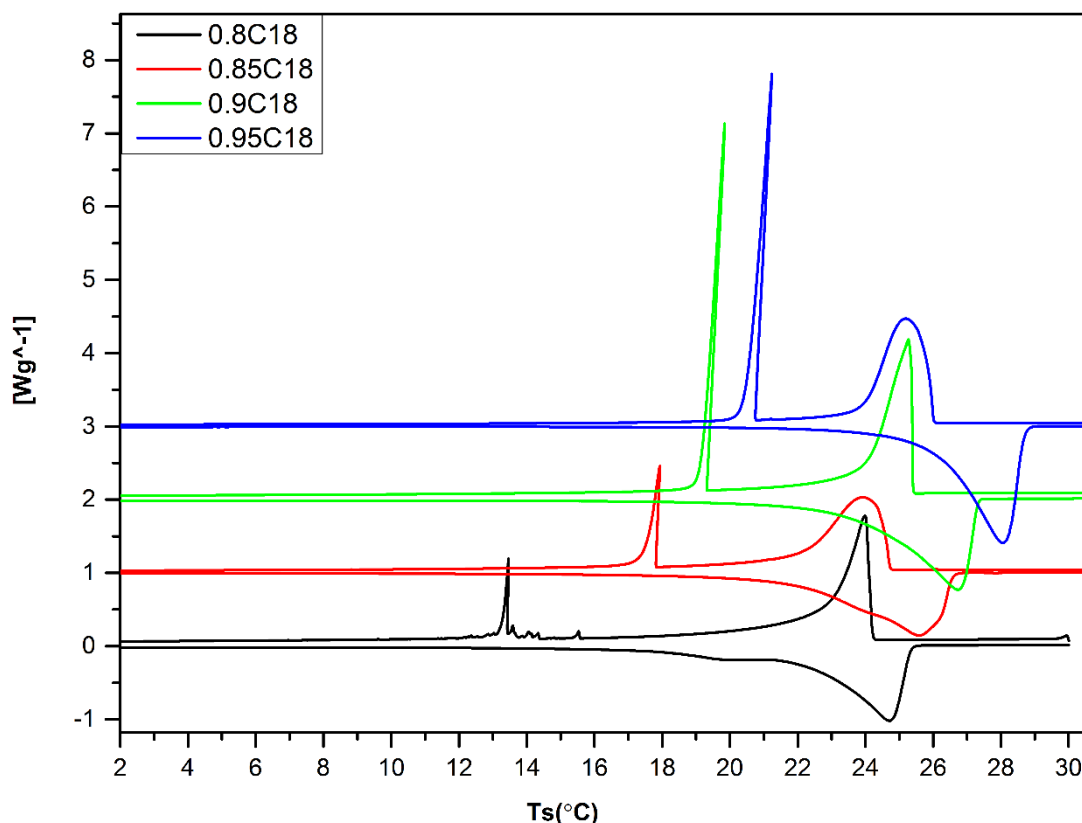


**Figure 6.7: DSC curves of binary mixtures of 0.8C18, 0.85C18, 0.9C18 and 0.95C18 from two cycles heating/cooling processes at 1°C/min from 2 to 30°C with phase transition peaks from exothermic (upper side) and endothermic (downside) reactions. Identical thermal traces from two cycles measurements indicating the state of rotator phase is stabilised and no longer a transient state.**

There is no doubt of chain length dependence on phase structure of normal alkanes [77]. This could be explained by the energy of a crystal should be broken down into two components, which are dependent on the lateral interaction of the chain molecules, the other on the interaction of the ends [36]. The relative values of these would alter changing to a shorter molecule, and this would produce a change in the crystal structure. This perhaps is the same reason for the phenomenon that the rotator phase induced nucleation crossover from the transient state to long-lived metastability as increasing the chain length studied from synchrotron XRD experiments [53, 54]. Especially, C18 reacts as a coherent set regarding the long life transient state to a metastable rotator phase which is not clearly defined from previous thermal analysis and regarded as there being no rotator phase involved. Interesting, in this study using DSC had identified C18 crystallised with a single

exothermic peak for the liquid to triclinic crystallisation and a twin peak with the rotator to triclinic phase transition on the second sequence of cooling. Moreover, the transient state of the rotator phase is not only influenced by normal alkane chain length but also the composition of homologue impurities, i.e. a shorter chain of C16 is not observable with any rotator phase. As a result, the metastability of rotator phase formation alters from transient to metastable to stable as the amount of homologue impurity increases.

### 6.3 Phase Identification from PXRD Analysis

#### 6.3.1 Disordered Phase at High Temperature Region (HT)

As introduced from the thermal analysis, C18/C16 binary mixtures could form a solid solution which is a new phase and it is a lower energy structure in comparison with the inherent triclinic phase. This phase has been studied for a long time from many homologues alkane mixtures which are a disordered rotator phase ( $R_1$ ) [113]. It is the most common disordered phase in single odd number alkane and homologue mixtures while it did not exist in single even carbon number ones. In order to study the structure of C18/C16 solid solution, based on the DSC results, three compositions of 0.3C18, 0.5C18 and 0.7C18 were collected with a high resolution XRD scanned from 2 to 80° in  $2\theta$ .

**Figure 6.8** shows an example of the high resolution XRD pattern for the composition of 0.3C18 collected at 5°C with the best fit from the “Pawley fit” and indexation peaks. Low angle (00l) peaks were detected by this transmission mode XRD with a rotational sample stage that highly reduced the texture effects. There were only two low-intensity peaks observed at high angles and no reflections presented beyond 40° in  $2\theta$ . This behaviour confirms this rotator only has an ordered packing with lamellar interchain packing and no long range order. Also, the high amorphous diffusion seen at 20° in  $2\theta$  was an indication of the poorer crystalline order corresponding to the interchain separation which was also observed in previous alkanes homologue studies [42, 72, 73].

Newborn unit cell parameters and refinement parameters are presented in **Table 6.5**, together with the literature parameters in **Table 6.6**. As expected,  $R_1$  unit cell packing was with four molecules in a bilayer with the c-axis length close to the calculation of chain length from the mixture composition.  $R_{wp}$  and  $R_p$  values are in a reasonable range for organic component fitting (<10%). The previous study for the C18/C16 solid solution of  $R_1$  phase is from Wang [114] with a mixture composition of 0.65C18 at 18°C where they proposed a unit cell with a c-axis of 97.95 angstroms which is not sensible for the packing preferences of  $R_1$  in binary mixtures. The reason for the wrong analysis could be due to no reflection peaks being observed for (00L) which could give the packing information and rough c-axis length. It needs to be noted that 0.5C18 has a shorter c-axis length and smaller molecular volume than the rest of the compositions. Hence, it seems that the length of the c-axis and molecular volume are not strongly related to the calculated chain length from the mixture, but more related to the packing with defects in the end methyl group. This could also be explained by the lower enthalpy fusion of 0.5C18 as compared with 0.3C18 and 0.7C18 from DSC (**Table 6.3**) which indicated that 0.5C18 has a rotator crystalline which can be more disordered with more defects.

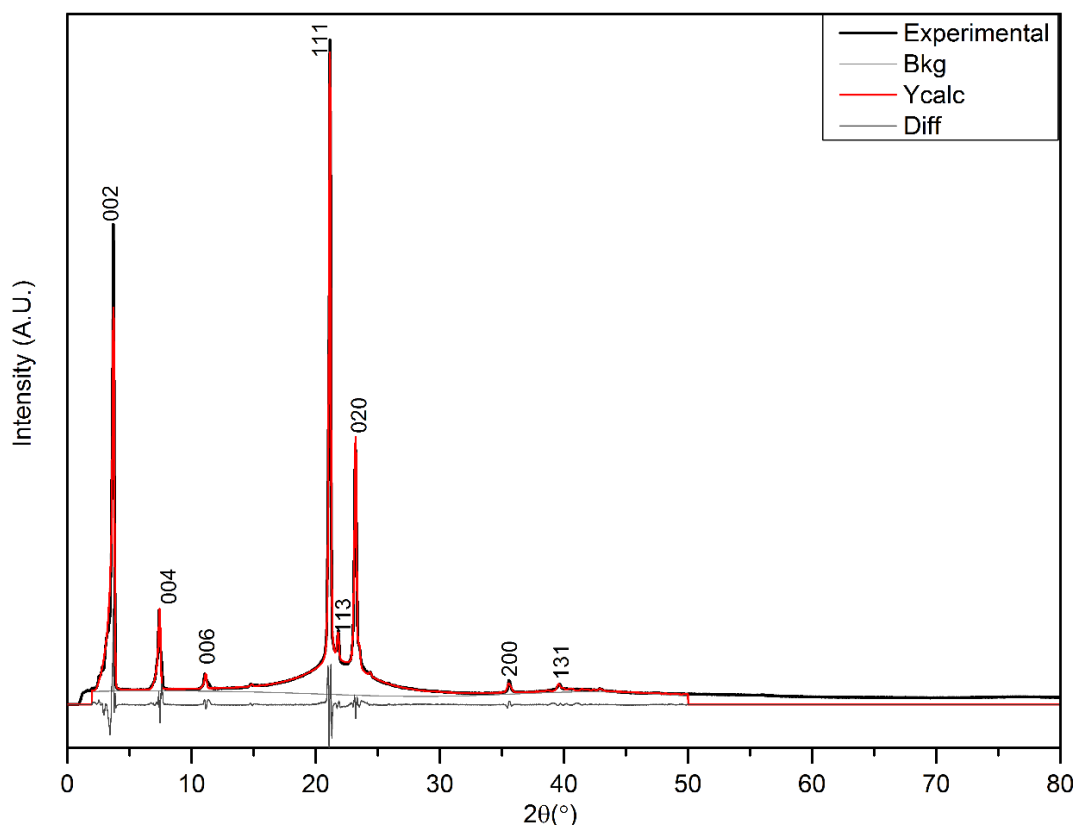


**Figure 6.8: Example of “Pawley fit” of sample 0.3C18 from experimentally collected XRD scan at 5°C; determined background; calculated reflection pattern from the determined unit cell; the difference between the experimental and calculated data is also shown.**

**Table 6.5 Unit cell parameters of R<sub>1</sub> from C16/C18 mixture obtained from STOE© and refined by TOPAS [87]**

Sample	Temp. °C	Space group	a/Å	b/Å	c/Å	α/°	β/°	γ/°	V/Å <sup>3</sup>	R <sub>wp</sub> %	R <sub>p</sub> %
0.3C18	5	Fmmm Z=4	5.048	7.657	47.54	90	90	90	459.385	7.0	4.07
0.5C18	10	Fmmm Z=4	5.038	7.534	46.24	90	90	90	438.838	9.7	6.2
0.7C18	10	Fmmm Z=4	5.046	7.66	48.75	90	90	90	471.076	7.5	4.9

**Table 6.6 Literature determined unit parameters of R<sub>1</sub>**

Phase	Author	Sample	Space group	a/Å	b/Å	c/Å	α/°	β/°	γ/°	T/°C
R <sub>1</sub>	Wang[114]	0.65C18	Fmmm (Z=4)	8.17	4.92	97.95	90	90	90	18
R <sub>1</sub>	Luth[115]	0.28C22	Fmmm (Z=4)	5.02	7.711	58.1	90	90	90	RT

### 6.3.2 Intermediate Ordered Crystalline Phases in the Low-Temperature Region (LT)

In addition to the newborn phase of  $R_1$  from the solid solution of C18/C16 at HT, some more intermediate structures of  $M_{dcp}$  and  $O_p$  [65, 113], as observed from DSC at LT were also detected from XRD measurements at an isothermal temperature of  $-30^\circ\text{C}$ , as shown in **Figure 6.9**. First of all, diffraction patterns of the single phase of triclinic for C16 and C18 with its reflection peaks were detected in the bottom and top of **Figure 6.9** respectively. The mixed sample 0.05C18 with a minimum amount of homologue impurity was also crystallised with a triclinic solid solution.

Secondly, it is easy to identify the high symmetry structural phases in the middle range with mixed molar compositions from 0.3C18 to 0.6C18. However, to distinguish from the two intermediate phases of  $M_{dcp}$  and  $O_p$  is difficult due to the similar unit cell symmetry arising from the only difference being the end group packing arrangement between chain layers. **Figure 6.10** shows the similarity between the two intermediate phases with close c-axis length resulting in comparable reflections at low angles. Nevertheless, peak positions observed near  $2\theta$  of  $36^\circ$  and  $38^\circ$  are closer to the high angles direction which is relative to the  $M_{dcp}$  phase for 0.3C18 and 0.4C18, whereas peaks towards to low angles direction correspond to the  $O_p$  phase for 0.6C18 and 0.7C18. The peaks belong to middle compositions of 0.45C18 and 0.5C18 which are located in the middle position of the previous two cases indicating mixture phases of  $M_{dcp}$  and  $O_p$ . Overall, the high symmetry phases at LT are not easily distinguishable from XRD but as DSC curves clearly show, the eutectoid and peritectoid three-phase equilibrium invariants strongly demonstrate it is not a continuous solid solution.

Last but not least, mixed samples with multiple phases were indexed with relative structures. An example of indexing triclinic and monoclinic phases for mixture sample of 0.1C18 is represented in **Figure 6.11** from a Pawley fit using TOPAS software [87] which enabled recognition of individual peak position with an indexed plane to the respective structure. Refined unit cell parameters and fitting information are listed in **Table 6.7**.

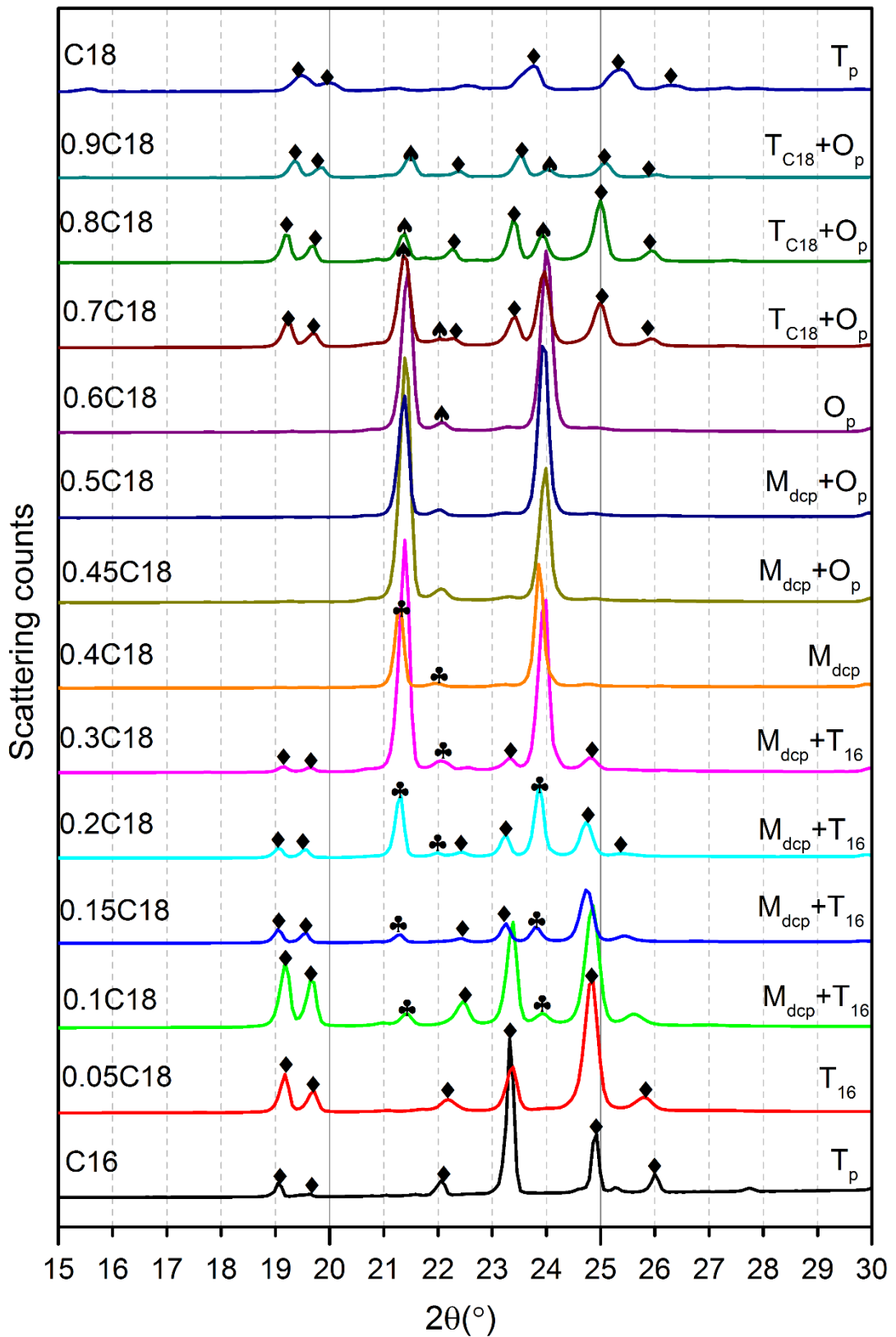
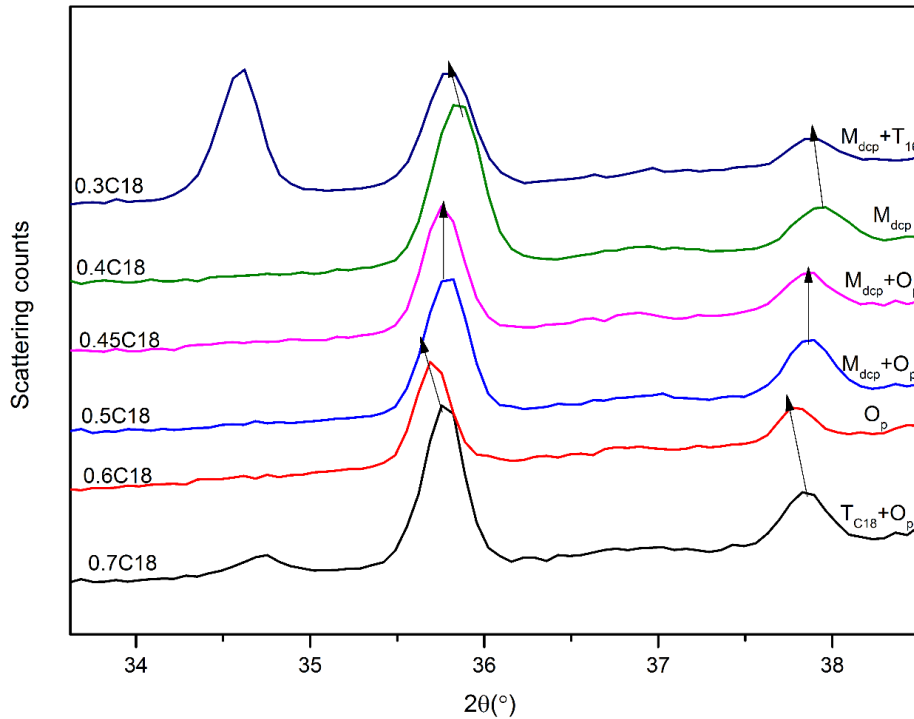
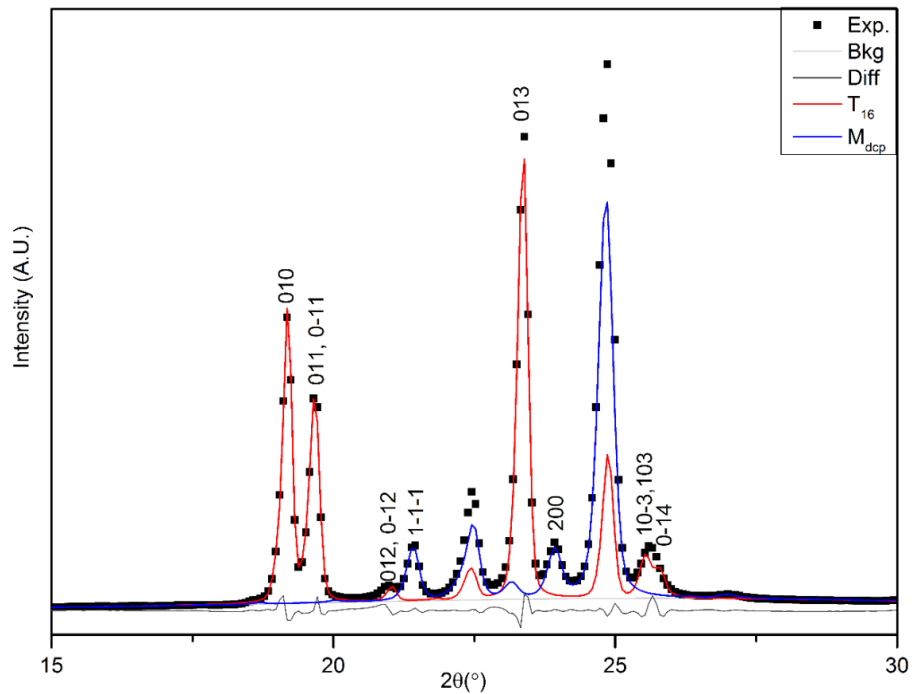


Figure 6.9: XRD patterns collected at  $-30^\circ\text{C}$  of C16/C18 binary mixtures with two theta range from 15 to  $30^\circ$  at a wavelength of 1.54 angstrom:  $\blacklozenge$  T (P-1, Z=1),  $\clubsuit$  M<sub>dcp</sub> (Aa, Z=4) and  $\heartsuit$  O<sub>p</sub> (Pca21, Z=4).



**Figure 6.10: Example illustrating the difference between pure solid solution  $O_p$  or  $M_{dcp}$  and the mixture phases of both for mixture samples collected at  $-30^\circ\text{C}$**



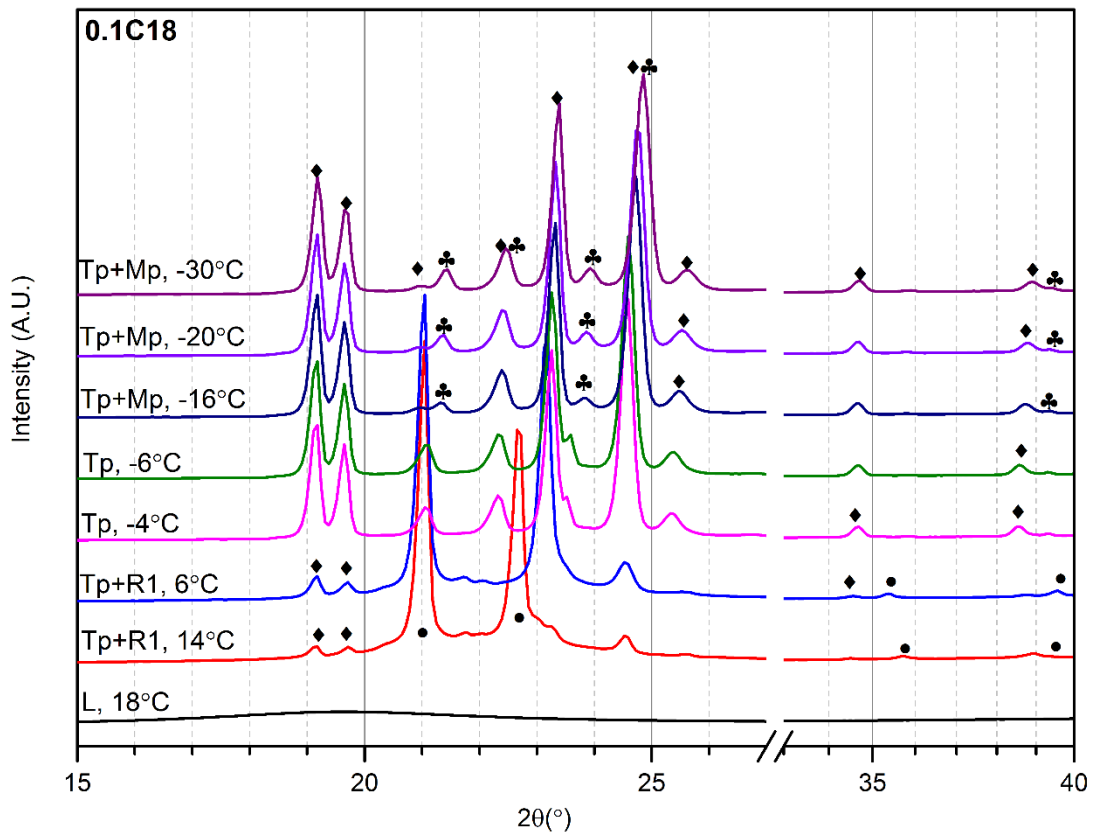
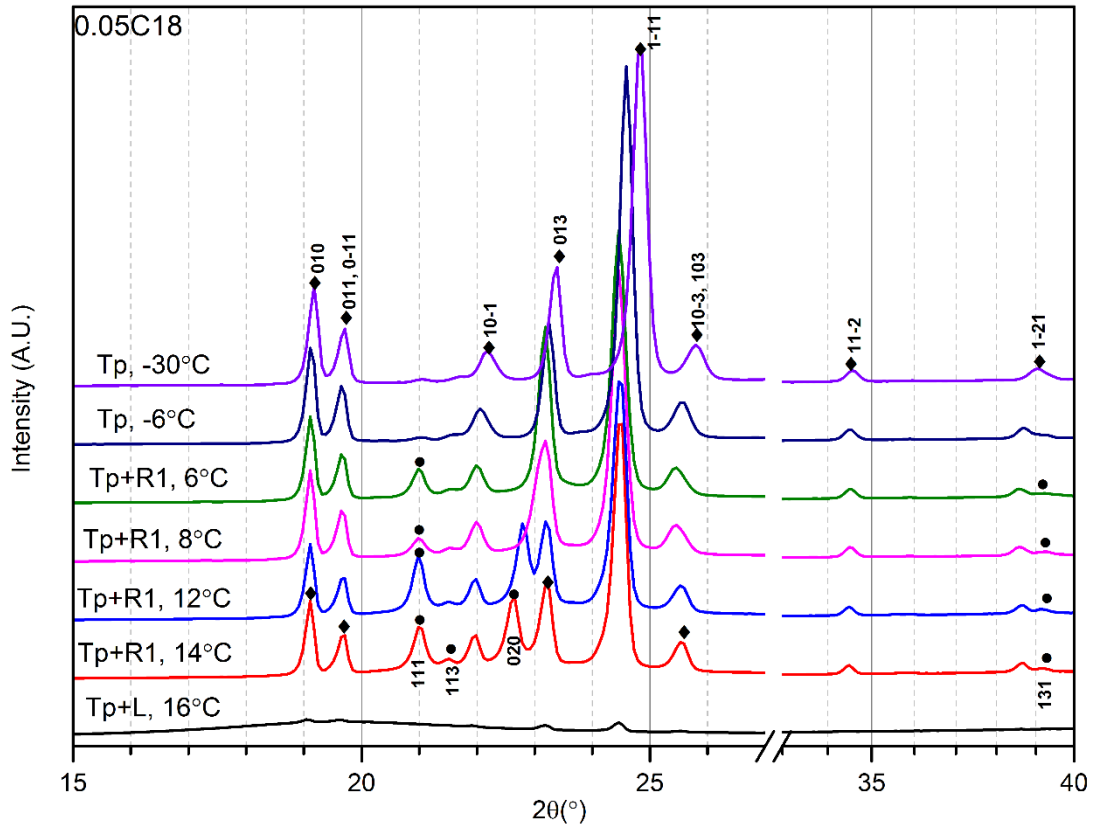
**Figure 6.11: Example of multiple phases “Pawley fit” of sample 0.1C18 from experimental data collected at  $-30^\circ\text{C}$ ; determined background; Calculated reflection pattern from the determined unit cell of  $T_{16}$  and  $M_{dcp}$ ; Difference between the experimental and calculation data is also shown.**

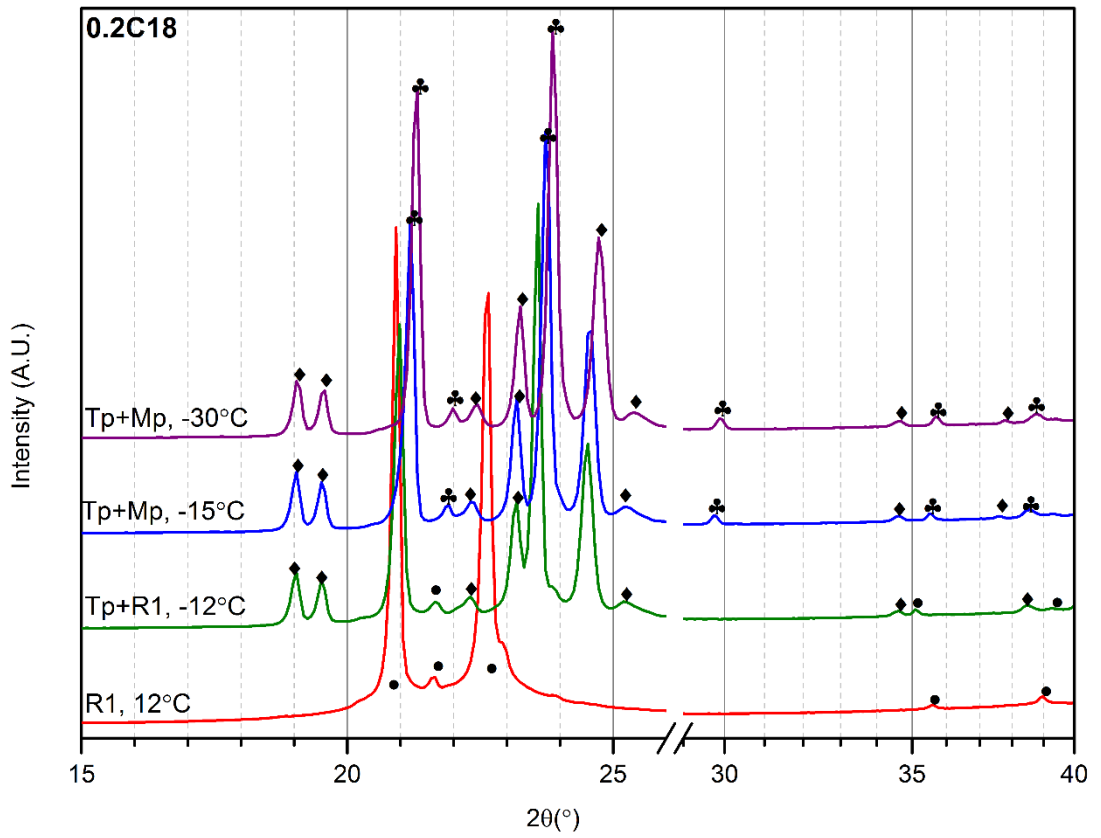
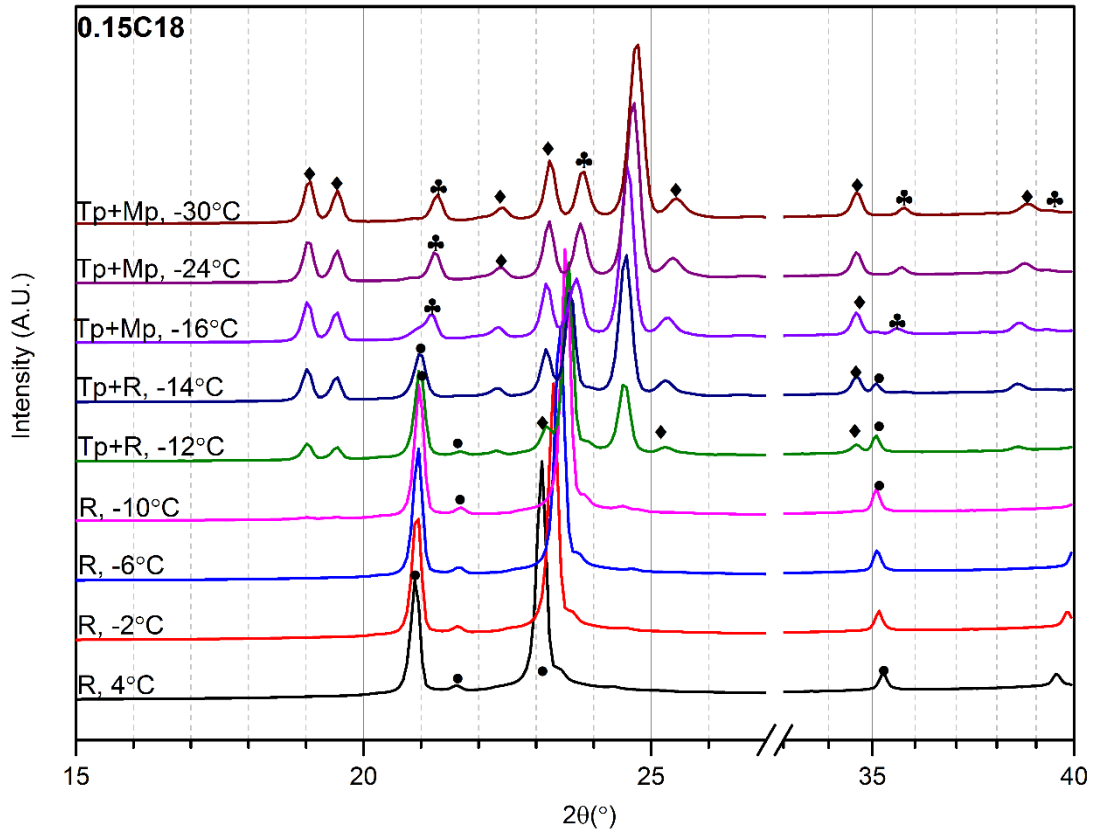
**Table 6.7 Unit cell parameters determined from XRD patterns collected by X'pert and Pawley refinement using TOPAS software.**

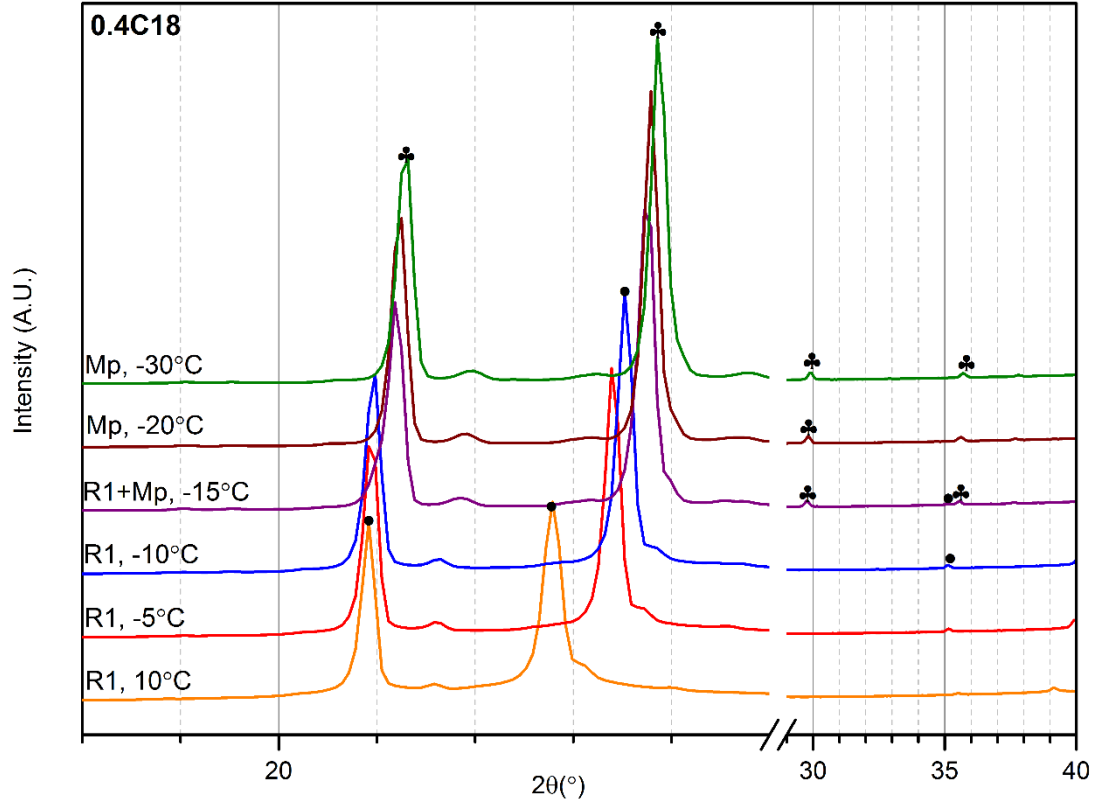
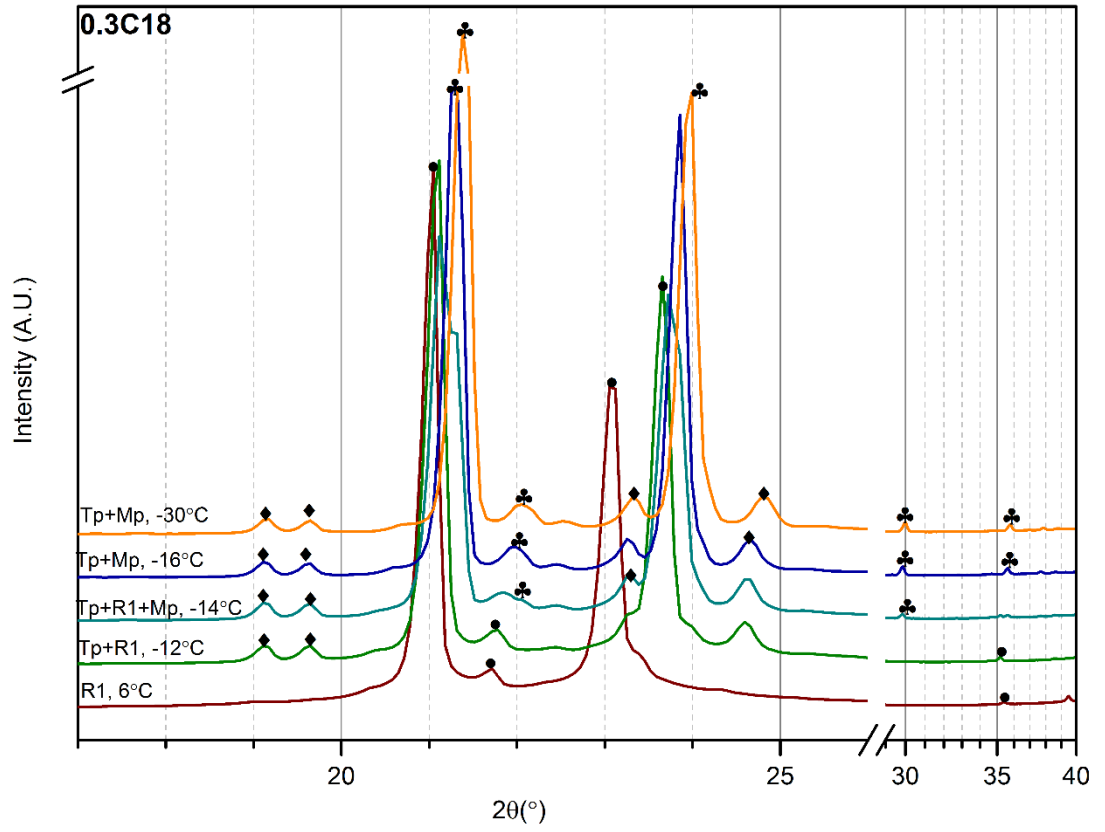
Sample	phase	Space group	a/ Å	b/ Å	c/ Å	$\alpha$ / °	$\beta$ / °	$\gamma$ / °	R <sub>wp</sub> / %	R <sub>p</sub> / %
C16	T16	<i>P-1</i> , (Z=1)	4.258	4.832	20.465	91.121	90.184	106.564	5.01	2.96
0.05C18	T16	<i>P-1</i> , (Z=1)	4.205	4.775	20.339	90.126	91.140	106.115	4.40	2.82
0.1C18	Mdcp	<i>Aa</i> (Z=4)	7.384	4.979	47.688	90	91.430	90	3.05	2.19
	T16	<i>P-1</i> , (Z=1)	4.232	4.846	20.320	90.347	90.319	107.532	4.16	2.540
0.15C18	Mdcp	<i>Aa</i> (Z=4)	7.397	4.991	47.858	90	91.333	90	1.94	1.38
	T16	<i>P-1</i> , (Z=1)	4.194	4.798	20.877	89.855	91.645	106.676		
0.2C18	Mdcp	<i>Aa</i> (Z=4)	7.402	5.006	48.077	90	91.207	90	3.28	2.25
	T16	<i>P-1</i> , (Z=1)	4.199	4.789	20.798	89.822	91.658	106.889		
0.3C18	Mdcp	<i>Aa</i> (Z=4)	7.378	4.974	47.433	90	90.99	90	5.61	3.95
	T16	<i>P-1</i> , (Z=1)	4.256	4.813	20.616	91.115	89.648	107.205		
0.4C18	Mdcp	<i>Aa</i> (Z=4)	7.383	4.998	47.938	90	91.278	90	3.37	1.79
0.45C18	Op	<i>Pca21</i> (Z=4)	7.309	4.993	46.850	90	90	90	3.90	2.93
	Mdcp	<i>Aa</i> (Z=4)	7.382	4.759	47.489	90	94.130	90		
0.5C18	Op	<i>Pca21</i> (Z=4)	7.324	4.996	46.886	90	90	90	2.89	2.10
	Mdcp	<i>Aa</i> (Z=4)	7.382	4.770	47.726	90	94.148	90		
0.6C18	Op	<i>Pca21</i> (Z=4)	7.391	4.993	47.525	90	90	90	6.08	3.76
0.7C18	Op	<i>Pca21</i> (Z=4)	7.427	5.023	47.810	90	90	90	2.75	1.78
	T18	<i>P-1</i> , (Z=1)	4.268	4.817	22.803	80.746	85.296	73.168		
0.8C18	Op	<i>Pca21</i> (Z=4)	7.435	5.021	47.828	90	90	90	3.36	2.05
	T18	<i>P-1</i> , (Z=1)	4.265	4.816	22.844	80.401	85.180	73.506		
0.9C18	Op	<i>Pca21</i> (Z=4)	7.437	5.018	47.823	90	90	90	5.71	2.67
	T18	<i>P-1</i> , (Z=1)	4.270	4.812	22.826	80.286	85.070	73.441		
C18	T18	<i>P-1</i> , (Z=1)	4.224	4.724	24.695	85.846	67.759	71.672	6.35	3.94

### 6.3.3 Variable Temperature XRD Analysis

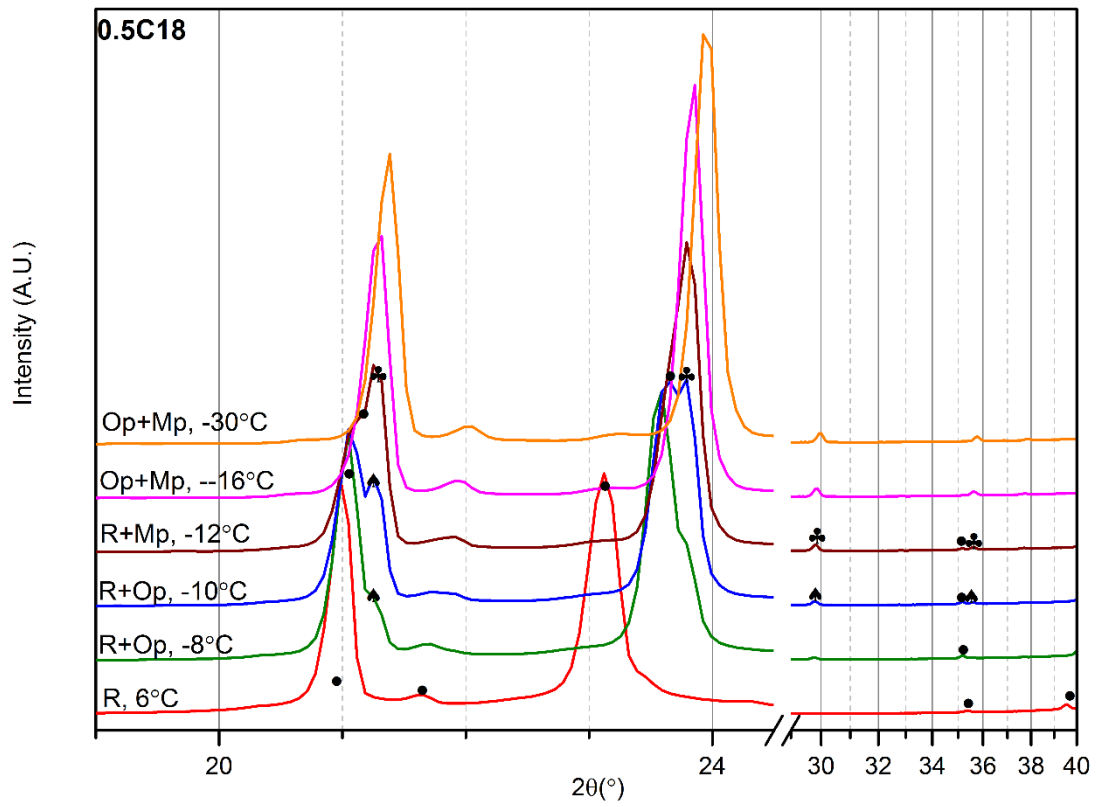
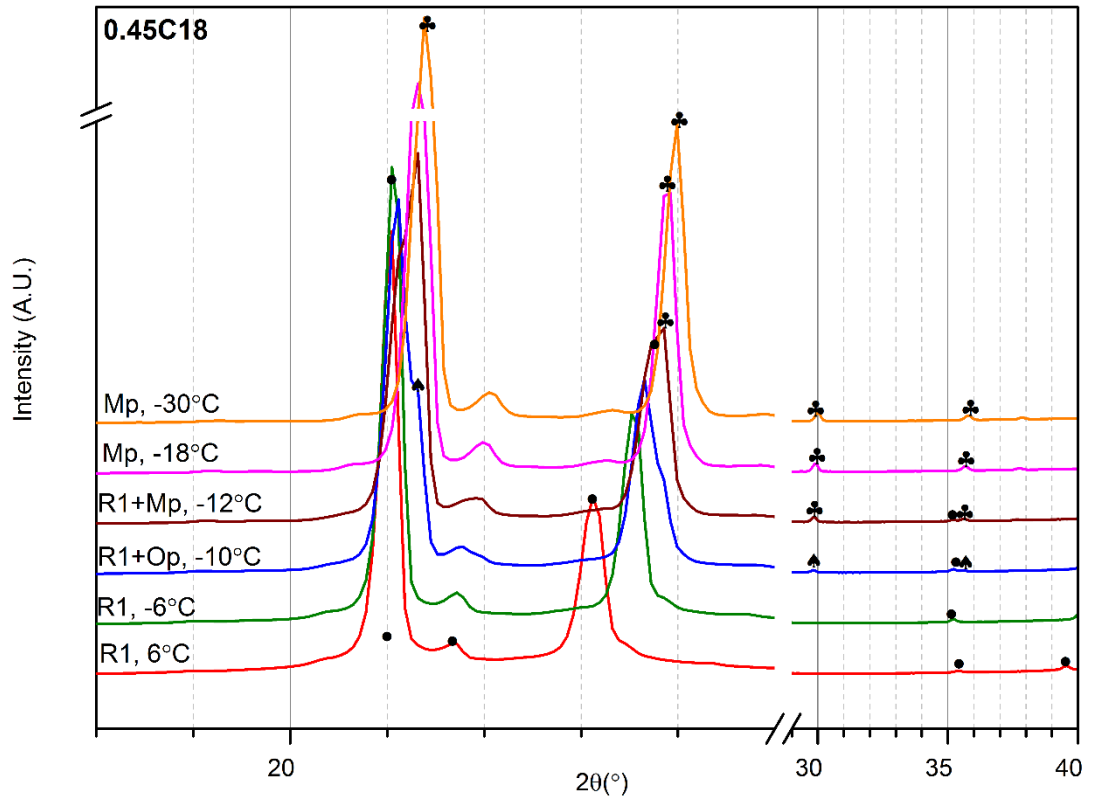
Temperature dependent XRD were collected for binary mixture samples according to the phase transition temperatures as determined from DSC, the stack plots for representative compositions with fraction C18 of  $x=0.05, 0.1, 0.15, 0.2, 0.3, 0.4, 0.45, 0.5, 0.6, 0.7$  and  $0.8$  are shown in **Figure 6.12**. According to the single phase identification in 6.3.1 and 6.3.2 with indexed peak positions, the sequences of phase transitions as increasing temperature for each mixed sample are presented. The specific peak positions with respect to  $T, M_{dcp}, O_p$  and  $R_1$  are marked with the following symbols:  $\blacklozenge$   $T$  ( $P-1, Z=1$ ),  $\bullet$   $R_1$  ( $F_{mmm}, Z=4$ ),  $\clubsuit$   $M_{dcp}$  ( $Aa, Z=4$ ) and  $\heartsuit$   $O_p$  ( $P_{ca21}, Z=4$ ). Notably, samples of  $0.45C18$  and  $0.5C18$  with peak positions of  $M_{dcp}$  and  $O_p$  which are hard to distinguish. According to the interpretation from DSC and isothermal XRD phase analysis at  $-30^\circ\text{C}$ , phase evolution is interpreted and presented (**Figure 6.12**) as a function of the temperature of these mixtures. It should be noted that the  $R_1$  phase ( $F_{mmm}$ ) forms an obvious shift of (020) plane around  $23^\circ$  in two theta due to the remarkable unit cell expansion of area ( $b/a$ ) as the temperature increased [73].

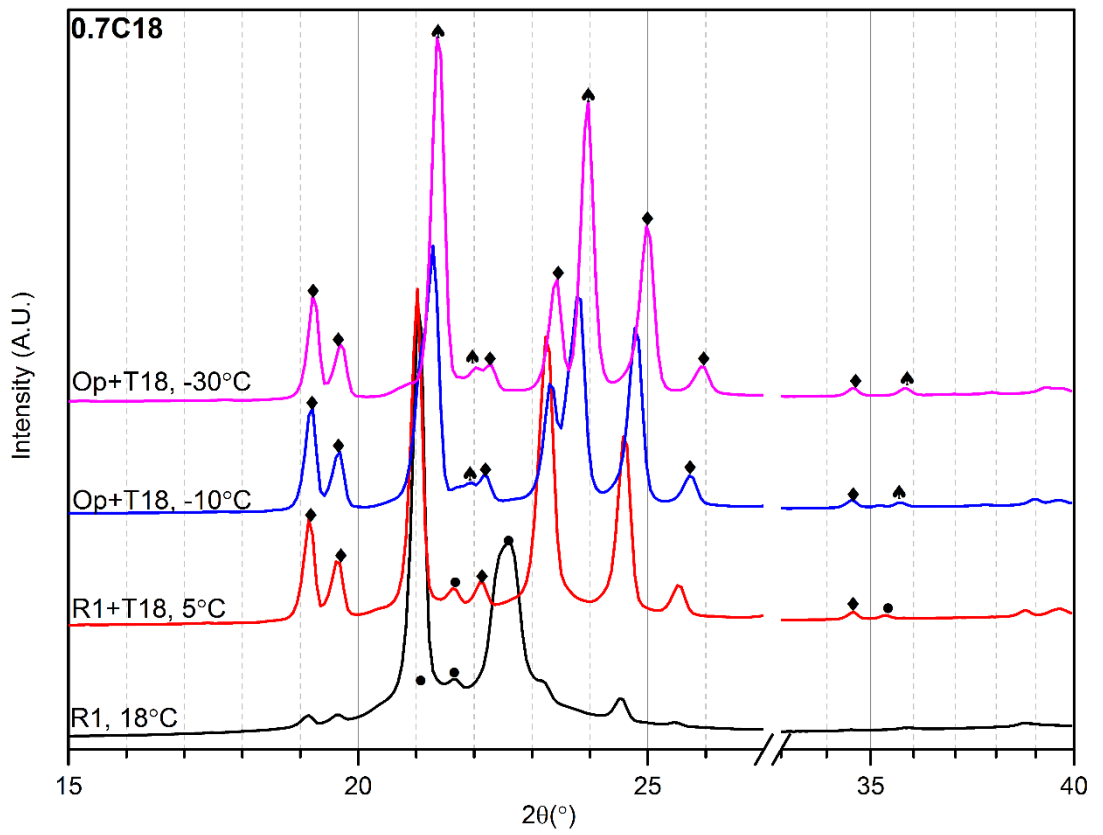
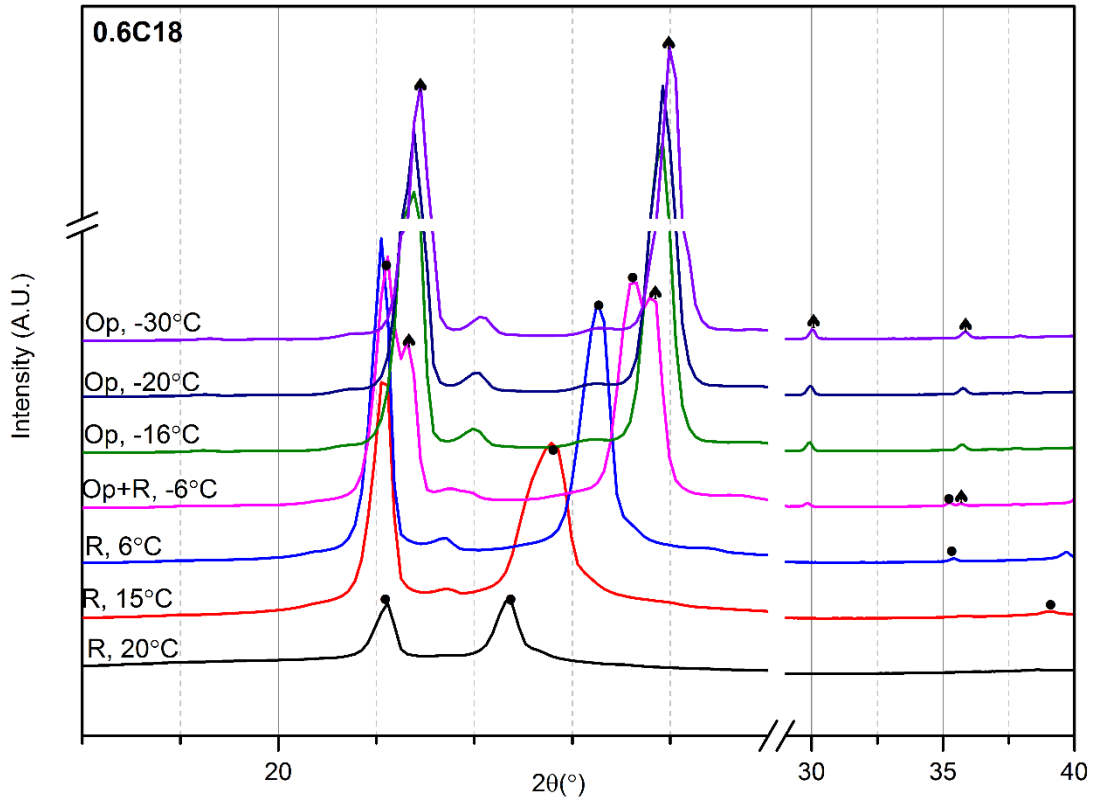






-1620





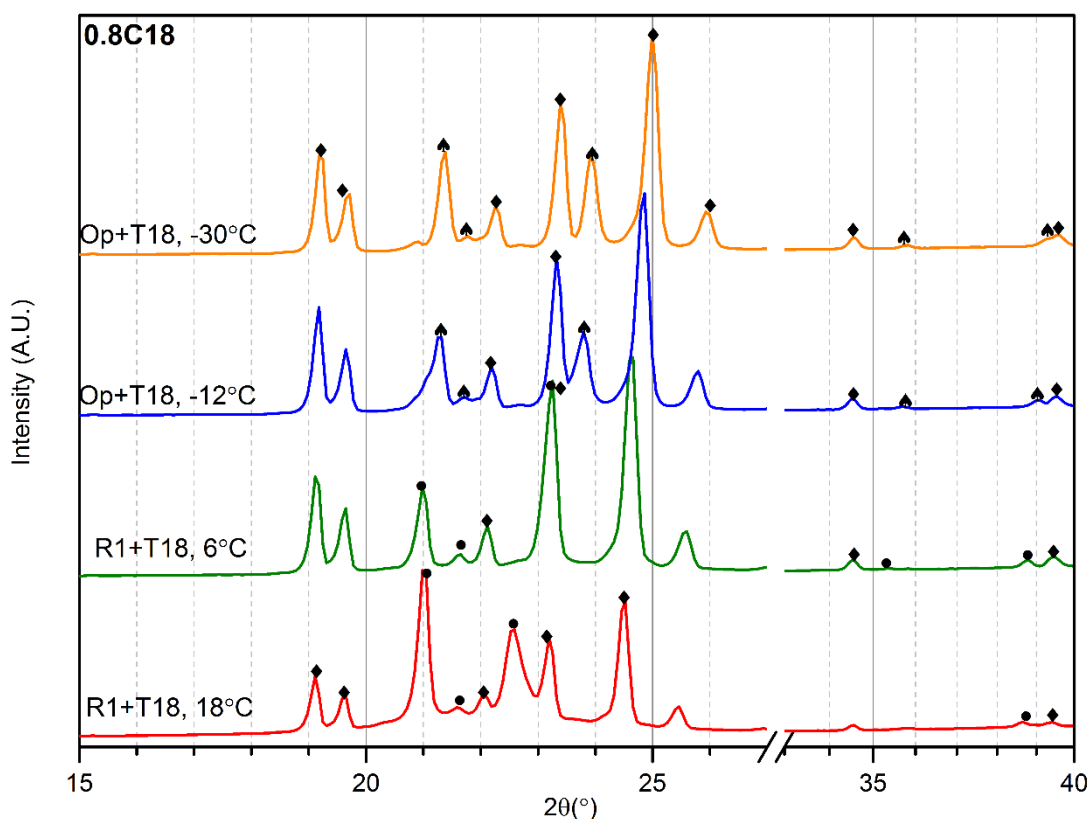


**Figure 6.12: Temperature dependent PXRD collected from X'Pert for C18/C16 binary with molar composition  $x= 0.05, 0.1, 0.15, 0.2, 0.3, 0.4, 0.45, 0.5, 0.6, 0.7$  and  $0.8$  of C18. Symbols:  $\blacklozenge$  T ( $P_{-1}, Z=1$ ),  $\bullet$  R1 ( $F_{mmm}, Z=4$ ),  $\clubsuit$  M<sub>dcp</sub> ( $A_a, Z=4$ ) and  $\blacktriangledown$  Op ( $P_{ca21}, Z=4$ ).**

#### 6.4 Equilibrium Binary Phase Diagram of Octadecane and Hexadecane

A complex phase diagram of C18/C16 had been determined from melting transition temperatures with associated structural information resolved by XRD patterns from 21 molar ratio compositions is shown in **Figure 6.13**. The boundary lines observed from the melting temperatures as measured by DSC with solvus lines representing the peak points, the solidus line was the onset point. The liquidus line was determined from the real end point calculated using the “peak shape” method.

In between, five monophasic solid phases (liquid, R<sub>1</sub>, T<sub>16</sub>, M<sub>dcp</sub>, O<sub>p</sub> and T<sub>18</sub>), two limited solid solution regions with respect to T<sub>16</sub> and T<sub>18</sub> which have the same structure of pure alkanes existed in mixtures having compositions next to the pure C16 and C18. The disordered R<sub>1</sub> phase was observed in a large

composition and temperature range at HT.  $M_{dcp}$  and  $O_p$  at LT referred to as the intermediate ordered phases that were obtained from mixing of two components with certain packing defects. These two phases are also observable in longer chain length of even alkanes. Thus mixing of alkanes helps generate new phases which only appear in longer chain molecules. Seven bi-phasic solid phases are presented in between the adjutant monophasic phases:  $T_{16}+R_1$ ,  $T_{18}+R_1$ ,  $M_{dcp}+R_1$ ,  $O_p+R_1$ ,  $M_{dcp}+T_{16}$ ,  $M_{dcp}+O_p$  and  $O_p+T_{18}$ .

The phase diagram (**Figure 6.13**) immediately demonstrates the existence of two intermediate phases in the LT domain which is not a continuous solid solution as the presence of two solid three-phase-equilibrium lines as measured by DSC and proved by XRD analysis. In total, five three-phase-equilibrium invariants are revealed. The eutectic reaction of the liquid phase crystallises into mixture phases of  $T_{16}$  and  $R_1$  at a constant temperature of  $T_E$  around  $16^\circ\text{C}$ . The peritectic reaction of mixture phases of liquid and  $T_{18}$  transform to  $R_1$  at  $T_P$  around  $25^\circ\text{C}$ . At low temperatures, eutectoid and peritectoid equilibrium constants are also observed with respect to the transitions of  $O_p \leftrightarrow T_p + M_{dcp}$ ,  $R_1 + O_p \leftrightarrow M_{dcp}$  and  $T_{18} + R_1 \leftrightarrow O_p$ , the last one which was not detectable from DSC.

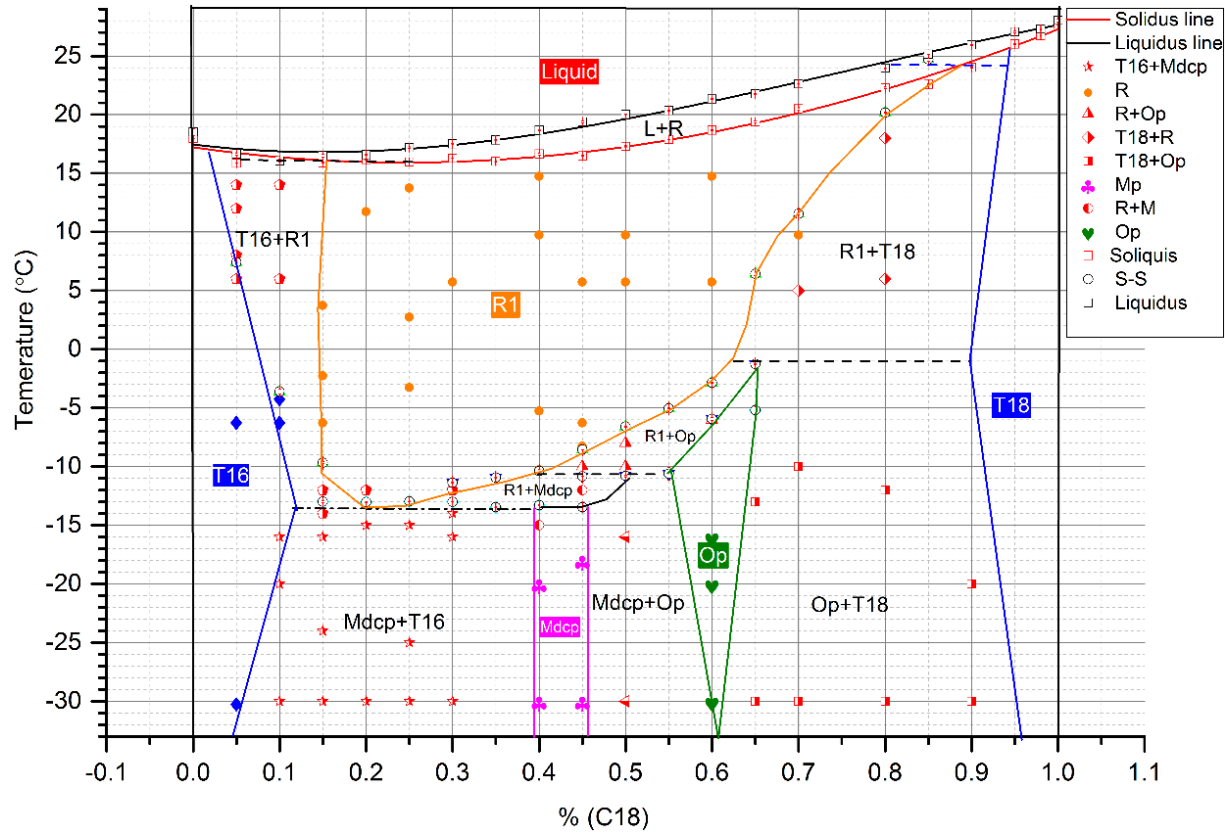


**Figure 6.13: Experimental determined binary phase diagram of C16/C18 mixtures as a function of composition and temperature towards heating processes. Phase transition temperatures are determined by DSC represented by symbols of  $\square$  (Solid-liquid),  $\diamond$  (liquid-solid) and  $\circ$  (solid-solid). Structural evolution was determined from PXRD:  $\blacklozenge$  T (P-1, Z=1),  $\bullet$  R1 (F<sub>mmm</sub>, Z=4),  $\clubsuit$  M<sub>dcp</sub> (A<sub>a</sub>, Z=4) and  $\heartsuit$  O<sub>p</sub> (P<sub>ca21</sub>, Z=4). In between of the adjacent monophasic phases are bi-phasic solid phases: Liquid+R<sub>1</sub>, T<sub>16</sub>+R<sub>1</sub>, T<sub>18</sub>+R<sub>1</sub>, M<sub>dcp</sub>+R<sub>1</sub>, O<sub>p</sub>+R<sub>1</sub>, M<sub>dcp</sub>+T<sub>16</sub>, M<sub>dcp</sub>+O<sub>p</sub> and O<sub>p</sub>+T<sub>18</sub>. Three-phase-equilibrium invariants are represented by dash line (---).**

## 6.5 Structural Analysis for Binary Mixture Formation by Rapid Quenching

Structural behaviour of the disordered  $R_1$  phase at HT transforming into the ordered crystalline at LT associated with the effects of cooling kinetics was studied by crash cooling crystallisation to a low temperature of  $-30^\circ\text{C}$ .

Collected XRD patterns for mixed samples of 0.3C18, 0.5C18 and 0.7C18 as crash cooled to  $-30^\circ\text{C}$  from  $R_1$  phase at HT, are shown in Figure 6.11 (a) and (b) with respect to the low angle and high angle reflections. As seen from **Figure 6.14**, crash cooled 0.7C18 crystallised in a mixture of triclinic phase indicated from the representative reflections at  $19$  and  $20^\circ$  in  $2\theta$ , and the other one having similar reflection peaks from crash cooled samples of 0.5C18 and 0.3C18 was high possibly phase of  $O_p$ . The two samples of 0.5 C18 and 0.3 C18 with reflections consistent with each other as seen from the XRD patterns collected from both low angle (a) and high angles (b). However, instead of a single phase of  $O_p$ , a formation of mixture phases was present with close structures illustrated by the highlighted peaks from **Figure 6.14**.

According to the equilibrium phase diagram determined in section 6.4, at LT, the composition of 0.7C18 crystallised into mixtures of  $T_{18}$  and  $O_p$ , for 0.5C18 are mixtures of  $M_{dcp}$  and  $O_p$ , for 0.3C18 are  $T_{16}$  and  $M_{dcp}$ . Apparently, different phase behaviour was observed for 0.3C18 from equilibrium phase diagram and crash cooling conditions. **Figure 6.15** (a) and (b) shows the XRD patterns in  $q$  vector both collected at  $-30^\circ\text{C}$  from diffractometers of Expert and STOE with respect to the equilibrium and crash cooling crystallisation. The crash cooled structure has no reflection peaks with respect to the triclinic phase as observed in equilibrium. Highlighted peaks are inconsistent positions with the  $M_{dcp}$  phase, while some extra peaks can also be observed indicating a second phase is also formed. This phase obtained here differs from the equilibrium determination phase diagram. The reason can be explained due to the crashed cooling process was without sufficient time for triclinic phase formation and therefore crystallised into the intermediate kinetically favoured phases of  $M_{dcp}$  and  $O_p$ . This can also correlate to the DSC observation that the solid-solid transition which occurred in the LT region was a poly-thermal process with mass transportation. Thus, without sufficient time to transfer, it will result in a closer packing phase to the original  $R_1$  phase.

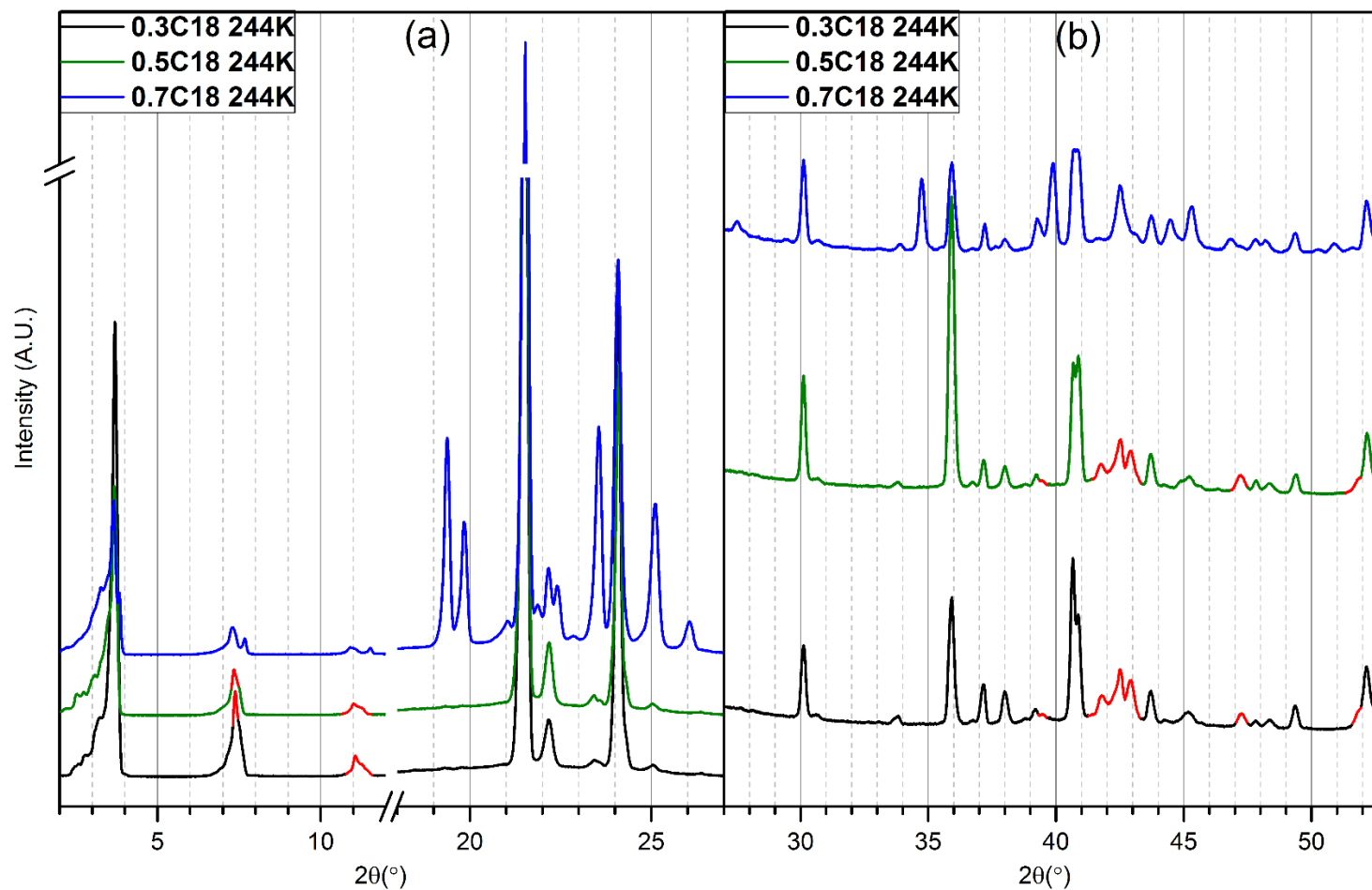


Figure 6.14: Collected XRD patterns for mixed samples of 0.3C18, 0.5C18 and 0.7C18 as crashed cooled to  $-30^\circ\text{C}$  from R<sub>1</sub> phase at HT; (a) low angle and (b) high angle reflections

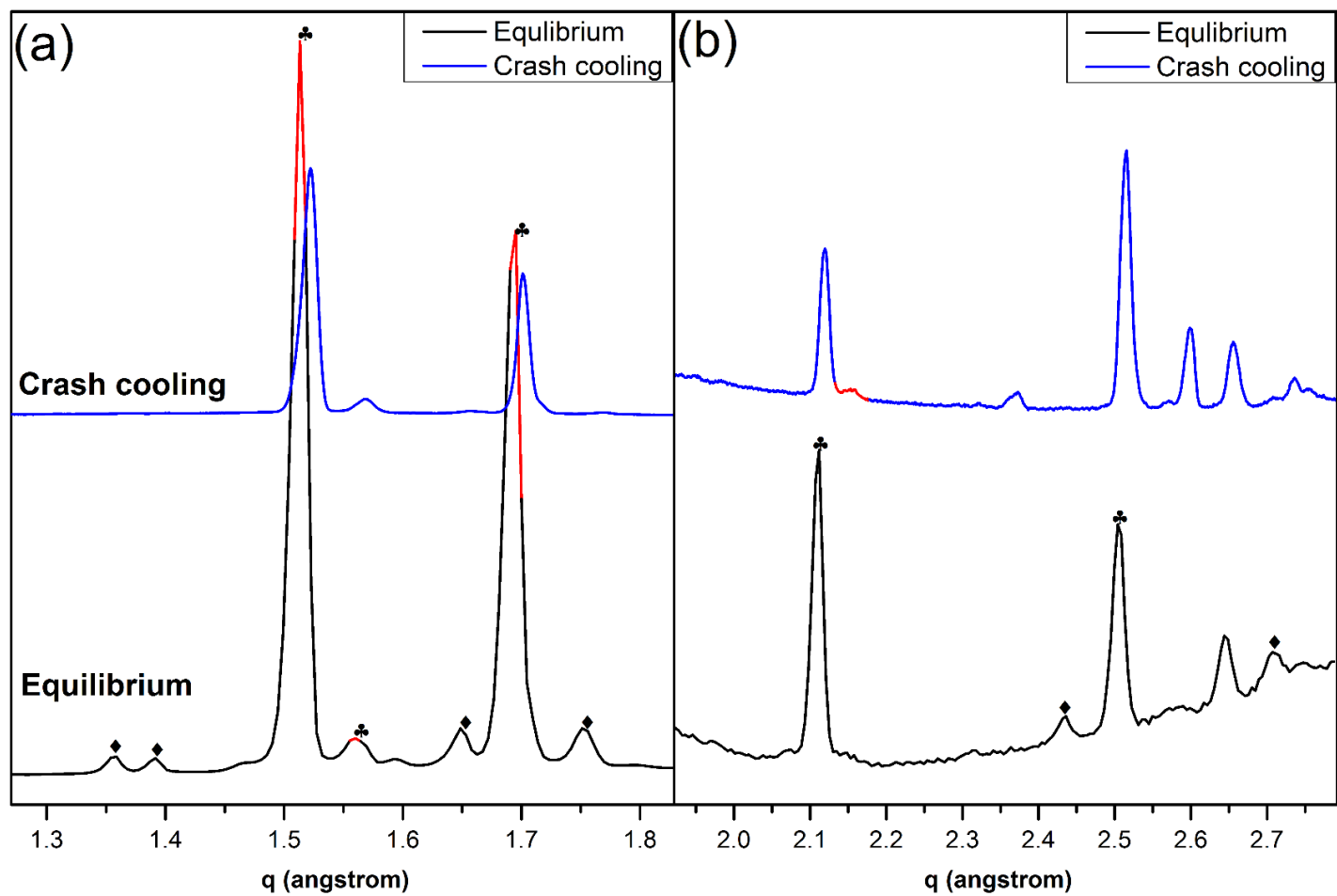


Figure 6.15: XRD patterns in q vector of sample 0.3C18 collected both at - 30°C from diffractometers of Expert and STOE with respect to the equilibrium and crash cooling crystallisation. (a) Low angles and (b) high angle reflections. ♣ Mdcp (Aa, Z=4); ♦ T (P-1, Z=1)

## 6.6 Nucleation Kinetic Assessment Using the KBHR Approach

The nucleation mechanism for a single component (C16 and C18) and binary mixture sample (0.4C18) was assessed by applying the KBHR [31] approach with values of relative critical undercooling  $u_c$  and cooling rate  $q$ . The  $u_c$  values of all three samples are within the limits specified by inequalities. **Figure 6.16** (a, b and c) shows the plots of  $\ln q$  vs  $\ln u_c$  with the best linear fits with respect to samples of C16, 0.4C18 and C18. The slopes and their indicated nucleation mechanism and correlated coefficients  $R^2$  are presented in **Table 6.8**. According to the “rule of three” [29, 30], in the case of the pure component of C16 or C18, having a slope larger than three which indicated a progressive nucleation (PN) mechanism. In contrast, 0.4C18 binary mixture is suggested with crystallising through the instantaneous nucleation (IN) mechanism in which the slope was smaller than three. Single alkanes of C16 and C18 as ruled by PN nucleation were further investigated by application of **Equation (2.26)**. To obtain the relative values from this equation,  $\ln q$  vs  $u_c$  was plotted and fitted by a non-linear curve as shown in **Figure 6.17 (a) and (b)** for C16 and C18. The parameters obtained from the fitted expressions correlated coefficients  $R^2$  are listed in **Table 6.8**. The values of  $a^2$  which are equal to the value of b, were used to calculate the effective interfacial tension ( $r_{eff}$ ) which are also presented in **Table 6.8**, using **Equation (2.27)**. Within the equation,  $v_0$  of 0.406 nm<sup>3</sup> and 0.456 nm<sup>3</sup> were used for C16 and C18 triclinic unit cells as determined from XRD analysis in **5.2.2** and **5.3.1**, respectively;  $v_0 = 0.459$  nm<sup>3</sup> was used for binary mixture 0.4 C18 of R<sub>1</sub> phase determined in **6.3.1**. Equilibrium temperature ( $T_e$ ) and the latent heat of  $\lambda$  were obtained previously from DSC measurements (**Table 6.3**);  $k_n = \frac{16}{3} \pi$  for spherical nuclei.

Regardless of the solvent effects playing an important role on solution crystallisation, melt phase crystallisation is mainly controlled by the diffusion and internal lattice energy [116]. From the empirical nucleation (**Equation 2.16**), the nucleation rate relates to the nucleation rate constant ( $K_J$ ) and exponential factor associated with the interfacial tension. Where the  $K_J$  relates

to the concentration of available nucleation sites ( $C_0$ ) and the attachment frequency ( $f^*$ ) of molecules to the nucleus. As a consequence, interfacial tension is controlled by the lattice energy and attachment frequency which is a diffusion factor.

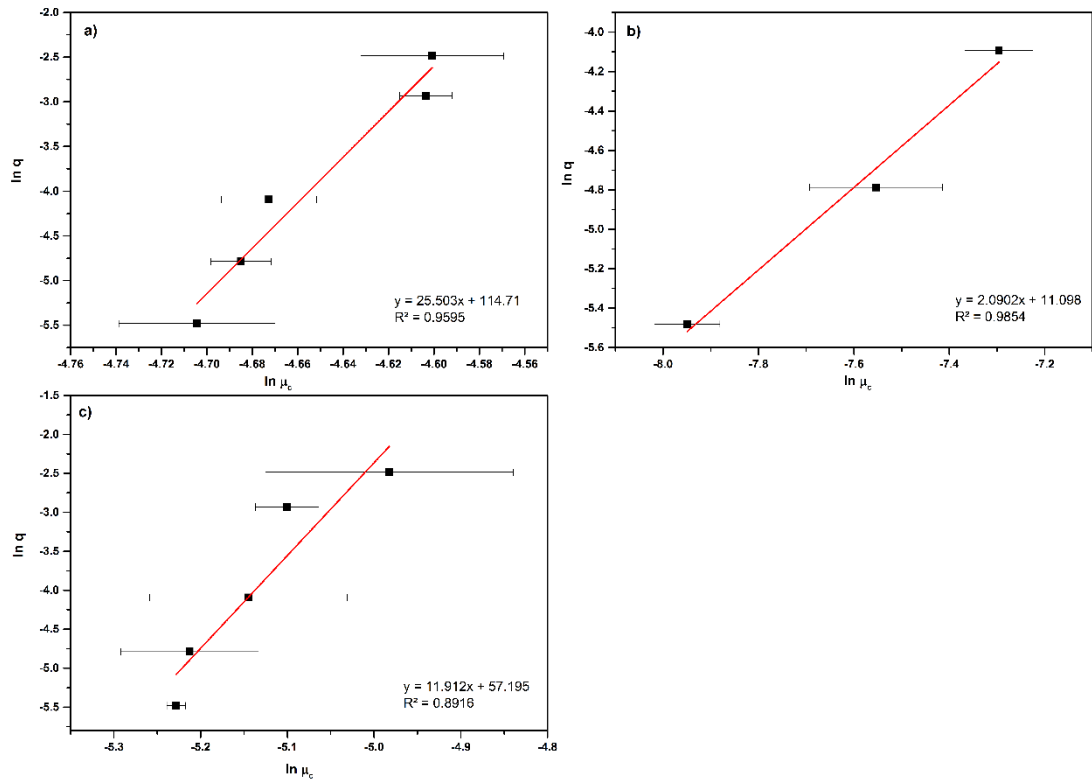


**Figure 6.16: Nucleation mechanism assessment plot of  $\ln q$  vs  $\ln \mu_c$  for a) C16, b) 0.4C18 and c) C18 in melt phase crystallisation**

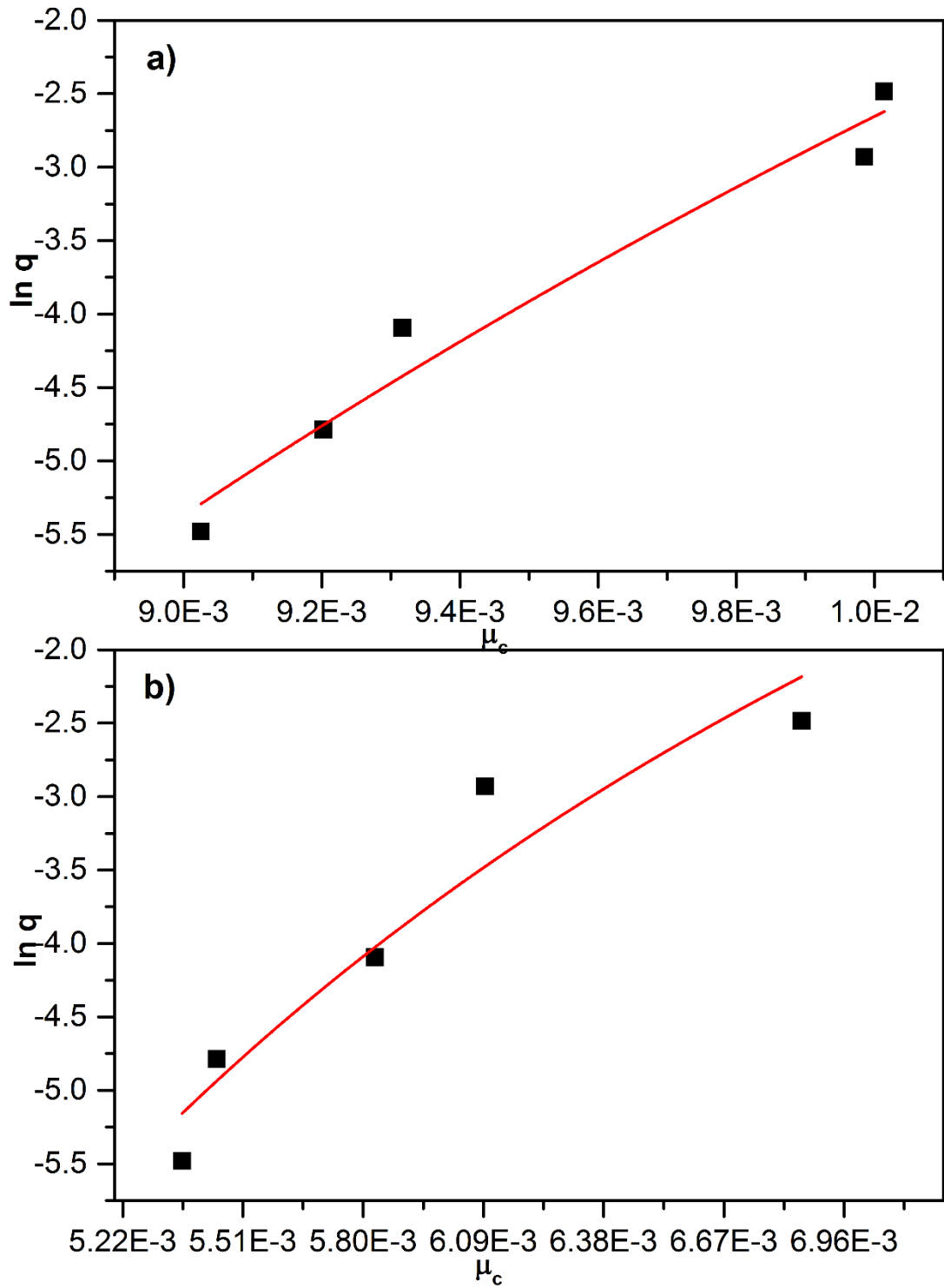


Figure 6.17:  $\ln q$  vs  $uc$  for C16 with the best non-linear fit according to PN mechanism expression from KBHR for a) C16 and b) C18.



## 6.7 Conclusions

In the binary phase diagram of C18/C16 mixtures are revealed as a function of mixture composition and temperature by energetic and structural analysis. In between the phase diagram, five monophasic solid phases existed, i.e. the liquid,  $R_1$ ,  $T_{16}$ ,  $M_{dcp}$ ,  $O_p$  and  $T_{18}$ . In total five three-phase-equilibrium invariants are revealed including eutectic and peritectic, in a high temperature region and eutectoid and peritectoid transitions in a low temperature region.

Lattice parameters of the disordered  $R_1$  phase are determined by indexation of the high resolution powder diffraction data showing the c-axis length of this  $R_1$  structure is not strongly related to the chain length of mixtures. However, the lower stability with lower enthalpy fusion will result in a shorter chain length. By further cooling at low temperatures, the multiple intermediate ordered phases are detected with high symmetry crystalline structures having very similar diffraction peaks for diffraction data.

Thermal analysis of DSC heating/cooling examination on pure C16, C18 and mixtures rich in C18 shows the crossover behaviour of the  $R_1$  existing in a transient to metastable to stable phase, which again confirmed the stability of the  $R_1$  phase affected by both composition and alkane chain length. This induced rotator phase from nucleation is further studied in a solution state.

As an alternative to the equilibrium phase behaviour, binary mixtures have shown a different phase formation by the crash cooling crystallisation method. The triclinic structure is difficult to form than the more packing similar phase of intermediate phases of  $M_{dcp}$  and  $O_p$ .

## **Chapter 7 In-situ High Resolution XRD Studies of Phase Behaviour of the Octadecane, Hexadecane and Kerosene Solution Ternary System**

### *Summary:*

*This chapter will address phase behaviour in the ternary system of octadecane/hexadecane/kerosene mixtures as a function of composition and temperature using in-situ synchrotron powder diffraction.*

## 7.1 Introduction

Normal alkanes have been intensively studied for decades in terms of phase diagram determination and thermal analysis. However, the solvent effect on the formation of solid solution homologue mixtures is rarely studied. In the previous chapter, we have fully characterised C18/C16 mixtures in melt phase crystallisation, following on from that, how the solvent influences solution conditions from in-situ crystallisation are essential to be researched further.

This chapter addresses the application of in-situ synchrotron powder diffraction on real-time crystallisation studies for single and mixed alkanes in a solution of kerosene (308 g/l) which is a representative fuel solvent. The structure refinement for a single component of C16 and C18 in kerosene and associated thermal expansion properties analysis were carried out. For mixed samples, the phase transition behaviour as a function of temperature and composition as crystallising in kerosene from a liquid phase at the early stage to the limited low temperature at LT (- 40°C) are illustrated.

## 7.2 Isothermal Analysis at LT (- 40°C)

### 7.2.1 LT Phase Behaviour as a Function of Composition

Isothermal structural characterisation as a function of C18 molar composition was carried out at the low temperature of - 40°C to determine the terminal phase behaviour and associated crystallographic parameters. High resolution diffraction patterns collected via the Multi-Analysing Crystal (MAC) detector for the mixed samples are represented in **Figure 7.1**, in which are the selected reflection regions referred to as “low angle” and “high angle”. The structural evolution versus composition could be separated into two sections: samples (C16, 0.1C18, 0.7C18 0.9C18 and C18) close to the pure component of C18 or C16 at both sides; samples (0.3C18, 0.4C18 and 0.5C18) close to the equalised percentage of C18 and C16. Mixture samples within section one formed solid solution type in triclinic structure identical to the chain length of the dominant homologue. This could be illustrated from the identical indexed (00L) peaks at a low angle and also reflections in the high angle region. It should be noted that the peak number was reduced and had a broader shape

than the mixed sample of 0.1C18 in comparison with pure C16. This can be explained by a small amount of longer chain homologue of C18 could result in a disordering effect on the triclinic solid solution.

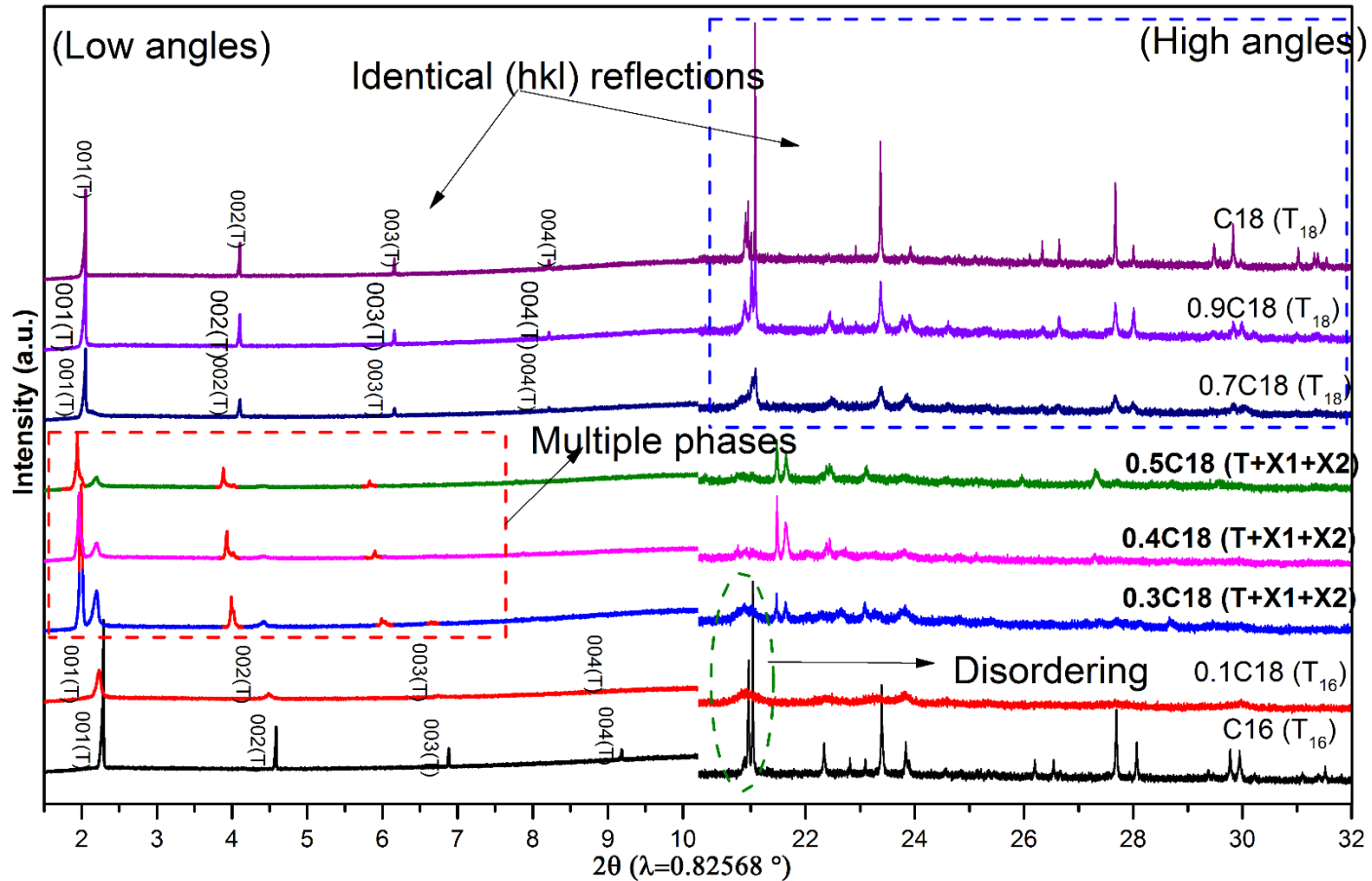
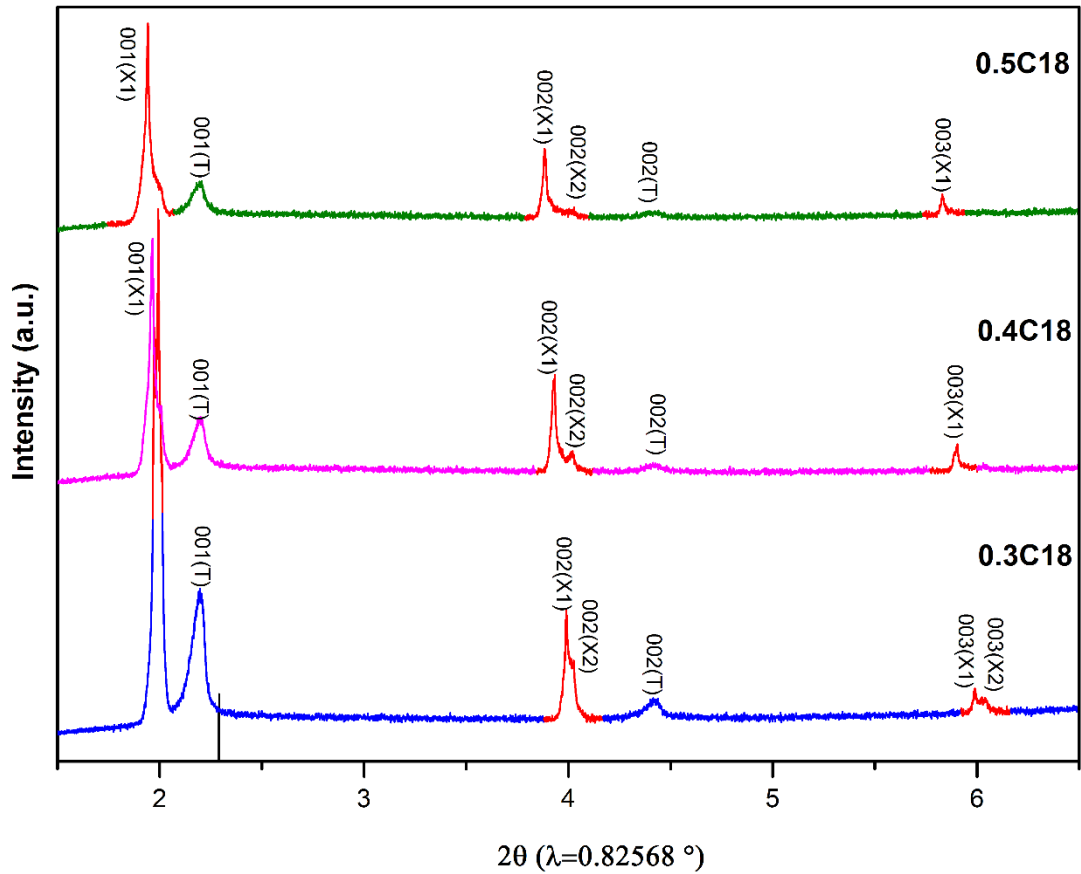


Figure 7.1: Stack plot of high resolution XRD (MAC detector) with  $\lambda = 0.82568^\circ$  at  $-40^\circ\text{C}$  for C18/C16 mixtures crystallising from kerosene; selected “low angles” with  $2\theta$  from 1 to  $10^\circ$  and “high angles” with  $2\theta$  from 20 to  $32^\circ$ . Single triclinic phase with low angles reflections indexed; the low angles region for mixtures of 0.3C18, 0.4C18 and 0.5C18 presenting multiple phases are enlarged and shown in Figure 7.3.



**Figure 7.2: Set of (00L) peaks at low angle range for mixture samples crystallising from kerosene with molar compositions of x= 0.3, 0.4 and 0.5) C18 in C16. Multiple phases were detected in all three samples, i.e. triclinic (T) and unknown phases (X1 and X2).**

On the other hand, 0.3C18, 0.4C18 and 0.5C18 were formed in multiple phases indicated by the triple number of low angle (00L) reflections as highlighted by red dashed lines and enlarged shown in **Figure 7.2**. Nevertheless, it was not difficult to distinguish that one of the mixed phases was triclinic, the indexations were also given for the relative diffraction peaks. The proportion of triclinic phase decreased with increasing the amount of longer homologue component of C18 as seen from the deduction intensity of its reflection peaks. Apart from this, two more new phases were also observed: (X1) was the one having higher intensity peaks and longer chain length as indicated from the (00L) reflections more towards to the low angle; limited amount of phase (X2) with similar long chain length represented by a small shoulder was detected next to reflection peaks of phase (X1).

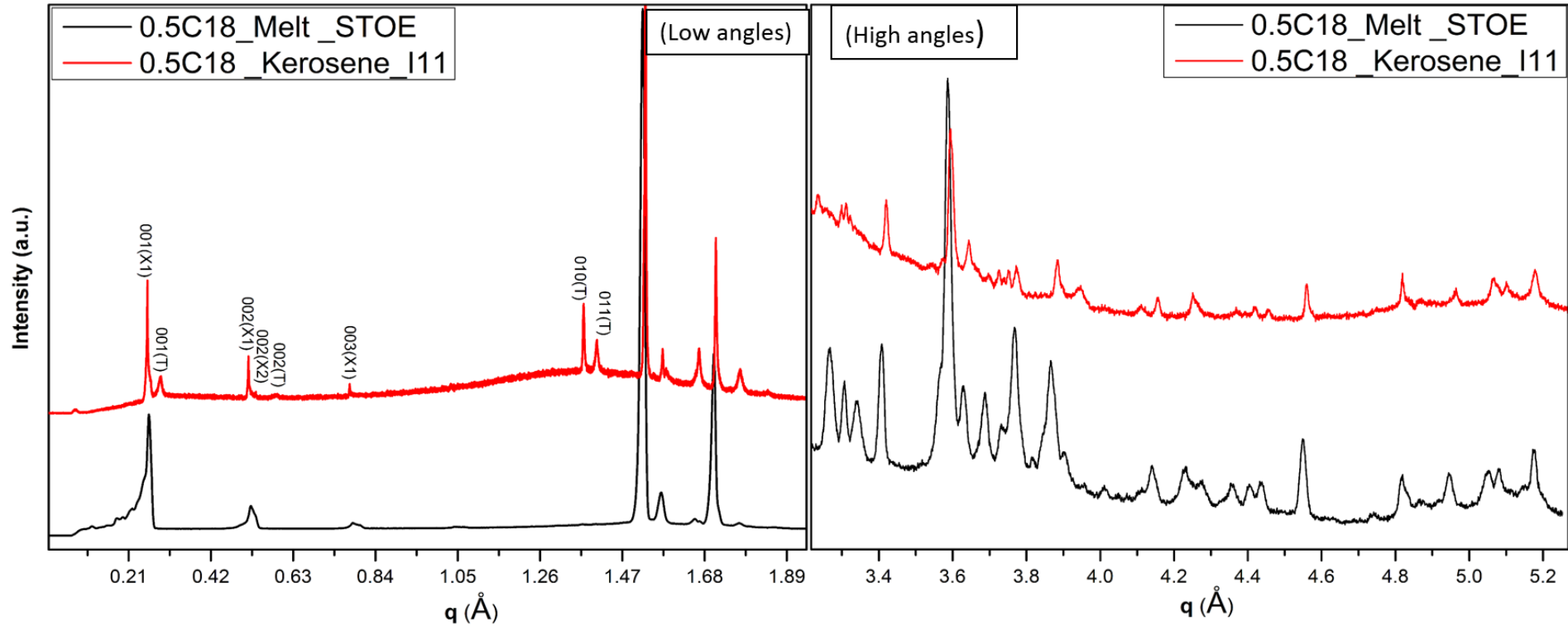


Figure 7.3: Stack XRD plot in  $q$  vector of 0.5C18 with the melt crystallisation crash cooling process at  $-30^{\circ}\text{C}$  collected using STOE lab diffractometer and 0.5C18 with kerosene crystallisation at  $-40^{\circ}\text{C}$  collected using high resolution synchrotron beamline. Selected reflections from the low angles ( $q$  from 0.21 to 1.89  $\text{\AA}^{-1}$ ) and high angles ( $q$  from 3.2 to 5.3  $\text{\AA}^{-1}$ ) regions.

The multiple phases of X1 and X2 are possibly the intermediate low temperature crystalline of orthorhombic with a space group  $P_{ca21}$  ( $O_p$ ) and monoclinic with a space group of  $Aa$  ( $M_{dcp}$ ) obtained from the binary mixtures in the melt phase as discussed in **Chapter 6**. In **Figure 7.3**, it clearly shows the diffraction pattern of 0.5C18 crystallised from kerosene, except the obvious triclinic phase (referred to as T), having identical reflections (X1 and X2) as to the peak positions of its binary mixture at LT. This multiple phase behaviour with a set of (00L) peaks was also observed for C20/C22 mixtures in n-dodecane by Gerson [117] which were defined as three different orthorhombic phases without any further information relating to the unit cell parameters.

To further confirm and determine the unit cell parameters for C18/C16 mixtures crystallised in kerosene solution, experimentally collected XRD patterns at the limited low temperature of  $-40^{\circ}\text{C}$  were refined with respective phases by "Pawley fit". The resultant crystallographic information and fitting parameters are given in **Table 7.1**. It should be noted, for sample 0.3C18, the X2 phase as shown in **Figure 7.2** was hardly fitted with the proposed  $O_p$  structure. In this case, only the X1 phase as referred to as the  $M_{dcp}$  structure together with the inherent triclinic phase which was employed during the Pawley refinement. As a good value of  $R_{wp}$  was obtained, this indicated that the X2 phase observed by the 00l reflections at low angles is in a limited amount for 0.3C18 crystallisation in kerosene.

**Table 7.1 Unit cell parameters of C18/C16 mixtures crystallising from kerosene at - 40°C**

Sample	phase	Space group	a/ Å	b/ Å	c/ Å	$\alpha$ /°	$\beta$ /°	$\gamma$ /°	R <sub>wp</sub> /%
C16	T <sub>16</sub>	P-1 (Z=1)	4.228	4.773	20.621	90.786	90.281	106.47	9.0
0.1C18	T <sub>16</sub>	P-1 (Z=1)	4.239	4.820	21.092	89.999	90.617	107.244	4.28
0.3C18	Mdcp	Aa (Z=4)	7.366	4.997	47.183	90	90.858	90	5.04
	T16	P-1 (Z=1)	4.245	4.794	21.451	90.022	90.929	107.034	
0.4C18	Mdcp	Aa (Z=4)	7.279	4.852	48.120	90	93.822	90	5.05
	Op	P <sub>ca21</sub> (Z=4)	7.348	4.987	46.791	90	90	90	
	Tp	P-1 (Z=1)	4.246	4.789	21.443	90.107	91.332	107.048	
0.5C18	Mdcp	Aa (Z=4)	7.412	4.753	48.682	90	93.725	90	5.05
	Op	P <sub>ca21</sub> (Z=4)	7.352	4.981	48.814	90	90	90	
	T18	P-1 (Z=1)	4.232	4.784	21.449	90.263	90.995	106.815	
0.7C18	T18	P-1 (Z=1)	4.217	4.775	23.452	79.026	84.779	73.299	3.59
0.9C18	T18	P-1 (Z=1)	4.223	4.770	23.484	78.982	84.566	73.521	4.07

## 7.2.2 Structure Refinement

The high resolution XRD data of C16 crystallised from solution at  $-40^{\circ}\text{C}$  is presented in **Figure 7.4** as an example showing consistent reflections from the melt phase structure. Nevertheless, higher preferred orientation was observed, as seen from the high-intensity peaks (010) and (011) at  $2\theta$  around  $10.5^{\circ}$ . Rietveld refinement of C16 and C18 crystallised from solution kerosene with calculated and experimental observation XRD patterns are given in **Figures 7.5 and 7.6**, respectively. The determined crystallographic cell dimension parameters of a, b and c were smaller than crystal determined in the melt phase, together with the detailed refinement data provided in **Tables 7.2 and 7.3** for C16 and C18 respectively.

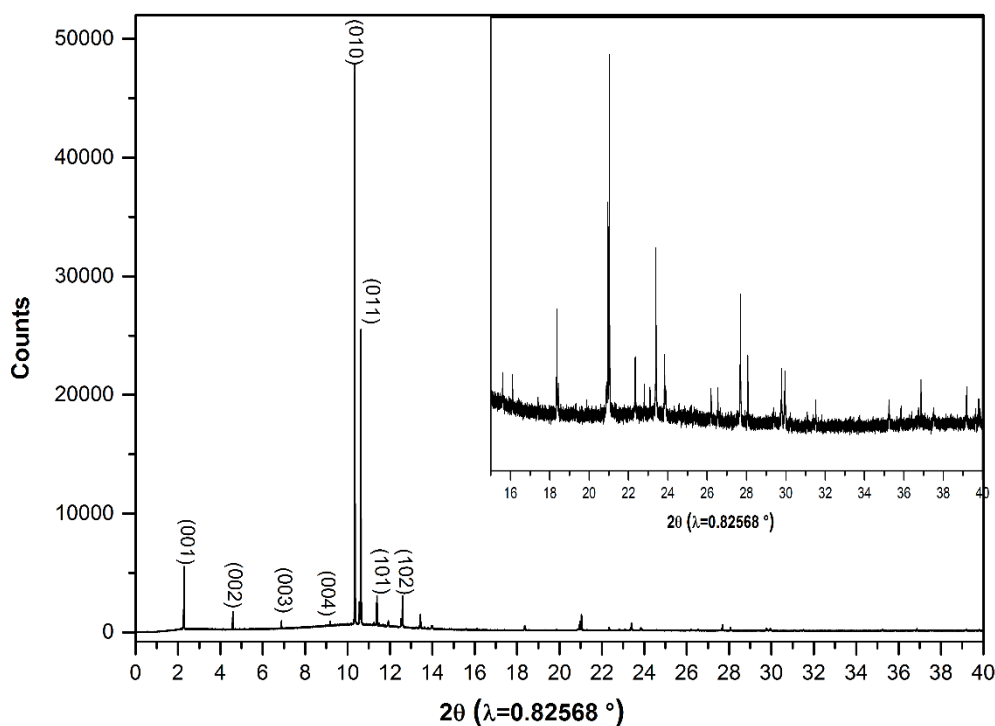


**Figure 7.4:** High resolution synchrotron XRD pattern of C16 in Kerosene at  $-40^{\circ}\text{C}$  collected on beamline I11 from Diamond Light Source. Low-intensity peaks are scaled up from  $2\theta$  of  $15$  to  $40^{\circ}$ .

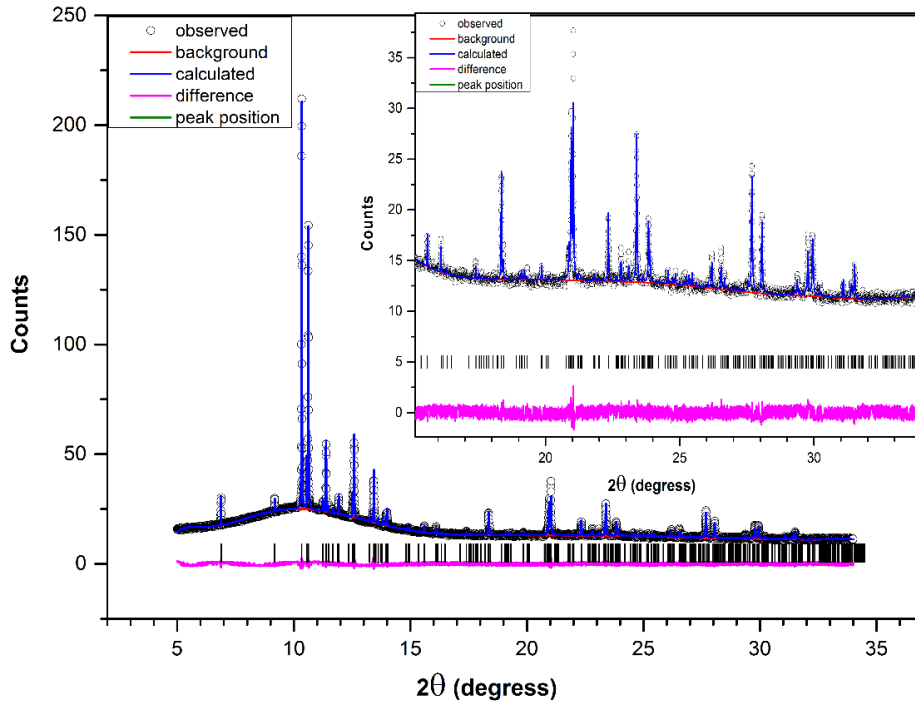


**Figure 7.5: Rietveld refinement of C16 crystalline formed from Kerosene in the range of 5 to 35° 2θ with  $\lambda = 0.825678 \text{ \AA}$  with different scale of amplification according to the intensity of the reflection peaks. Observed (o), calculated (—), difference (—) and positions of calculated reflections (!)**

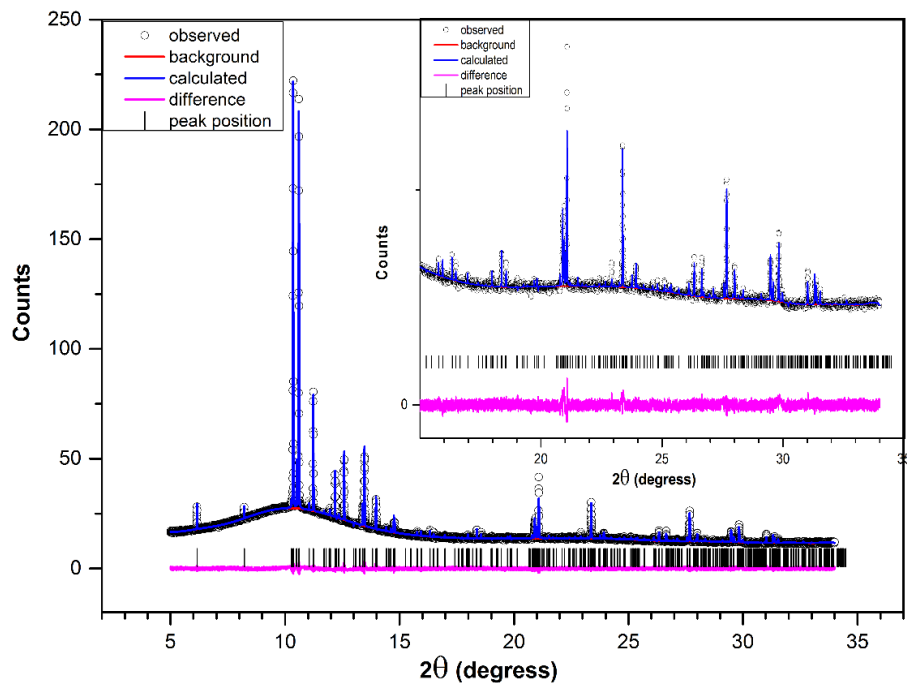


**Figure 7.6: Rietveld refinement of C18 crystalline formed from Kerosene in the range of 5 to 35° 2θ with  $\lambda = 0.825678 \text{ \AA}$  with different scale of amplification according to the intensity of the reflection peaks. Observed (o), calculated (—), difference (—) and positions of calculated reflections (!).**

**Table 7.2 Crystallographic data of C16 crystalline formed from Kerosene obtained from Rietveld refinement using Topas software**

	<b>C16 melt -40 °C</b>	<b>C16 in Kerosene -40 °C</b>
<b>a/Å</b>	4.229	4.228
<b>b/Å</b>	4.773	4.773
<b>c/Å</b>	20.623	20.621
<b>α/°</b>	90.789	90.786
<b>β/°</b>	90.297	90.281
<b>γ/°</b>	106.368	106.389
<b>V/Å<sup>3</sup></b>	399.32	399.23
<b>C-C-C/°</b>	110.4	110.4
<b>C-C/ Å</b>	1.531	1.531
<b>R<sub>wp</sub>/%</b>	10.08	6.26
<b>R<sub>p</sub>/%</b>	6.64	4.32
<b>Gof (χ<sup>2</sup>)</b>	2.16	1.50
<b>Number of reflections</b>	304	304
<b>Number of independent parameters</b>	63	52
<b>2θ range/°</b>	5-34	5-34
<b>D<sub>c</sub>/ g cm<sup>-3</sup></b>	0.94	0.94

**Table 7.3 Crystallographic data of C18 crystalline formed from Kerosene obtained from Rietveld refinement using Topas software**

	<b>C18 melt -40 °C</b>	<b>C18 in Kerosene -40 °C</b>
<b>a/Å</b>	4.224 (4.224)	4.223
<b>b/Å</b>	4.771 (4.771)	4.768
<b>c/Å</b>	23.488 (23.056)	23.490
<b>α/°</b>	78.982 (90.700)	78.979
<b>β/°</b>	84.548 (92.199)	84.535
<b>γ/°</b>	73.600 (106.400)	73.638
<b>V/Å<sup>3</sup></b>	445.26	445.053
<b>C-C-C/°</b>	113.9	112.959
<b>C-C/ Å</b>	1.520	1.533
<b>R<sub>wp</sub>/%</b>	10.46	6.18
<b>R<sub>p</sub>/%</b>	6.79	3.96
<b>Gof (χ<sup>2</sup>)</b>	2.15	1.56
<b>Number of reflections</b>	337	337
<b>Number of independent parameters</b>	63	91
<b>2θ range/°</b>	5-34	5-34
<b>D<sub>c</sub>/ g cm<sup>-3</sup></b>	0.95	0.95

## 7.3 In-situ Dynamic Diffraction from Poly-thermal Crystallisation

### 7.3.1 Pure Octadecane and Hexadecane

An overview of crystallographic diffractions collected from in-situ synchrotron powder X-ray diffraction (SPXD) during continuous cooling from the early stage of solidification to the very low temperature of  $-40^{\circ}\text{C}$  for C18 and C16 in kerosene are presented in **Figures 7.7 and 7.8**, respectively. The phase behaviour is consistent as in melt phase, the unique triclinic structure is observed at all temperatures. Preferred orientation can be clearly seen from high-intensity peaks around  $10$  to  $15^{\circ}$  in  $2\theta$  with high amorphous phase underneath the Bragg peaks. The smaller shoulder peak behaviour as observed from (00L) reflections (5.2.3) of C18 at the onset of crystallisation in melt phase is, however, not detectable from the solution phase.

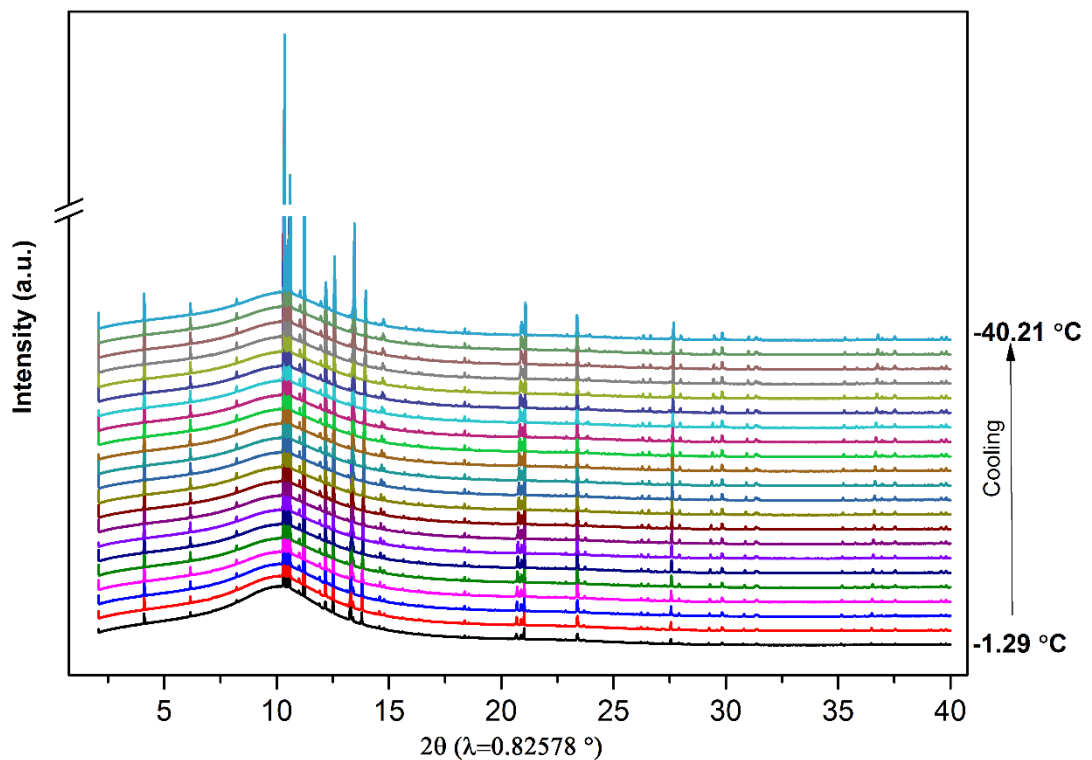


**Figure 7.7: In-situ SPXD patterns for C18/Kerosene collected from the onset of crystallisation at  $-1.29^{\circ}\text{C}$  to a limited low temperature at  $-40.21^{\circ}\text{C}$  at  $2^{\circ}\text{C}$  intervals during cooling at  $1.67^{\circ}\text{C}/\text{min}$ .**

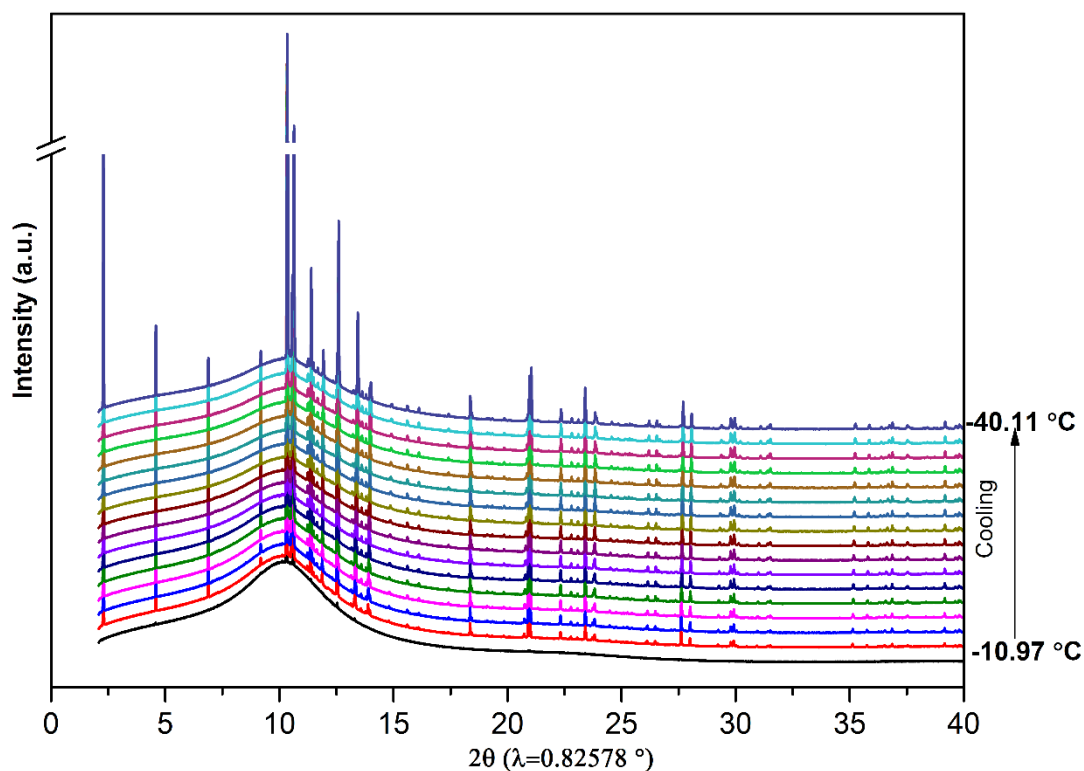


**Figure 7.8: In-situ SPXD patterns for C16/Kerosene collected from the onset of crystallisation at - 10.97 °C to a limited low temperature at - 40.11 °C with 2 °C intervals during cooling at 1.67 °C /min.**

The unit cell parameters of triclinic as a function of temperature are determined from high quality “Pawley fit” analysis indicated by low values of  $R_{wp}$  averaged at  $3.21(\pm 1.43)$  % and  $R_p$  averaged at  $0.53(\pm 0.27)$  % for C18/Kerosene;  $R_{wp}$  averaged at  $2.94(\pm 0.28)$  % and  $R_p$  averaged at  $2.28(\pm 0.25)$  % for C16/Kerosene.

C18/Kerosene shows a less ideal linear thermal expansion trend of unit cell parameters, as seen in **Figures 7.9 and 7.10**, as well as high errors of  $R_{wp}$  and  $R_p$  from the refinement. Particularly, for the beta angle, thermal expanding behaviour shows two regions (- 40 to - 20 °C) and (- 20 to - 1 °C) with positive and negative trends as temperature increased. While the middle temperature in between the two regions at a temperature of - 21 °C is at the breaking point of the two regions showing highly off trend behaviour. The volume thermal expansion coefficient of the triclinic cell of C18 was  $(3.54 \pm 3.10) \times 10^{-4} \text{ } ^\circ\text{C}^{-1}$  over the studied temperature range from - 40.21 to - 1.29 °C.

For C16/Kerosene, the thermal expansion coefficient of the triclinic cell of C16/Kerosene over temperature range - 40.11 °C to - 10.97 °C was calculated

to be  $(4.24 \pm 3.25) \times 10^{-4} \text{ }^\circ\text{C}^{-1}$  in volume. This value is very close to the triclinic cell from C18, whilst the lower value of deviation from C16 indicates the disordering effects are reduced with decreasing chain length. This can also be seen from **Figures 7.11 and 7.12** with a more regular linear trend of thermal expansion from C16 unit cell parameters especially the c-axis direction.

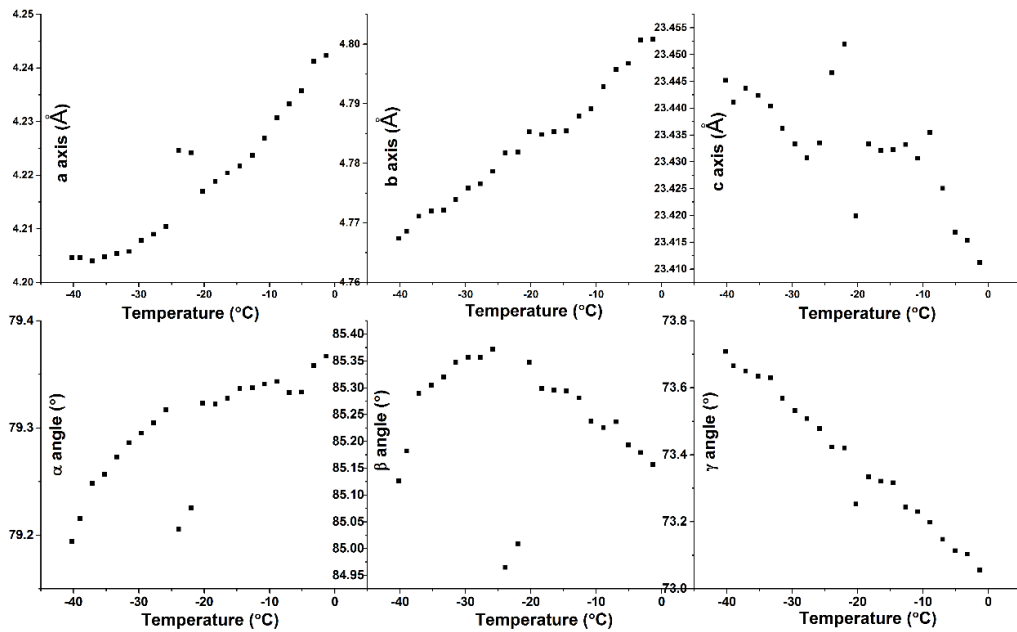


**Figure 7.9: Unit cell parameters (a, b c axis and  $\alpha$ ,  $\beta$ ,  $\gamma$  angels) obtained from “Pawley fit” using Topas software are plotted as a function temperature for C18 in kerosene**

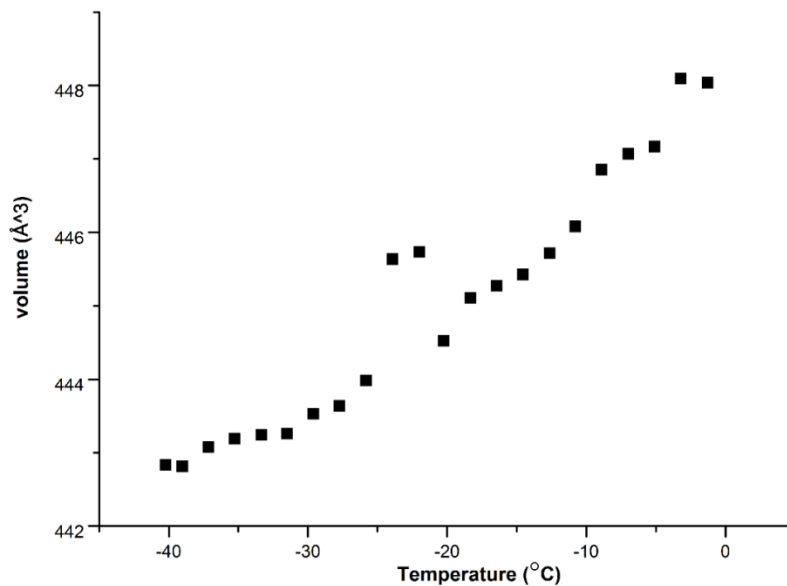


**Figure 7.10: Volume of C18 in kerosene unit cell obtained from “Pawley fit” using Topas software are plotted as a function temperature**

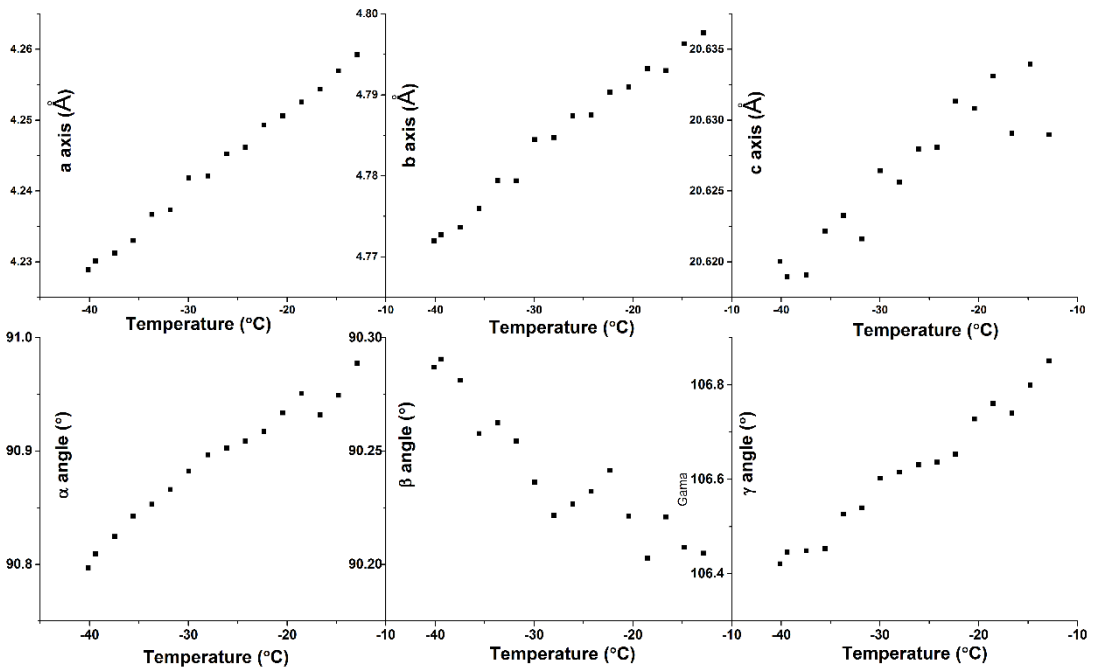


**Figure 7.11: Unit cell parameters (a, b c axis and  $\alpha$ ,  $\beta$ ,  $\gamma$  angles) obtained from “Pawley fit” using Topas software are plotted as a function of temperature for C16 in kerosene**

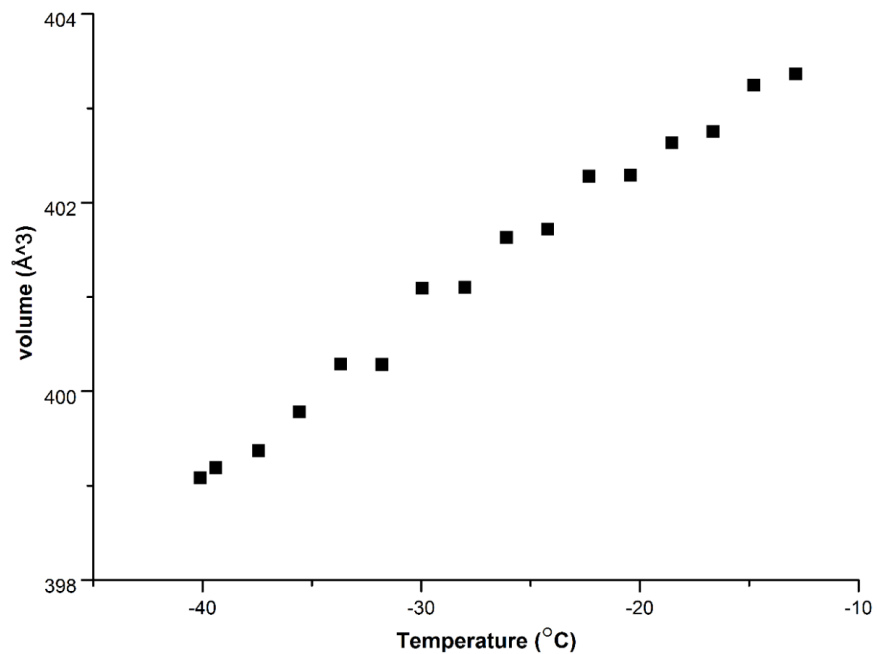


**Figure 7.12: Volume of C16 in kerosene unit cell obtained from “Pawley fit” using TOPAS software are plotted as a function of temperature.**

### 7.3.2 Octadecane and Hexadecane Mixtures

Diffractions were detected at a small temperature interval (2°C) during the in-situ crystallisation process to reveal the phase transition behaviour from liquid to low temperatures. The transitional behaviour of C18/C16 mixtures crystallising from kerosene varied with the composition of C18/C16 and controlled by the presence of an unstable rotator phase (R1) which is observed in the binary system of C18/C16 mixtures.

#### 7.3.2.1 Rotator phase induced crystallisation

##### 7.3.2.1.1 0.1C18/0.9C16/Kerosene

In-situ XRD patterns collected from mixtures of 0.1C18 crystallising from kerosene are shown in **Figure 7.13** from the onset of crystallisation at -14.65°C to -40°C. High amorphous content existed along with the cooling even though at -40°C. The indistinct triclinic phase was observed along the cooling at lower temperatures. However, the high temperature diffractions have shown the differential peak positions at low angles indicating a different phase formation which is enlarged and shown in **Figure 7.14** for the early stage crystallisation from -14.65 to -18.45°C.

The three diffraction peaks at 4.16, 11.33 and 12.69° in  $2\theta$  representing the R<sub>1</sub> phase were first formed at -14.65°C. From -16.55°C, peaks for the T16 phase began to form with simultaneous reduction of intensity of the peaks from the R<sub>1</sub> phase and disappeared at -20.32°C. The T16 was composed entirely of the phase along with further cooling to a terminal temperature at -40°C. From this, we could conclude that the mixture of 0.1 C18 in kerosene crystallised into a T16 solid solution as the terminal phase but early stage nucleation was induced by a rotator phase formation and it was not in a stable state as indicated by the rare number of reflections and short period of existence.

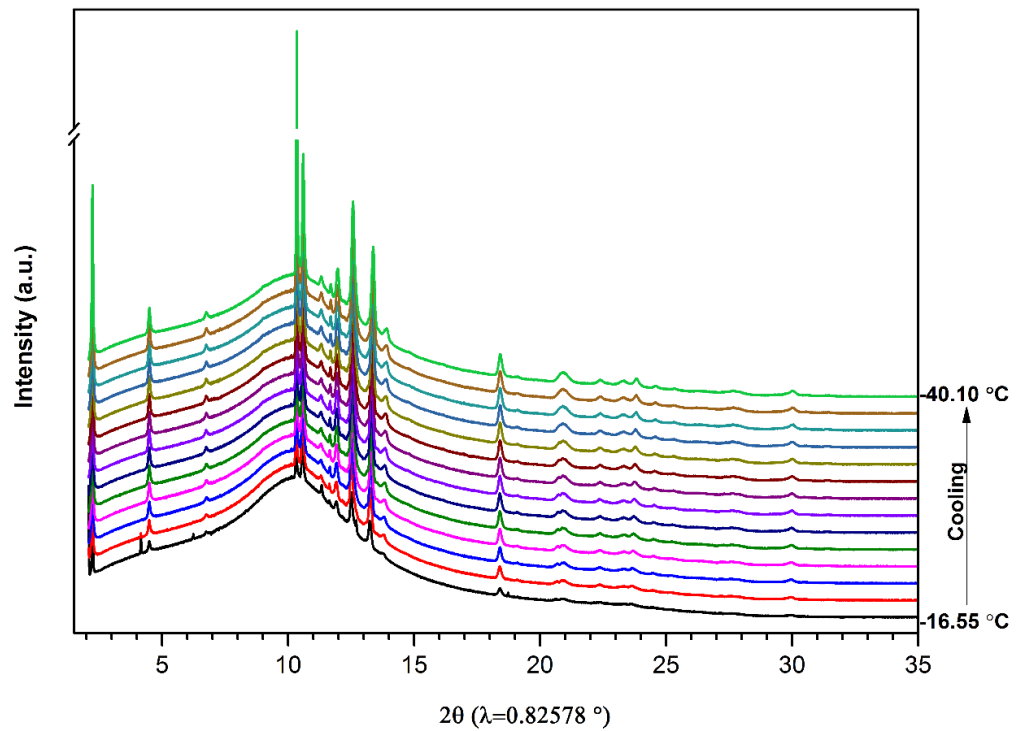


Figure 7.13: In-situ SPXD patterns for 0.1 C18 in kerosene (308 g/l) collected from -16.55 to -40.10 °C at 2 °C intervals during cooling crystallisation at 1.67 °C /min

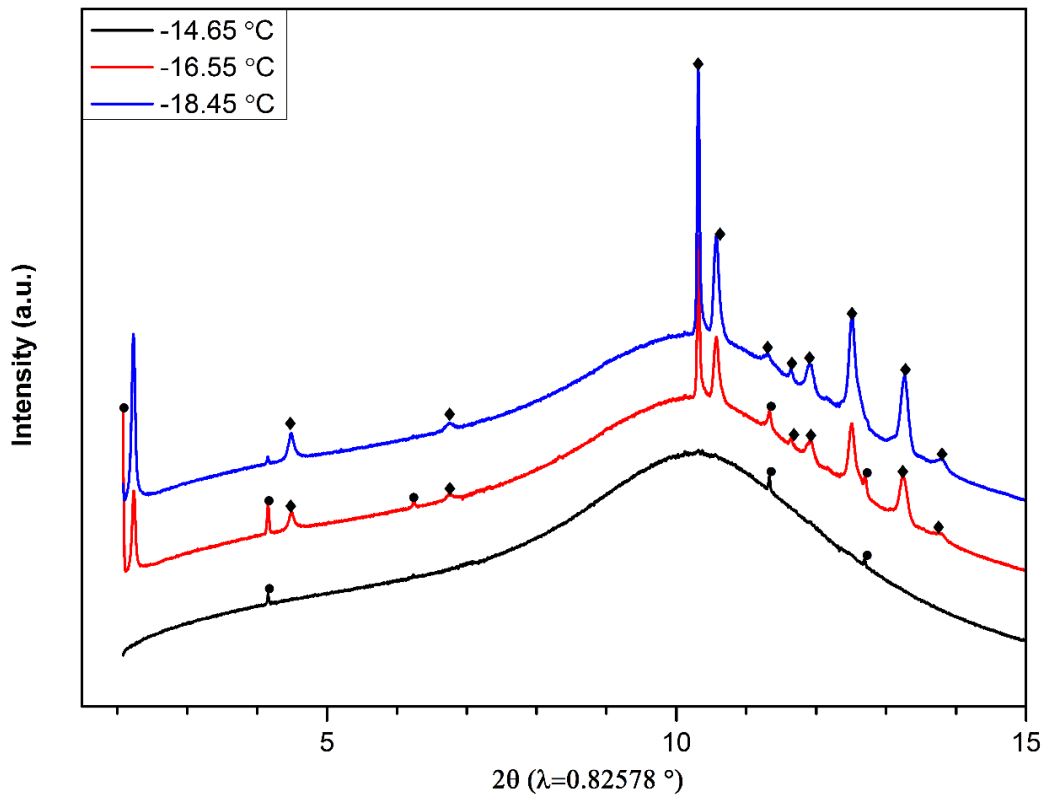
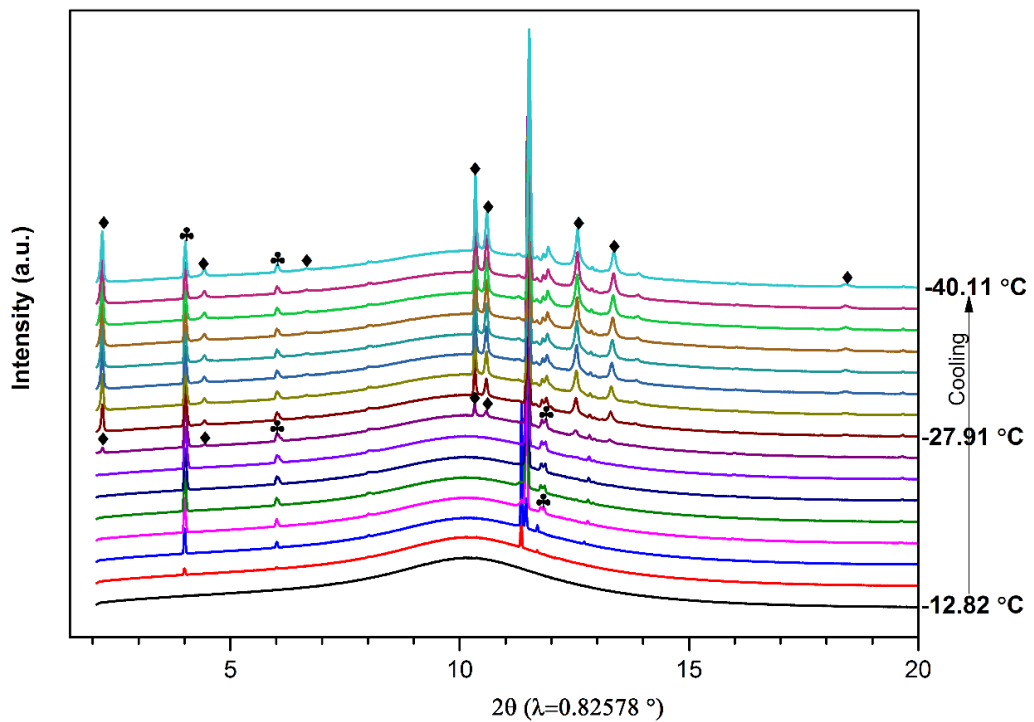


Figure 7.14: Stack plot in  $2\theta$  of 2 to 15° of early stage crystallisation from -14.65 to -18.45 °C showing phase transition with reflection peak position changed from R (•) to T (◆).

### 7.3.2.1.2 0.3 C18/0.7 C16/Kerosene

Multiple phase transitions can be seen from the full data set of in-situ SPXD in **Figure 7.15** for mixtures of 0.3C18 in kerosene from the cooling process (-12.82 to -40°C). The appearance of the triclinic phase at -27.91°C is easy to distinguish from both low angle (00L) peaks and typical reflections (010) and (011) around 10.5° in  $2\theta$ . Early stage crystallisation is enlarged and shown in **Figure 7.16**, the  $R_1$  phase was initially formed at -14.68°C with reflections at 11.3°, 11.7° and 12.6° in two theta. Following the appearance of peaks at 11.4°, 11.8° and 11.9° and 12.8° for a new formed high-symmetry structure of  $M_{dcp}$  (see later) at -18.46°C accompanied with the decreasing intensity of  $R_1$  peaks which had completely disappeared at -20.42°C.



**Figure 7.15: In-situ SPXD patterns for 0.3C18 in kerosene (308 g/l) collected from -12.82°C to -40.11°C with 2°C intervals during cooling crystallisation at 1.67°C/min. Symbol of ♣ represents for  $M_{dcp}$  structure; ♦: Triclinic structure.**

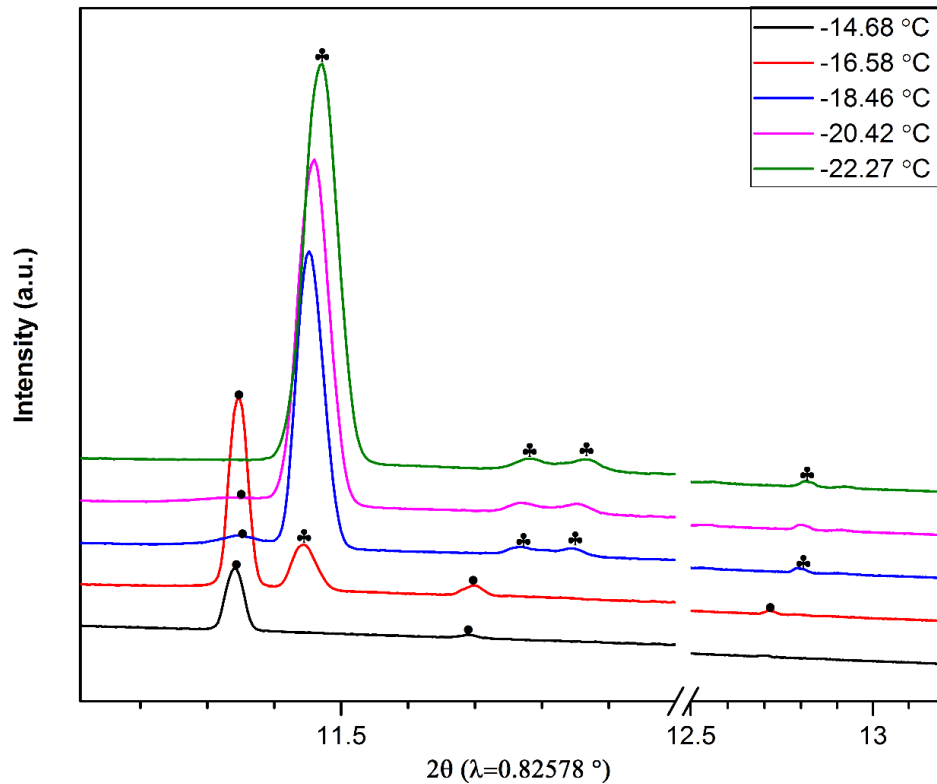


**Figure 7.16: Stack plot in  $2\theta$  (11 to 15°) of 0.3C18 in kerosene early stage crystallisation from - 14.68 to - 22.42°C showing phase transition with reflection peak position changed from  $R_1$  (•) to  $M_{dcp}$  (♣).**

The high symmetrical structure formed is deduced to be either in  $M_{dcp}$  ( $A_a$ ,  $Z=4$ ) or  $O_p$  ( $P_{ca21}$ ,  $Z=4$ ) according to the isothermal X-ray diffraction at the low temperature - 40°C in section 7.2.1. Hence, the experimental data of this phase observed at - 20.42°C was refined with both structures of  $M_{dcp}$  and  $O_p$ , as shown in **Figure 7.17**. The  $M_{dcp}$  phase is more likely to be the right structure as indicated by the enlarged reflections at approximately 12° in  $2\theta$  showing a double peak was consistent with the experimental observation, which is only one for the  $O_p$  calculated pattern.

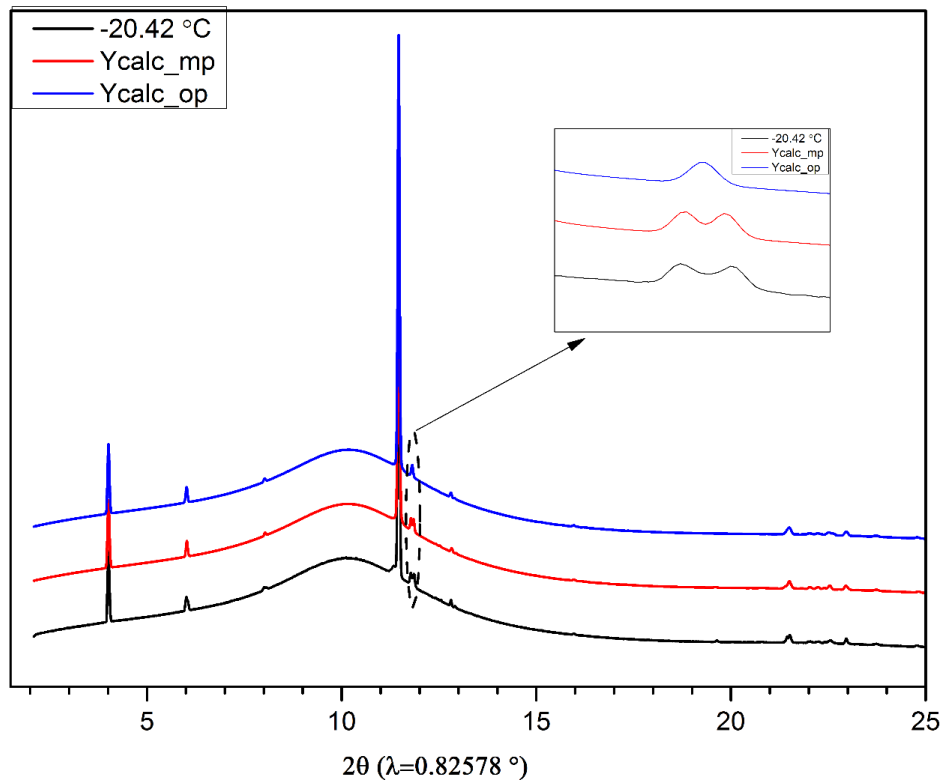


**Figure 7.17: A comparison of “Pawley fit” of  $M_{dcp}$  and  $O_p$  lattice parameters to simulate XRD pattern of 0.3C18 in kerosene at -20.42°C. Scaled peaks have shown the main difference.**

### 7.3.2.1.3 0.4C18/0.6C16/Kerosene

The full dataset for mixture sample 0.4 C18 in kerosene during the cooling process from the onset point of crystallisation of -12.8 to -40°C is presented in **Figure 7.18**. Similarly to 0.3C18 in kerosene, high-symmetry structure was initially crystallised (-12.88°C) in the HT region followed by formation of the triclinic phase (-29.9°C) and terminated with the mixture phases in the LT region (-40°C). Peculiar peaks are also seen at low angles around 5° in  $2\theta$  which are highlighted in the amplified scale figure. Therefore, another phase (X2) apart from the high-symmetry structure (X1) was formed with slightly smaller c-axis length at -22.28°C.

Inspection in early stage crystallisation is shown in **Figure 7.19**, the  $R_1$  phase can also be seen with reflections of 11.3, and 12.6° in  $2\theta$  at -12.88°C. The appearance of peaks at 11.4, 11.8 and 12.8° were the three main peaks for the high symmetry phase (X1) at -14.74°C accompanied with removal of two peaks for  $R_1$ .

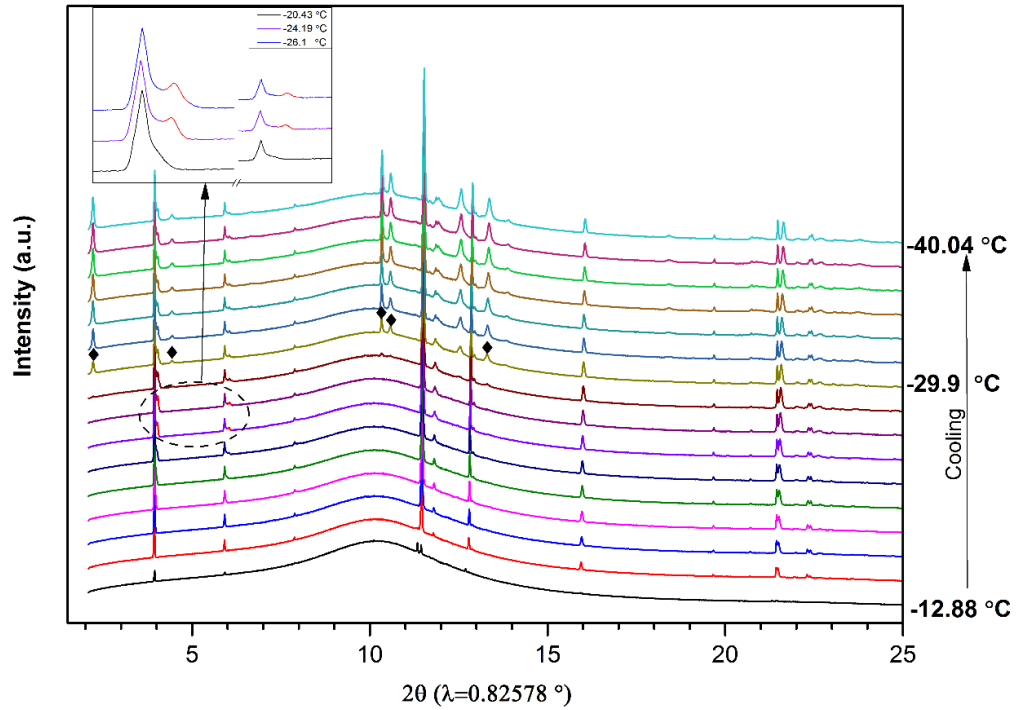


Figure 7.18: In-situ SPXD patterns for 0.4C18 in kerosene (308 g/l) collected from - 12.88 to - 40.04°C with 2°C intervals during cooling crystallisation at 1.67°C/min. Scaled insert figure shows the appearance of the (X2) phase at - 24.19°C. Symbol ♦ represents the triclinic structure.

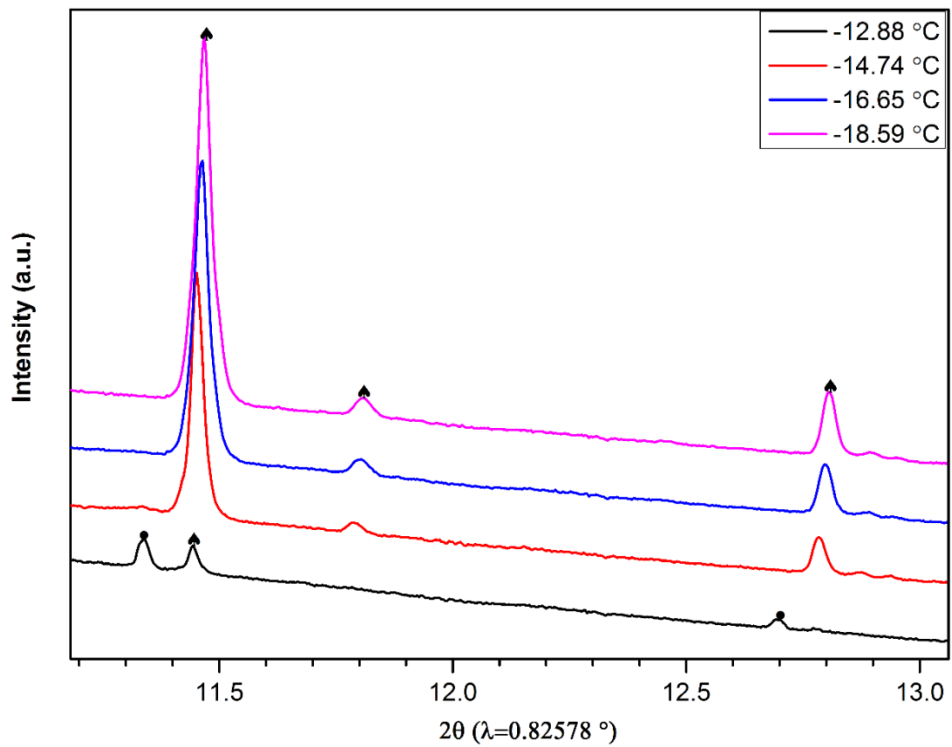
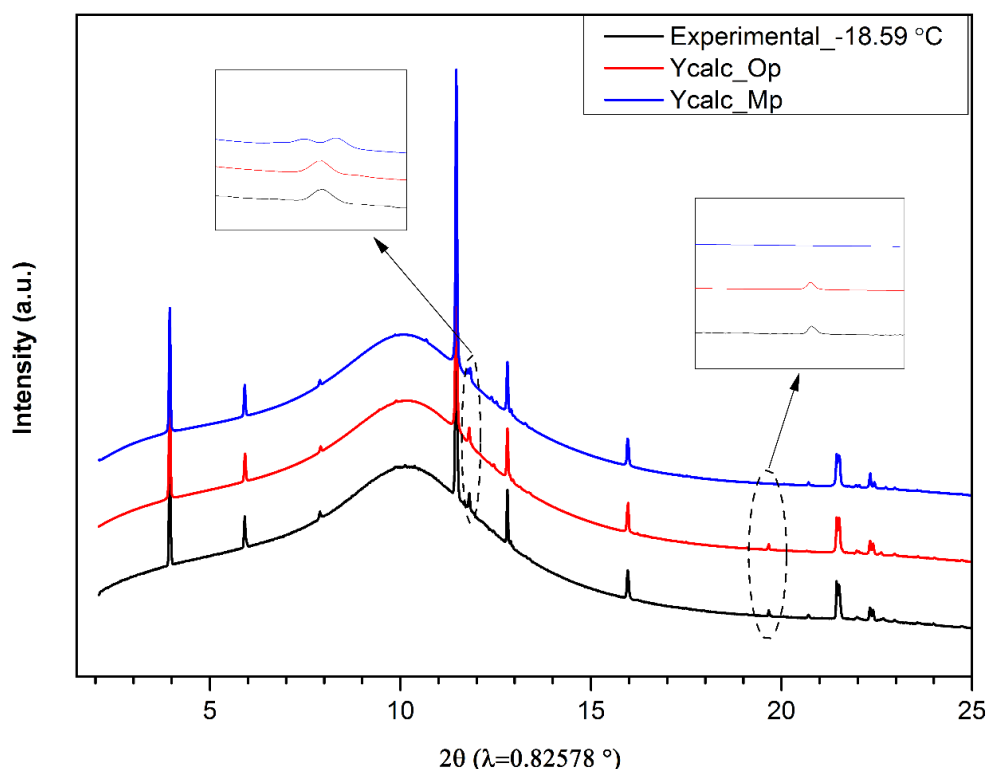


Figure 7.19: Stack plot in  $2\theta$  (11 to 13°) of 0.4 C18 in kerosene at early stage crystallisation from - 12.88 to - 18.59°C showing the phase transition with reflection peak position changed from  $R_1$  (♦) to  $O_p$  (♥).

The most possible structures of  $M_{dcp}$  and  $O_p$  were both employed to fit the X1 phase observed from 0.4C18 in kerosene at  $-18.59^\circ\text{C}$ , presented in **Figure 7.20**. As seen from the enlarged figure, the two phases are quite close and both fit the experimental data, while the  $M_{dcp}$  simulation, having two peaks and no reflection with respect to 12 and 20 in  $2\theta$ , which are different in comparison with the experimental pattern. This illustrates the structure of  $O_p$  was crystallised out as an X1 phase.



**Figure 7.20:** A comparison of “Pawley fit” of  $M_{dcp}$  and  $O_p$  lattice parameters to simulate XRD pattern of 0.4C18 in kerosene at  $-20.42^\circ\text{C}$  at the early stage of crystallisation. Scaled peaks have shown the main difference.

#### 7.3.2.1.4 0.5C18/0.5C16/kerosene

**Figure 7.21** provides the full data set of in-situ diffractions for 0.5C18 in kerosene during cooling from the onset point of  $-10.82^\circ\text{C}$  to  $-40.11^\circ\text{C}$ . Similarly to 0.3C18 and 0.4C18 in kerosene, high-symmetry structure crystallised in the HT region followed by the triclinic phase ( $-31.64^\circ\text{C}$ ) to be a mixture dominant in the LT region.

Inspection of early stage crystallisation is given in **Figure 7.22**, the phase formation of R<sub>1</sub> peaks was first observed around 11.5, and 12.6° in 2θ at -10.83°C. Consistent with the observation in 0.4C18/Kerosene, reflections of 11.4, 11.8 and 12.8° also can be seen for 0.5C18 from kerosene crystallisation which was referred to as the X1 phase. It needs to be noted that the existence of this R<sub>1</sub> phase was even more unstable with limited intensity and reflection peaks, see **Figure 7.22**.

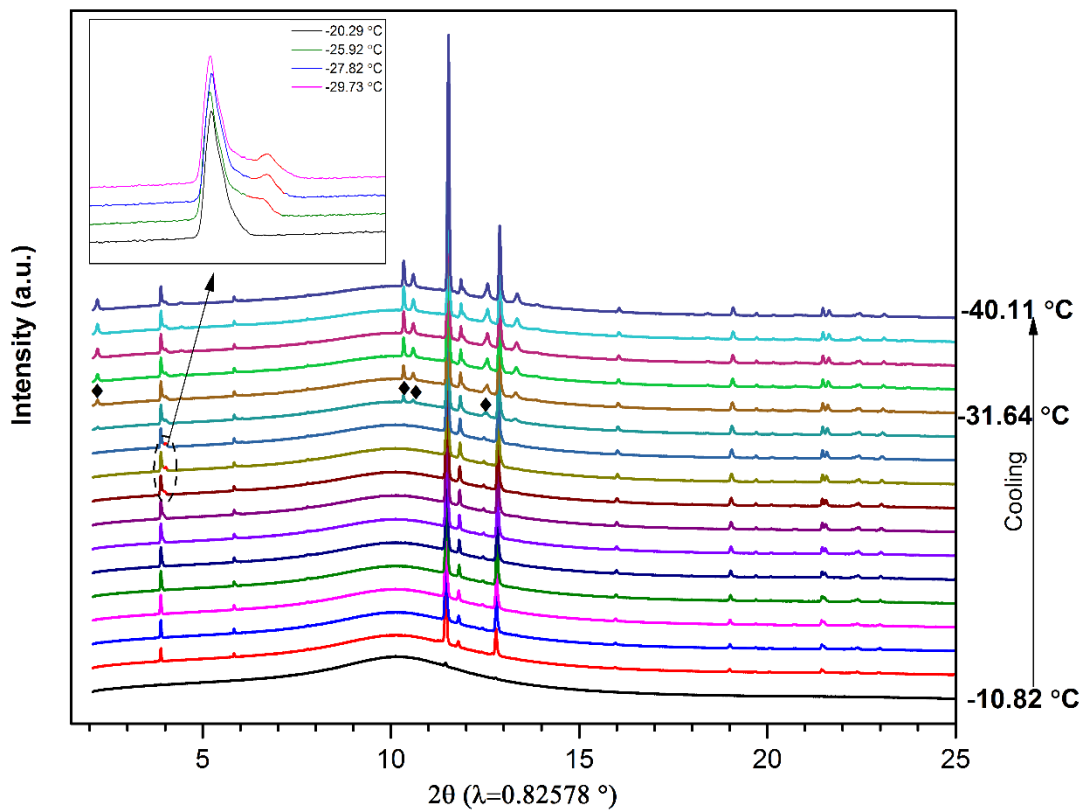


**Figure 7.21: In-situ SPXD patterns for 0.5C18 in kerosene (308 g/l) collected from -10.80 to -40.11°C with 2°C intervals during cooling crystallisation at 1.67°C/min. Scaled inserted figure shows the appearance of the (X2) phase at -25.92°C. The symbol ◆ represents the triclinic structure.**

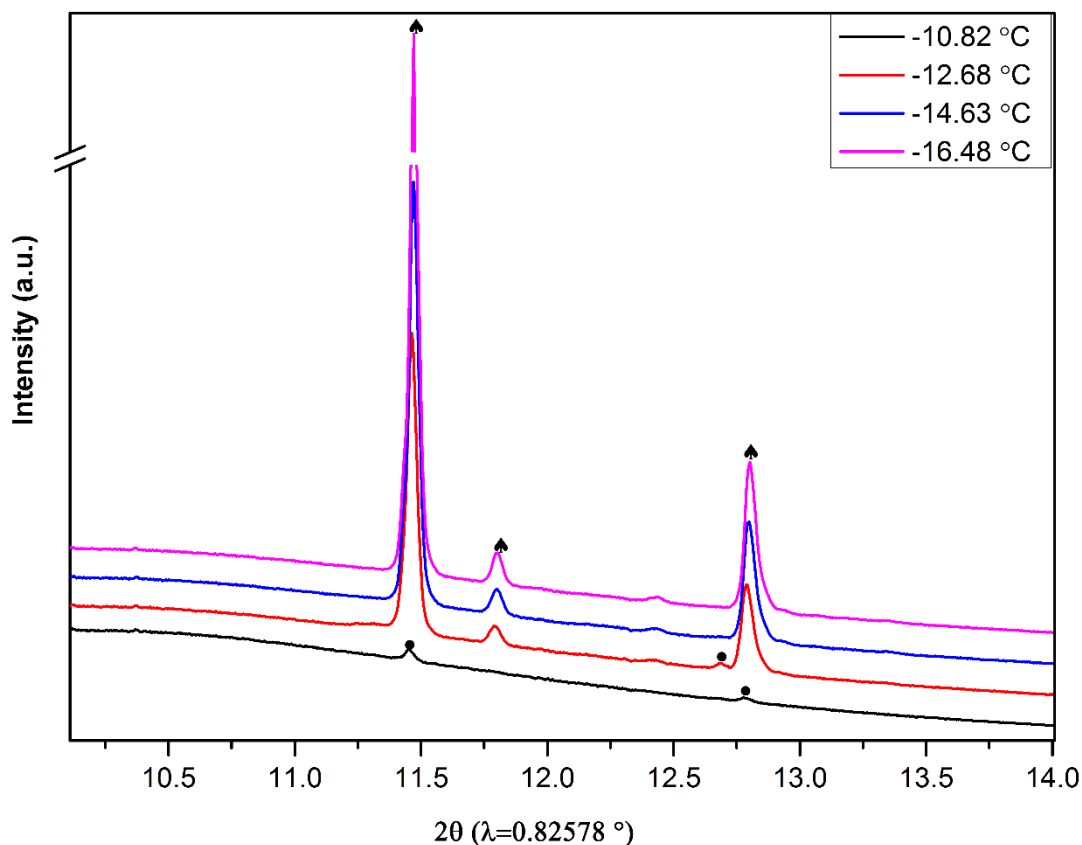


**Figure 7.22: Stack plot in  $2\theta$  (10 to 14°) of 0.5C18 in kerosene at early stage crystallisation from - 10.82 to - 16.48°C showing phase transition with reflection peak position changed from  $R_1$  (•) to  $O_p$  (♥).**

The diffraction pattern referred to the X1 phase of 0.5 C18/Kerosene was refined to the unit cell of  $M_{dcp}$  and  $O_p$  as shown in **Figure 7.23**. From the comparisons of these two similar structures is unlikely to elucidate the difference. However, the  $O_p$  structure is more likely to be the X1 phase as indicated by the lower  $R_{wp}$  fitting value from “Pawley fit”, as presented in **Table 7.4** together with the X1 phase simulation for XRD patterns of 0.3C18 and 0.4C18 in kerosene solution at the early stage of crystallisation.

Together with the comparison of fitting simulations in **Figures 7.17, 7.20 and 7.23** for samples of 0.3C18, 0.4C18 and 0.5C18 in kerosene solution and resultant fitting parameters of  $R_{wp}$  and  $R_p$  values in **Table 7.4**. It can be interpreted with 0.3C18/Kerosene crystallised with the  $M_{dcp}$  phase at - 20.42°C while 0.4C18 and 0.5C18 from kerosene were crystallised with  $O_p$  at - 18.59°C and - 16.48°C respectively.

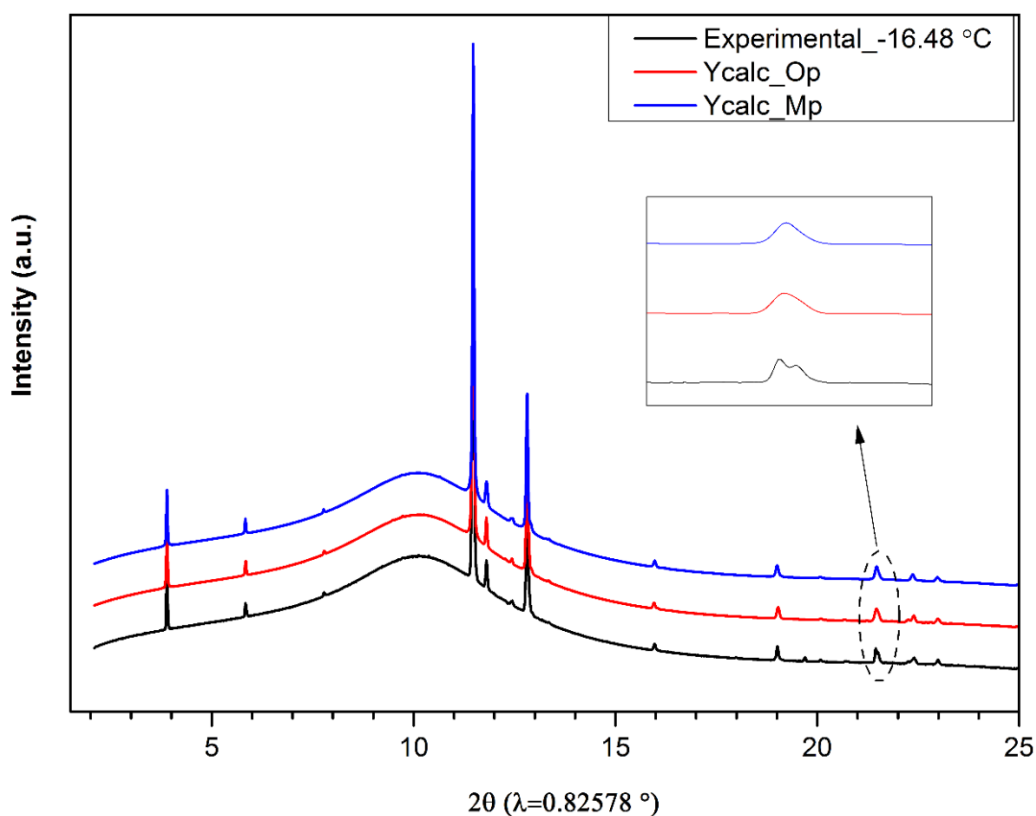


**Figure 7.23: The comparison of “Pawley fit” of  $M_{dcp}$  and  $O_p$  lattice parameters to simulate XRD pattern of 0.5C18 in kerosene at -16.48°C at the early stage of crystallisation. Scaled peaks have shown the main difference.**

**Table 7.4 Comparison results (lattice parameters and  $R_{wp}$ ,  $R_p$  values ) between  $M_{dcp}$  and  $O_p$  as applied to fit X1 phase by “Pawley fit” for three samples at the early stage of crystallisation of composition 0.3C18, 0.4C18 and 0.5 C18 in kerosene solution (308 g/l).**

Sample	$T$ °C	Phase	$a/\text{Å}$	$b/\text{Å}$	$c/\text{Å}$	$\alpha/^\circ$	$\beta/^\circ$	$\gamma/^\circ$	$R_{wp}\%$	$R_p\%$
0.3C18	-20.42	$M_p$	7.394	5.014	47.156	90	91.162	90	0.94	0.47
		$O_p$	7.412	5.018	47.292	90	90	90	1.17	0.54
0.4C18	-18.59	$M_p$	7.421	5.010	48.211	90	91.427	90	1.18	0.71
		$op$	7.401	5.006	47.884	90	90	90	0.77	0.43
0.5C18	-16.48	$M_p$	7.411	5.005	48.804	90	90.499	90	1.27	0.57
		$O_p$	7.429	4.996	48.678	90	90	90	0.93	0.45

### 7.3.2.2 No rotator phase induced crystallisation

Homogeneously mixed liquid of 0.7C18 and 0.9C18 mixtures were found to be crystallised into a solid solution with T18 structure without rotator phase involvement or any phase transition, as shown by the observed in-situ XRD patterns collected (-5.18 to -40°C) and (-1.38 to -40°C) in **Figure 7.24** and **Figure 7.25**, respectively.

It can be concluded when longer chain C18 is dominant in the mixture it will lead the crystallisation into the inherent T18 phase. In this case, the formed solid solution is in the same structure and space group from the original C18, and the shorter chain C16 possibly acts as an inclusive small molecule inside of C18.

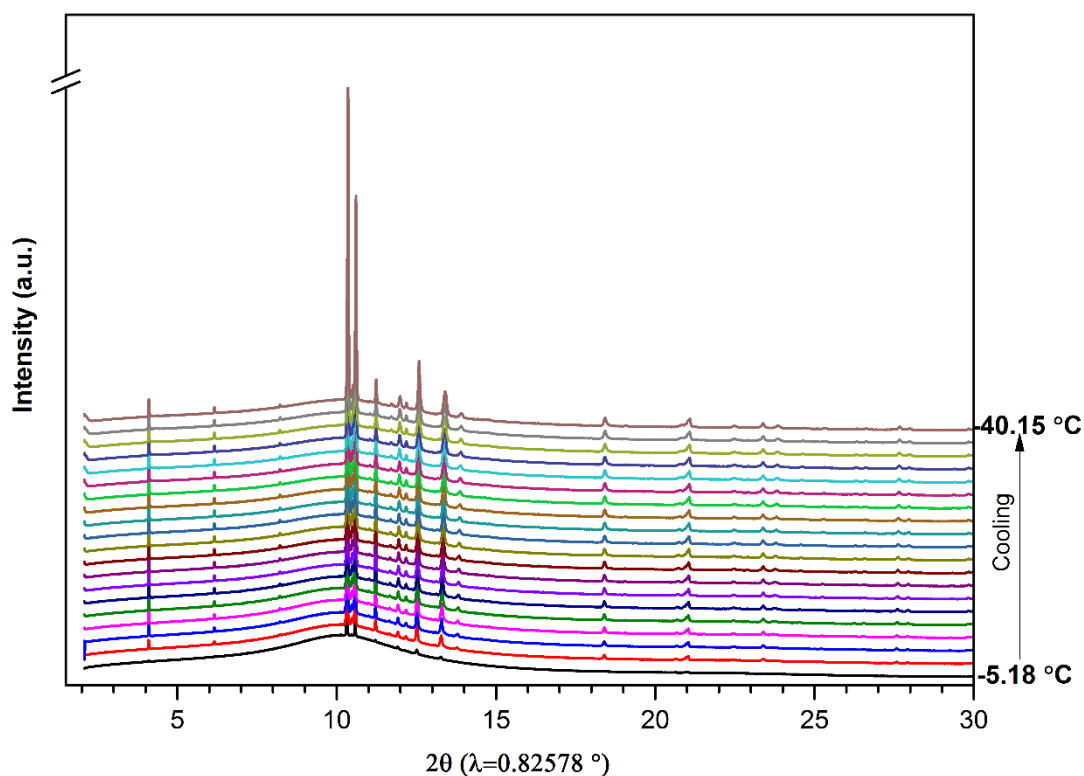


**Figure 7.24: In-situ SPXD patterns for pure 0.7C18 in kerosene collected from - 5.18°C to - 40.15°C with 2°C intervals during cooling crystallisation at 1.67°C /min.**

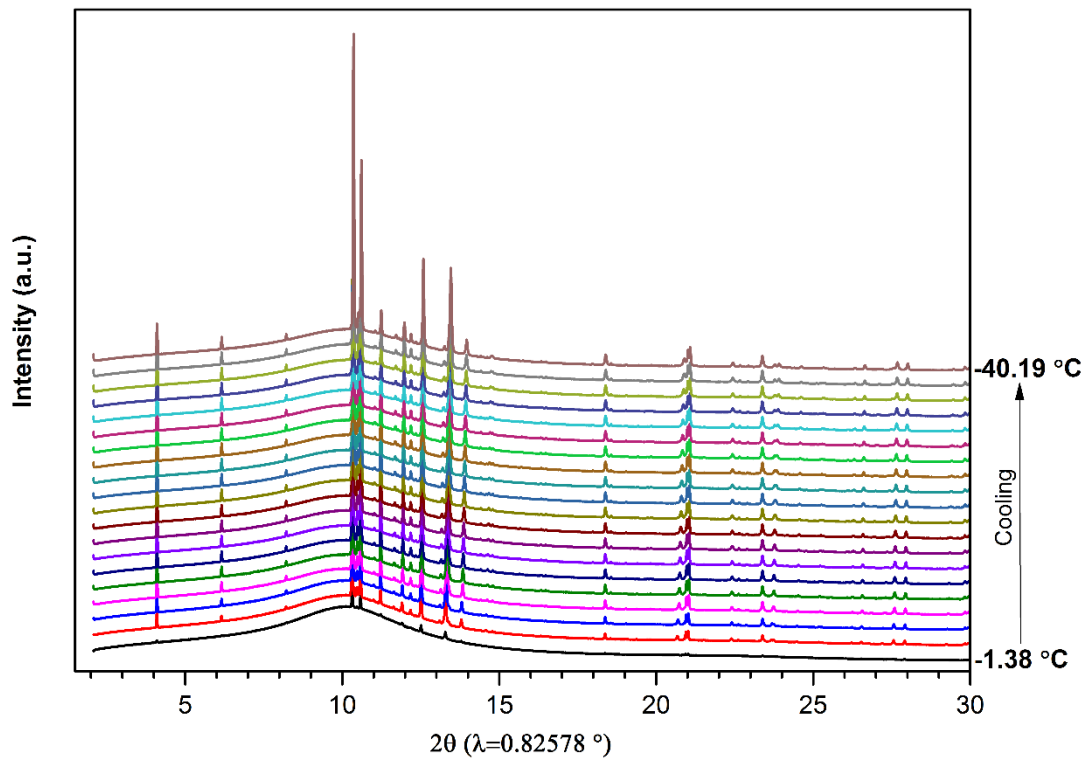


**Figure 7.25: In-situ SPXD patterns for pure 0.9C18 in kerosene solution collected from - 1.38 °C to - 40.19 °C with 2 °C intervals during cooling crystallisation at 1.67 °C/min.**

#### **7.4 Ternary Phase Diagram of C18/C16/Kerosene (308 g/l)**

Structural evolution of C18/C16 mixtures in kerosene solution (308g/l) as a function of composition and temperature is shown in **Figure 7.26** using in-situ high resolution PXRD during crystallisation at a slow cooling rate of 1.67 °C/min. Previous studies of binary homologue alkane mixtures in a light solvent (ternary system) determined a consistent behaviour of solid solution R<sub>1</sub> the same as the achievement from the respective melt phase (binary system) [72, 73]. However, with the help of the in-situ synchrotron PXRD with a small scanning interval of 2 °C, the observed R<sub>1</sub> phase in solution situation was not a stable phase with only a short period and small number of reflections in comparison with the high stability that existed in a large temperature and composition range in binary melt mixtures.

The R<sub>1</sub> phase in solution crystallisation is actually replaced by the intermediate ordered crystalline of O<sub>p</sub> or M<sub>dcp</sub>. This can be confirmed by no observation of

the large  $a/b$  change with temperature increasing which is the typical character of the  $R_1$  phase. Moreover, the  $R_1$  phase observed from the melt phase mixture of 0.3C18 in 5.3.2.1, the high-intensity peaks are (111) and (020) while the highest peaks are (111) and (200) for the ordered structures of  $O_p$  or  $M_{dcp}$  in the solution case. More importantly, the high disordering phase of  $R_1$  with the less long-range order in terms of atom positions with less high angle reflections, i.e. (200) and (131) while the fully ordered crystalline of  $O_p$  has more reflections.

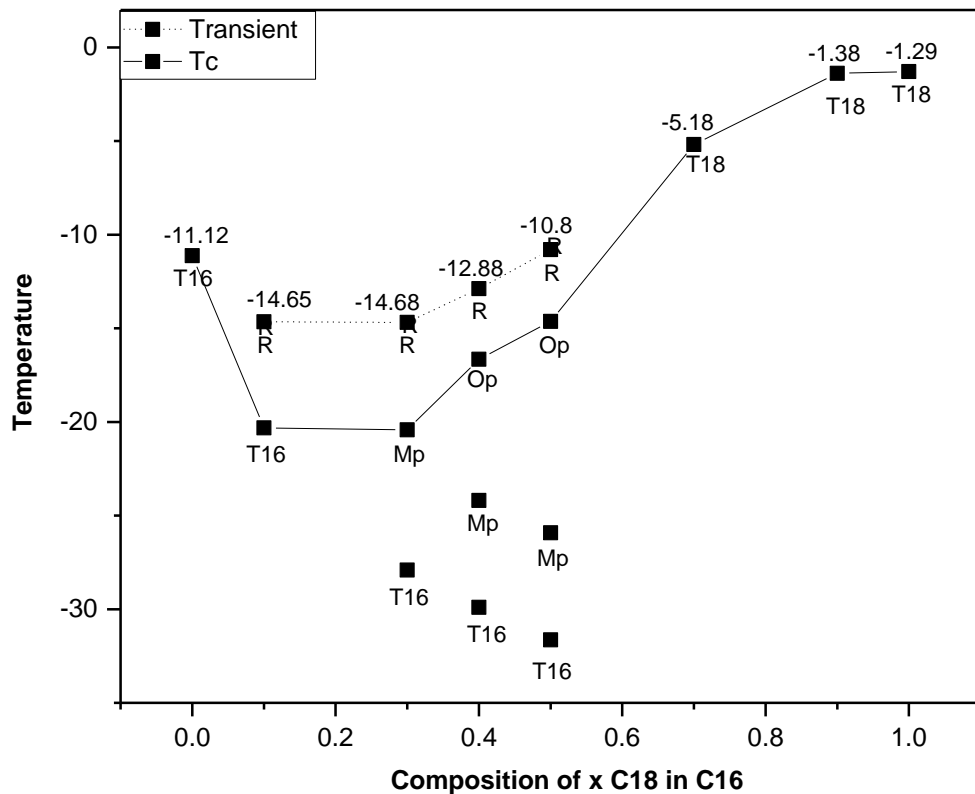


**Figure 7.26: The structural revolution of C18 and C16 mixtures in kerosene solution (308 g/l) as a function of composition and temperature. Solid lines represent the phase boundary of first ordered crystalline, the boundary for the disordered R phase presented with a dashed line.**

## 7.5 Conclusions

High resolution diffraction patterns collected with the MAC detector have revealed a variety of structural behaviour of mixed samples of C18/C16 as a function of composition at a low temperature of - 40°C. Samples having compositions (C16,0.1C18, 0.7C18 0.9C18 and C18) close to pure component of C18 or C16 at both sides formed solid solution types in triclinic structure with respect to the chain length of the dominant homologue. 0.3C18, 0.4C18 and 0.5C18 are multiple phases with the inherent triclinic structure and two high symmetry structures which are indicated as  $M_{dcp}$  and  $O_p$  which were found in melt phase mixtures.

The structure of C18 or C16 crystallising from kerosene solution was refined with the respective melt phase triclinic structure. Consistent with the melt phase observation, no polymorphic transition was observed in the solution crystallisation of C18 or C16 by in-situ cooling from liquid to - 40°C. However, thermal expansion of the molecular volume of the triclinic cell in a solution of these two components has shown some disordering from the non-ideal linear trend and large deviation.

The mixed samples with compositions ( $x=0.1, 0.3, 0.4, 0.5C18$ ) having the multiple phases are found to be induced by a rotator phase at the onset of crystallisation and further replaced by the ordered crystalline structures at lower temperatures. Moreover, the stability of this rotator phase is reduced, as increasing the composition of the longer chain C18 to 0.4C18 and 0.5C18 which is possibly not observable during the dissolution process. Eventually, it is not present in the crystallisation of 0.7C18 and 0.9C18 as the longer chain C18 with triclinic structure is in dominant control.

Conclusively, the rotator induced crystallisation observed in melt phase alkanes is also observable in solution crystallisation. However, it only existed for the mixtures with the longer chain compositions smaller than the equimolar which is inclusive. The metastability of this induced rotator phase also depends on the mixture compositions which is reduced as increasing the composition of longer chain homologue.

**Chapter 8**  
**Solubility of Octadecane and Hexadecane**  
**Mixtures as a Function of Solution**  
**Environment**

*This chapter presents the poly-thermal data from crystallisation of C18/C16 mixtures in three representative solvents of n-dodecane, kerosene and toluene.*

*Saturation temperatures are assessed as a function of C18/C16 mixture composition in three representative fuel solvents. Solution solubility, ideality and associated dissolution enthalpies are analysed using Vant' Hoff plots.*

## 8.1 Introduction

Solubility assessment is always the first step to study and monitor a crystallisation process, especially for industrial applications. For C18/C16 mixtures as the main components of HVO biofuels, the solubility has not been reported previously and is assessed in this study with three representative fuel solvents, i.e. dodecane, kerosene and toluene.

Initially, equilibrium saturation temperatures ( $T_e$ ) and metastable zone widths (MSZW) are presented with respect to the composition of C18/C16 mixtures and the nature of the solvent. This is followed by activity coefficients, enthalpies ( $\Delta H_{diss}$ ) and entropies ( $\Delta S_{diss}$ ) of dissolution are calculated to access the solubility dependence on chain length, molecular structure and solvent interactions of the mixture components of C18/C16. In addition, the poly-thermal results will be utilised in further assessment of crystallisation kinetics in Chapter 9.

## 8.2 Results Using the Poly-thermal Method

Temperatures of crystallisation ( $T_c$ ) and dissolution ( $T_{diss}$ ) as measured with four concentrations and four cooling/heating rates ( $q$ ) obtained from poly-thermal experiments of C18/C16 mixtures in 11 compositions are given in **Tables 8.1, 8.2 and 8.3** with respect to the three solvents of n-dodecane, kerosene and toluene. An example of these results at a concentration of 300g/l in toluene is displayed in **Figure 8.1**.

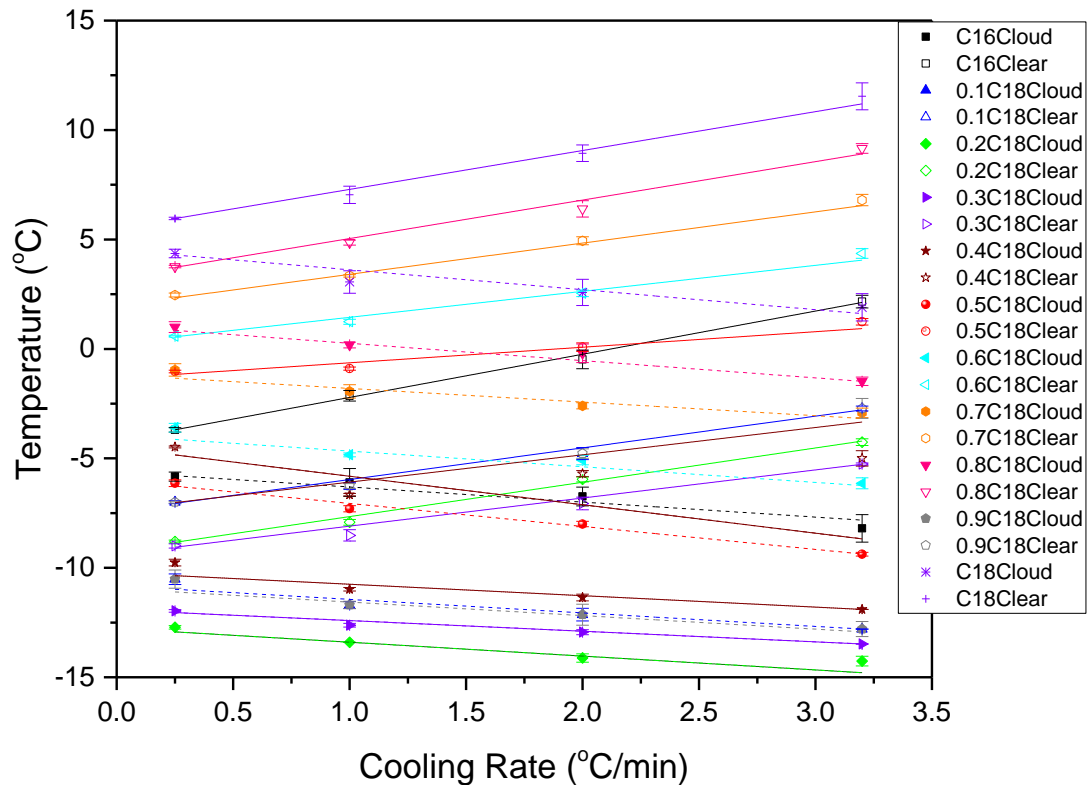


**Figure 8.1: Crystallisation ( $T_c$ ) and dissolution ( $T_{diss}$ ) temperatures as a function of heating/cooling rate ( $q$ ) for C18/C16 mixtures (eleven compositions varied in 10% molar concentration of C18) in toluene at a concentration of 300 g/l. Error bars are presented with standard deviation from five recycles of repeats**

**Table 8.1 Average temperatures of crystallisation  $T_c$  and dissolution  $T_{diss}$  as a function of cooling rate and binary mixture composition of C18/C16 in n-dodecane solution at concentrations of 192, 231, 269, 308 g/l. STD: standard deviation of the measured  $T_c$  and  $T_{diss}$  from 5 recycles of repeats.**

x C18 / q(°C/mi n)	$T_c$	STD	$T_{diss}$	STD	$T_c$ (°C)	STD	$T_{diss}$	STD	$T_c$ (°C)	STD	$T_{diss}$	STD	$T_c$ (°C)	STD	$T_{diss}$	STD
	(°C)	(°C)	(°C)	(°C)												
	<u>C16:C18 (100:0)</u>				<u>C16:C18 (90:10)</u>				<u>C16:C18 (80:20)</u>				<u>C16:C18 (70:30)</u>			
	192 g/l				192 g/l				192 g/l				192 g/l			
0.25	-8.88	0.51	-3.7	0.07	-13.26	0.09	-7.02	0.08	-12.74	0.05	-7.7	0	-11.93	0.04	-7.68	0.09
1	-10.44	0.41	-0.2	0.21	-14.5	0.07	-3.38	0.13	-14.08	0.04	-4.78	0.19	-12.58	0.08	-3.58	0.19
2	-11.48	0.61	3.36	0.4	-14.72	0.08	2.38	0.19	-14.8	0	-1.18	0.04	-13.42	0.08	-0.14	0.36
3.2	-12.68	0.25	8.2	0.25	-14.88	0.04	6.36	0.32	-14.78	0.04	4.12	0.16	-14.06	0.09	3.22	0.5
	231 g/l				231 g/l				231 g/l				231 g/l			
0.25	-6.26	0.67	-1.72	0.04	-11.12	0.11	-4.68	0.08	-10.44	0.05	-7.2	0	-9.63	0.04	-7.3	0.04
1	-7.16	0.25	1.04	0.13	-12.46	0.05	-1.46	0.09	-11.68	0.04	-4.46	0.21	-10.48	0.11	-3.42	0.08
2	-8.02	0.2	4.32	0.24	-12.98	0.08	3.78	0.19	-12.56	0.05	-0.66	0.15	-11.18	0.04	0.38	0.18
3.2	-9.08	0.26	9.54	0.59	-13.64	0.11	7.12	0.45	-12.82	0.11	4.72	0.24	-12.2	0	3.96	0.54
	269 g/l				269 g/l				269 g/l				269 g/l			
0.25	-3.94	0.44	-0.18	0.04	-9.42	0.08	-2.84	0.05	-8.86	0.05	-6.04	0.05	-7.8	0.07	-6.08	0.04
1	-4.64	0.62	2.44	0.48	-10.34	0.09	-0.24	0.05	-10.16	0.05	-3.56	0.13	-8.54	0.05	-3.72	0.08
2	-6.18	0.33	7.28	0.18	-10.48	0.18	4.46	0.09	-11.16	0.09	0.54	0.25	-9.2	0.07	0.2	0.07
3.2	-6.92	0.37	10.6	0.58	-11.98	0.04	9.42	0.2	-11.14	0.13	4.96	0.13	-10.3	0.21	3.04	0.57
	308 g/l				308 g/l				308 g/l				308 g/l			
0.25	-2.74	0.56	1.04	0.05	-8.3	0.07	-1.48	0.08	-7.24	0.05	-4.48	0.2	-6.54	0.05	-5.22	0.08
1	-3.54	0.47	3.02	0.11	-9.12	0.04	0.36	0.09	-8.54	0.05	-3.12	0.11	-7.4	0.1	-3.38	0.08
2	-5.02	0.22	8.08	0.08	-9.52	0.08	4.94	0.09	-9.48	0.11	0.98	0.18	-7.9	0.07	-0.62	0.13
3.2	-6.12	0.54	11.42	0.36	-10.54	0.13	10.04	0.09	-9.76	0.15	5.3	0.26	-9.3	0	2.38	0.22
	<u>C16:C18 (60:40)</u>				<u>C16:C18 (50:50)</u>				<u>C16:C18 (40:60)</u>				<u>C16:C18 (30:70)</u>			

	192 g/l				192 g/l				192 g/l				192 g/l			
0.25	-10.34	0.13	-3.62	0.04	-6.46	0.32	-0.6	0.07	-3.14	0.13	1.28	0.04	-0.58	0.39	3.1	0
1	-11.56	0.05	-2.88	0.13	-7.64	0.18	0.72	0.11	-4.22	0.19	2.34	0.05	-1.72	0.78	3.7	0.1
2	-12.44	0.13	0.22	0.08	-8.88	0.39	2.5	0.2	-5.12	0.15	6.44	0.22	-2.1	0.14	7.18	0.11
3.2	-13.18	0.13	4.58	0.27	-10.54	0.09	7.06	0.25	-7.18	0.04	12.04	0.18	-3.96	0.36	11.38	0.29
	231 g/l				231 g/l				231 g/l				231 g/l			
0.25	-8.38	0.08	-1.8	0	-4.82	0.13	1.24	0.05	-1.66	0.23	2.9	0	0.6	0.27	4.8	0.07
1	-9.42	0.11	-2.06	0.05	-5.76	0.26	2.22	0.15	-2.56	0.09	3.58	0.04	0.06	0.55	5.54	0.09
2	-10.2	0.07	0.34	0.11	-7.34	0.18	4.98	0.18	-3.7	0.14	6.04	0.09	-0.58	0.08	8.42	0.29
3.2	-10.32	0.22	3.64	0.15	-8.14	0.11	8.56	0.23	-4.46	0.17	10.02	0.27	-1.86	0.54	12.84	0.49
	269 g/l				269 g/l				269 g/l				269 g/l			
0.25	-6.64	0.09	-0.6	0.07	-3.48	0.39	2.72	0.04	-0.1	0.16	4.5	0	2.68	0.28	6.2	0
1	-7.6	0	-1.1	0.12	-4.38	0.11	3.34	0.09	-1.1	0.1	5.16	0.09	1.7	0.31	6.7	0.07
2	-8	0	0.3	0.07	-5.76	0.17	6.02	0.08	-2.5	0.12	7.96	0.23	0.76	0.11	9.38	0.11
3.2	-8.88	0.04	4.72	0.2	-6.48	0.19	8.88	0.2	-3.22	0.19	12.2	0.39	-0.06	0.15	12.68	0.36
	308 g/l				308 g/l				308 g/l				308 g/l			
0.25	-5.24	0.05	0.34	0.05	-2.42	0.26	3.76	0.05	1.08	0.08	5.62	0.04	3.76	0.11	7.48	0.04
1	-6.2	0	-0.42	0.08	-3.52	0.08	4.6	0.1	-0.06	0.15	6.18	0.04	2.42	0.4	8.42	0.04
2	-7.12	0.11	0.58	0.04	-4.5	0.14	6.74	0.05	-0.96	0.09	7.62	0.22	1.88	0.04	10.4	0.28
3.2	-7.32	0.16	3.1	0.19	-5.06	0.09	9.26	0.25	-2.52	0.2	13.02	0.11	1.02	0.22	13.7	0.21
	<u>C16:C18 (20:80)</u>				<u>C16:C18 (10:90)</u>				<u>C16:C18 (0:100)</u>							
	192 g/l				192 g/l				192 g/l							
0.25	2	0.1	4.28	0.04	3.66	0.11	5.54	0.05	4.56	0.35	6.8	0				
1	1.12	0.08	5.18	0.13	2.94	0.29	6.8	0.1	3.16	0.55	7.8	0				
2	-0.32	0.27	8.4	0.12	2.28	0.18	9.7	0.14	1.88	0.26	11.9	0.24				
3.2	-1.22	0.18	13.38	0.18	0.82	0.38	14.08	0.37	1.38	0.52	14.86	0.28				
	231 g/l				231 g/l				231 g/l							
0.25	3.86	0.05	6.08	0.04	4.9	0.26	7.24	0.05	6.6	0.29	8.42	0.04				

1	2.94	0.09	7.16	0.09	4.7	0.16	8.42	0.04	5.16	0.51	9.68	0.11
2	1.88	0.16	9.72	0.16	4.04	0.17	10.64	0.26	4.2	0.2	12.46	0.27
3.2	1.02	0.18	13.66	0.76	3.18	0.26	14.62	0.25	3.38	0.54	16.02	0.49
	269 g/l				269 g/l				269 g/l			
0.25	5.36	0.09	7.54	0.05	6.84	0.11	8.7	0	8.1	0.23	10	0.07
1	4.38	0.04	8.64	0.13	5.78	0.2	10.08	0.04	6.66	0.21	11.18	0.15
2	3	0.35	10.2	0.22	4.94	0.09	11.74	0.26	5.54	0.29	13.68	0.16
3.2	2.5	0.16	15.64	0.26	4.6	0.14	16.28	0.23	5.42	0.31	17.1	0.34
	308 g/l				308 g/l				308 g/l			
0.25	6.42	0.04	8.72	0.04	7.74	0.36	10.04	0.05	9.5	0.1	11.16	0.05
1	5.46	0.09	9.78	0.18	6.3	0.42	11.44	0.11	8.3	0.3	12.46	0.24
2	4.4	0	11.24	0.11	5.66	0.13	14.08	0.22	7.3	0.46	14.98	0.15
3.2	3.96	0.15	15.16	0.35	5.3	0.24	16.94	0.33	6.64	0.36	18.68	0.28

**Table 8.2 Average temperatures of crystallisation  $T_c$  and dissolution  $T_{diss}$  as a function of cooling rate and binary mixture composition of C18/C16 in kerosene solution at concentrations of 231, 269, 308, 350 g/l. STD: standard deviation of the measured  $T_c$  and  $T_{diss}$  from 5 recycles of repeats.**

x C18 / q(°C/mi n)	$T_c$	STD	$T_{diss}$	STD												
	(°C)	(°C)	(°C)	(°C)												
	C16:C18 (100:0)				C16:C18 (90:10)				C16:C18 (80:20)				C16:C18 (70:30)			
	231 g/l				231 g/l				231 g/l				231 g/l			
0.25	-5.98	0.26	-2.68	0.04	-11.62	0.31	-5.78	0.04	-12.70	0.07	-8.14	0.05	-11.40	0.10	-9.06	0.11
1	-6.54	0.42	-1.46	0.05	-12.14	0.18	-5.34	0.05	-13.18	0.04	-7.32	0.04	-12.16	0.05	-8.72	0.04
2	-6.78	0.40	0.52	0.08	-13.24	0.18	-4.00	0.14	-13.82	0.04	-6.02	0.08	-12.98	0.22	-7.62	0.08
3.2	-8.46	0.49	3.26	0.37	-14.46	0.05	-2.56	0.34	-14.52	0.04	-4.58	0.18	-14.34	0.05	-7.00	0.24
	269 g/l				269 g/l				269 g/l				269 g/l			
0.25	-4.74	0.29	-1.22	0.04	-9.76	0.34	-4.00	0.14	-10.64	0.05	-5.98	0.04	-9.44	0.05	-7.40	0.07
1	-4.46	0.56	0.04	0.05	-10.66	0.15	-3.64	0.05	-11.24	0.05	-5.52	0.13	-10.24	0.09	-6.76	0.11

2	-5.16	0.66	2.12	0.26	-11.44	0.22	-2.22	0.30	-11.86	0.15	-4.18	0.13	-11.02	0.11	-5.62	0.04
3.2	-6.14	0.25	4.68	0.04	-12.50	0.00	-0.52	0.37	-13.04	0.13	-2.72	0.04	-12.24	0.22	-4.52	0.11
	308 g/l				308 g/l				308 g/l				308 g/l			
0.25	-2.82	0.30	0.12	0.04	-8.42	0.26	-2.78	0.04	-9.10	0.00	-4.52	0.04	-7.88	0.04	-5.70	0.00
1	-3.52	0.35	1.68	0.11	-9.24	0.05	-2.06	0.05	-9.58	0.04	-4.02	0.04	-8.68	0.08	-5.02	0.04
2	-4.54	0.63	3.70	0.12	-10.06	0.13	-0.66	0.09	-10.34	0.11	-2.64	0.11	-9.28	0.15	-3.50	0.12
3.2	-4.98	0.29	6.60	0.14	-12.50	0.00	1.42	0.20	-11.10	0.19	-1.44	0.17	-10.20	0.00	-2.10	0.17
	350 g/l				350 g/l				350 g/l				350 g/l			
0.25	-1.92	0.43	1.16	0.05	-7.06	0.24	-1.68	0.04	-7.82	0.04	-3.56	0.05	-6.46	0.05	-4.54	0.05
1	-2.18	0.60	2.66	0.15	-8.12	0.04	-0.92	0.04	-8.52	0.13	-3.06	0.09	-7.46	0.05	-3.92	0.08
2	-3.20	0.47	5.36	0.09	-8.90	0.07	0.78	0.16	-9.14	0.05	-1.52	0.13	-8.10	0.14	-1.98	0.18
3.2	-3.38	0.29	7.24	0.26	-9.88	0.04	2.54	0.26	-10.02	0.16	0.24	0.09	-9.12	0.04	0.02	0.19
	<u>C16:C18 (60:40)</u>				<u>C16:C18 (50:50)</u>				<u>C16:C18 (40:60)</u>				<u>C16:C18 (30:70)</u>			
	231 g/l				231 g/l				231 g/l				231 g/l			
0.25	-9.62	0.04	-3.80	0.00	-5.94	0.18	-0.56	0.09	-3.30	0.29	1.60	0.00	-0.96	0.24	3.18	0.04
1	-10.38	0.04	-4.60	0.12	-7.24	0.15	-0.18	0.08	-4.22	0.29	2.20	0.10	-1.88	0.23	3.96	0.09
2	-11.48	0.08	-5.00	0.10	-8.22	0.04	0.84	0.09	-5.42	0.20	3.40	0.10	-2.60	0.27	5.04	0.05
3.2	-12.38	0.16	-4.76	0.26	-9.46	0.09	2.14	0.09	-6.60	0.23	5.00	0.14	-3.94	0.22	7.20	0.31
	269 g/l				269 g/l				269 g/l				269 g/l			
0.25	-7.76	0.11	-2.80	0.10	-4.56	0.13	0.90	0.00	-1.82	0.28	3.14	0.05	0.46	0.09	4.54	0.09
1	-8.52	0.08	-5.06	0.11	-5.66	0.13	1.36	0.05	-2.40	0.10	3.76	0.09	-0.44	0.17	5.42	0.04
2	-9.62	0.04	-4.10	0.19	-6.68	0.13	2.52	0.13	-3.54	0.18	4.92	0.11	-1.50	0.20	6.58	0.13
3.2	-10.48	0.08	-2.48	0.68	-7.70	0.12	3.78	0.11	-4.54	0.15	6.48	0.29	-2.46	0.25	8.72	0.29
	308 g/l				308 g/l				308 g/l				308 g/l			
0.25	-6.28	0.08	-1.64	0.31	-3.58	0.16	2.10	0.00	-0.74	0.35	4.28	0.04	1.90	0.31	5.92	0.04
1	-7.20	0.07	-2.38	0.16	-4.92	0.18	2.66	0.15	-1.50	0.25	4.88	0.04	1.28	0.18	6.84	0.13
2	-7.90	0.07	-3.02	0.15	-5.54	0.09	3.66	0.18	-2.50	0.30	6.24	0.11	0.44	0.23	8.16	0.11
3.2	-8.90	0.00	-1.28	0.13	-6.64	0.05	5.08	0.04	-3.46	0.09	8.44	0.15	-0.70	0.32	10.48	0.36
	350 g/l				350 g/l				350 g/l				350 g/l			

0.25	-4.90	0.07	-0.28	0.04	-2.56	0.11	3.34	0.05	0.44	0.21	5.38	0.04	3.36	0.11	7.10	0.00
1	-5.90	0.00	-1.04	0.09	-3.90	0.14	3.94	0.09	-0.68	0.08	6.20	0.00	2.20	0.25	8.14	0.09
2	-6.60	0.00	-0.30	0.10	-4.76	0.11	5.16	0.09	-1.56	0.23	7.60	0.12	1.20	0.25	9.76	0.17
3.2	-7.36	0.22	0.52	0.24	-5.66	0.13	6.68	0.08	-2.38	0.16	9.02	0.16	0.28	0.11	11.70	0.14
<b>C16:C18 (20:80)</b>																
<u>C16:C18 (20:80)</u>				<u>C16:C18 (10:90)</u>				<u>C16:C18 (0:100)</u>								
231 g/l				231 g/l				231 g/l								
0.25	1.02	0.63	4.64	0.05	3.22	0.26	6.00	0.00	4.94	0.30	7.42	0.04				
1	0.50	0.35	5.68	0.08	2.78	0.11	7.30	0.12	4.18	0.27	8.68	0.04				
2	0.00	0.41	6.98	0.16	2.00	0.37	8.64	0.29	3.20	0.24	10.52	0.13				
3.2	-1.18	0.22	9.50	0.31	0.70	0.35	10.96	0.42	2.46	0.43	13.00	0.32				
269 g/l				269 g/l				269 g/l								
0.25	3.26	0.09	6.20	0.00	5.26	0.15	7.54	0.05	6.30	0.46	8.88	0.04				
1	2.30	0.23	7.32	0.04	4.46	0.18	8.96	0.09	5.70	0.40	10.42	0.11				
2	1.44	0.30	8.90	0.12	3.38	0.13	11.28	0.08	5.04	0.42	12.38	0.22				
3.2	0.24	0.38	11.50	0.30	2.48	0.22	12.84	0.33	4.24	0.47	14.64	0.15				
308 g/l				308 g/l				308 g/l								
0.25	4.14	0.28	7.48	0.04	6.30	0.20	8.70	0.00	7.78	0.19	10.10	0.07				
1	3.64	0.23	8.70	0.00	5.80	0.21	10.32	0.13	7.10	0.52	11.56	0.09				
2	2.74	0.32	10.16	0.18	4.56	0.27	12.36	0.18	6.24	0.30	13.70	0.33				
3.2	2.32	0.04	12.92	0.22	3.20	0.32	14.54	0.18	5.56	0.25	16.46	0.13				
350 g/l				350 g/l				350 g/l								
0.25	5.40	0.44	8.68	0.04	7.60	0.31	9.92	0.04	9.20	0.28	11.36	0.05				
1	4.82	0.08	10.02	0.04	6.90	0.14	11.60	0.00	8.38	0.16	12.80	0.12				
2	3.68	0.40	11.56	0.17	6.16	0.15	13.10	0.07	7.26	0.75	15.46	0.13				
3.2	2.84	0.48	14.18	0.25	5.38	0.16	15.46	0.26	6.98	0.16	18.18	0.16				

**Table 8.3 Average temperatures of crystallisation  $T_c$  and dissolution  $T_{diss}$  as a function of cooling rate and binary mixture composition of C18/C16 in toluene solution at concentrations of 300, 350, 400, 350 g/l. STD: standard deviation of the measured  $T_c$  and  $T_{diss}$  from 5 recycles of repeats.**

x C18 / q(°C/mi n)	$T_c$ (°C)	STD (°C)	$T_{diss}$ (°C)	STD (°C)	$T_c$ (°C)	STD (°C)	$T_{diss}$ (°C)	STD (°C)	$T_c$ (°C)	STD (°C)	$T_{diss}$ (°C)	STD (°C)	$T_c$ (°C)	STD (°C)	$T_{diss}$ (°C)	STD (°C)
	<u>C16:C18 (100:0)</u>				<u>C16:C18 (90:10)</u>				<u>C16:C18 (80:20)</u>				<u>C16:C18 (70:30)</u>			
	300 g/l				300 g/l				300 g/l				300 g/l			
0.25	-5.83	0.21	-3.70	0.10	-10.52	0.24	-7.00	0.07	-12.72	0.08	-8.80	0.07	-11.97	0.06	-9.00	0.10
1	-6.10	0.64	-2.14	0.24	-11.70	0.16	-6.26	0.15	-13.40	0.00	-7.92	0.13	-12.62	0.08	-8.52	0.26
2	-6.74	0.43	-0.48	0.43	-12.14	0.29	-4.78	0.28	-14.12	0.19	-5.96	0.11	-12.94	0.11	-7.06	0.29
3.2	-8.20	0.63	2.16	0.29	-12.80	0.00	-2.72	0.11	-14.26	0.22	-4.26	0.15	-13.48	0.00	-5.26	0.05
	350 g/l				350 g/l				350 g/l				350 g/l			
0.25	-4.24	0.26	-2.30	0.00	-9.30	0.08	-5.74	0.05	-11.18	0.04	-7.46	0.05	-10.70	0.07	-7.88	0.04
1	-4.42	0.33	-0.80	0.10	-10.60	0.23	-4.80	0.19	-12.02	0.08	-6.20	0.00	-11.00	0.19	-6.94	0.05
2	-4.96	0.15	1.38	0.50	-11.02	0.16	-2.90	0.34	-12.20	0.12	-4.70	0.16	-11.48	0.13	-5.40	0.19
3.2	-6.02	0.34	3.34	0.38	-11.46	0.11	-0.34	0.22	-13.10	0.14	-2.44	0.23	-12.48	0.18	-3.52	0.04
	400 g/l				400 g/l				400 g/l				400 g/l			
0.25	-3.74	0.43	-1.62	0.26	-8.60	0.07	-4.46	0.05	-10.04	0.11	-6.46	0.05	-9.34	0.17	-6.90	0.07
1	-3.56	0.30	0.14	0.05	-9.66	0.13	-3.70	0.19	-10.70	0.10	-5.26	0.09	-10.36	0.21	-5.80	0.16
2	-4.14	0.11	1.82	0.53	-10.42	0.23	-1.74	0.34	-11.18	0.15	-3.36	0.17	-10.68	0.16	-3.96	0.05
3.2	-4.74	0.13	4.40	0.74	-10.66	0.05	0.58	0.22	-11.70	0.07	-1.28	0.16	-11.24	0.40	-2.44	0.22
	450 g/l				450 g/l				450 g/l				450 g/l			
0.25	-2.32	0.36	-0.46	0.05	-7.43	0.22	-3.62	0.08	-9.32	0.13	-5.54	0.15	-8.22	0.04	-6.08	0.04
1	-2.98	0.36	1.16	0.09	-9.02	0.41	-2.68	0.04	-10.10	0.07	-4.32	0.04	-9.12	0.08	-4.88	0.08
2	-3.06	0.18	2.82	0.08	-9.56	0.24	-1.00	0.14	-10.54	0.15	-2.50	0.07	-9.68	0.25	-2.56	0.13
3.2	-3.98	0.11	6.00	0.31	-10.16	0.26	2.12	0.43	-11.70	0.07	-0.28	0.16	-10.62	0.18	-0.88	0.23
	<u>C16:C18 (60:40)</u>				<u>C16:C18 (50:50)</u>				<u>C16:C18 (40:60)</u>				<u>C16:C18 (30:70)</u>			
	300 g/l				300 g/l				300 g/l				300 g/l			
0.25	-9.76	0.15	-4.48	0.04	-6.13	0.15	-1.03	0.06	-3.60	0.20	0.58	0.04	-0.96	0.29	2.46	0.09

1	-10.98	0.08	-6.66	0.05	-7.30	0.14	-0.90	0.07	-4.84	0.09	1.24	0.11	-1.94	0.30	3.34	0.05
2	-11.36	0.15	-5.70	0.14	-8.00	0.12	0.08	0.19	-5.08	0.22	2.54	0.15	-2.60	0.14	4.94	0.18
3.2	-11.90	0.00	-5.00	0.35	-9.38	0.08	1.24	0.15	-6.14	0.25	4.36	0.22	-2.92	0.22	6.80	0.26
	350 g/l				350 g/l				350 g/l				350 g/l			
0.25	-8.52	0.04	-3.36	0.05	-4.86	0.05	0.00	0.00	-2.46	0.29	1.86	0.05	0.25	0.10	3.42	0.11
1	-9.40	0.10	-4.46	0.09	-6.08	0.13	0.24	0.05	-3.44	0.09	2.36	0.05	-1.04	0.15	4.54	0.05
2	-9.80	0.07	-3.64	0.05	-6.92	0.04	1.42	0.13	-4.08	0.22	4.00	0.10	-1.66	0.15	5.90	0.10
3.2	-10.72	0.13	-1.74	0.17	-8.06	0.05	2.64	0.17	-4.82	0.30	5.54	0.21	-2.40	0.12	7.80	0.12
	400 g/l				400 g/l				400 g/l				400 g/l			
0.25	-7.52	0.08	-2.20	0.00	-4.18	0.13	0.90	0.00	-1.32	0.16	2.78	0.08	0.90	0.20	4.40	0.00
1	-8.34	0.05	-2.78	0.13	-5.24	0.15	1.34	0.05	-2.24	0.15	3.56	0.05	0.04	0.05	5.44	0.05
2	-8.90	0.09	-2.08	0.00	-5.72	0.13	2.36	0.09	-3.22	0.13	4.90	0.07	-0.62	0.22	7.34	0.21
3.2	-9.70	0.16	-0.92	0.22	-6.96	0.05	3.74	0.13	-4.12	0.16	6.82	0.34	-1.72	0.29	9.02	0.16
	450 g/l				450 g/l				450 g/l				450 g/l			
0.25	-6.82	0.10	-1.44	0.09	-3.32	0.15	1.64	0.05	-0.74	0.11	3.44	0.05	2.18	0.11	5.22	0.08
1	-7.64	0.05	-1.92	0.11	-4.86	0.05	2.22	0.11	-1.64	0.09	4.22	0.11	0.86	0.11	6.40	0.00
2	-8.22	0.19	-0.58	0.23	-5.60	0.19	3.32	0.04	-2.48	0.28	5.78	0.15	-0.28	0.11	8.38	0.18
3.2	-9.46	0.21	1.68	0.25	-6.48	0.16	4.84	0.13	-4.00	0.00	8.54	0.22	-0.98	0.16	10.2 0	0.00
	<u>C16:C18 (20:80)</u>				<u>C16:C18 (10:90)</u>				<u>C16:C18 (0:100)</u>							
	300 g/l				300 g/l				300 g/l							
0.25	1.00	0.24	3.76	0.05	2.54	0.42	4.88	0.04	4.36	0.19	5.96					
1	0.18	0.13	4.86	0.11	1.93	0.17	6.08	0.11	3.06	0.51	7.04					
2	-0.20	0.42	6.40	0.37	0.73	0.48	8.14	0.22	2.58	0.60	8.94					
3.2	-1.48	0.19	9.16	0.22	0.24	0.34	10.92	0.45	1.90	0.62	11.54					
	350 g/l				350 g/l				350 g/l							
0.25	2.48	0.25	4.90	0.00	3.58	0.22	6.00	0.00	5.14	0.34	7.16					
1	1.64	0.21	6.32	0.11	3.00	0.25	7.72	0.15	4.50	0.31	8.78					
2	1.18	0.31	7.76	0.21	2.60	0.12	10.32	0.15	3.62	0.51	10.16					
3.2	-0.12	0.36	10.20	0.41	1.92	0.22	12.08	0.49	3.12	0.23	13.02					

	400 g/l				400 g/l				400 g/l			
0.25	3.16	0.25	5.80	0.00	4.54	0.27	7.06	0.05	6.38	0.38	8.14	
1	2.52	0.22	7.08	0.11	4.20	0.12	8.54	0.15	5.20	0.58	9.86	0.17
2	2.06	0.38	8.64	0.25	3.08	0.43	10.62	0.23	5.32	0.51	11.50	0.10
3.2	1.02	0.24	11.64	0.09	2.96	0.28	13.50	0.17	4.50	0.21	13.82	0.32
	450 g/l				450 g/l				450 g/l			
0.25	4.15	0.19	6.64	0.09	5.53	0.26	7.84	0.05	7.20	0.17	9.02	0.04
1	2.82	0.26	8.20	0.00	4.86	0.48	9.34	0.15	6.18	0.61	10.74	0.09
2	2.38	0.34	10.24	0.15	4.13	0.43	12.00	0.16	6.08	0.13	13.14	0.11
3.2	1.94	0.25	12.28	0.13	3.22	0.13	14.02	0.33	5.08	0.26	15.36	0.25

The equilibrium saturation temperature ( $T_e$ ) and supersaturation temperature ( $T_{c,lim}$ ) at each concentration measurement were observed from extrapolation of the cooling rate to 0°C/min of  $T_c - q$  and  $T_{diss} - q$  lines (4.4.2). All these values from C18/C16 mixtures, together with resultant equilibrium MSZW at the measured concentrations, are listed in **Tables 8.4, 8.5 and 8.6** with respect to the three solvents, n-dodecane, kerosene and toluene.

This enabled a solubility-supersolubility curve to be formed for each composition, giving a clear representation of how the change of composition affects the equilibrium saturation and crystallisation temperatures and resultant meta-stability. Typical examples of solubility-supersolubility curves showing C16, C18 and 0.5C18 (equimolar) binary mixtures in toluene give an overview of the meta-stable zone and the changes that occur with compositional effects, are given in **Figure 8.2**. It can be clearly seen that the mixture sample of 0.5C18 has an MSZW which is larger than the single component of C16 or C18 indicating greater supercooling is needed to overcome the nucleation barrier.

**Table 8.4 Solubility ( $T_e$ ) and supersolubility ( $T_{c,lim}$ ) data of C18/C16 mixtures in n-dodecane solvent, together with the calculated equilibrium MSZW ( $\Delta T$ ) at each concentration. std: standard deviation from five recycles of repeats.**

Con. (g/l)	$T_{c,lim}$ (°C)	std	$T_e$ (°C)	std	$\Delta T$ (°C)	std	Con. (g/l)	$T_{c,lim}$ (°C)	std	$T_e$ (°C)	std	$\Delta T$ (°C)	std
<b>C16</b>							<b>0.1C18</b>						
192	-8.87	0.32	-4.49	0.11	4.37	0.58	192	-13.56	0.07	-7.87	0.11	5.68	0.16
231	-6.11	0.44	-2.80	0.15	3.32	0.47	231	-11.27	0.08	-5.40	0.11	5.87	0.14
269	-3.72	0.49	-1.02	0.34	2.70	0.04	269	-9.27	0.07	-4.11	0.09	5.16	0.12
308	-2.46	0.66	-0.03	0.10	2.43	0.29	308	-8.21	0.05	-3.00	0.08	5.21	0.09
<b>0.2C18</b>							<b>0.3C18</b>						
192	-13.04	0.06	-8.80	0.07	4.24	0.12	192	-11.82	0.07	-7.86	0.10	3.96	0.15
231	-10.61	0.07	-8.41	0.15	2.21	0.21	231	-9.50	0.08	-7.69	0.14	1.81	0.21
269	-9.11	0.07	-7.11	0.06	2.00	0.11	269	-7.63	0.11	-6.73	0.14	0.90	0.21
308	-7.42	0.08	-5.86	0.14	1.56	0.17	308	-6.34	0.04	-5.89	0.09	0.45	0.12
<b>0.4C18</b>							<b>0.5C18</b>						
192	-10.38	0.10	-5.05	0.05	5.33	0.12	192	-6.18	0.24	-1.71	0.11	4.47	0.15
231	-8.54	0.10	-3.14	0.06	5.41	0.16	231	-4.65	0.13	0.15	0.07	4.80	0.11
269	-6.63	0.06	-2.16	0.05	4.47	0.04	269	-3.35	0.19	1.73	0.09	5.08	0.27
308	-5.34	0.08	-0.73	0.11	4.61	0.14	308	-2.45	0.18	3.01	0.12	5.46	0.27
<b>0.6C18</b>							<b>0.7C18</b>						
192	-2.77	0.15	-0.54	0.03	2.23	0.18	192	-0.36	0.13	1.62	0.06	1.98	0.12
231	-1.55	0.20	1.65	0.08	3.21	0.25	231	0.88	0.30	3.39	0.16	2.51	0.25
269	0.00	0.05	3.13	0.13	3.12	0.14	269	2.75	0.24	5.05	0.07	2.30	0.27
308	1.30	0.12	4.10	0.02	2.81	0.12	308	3.67	0.16	6.57	0.08	2.90	0.15
<b>0.8C18</b>							<b>0.9C18</b>						

<b>192</b>	2.20	0.10	2.71	0.12	0.52	0.15	<b>192</b>	3.94	0.18	4.29	0.09	0.36	0.26
<b>231</b>	3.98	0.06	4.95	0.23	0.98	0.26	<b>231</b>	5.17	0.23	6.18	0.08	1.01	0.30
<b>269</b>	5.41	0.04	6.16	0.09	0.75	0.12	<b>269</b>	6.74	0.10	7.63	0.07	0.89	0.16
<b>308</b>	6.41	0.06	7.75	0.08	1.35	0.13	<b>308</b>	7.50	0.24	9.29	0.14	1.79	0.31
<b>C18</b>													
<b>192</b>	4.47	0.50	5.68	0.09	1.22	0.52							
<b>231</b>	6.53	0.46	7.42	0.19	0.88	0.59							
<b>269</b>	7.87	0.31	9.05	0.13	1.19	0.36							
<b>308</b>	9.47	0.02	10.17	0.15	0.70	0.13							

**Table 8.5 Solubility ( $T_e$ ) and supersolubility ( $T_{c,lim}$ ) data of C18/C16 mixtures in kerosene solvent, together with the calculated equilibrium MSZW ( $\Delta T$ ) at each concentration. Std: standard deviation from five recycles of repeats.**

Con. (g/l)	$T_{c,lim}$ (°C)	std	$T_e$ (°C)	std	$\Delta T$ (°C)	std	Con. (g/l)	$T_{c,lim}$ (°C)	std	$T_e$ (°C)	std	$\Delta T$ (°C)	std
<b>C16</b>							<b>0.1C18</b>						
<b>231</b>	-5.66	0.33	-3.35	0.08	2.30	0.30	<b>231</b>	-11.28	0.22	-6.24	0.10	5.04	0.22
<b>269</b>	-4.28	0.24	-1.85	0.07	2.44	0.23	<b>269</b>	-9.63	0.28	-4.57	0.10	5.06	0.30
<b>308</b>	-2.76	0.19	-0.50	0.09	2.26	0.24	<b>308</b>	-7.88	0.17	-3.34	0.07	4.54	0.16
<b>350</b>	-1.80	0.53	0.70	0.09	2.49	0.58	<b>350</b>	-7.00	0.18	-2.18	0.05	4.81	0.16
<b>0.2C18</b>							<b>0.3C18</b>						
<b>231</b>	-12.56	0.05	-8.48	0.07	4.08	0.11	<b>231</b>	-11.14	0.07	-9.29	0.10	1.85	0.15
<b>269</b>	-10.41	0.08	-6.44	0.06	3.97	0.14	<b>269</b>	-9.23	0.08	-7.68	0.14	1.56	0.21
<b>308</b>	-8.92	0.07	-4.90	0.06	4.02	0.11	<b>308</b>	-7.78	0.11	-6.10	0.14	1.68	0.21
<b>350</b>	-7.70	0.05	-4.12	0.04	3.58	0.04	<b>350</b>	-6.39	0.04	-5.19	0.09	1.20	0.12
<b>0.4C18</b>							<b>0.5C18</b>						
<b>231</b>	-9.44	0.03	-4.05	0.09	5.39	0.08	<b>231</b>	-5.85	0.14	-0.95	0.08	4.90	0.21
<b>269</b>	-7.59	0.09	-4.07	0.20	3.52	0.14	<b>269</b>	-4.46	0.08	0.52	0.03	4.98	0.07
<b>308</b>	-6.18	0.08	-2.24	0.23	3.94	0.20	<b>308</b>	-3.59	0.09	1.73	0.07	5.33	0.11
<b>350</b>	-4.89	0.08	-0.84	0.05	4.05	0.10	<b>350</b>	-2.59	0.05	2.92	0.05	5.52	0.04
<b>0.6C18</b>							<b>0.7C18</b>						
<b>231</b>	-3.08	0.21	1.17	0.09	4.24	0.27	<b>231</b>	-0.77	0.19	2.67	0.12	3.43	0.20
<b>269</b>	-1.55	0.23	2.73	0.12	4.28	0.28	<b>269</b>	0.61	0.12	4.05	0.09	3.44	0.20
<b>308</b>	-0.56	0.18	3.66	0.06	4.22	0.22	<b>308</b>	2.15	0.32	5.37	0.13	3.22	0.41
<b>350</b>	0.46	0.09	5.03	0.05	4.57	0.11	<b>350</b>	3.41	0.17	6.64	0.08	3.23	0.17
<b>0.8C18</b>							<b>0.9C18</b>						
<b>231</b>	1.26	0.54	4.07	0.09	2.81	0.47	<b>231</b>	3.56	0.22	5.56	0.14	2.00	0.36
<b>269</b>	3.43	0.14	5.59	0.08	2.17	0.15	<b>269</b>	5.43	0.18	7.20	0.08	1.77	0.22
<b>308</b>	4.24	0.19	6.88	0.09	2.64	0.24	<b>308</b>	6.70	0.23	8.29	0.03	1.59	0.25
<b>350</b>	5.62	0.40	8.14	0.03	2.52	0.41	<b>350</b>	7.71	0.24	9.56	0.08	1.85	0.18
<b>C18</b>													
<b>231</b>	5.06	0.21	6.85	0.13	1.79	0.29							
<b>269</b>	6.44	0.39	8.44	0.10	2.00	0.39							
<b>308</b>	7.89	0.27	9.47	0.06	1.58	0.26							
<b>350</b>	9.20	0.22	10.66	0.11	1.46	0.26							

**Table 8.6 Solubility ( $T_e$ ) and supersolubility ( $T_{c,lim}$ ) data of C18/C16 mixtures in toluene solvent, together with the calculated equilibrium MSZW ( $\Delta T$ ) at each concentration. std: standard deviation from five recycles of repeats.**

Con. (g/l)	$T_{c,lim}$ (°C)	std	$T_e$ (°C)	std	$\Delta T$ (°C)	std	Con. (g/l)	$T_{c,lim}$ (°C)	std	$T_e$ (°C)	std	$\Delta T$ (°C)	std
<b>C16</b>							<b>0.1 C18</b>						
300	-5.42	0.40	-4.20	0.15	1.22	0.53	300	-10.63	0.23	-7.56	0.12	3.07	0.31
350	-3.92	0.32	-2.71	0.11	1.22	0.40	350	-9.51	0.26	-6.44	0.42	3.07	0.46
400	-3.44	0.27	-2.04	0.35	1.39	0.26	400	-8.74	0.06	-5.16	0.20	3.59	0.20
450	-2.26	0.39	-1.09	0.11	1.17	0.39	450	-7.66	0.25	-4.44	0.13	3.23	0.22
<b>0.2C18</b>							<b>0.3C18</b>						
300	-12.78	0.06	-9.29	0.10	3.49	0.12	300	-11.97	0.21	-9.56	0.13	2.41	0.22
350	-11.16	0.06	-7.92	0.10	3.24	0.12	350	-10.45	0.10	-8.34	0.06	2.11	0.15
400	-10.03	0.12	-6.95	0.05	3.08	0.10	400	-9.45	0.20	-7.26	0.13	2.19	0.19
450	-9.17	0.09	-6.05	0.12	3.13	0.17	450	-8.15	0.10	-6.55	0.09	1.60	0.11
<b>0.4C18</b>							<b>0.5C18</b>						
300	-9.92	0.11	-5.47	0.13	4.45	0.18	300	-6.01	0.11	-1.46	0.09	4.55	0.05
350	-8.84	0.09	-4.33	0.07	4.14	0.03	350	-4.79	0.08	-0.44	0.07	4.36	0.12
400	-7.47	0.09	-2.80	0.05	4.67	0.11	400	-4.09	0.16	0.50	0.03	4.59	0.16
450	-6.65	0.12	-2.40	0.12	4.25	0.21	450	-3.43	0.14	1.24	0.04	4.67	0.16
<b>0.6C18</b>							<b>0.7C18</b>						
300	-3.65	0.13	0.09	0.15	3.74	0.19	300	-1.07	0.31	1.98	0.15	3.05	0.18
350	-2.46	0.18	1.35	0.10	3.80	0.14	350	0.15	0.26	3.04	0.08	2.88	0.23
400	-1.21	0.09	2.29	0.07	3.50	0.06	400	1.04	0.20	3.97	0.03	2.93	0.18
450	-0.47	0.08	2.69	0.12	3.16	0.18	450	2.14	0.11	4.78	0.05	2.64	0.15
<b>0.8C18</b>							<b>0.9C18</b>						
300	1.16	0.21	3.11	0.13	1.95	0.21	300	2.67	0.28	4.18	0.17	1.51	0.43
350	2.65	0.24	4.45	0.15	1.80	0.29	350	3.65	0.25	5.65	0.20	2.01	0.33
400	3.32	0.27	5.14	0.03	1.82	0.27	400	4.64	0.23	6.41	0.11	1.77	0.13
450	3.93	0.46	6.25	0.08	2.32	0.47	450	5.68	0.27	7.34	0.11	1.66	0.30
<b>C18</b>													
300	4.22	0.20	5.29	0.38	1.07	0.40							
350	5.21	0.19	6.66	0.12	1.45	0.27							
400	6.23	0.49	7.78	0.14	1.55	0.50							
450	7.18	0.31	8.58	0.12	1.40	0.26							

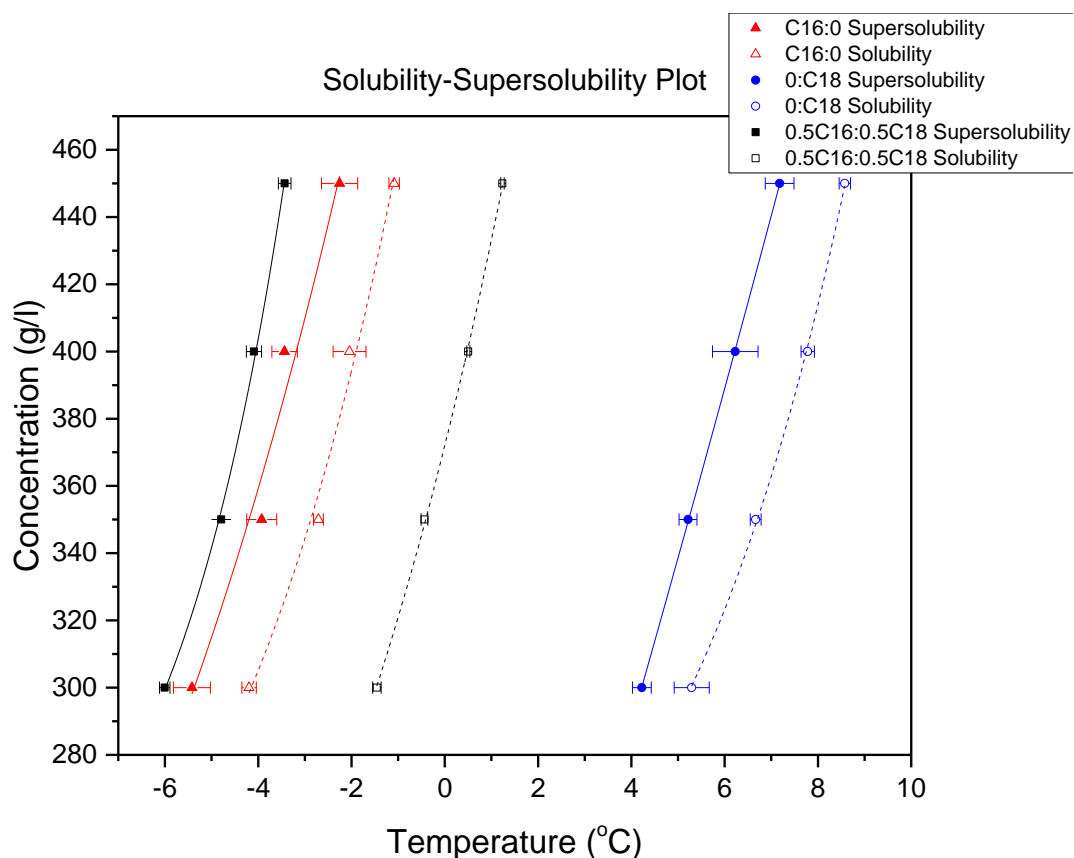


**Figure 8.2: Solubility-supersolubility curves for samples of C16, C18 and equimolar composition of both 0.5C18. Determined from extrapolation of the poly-thermal data from four concentrations (300, 350, 400 and 450 g/l).**

Overall, the concentration effect on meta-stability was rarely observable from the range studied (192g/l – 450 g/l) with three solvents. The only exceptions are shown in **Figure 8.3 (a, b)** in the solution of n-dodecane for mixtures of 0.2C18 and 0.3C18, illustrated by the discontinuous solubility curve with the abnormal behaviour of the saturation temperature at the lowest concentration of 192 g/l. Considering the accuracy of these measurements, as collected in five cycles of repeats, this abnormal point could be referred to as a polymorphic phase formation with higher solubility. The hypothesis can be made that the solvent molecules are involved in crystallisation and act as a part of the formed crystals. For consistency, the phase has been studied for solubility determination, the saturation temperature of a possible polymorph at a concentration of 192 g/l for the two mixtures, has not been adopted in further studies of Van't Hoff plots.

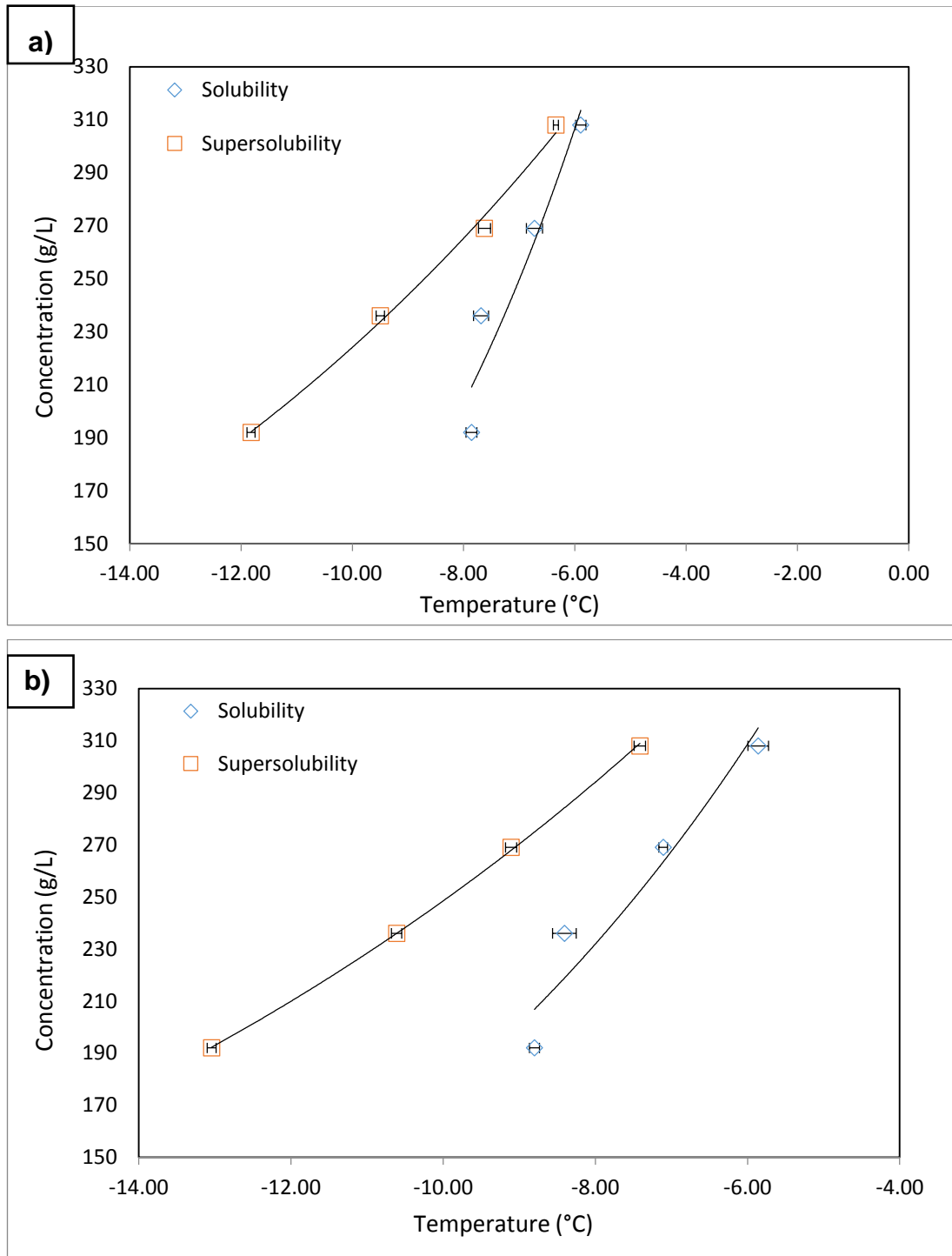


**Figure 8.3: Solubility-supersolubility curves for binary mixture samples a) 0.2C18 and b) 0.3C18 in n-dodecane solution determined from extrapolation of poly-thermal data from four concentrations (192, 231, 269 and 380 g/l).**

### 8.3 Saturation Temperature

The equilibrium saturation temperatures, together with their standard deviation from five cycles of repeats, are plotted as a function of molar composition for C18/C16 mixtures in three solvents of n-dodecane, kerosene and toluene as shown in **Figure 8.4 (a, b and c)**, respectively. The resultant saturation patterns in four concentrations of each solvent are quite consistent. For the purpose of clarification, the inter-relationship between saturation temperature and mixture composition with associated structural changes is compared in terms of the single concentration of each solvent: 308 g/l for n-dodecane or kerosene and 350 g/l for toluene (**Figure 8.5**).

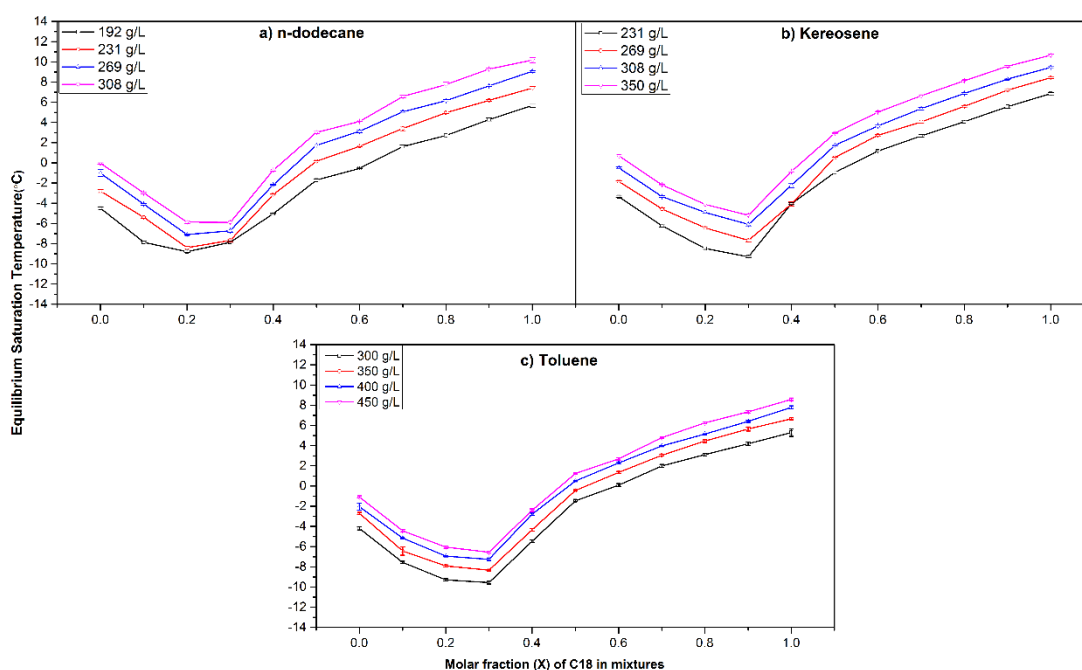


**Figure 8.4: Equilibrium saturation temperature patterns as a function of C18/C16 mixture composition in three solvents of (a) n-dodecane with four concentrations of (192, 231, 269 and 308 g/l); (b) kerosene (231, 269, 308 and 350 g/l) and (c) toluene (300, 350, 400 and 450 g/l)**

As seen from **Figure 8.5**, the saturation pattern trend versus mixture composition was in agreement within the three solvents, which indicates the structural behaviour could be solvent nature independent of this work. Moreover, the saturation temperature ( $T_e$ ) of pure C18 is largely higher than that of C16 due to the inter-chain interactions between  $-\text{CH}_2$  methylene group increasing as the chain length increases. Hence, more energy is required to break the lattice packing, which will increase the saturation temperature. This

result has been noted in many n-alkane solubility studies with solubility of pure C<sub>n</sub> in organic solvents decreasing with C<sub>n</sub> number increases [70, 72, 118].

Furthermore, there was an overall decline in  $T_e$  for binary mixture samples over the temperature range with several transit points according to the slope changes of the saturation pattern. This could be explained by the formation of new phases within the binary mixtures were crystallised in structures with reduced stability and packing density. The possibly corresponding structures of the formed phases within these binary mixtures were given in Figure 8.5. With the help of in-situ X-ray diffraction studies (Chapter 7), the phases observed from C18/C16 mixtures crystallised in kerosene solution were resolved (Figure 7.26).

Overall, the saturation pattern as a function of the composition can be separated into five sections associated with structural stability. Decreased  $T_e$  was observed with the addition of the longer chain alkane of C18 into C16 with limited molar fraction ( $x=0$  to 0.1). Even though the C18/C16 mixtures formed into a solid solution which crystallised in the original triclinic structure of C16, chain length difference increased disordering in the lattice therefore decreasing the saturation temperature. From  $x=0.1$  to 0.5 molar fraction of C18, the apparent lower values of  $T_e$  are relative to the alert of packing arrangement from the high density structure of triclinic to much lower orthorhombic structures within these composition mixtures. Particularly, the highly disordered rotator phase ( $R_1$ ) observed in mixtures from  $x=0.1$  to 0.3 with resultant lowest  $T_e$ . Consequently this was replaced by a fully crystalline orthorhombic structure ( $O_p$ ) from  $x=0.3-0.5$  mixtures. Within this section,  $T_e$  increased linearly with a steep slope as the proportion of C18 in mixtures rose. Afterwards ( $x=0.5-1.0$ ),  $T_e$  increased as chain length increased in a flatter linear trend indicating a phase change to the more dense lattice of triclinic which was identical to the longer chain alkane of C18. Although the phases between  $x=0.5$  to 0.7 were not defined, these binary mixtures behaved like a connection between the less dense packed orthorhombic phase and high density triclinic structure, indicating a difference between the two packing arrangements declined as an increasing amount of longer chain molecules in the mixture eventually dominating the final structure.

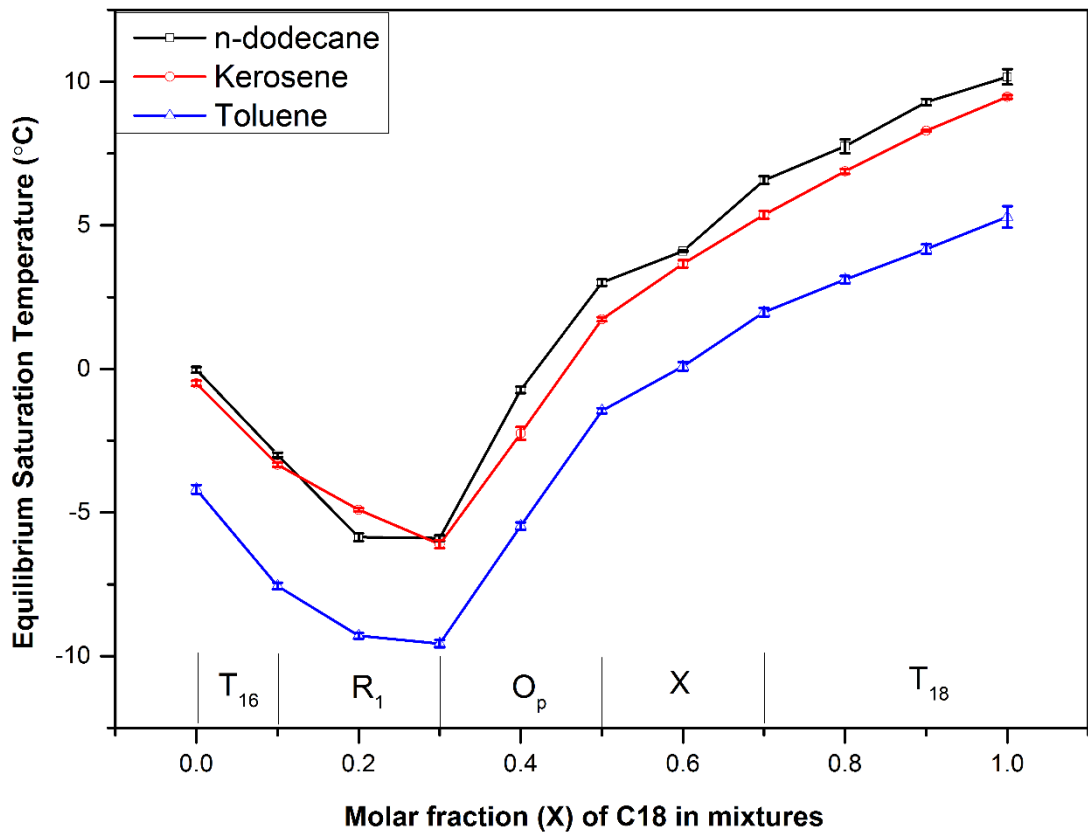


**Figure 8.5: Patterns of equilibrium saturation temperatures ( $T_e$ ) as a function of C18/C16 mixture composition in three representative solvents: n-dodecane, kerosene (at concentration of 308 g/l) and toluene (350 g/l). The corresponding structural phases are presented as obtained from in-situ synchrotron X-ray diffraction analysis of C18/C16/kerosene in Chapter 7 (Figure 7.26).**

## 8.4 Van't Hoff Analysis

The solubility plots using the Van't Hoff model (**Equation (2.1)**) for C18/C16 mixtures in three solvents of n-dodecane, kerosene and toluene are shown in **Figures 8.6, 8.7 and 8.8** respectively. The resultant solubility behaviour in relation to the compositional effects of binary mixtures was quite compatible with all three solvents which were consistent with the observation from saturation temperature patterns. Higher solubility was observed with components having a shorter chain length of C16 and binary mixtures with a C18 molar fraction from  $x=0.1$  to 0.4 due to the formation of less stable phases. Interestingly, the mixture component of 0.4C18 had a solubility close to pure C16, indicating balanced effects from the structural packing arrangement and chain length differences.

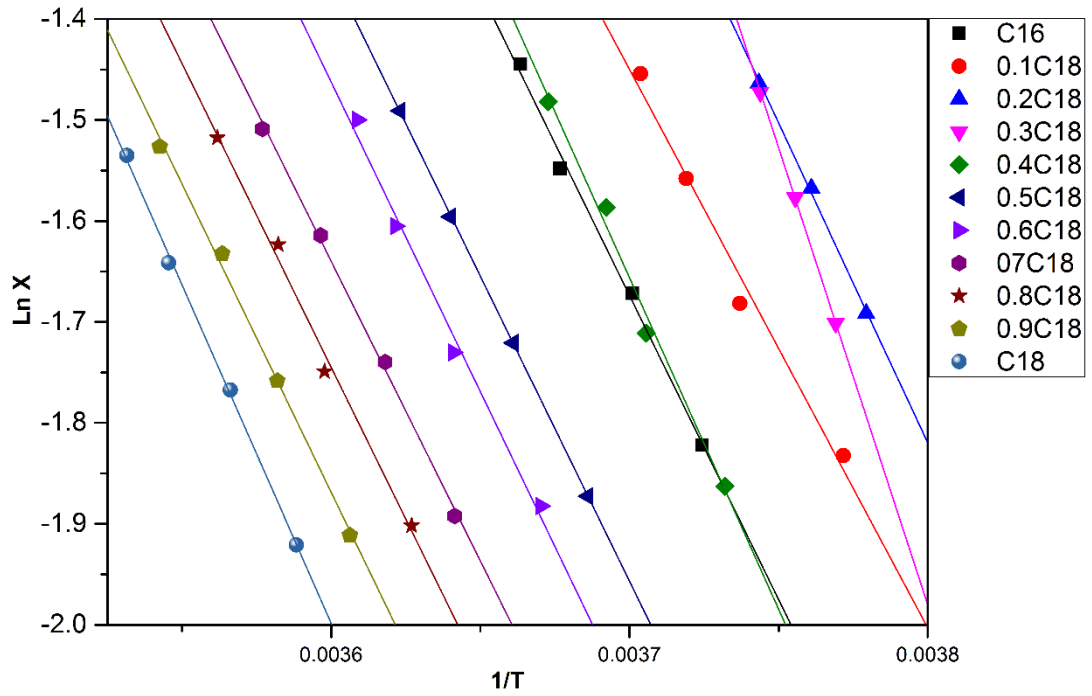


Figure 8.6: Solubility plots applied with Van's Hoff model for C18/C16 mixtures in n-dodecane. Experimental solubility data derived by extrapolation of  $T_{diss-q}$  lines at each concentration.

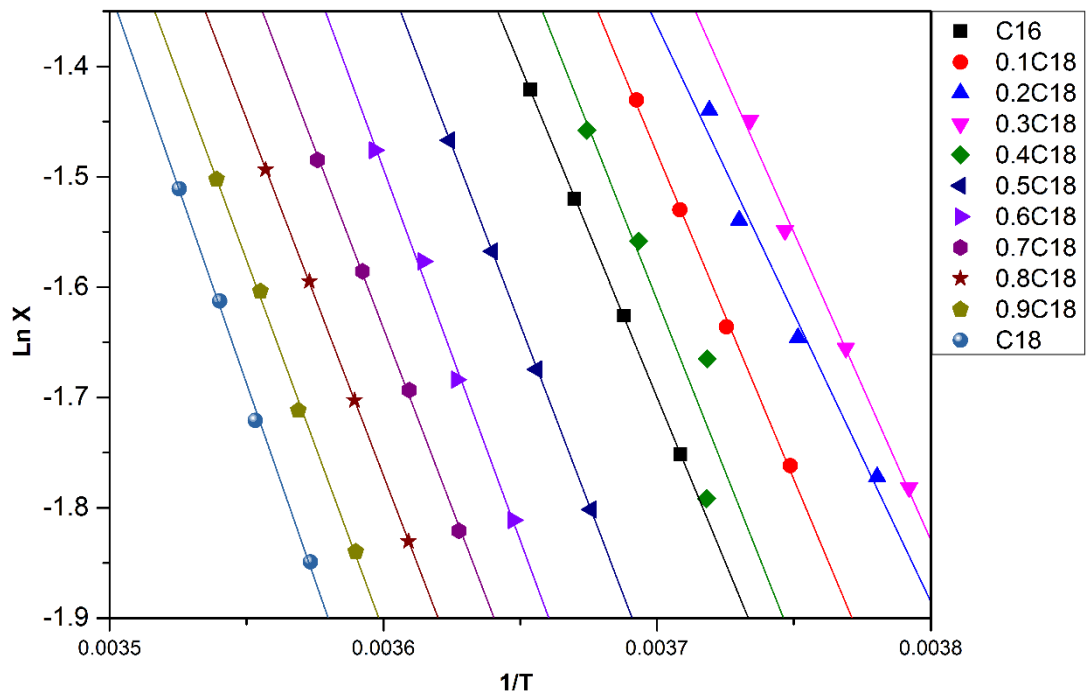
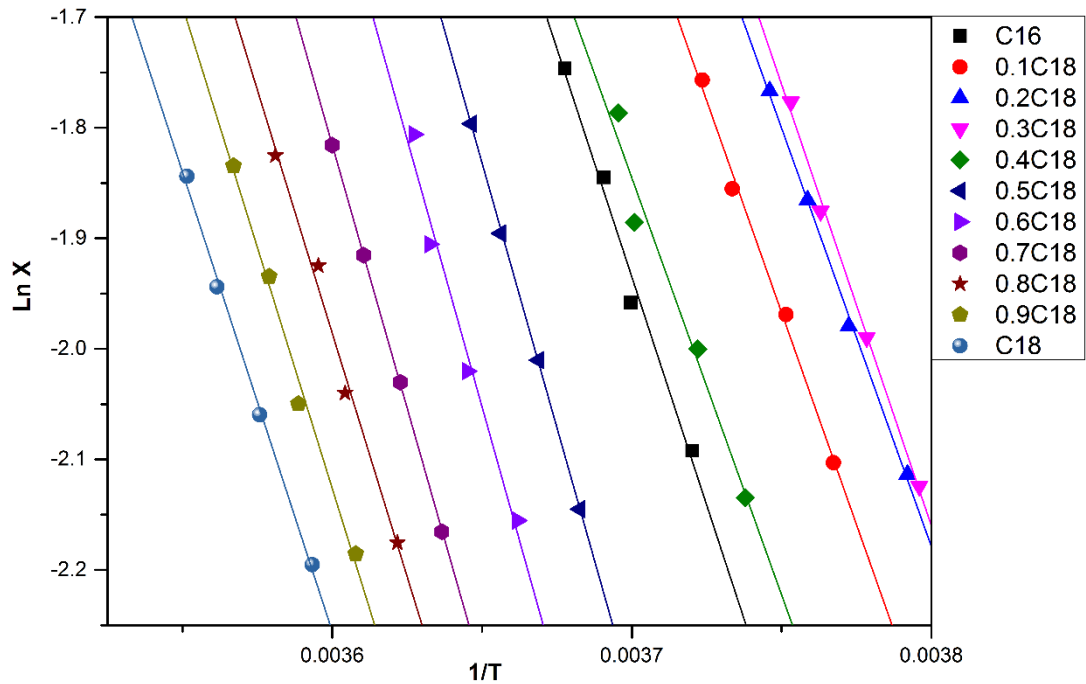


Figure 8.7: Solubility plots applied with Van's Hoff's model for C18/C16 mixtures in kerosene. Experimental solubility data derived by extrapolation of  $T_{diss-q}$  lines at each concentration.



**Figure 8.8: Solubility plots applied with using Van's Hoff model for C18/C16 mixtures in toluene. Experimental solubility data was derived by extrapolation of  $T_{\text{diss-q}}$  lines at each concentration.**

Furthermore, the Van't Hoff plots were employed to access the ideality behaviour with respect to the solvent nature and compositional effects as compared to the non-solvent ideal condition. Examples of pure C16, C18 and equimolar composition component of 0.5C18 in three solvents of n-dodecane, kerosene and toluene are shown in **Figure 8.9 (a-c)**. The non-ideal behaviour was observed from all three samples with solubility less than ideal in the three solvents studied. Among these, n-dodecane showed the best ideality with the highest solubility for all three samples. This was followed immediately by kerosene and was least ideal in toluene. This is due to the n-alkane solute being non-polar in nature, therefore it has the least solubility in the highest polar solvent of toluene. Hence, the solute will be more favourable to be dissolved in the hydrocarbon molecules of n-dodecane with the strongest solute-solvent interactions, resulting in the highest solubility and the closest to the ideal condition. Kerosene is a mixture solvent containing both hydrocarbon molecules and aromatic chemicals, then has a solubility between that of n-dodecane and toluene.

The calculated values of activity coefficients ( $\gamma$ ), enthalpies and entropies of dissolution for C18/C16 mixtures in three solvents as derived from model solubility plots are provided in **Table 8.7** and plotted as a function of mixture composition in **Figures 8.10, 8.11 and 8.12**, respectively.

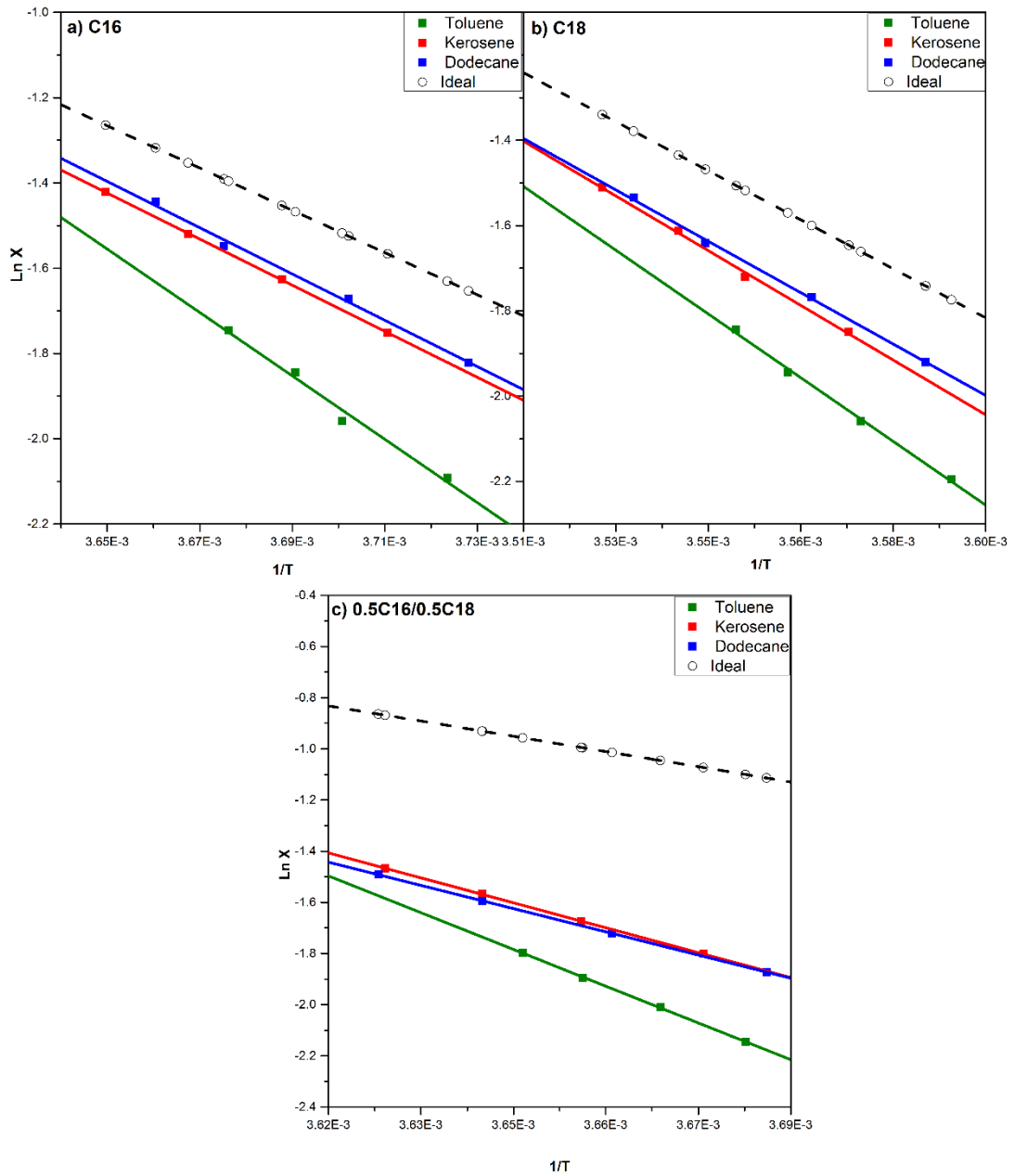


**Figure 8.9: Van't Hoff ideality plots for C18/C16 binary mixtures in three solvents of n-dodecane, kerosene and toluene. a) Pure C16. b) Pure C18. c) The equimolar composition of 0.5C16/0.5C18. The ideal solubility was calculated according to the enthalpy of fusion of each composition as provided by DSC measurements in Chapter 6.**

**Table 8.7 Thermodynamic parameters derived from the Van't Hoff plots for C18/C16 mixtures in three solvents of n-dodecane, kerosene and toluene with high correlation  $R^2 > 0.97$  from a linear fit of  $\ln x$  versus  $1/T$  except for mixture component of 0.4C18 in kerosene with  $R^2 = 0.79$ . Activity coefficient ( $\gamma$ )**

Composition: mol fraction C18	$\Delta H_{diss}$ (KJ /mol)			$\Delta S_{diss}$ (KJ /K.mol)			Activity coefficient ( $\gamma$ )		
	Dodecane	Kerosene	Toluene	Dodecane	Kerosene	Toluene	Dodecane	Kerosene	Toluene
0	-50.12	-49.90	-68.66	0.17	0.17	0.24	1.18-1.14	1.20-1.17	1.59-1.42
0.1	-45.97	-49.17	-63.75	0.16	0.17	0.22	1.81-1.61	1.84-1.64	2.41-2.02
0.2	-68.92	-43.43	-62.91	0.25	0.15	0.22	1.34-1.24	1.45-1.34	1.94-1.66
0.3	-100.23	-46.34	-66.34	0.36	0.16	0.23	1.41-1.24	1.39-1.26	1.93-1.62
0.4	-54.64	-51.91	-62.72	0.19	0.18	0.22	1.81-1.57	1.79-1.53	2.32-1.95
0.5	-50.26	-54.00	-79.62	0.17	0.18	0.28	2.14-1.87	2.07-1.82	2.84-2.32
0.6	-51.01	-56.02	-80.41	0.17	0.19	0.28	2.08-1.82	2.13-1.87	2.83-2.30
0.7	-49.38	-54.02	-79.12	0.16	0.18	0.27	2.13-1.91	2.10-1.87	2.86-2.36
0.8	-49.99	-53.73	-73.21	0.17	0.18	0.25	1.61-1.55	1.64-1.55	2.17-1.90
0.9	-50.74	-55.85	-72.53	0.17	0.19	0.24	1.41-1.39	1.44-1.38	1.84-1.64
1	-55.68	-59.29	-69.06	0.18	0.20	0.23	1.20-1.17	1.22-1.19	1.52-1.40

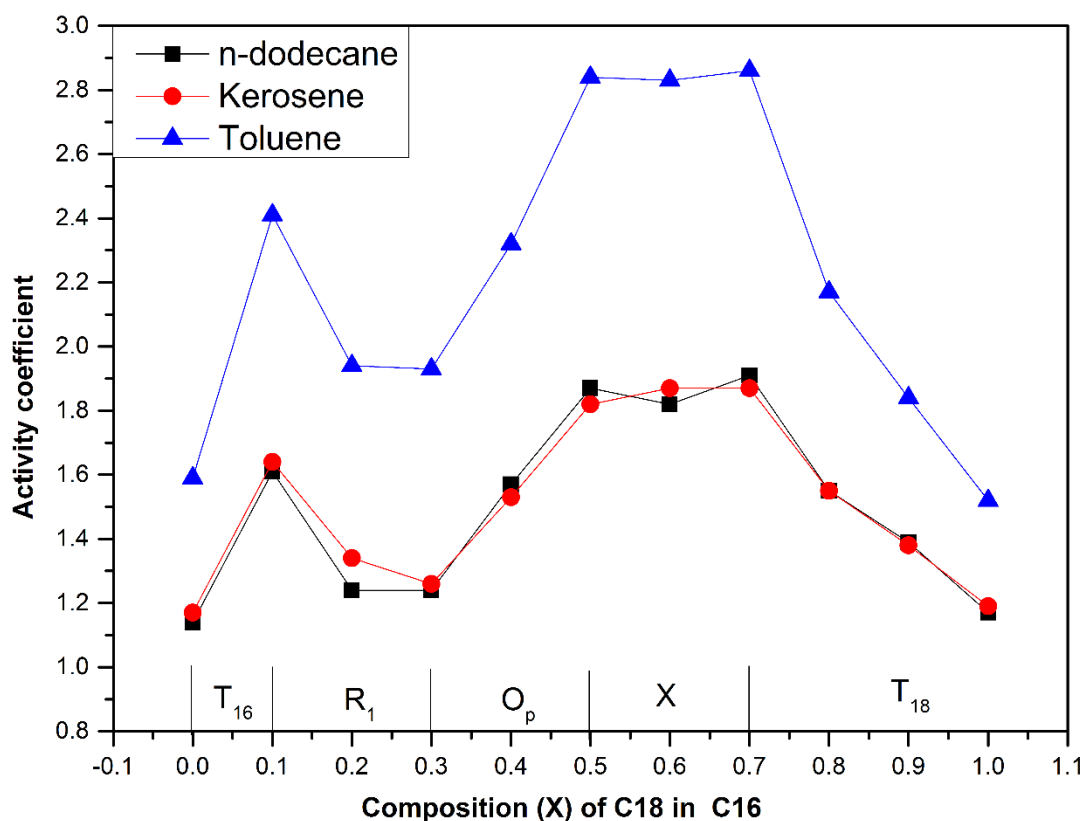


**Figure 8.10: Activity coefficient ( $\gamma$ ) patterns as a function of C18/C16 mixture compositions in three representative solvents: n-dodecane, kerosene at concentration of 308 g/l and 350 g/l in toluene. Resultant structural phases are also presented as obtained from in-situ synchrotron X-ray diffraction analysis of C18/C16/kerosene in Chapter 7.**

**Figure 8.10** reveals a consistent trend of activity coefficient pattern as a function of mixture composition in all three solvents and the highest deviation in toluene was due to the lowest solubility. Notably, in each solvent, two regions of mixtures have the protruding higher deviations: one is at a molar fraction of C18  $x=0.1$ , and the other one is between  $x=0.5-0.7$ . As less than ideal, this means the solubility of the phases formed in solution largely deviates from the ideally non-solvent environment within these mixtures. Hence, a non-identical phase formation in solution crystallisation would be expected in comparison with the structural behaviour in the melt. Indeed, the component 0.1C18 formed a rotator phase of  $R_1$  structure from kerosene solution rather than mixed phases of triclinic (T) +  $R_1$  as determined in the melt (Chapter 6). For  $x=0.5-0.7$  mixtures formed in a  $R_1$  solid solution from homogenous melt mixtures, while in solution, the stabilised  $R_1$  became a metastable phase and was likely not existed during the dissolution process which was replaced by the fully crystalline structures of  $O_p$  or T. Whereas for samples of pure C16, 0.2C18, 0.3C18 and pure C18 having the

least deviation in each solvent, were possibly due to the identical structures with close stability to the phases formed in the melt environment.

Unlike the usual observations obtained from solubility studies ( $T_e$ , Van't Hoff plots and activity coefficient), more variety in behaviour was found in enthalpies and entropies of dissolution with respect to the mixture composition and solution environment, **Figure 8.11**. The  $\Delta H_{diss}$  of related solvents should obey the solubility characteristics diametrically as the less solute-solvent molecular interactions, more energy would be required for dissolution reaction. Therefore, we could expect the  $\Delta H_{diss}$  was the highest in toluene and followed by kerosene and the least in n-dodecane. The normal order was observable for components of C18, C16 and mixtures with molar fractions of C18 ( $x=0.1, 0.5$  to  $0.9$ ) with fully crystalline crystals. Whereas, the mixtures between  $x=0.2-0.4$  formed in a disordered phase ( $R_1$ ) with least  $\Delta H_{diss}$  observed in kerosene. This was, however, in conflict with the least solubility which was actually in n-dodecane.

For each solvent, samples with a composition of  $x=0.1-0.4$  were expected to have lower values of  $\Delta H_{diss}$  as these components had lower solubility with the lower stability of the formed phases and, as a result, the energy required to break the intermolecular packing of solute molecules was reduced to some extent. The protruding point of 0.3C18 in n-dodecane with extremely high  $\Delta H_{diss}$  and  $\Delta S_{diss}$  can possibly be explained by n-dodecane crystallising or highly ordering with strong packing force which resulted in high interaction energy. It can also be seen from the solubility Van't Hoff plot (**Figure 8.6**), in which the 0.3C18 composition has a solubility plot not parallel to others.

The energy of  $\Delta H_{diss}$  includes an energy break in the intermolecular packing and mixing of the separated C16 and C18 molecules. In other words, it is not only affected by the structural stability but also the solvation enthalpy from mixing. For example, in kerosene for which the phase formed is known, the enthalpy reduced to  $x=0.2$  from  $0.3$ , whereas 0.3C18 has the lowest stability and is due to the chain length is increased from 0.3C18 resulting in a higher energy of mixing being required. The increase from  $x=0.4$  to  $0.6$  is due to the increased stability of the formed phase and relatively longer chain length of the structure. Dissolution enthalpy was expected to show structural behaviour from the discussion of Gerson's observation in C20/C22 mixtures in n-dodecane showing the maxima enthalpy reflecting phase change [72]. Consistency had been observed in our work on kerosene and n-dodecane, except the abnormal point of 0.3C18. However, in the aromatic solvent of toluene, the trend is special with 0.4C18 having the lowest  $\Delta H_{diss}$  while maxima with  $x=0.5-0.7$ . Interpretation can also be made with dissolution enthalpy which could be more easily affected by the nature of the solution, especially involving disordering solutes.

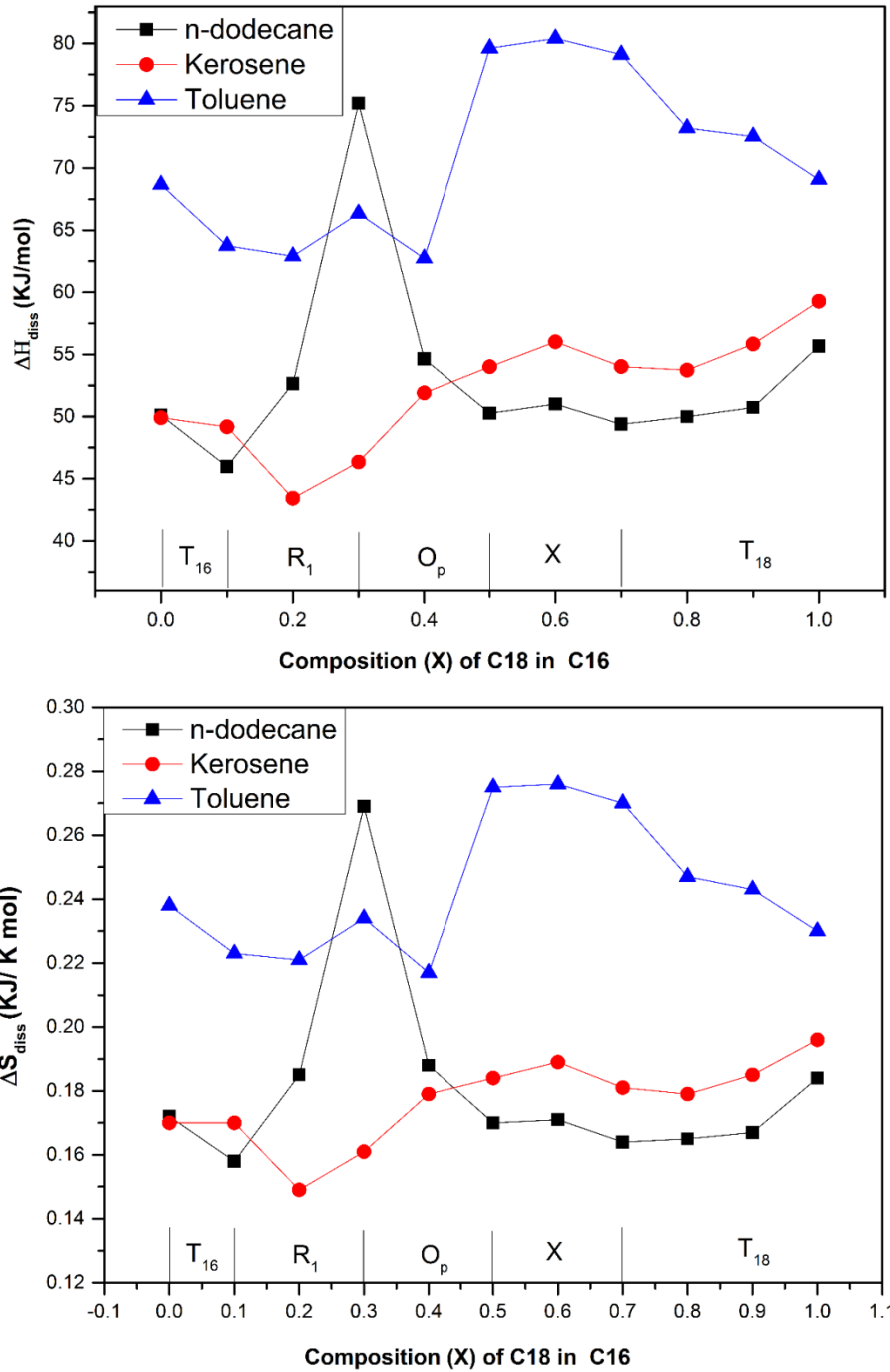


**Figure 8.11:  $\Delta H_{diss}$  (a) and  $\Delta S_{diss}$  (b) patterns as a function of C18/C16 mixture compositions in three representative solvents: n-dodecane, kerosene at concentration of 308 g/l and 350 g/l in toluene. Resultant structural phases are also presented as obtained from in-situ synchrotron X-ray diffraction analysis of C18/C16/kerosene in Chapter 7.**

## 8.5 Conclusions

By a poly-thermal method, solubility is determined and assessed with saturation temperature and Van't Hoff analysis for C18/C16 mixtures in three representative solvents of n-dodecane, kerosene and toluene. Solubility is found to be in good agreement with activity coefficients with higher solubility in n-dodecane and the closest to the ideal condition, followed by kerosene and toluene. The saturation temperature reveals the structural transition behaviour as a function of a mixture solubility with consistent behaviour in all three solvents.

Furthermore, the activity coefficient is found to reflect the non-identical phase formation in solution crystallisation as the high deviation value was observed from the C18 molar composition of  $x=0.1$ ,  $0.5-0.7$  in all three solvents. Dissolution enthalpy has some inconsistent behaviour in three solvents especially for the mixtures crystallised in disordered structures from  $x=0.2-0.4$ .

We could conclude that the nature of solvents within this study has no major effect on the structural behaviour of C18/C16 mixtures. However, patterns of dissolution enthalpy could give more information than the saturation temperature in the case where mixture samples are formed continuously which is non-distinguishable from transmission detection, i.e. effects from disordering structures or multiple phase formations. Further in-situ XRD experiments are needed to reveal detailed information on structural behaviour in n-dodecane and toluene.

## **Chapter 9 Nucleation Kinetics and Mechanism of Octadecane and Hexadecane Mixtures as a Function of Solution Environment**

### *Summary:*

*The poly-thermal data obtained from crystallisation measurements of octadecane and hexadecane mixtures in three model solvents is further assessed by nucleation mechanism and kinetics.*

## 9.1 Introduction

Following the solubility and thermodynamic analysis of octadecane (C18) and hexadecane (C16) mixtures in solutions using a poly-thermal method, the metastability and associated nucleation kinetics are further assessed for the ternary system studied.

The metastability is initially compared as a function of mixture composition of the solutes and the nature of the model solvents. Nucleation kinetics are studied using the KBHR approach employing the equilibrium solubility and crystallisation temperature from poly-thermal data and assessing the nucleation mechanism to derive the essential nucleation parameters.

## 9.2 Metastable Zone Width (MSZW)

Data for the MSZW as provided in **Tables 8.4-8.6** (Chapter 8) was employed to plot the pattern as a function of C18/C16 mixture composition in three solvents of n-dodecane (308 g/l), kerosene (308 g/l) and toluene (350 g/l), as shown in **Figure 9.1**. The respective structural information is provided from in-situ XRD measurements in kerosene (Chapter 7). The maxima MSZW for 0.1C18 and 0.5C18 in the solute corresponded to the endpoint of  $T_{16}$  and  $O_p$  phases correlating to phase transition phenomenon. As the two mixtures had relatively low saturation temperatures, as determined in Chapter 8, the resultant greater MSZW could only be explained by the relatively lower temperature of crystallisation corresponding to a larger nucleation barrier.

MSZW had more variable behaviour compared to the regular trend observed from saturation temperature as seen from **Figure 9.1**, the scatter data points had a linear trend which was less than ideal. Moreover, the saturation temperatures were always the highest in n-dodecane for all the mixture samples with the greatest solubility. However, n-dodecane had the largest MSZW for C18/C16 mixture within a composition range of  $x=0-0.1$  and  $0.4-0.5$ , while having the lowest for samples of  $x=0.1-0.4$  and  $0.5-1.0$ . Interestingly, the overall largest and narrowest MSZW were both observed in n-dodecane corresponding to compositions of 0.5C18 ( $5.5^\circ\text{C}$ ) and 0.3C18 ( $0.5^\circ\text{C}$ ).

In conclusion, the driving force of crystallisation notably by MSZW was not only controlled by the structure of the phase formed but also by nucleation kinetics which was essentially assessed.

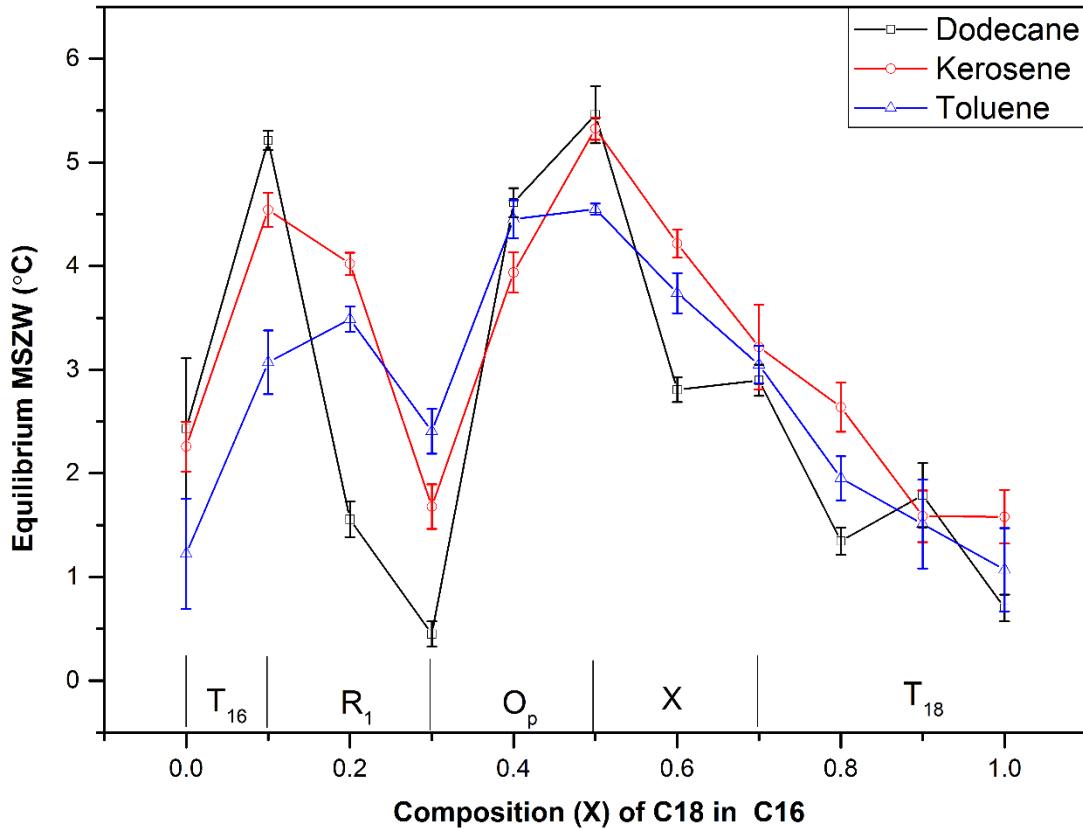


**Figure 9.1: Equilibrium MSZW patterns as a function of composition for C18/C16 binary mixtures in three solvents of n-dodecane (308 g/l), kerosene (380 g/l) and toluene (350 g/l). Resultant structural phases are also presented as obtained from in-situ synchrotron X-ray diffraction analysis of C18/C16/kerosene in Chapter 7.**

### 9.3 Nucleation Mechanism and Kinetic Assessment

The KBHR approach was applied in order to gain results for the nucleation kinetics. The relative critical undercooling ( $u_c$ ) data was initially calculated from **Equation (2.24)** employing values of equilibrium saturation temperatures ( $T_e$ ) and crystallisation temperatures ( $T_c$ ) as provided in **Tables 8.4-8.6** (Chapter 8). **Table 9.1 (a-c)** presents the calculated  $u_c$  values as a function of cooling rate and solution concentration for C18/C16 mixtures crystallising from n-dodecane, kerosene and toluene respectively. All the values of  $u_c$  are lower than 0.1, reaching the criteria of application of the KBHR

approach which required relatively low supersaturation solutions. The highlighted  $u_c$  values of 0.2C18 and 0.3C18 in n-dodecane at concentration of (192 g/l) were not taken into account for further discussion due to the high possibility of the presence of a different polymorph as observed from the variation solubility behaviour (Chapter 8).

**Table 9.1 (a-c) Relative critical undercooling ( $u_c$ ) as a function of cooling rate (q) and solution concentration of eleven compositions of C16/C18 mixture crystallising from three solvents: (a) n-Dodecane, (b) Kerosene and (c) Toluene.**

<b>(a) n-Dodecane</b>								
<b>q (K/s)</b>	<b>C16</b>				<b>0.1 C18</b>			
	<b>192 (g/l)</b>	<b>231 (g/l)</b>	<b>269 (g/l)</b>	<b>308 (g/l)</b>	<b>192 (g/l)</b>	<b>231 (g/l)</b>	<b>269 (g/l)</b>	<b>308 (g/l)</b>
<b>0.004</b>	0.016	0.013	0.011	0.010	0.020	0.021	0.020	0.020
<b>0.017</b>	0.022	0.016	0.013	0.013	0.025	0.026	0.023	0.023
<b>0.033</b>	0.026	0.019	0.019	0.018	0.026	0.028	0.024	0.024
<b>0.053</b>	0.030	0.023	0.022	0.022	0.026	0.031	0.029	0.028
<b>q (K/s)</b>	<b>0.2 C18</b>				<b>0.3 C18</b>			
	<b>192 (g/l)</b>	<b>231 (g/l)</b>	<b>269 (g/l)</b>	<b>308 (g/l)</b>	<b>192 (g/l)</b>	<b>231 (g/l)</b>	<b>269 (g/l)</b>	<b>308 (g/l)</b>
<b>0.004</b>	0.015	0.008	0.007	0.005	0.015	0.007	0.004	0.002
<b>0.017</b>	0.020	0.012	0.011	0.010	0.018	0.011	0.007	0.006
<b>0.033</b>	0.023	0.016	0.015	0.014	0.021	0.013	0.009	0.008
<b>0.053</b>	0.023	0.017	0.015	0.015	0.023	0.017	0.013	0.013
<b>q (K/s)</b>	<b>0.4 C18</b>				<b>0.5 C18</b>			
	<b>192 (g/l)</b>	<b>231 (g/l)</b>	<b>269 (g/l)</b>	<b>308 (g/l)</b>	<b>192 (g/l)</b>	<b>231 (g/l)</b>	<b>269 (g/l)</b>	<b>308 (g/l)</b>
<b>0.004</b>	0.020	0.019	0.017	0.017	0.018	0.018	0.019	0.020
<b>0.017</b>	0.024	0.023	0.020	0.020	0.022	0.022	0.022	0.024
<b>0.033</b>	0.028	0.026	0.022	0.023	0.026	0.027	0.027	0.027
<b>0.053</b>	0.030	0.027	0.025	0.024	0.033	0.030	0.030	0.029
<b>q (K/s)</b>	<b>0.6 C18</b>				<b>0.7 C18</b>			
	<b>192 (g/l)</b>	<b>231 (g/l)</b>	<b>269 (g/l)</b>	<b>308 (g/l)</b>	<b>192 (g/l)</b>	<b>231 (g/l)</b>	<b>269 (g/l)</b>	<b>308 (g/l)</b>
<b>0.004</b>	0.010	0.012	0.012	0.011	0.008	0.010	0.009	0.010
<b>0.017</b>	0.014	0.015	0.015	0.015	0.012	0.012	0.012	0.015
<b>0.033</b>	0.017	0.019	0.020	0.018	0.014	0.014	0.015	0.017
<b>0.053</b>	0.024	0.022	0.023	0.024	0.020	0.019	0.018	0.020
<b>q (K/s)</b>	<b>0.8 C18</b>				<b>0.9 C18</b>			
	<b>192 (g/l)</b>	<b>231 (g/l)</b>	<b>269 (g/l)</b>	<b>308 (g/l)</b>	<b>192 (g/l)</b>	<b>231 (g/l)</b>	<b>269 (g/l)</b>	<b>308 (g/l)</b>
<b>0.004</b>	0.003	0.004	0.003	0.005	0.002	0.005	0.003	0.005
<b>0.017</b>	0.006	0.007	0.006	0.008	0.005	0.005	0.007	0.011
<b>0.033</b>	0.011	0.011	0.011	0.012	0.007	0.008	0.010	0.013
<b>0.053</b>	0.014	0.014	0.013	0.014	0.013	0.011	0.011	0.014
<b>q (K/s)</b>	<b>C18</b>							
	<b>192 (g/l)</b>	<b>231 (g/l)</b>	<b>269 (g/l)</b>	<b>308 (g/l)</b>				
<b>0.004</b>	0.004	0.003	0.003	0.002				
<b>0.017</b>	0.009	0.008	0.008	0.007				
<b>0.033</b>	0.014	0.011	0.012	0.010				
<b>0.053</b>	0.015	0.014	0.013	0.012				

<b>(b) Kerosene</b>								
<b>q (K/s)</b>	<b>C16</b>				<b>0.1 C18</b>			
	<b>231 (g/l)</b>	<b>269 (g/l)</b>	<b>308 (g/l)</b>	<b>350 (g/l)</b>	<b>231 (g/l)</b>	<b>269 (g/l)</b>	<b>308 (g/l)</b>	<b>350 (g/l)</b>
<b>0.004</b>	0.010	0.011	0.009	0.010	0.020	0.019	0.019	0.018
<b>0.017</b>	0.012	0.010	0.011	0.011	0.022	0.023	0.022	0.022
<b>0.033</b>	0.013	0.012	0.015	0.014	0.026	0.026	0.025	0.025
<b>0.053</b>	0.019	0.016	0.016	0.015	0.031	0.030	0.034	0.028
<b>q (K/s)</b>	<b>0.2 C18</b>				<b>0.3 C18</b>			
	<b>231 (g/l)</b>	<b>269 (g/l)</b>	<b>308 (g/l)</b>	<b>350 (g/l)</b>	<b>231 (g/l)</b>	<b>269 (g/l)</b>	<b>308 (g/l)</b>	<b>350 (g/l)</b>
<b>0.004</b>	0.016	0.016	0.016	0.014	0.008	0.007	0.007	0.005
<b>0.017</b>	0.018	0.018	0.017	0.016	0.011	0.010	0.010	0.008
<b>0.033</b>	0.020	0.020	0.020	0.019	0.014	0.013	0.012	0.011
<b>0.053</b>	0.023	0.025	0.023	0.022	0.019	0.017	0.015	0.015
<b>q (K/s)</b>	<b>0.4 C18</b>				<b>0.5 C18</b>			
	<b>231 (g/l)</b>	<b>269 (g/l)</b>	<b>308 (g/l)</b>	<b>350 (g/l)</b>	<b>231 (g/l)</b>	<b>269 (g/l)</b>	<b>308 (g/l)</b>	<b>350 (g/l)</b>
<b>0.004</b>	0.021	0.014	0.015	0.015	0.018	0.019	0.019	0.020
<b>0.017</b>	0.024	0.017	0.018	0.019	0.023	0.023	0.024	0.025
<b>0.033</b>	0.028	0.021	0.021	0.021	0.027	0.026	0.026	0.028
<b>0.053</b>	0.031	0.024	0.025	0.024	0.031	0.030	0.030	0.031
<b>q (K/s)</b>	<b>0.6 C18</b>				<b>0.7 C18</b>			
	<b>231 (g/l)</b>	<b>269 (g/l)</b>	<b>308 (g/l)</b>	<b>350 (g/l)</b>	<b>231 (g/l)</b>	<b>269 (g/l)</b>	<b>308 (g/l)</b>	<b>350 (g/l)</b>
<b>0.004</b>	0.016	0.016	0.016	0.017	0.013	0.013	0.012	0.012
<b>0.017</b>	0.020	0.019	0.019	0.021	0.016	0.016	0.015	0.016
<b>0.033</b>	0.024	0.023	0.022	0.024	0.019	0.020	0.018	0.019
<b>0.053</b>	0.028	0.026	0.026	0.027	0.024	0.023	0.022	0.023
<b>q (K/s)</b>	<b>0.8 C18</b>				<b>0.9 C18</b>			
	<b>231 (g/l)</b>	<b>269 (g/l)</b>	<b>308 (g/l)</b>	<b>350 (g/l)</b>	<b>231 (g/l)</b>	<b>269 (g/l)</b>	<b>308 (g/l)</b>	<b>350 (g/l)</b>
<b>0.004</b>	0.011	0.008	0.010	0.010	0.008	0.007	0.007	0.007
<b>0.017</b>	0.013	0.012	0.012	0.012	0.010	0.010	0.009	0.009
<b>0.033</b>	0.015	0.015	0.015	0.016	0.013	0.014	0.013	0.012
<b>0.053</b>	0.019	0.019	0.016	0.019	0.017	0.017	0.018	0.015
<b>q (K/s)</b>	<b>C18</b>							
	<b>231 (g/l)</b>	<b>269 (g/l)</b>	<b>308 (g/l)</b>	<b>350 (g/l)</b>				
<b>0.004</b>	0.007	0.008	0.006	0.005				
<b>0.017</b>	0.010	0.010	0.008	0.008				
<b>0.033</b>	0.013	0.012	0.011	0.012				
<b>0.053</b>	0.016	0.015	0.014	0.013				

<b>(c) Toluene</b>								
<b>q (K/s)</b>	<b>C16</b>				<b>0.1 C18</b>			
	<b>300 (g/l)</b>	<b>350 (g/l)</b>	<b>400 (g/l)</b>	<b>450 (g/l)</b>	<b>300 (g/l)</b>	<b>350 (g/l)</b>	<b>400 (g/l)</b>	<b>450 (g/l)</b>
<b>0.004</b>	0.006	0.006	0.006	0.005	0.011	0.011	0.013	0.011
<b>0.017</b>	0.007	0.006	0.006	0.007	0.016	0.016	0.017	0.017
<b>0.033</b>	0.009	0.008	0.008	0.007	0.017	0.017	0.020	0.019
<b>0.053</b>	0.015	0.012	0.010	0.011	0.020	0.019	0.021	0.021
<b>q (K/s)</b>	<b>0.2 C18</b>				<b>0.3 C18</b>			
	<b>300 (g/l)</b>	<b>350 (g/l)</b>	<b>400 (g/l)</b>	<b>450 (g/l)</b>	<b>300 (g/l)</b>	<b>350 (g/l)</b>	<b>400 (g/l)</b>	<b>450 (g/l)</b>
<b>0.004</b>	0.013	0.012	0.012	0.012	0.009	0.009	0.008	0.006
<b>0.017</b>	0.016	0.015	0.014	0.015	0.012	0.010	0.012	0.010
<b>0.033</b>	0.018	0.016	0.016	0.017	0.013	0.012	0.013	0.012
<b>0.053</b>	0.019	0.020	0.018	0.021	0.015	0.016	0.015	0.015
<b>q (K/s)</b>	<b>0.4 C18</b>				<b>0.5 C18</b>			
	<b>300 (g/l)</b>	<b>350 (g/l)</b>	<b>400 (g/l)</b>	<b>450 (g/l)</b>	<b>300 (g/l)</b>	<b>350 (g/l)</b>	<b>400 (g/l)</b>	<b>450 (g/l)</b>
<b>0.004</b>	0.016	0.016	0.017	0.016	0.017	0.016	0.017	0.017
<b>0.017</b>	0.021	0.019	0.021	0.019	0.022	0.021	0.021	0.022
<b>0.033</b>	0.022	0.020	0.023	0.021	0.024	0.024	0.023	0.025
<b>0.053</b>	0.024	0.024	0.026	0.026	0.029	0.028	0.027	0.028
<b>q (K/s)</b>	<b>0.6 C18</b>				<b>0.7 C18</b>			
	<b>300 (g/l)</b>	<b>350 (g/l)</b>	<b>400 (g/l)</b>	<b>450 (g/l)</b>	<b>300 (g/l)</b>	<b>350 (g/l)</b>	<b>400 (g/l)</b>	<b>450 (g/l)</b>
<b>0.004</b>	0.014	0.014	0.013	0.012	0.011	0.010	0.011	0.009
<b>0.017</b>	0.018	0.017	0.016	0.016	0.014	0.015	0.014	0.014
<b>0.033</b>	0.019	0.020	0.020	0.019	0.017	0.017	0.017	0.018
<b>0.053</b>	0.023	0.022	0.023	0.024	0.018	0.020	0.021	0.021
<b>q (K/s)</b>	<b>0.8 C18</b>				<b>0.9 C18</b>			
	<b>300 (g/l)</b>	<b>350 (g/l)</b>	<b>400 (g/l)</b>	<b>450 (g/l)</b>	<b>300 (g/l)</b>	<b>350 (g/l)</b>	<b>400 (g/l)</b>	<b>450 (g/l)</b>
<b>0.004</b>	0.008	0.007	0.007	0.008	0.006	0.007	0.007	0.006
<b>0.017</b>	0.011	0.010	0.009	0.012	0.008	0.010	0.008	0.009
<b>0.033</b>	0.012	0.012	0.011	0.014	0.012	0.011	0.012	0.011
<b>0.053</b>	0.017	0.016	0.015	0.015	0.014	0.013	0.012	0.015
<b>q (K/s)</b>	<b>C18</b>							
	<b>300 (g/l)</b>	<b>350 (g/l)</b>	<b>400 (g/l)</b>	<b>450 (g/l)</b>				
<b>0.004</b>	0.003	0.005	0.005	0.005				
<b>0.017</b>	0.008	0.008	0.009	0.009				
<b>0.033</b>	0.010	0.011	0.009	0.009				
<b>0.053</b>	0.012	0.013	0.012	0.012				

From the values of  $u_c$  it was possible to determine the nucleation mechanism by plotting  $\ln q$  against  $\ln u_c$  and fitting a straight line through the data points. The slope of this line provided an indication of the nucleation mechanism according to the “rule of three” a slope larger than three corresponds to progressive nucleation (PN) and a slope smaller than three corresponds to instantaneous nucleation (IN). Selected results of  $\ln q$  vs.  $\ln u_c$  fitting are shown in **Figure 9.2** for the equi-molar sample of 0.5C18 in toluene at concentrations of 300, 350, 400 and 450 g/l. The resulting slope

values and indicated nucleation mechanism together with the correlation values of  $R^2$  are listed in **Tables 9.2-9.4** with respect to the three solvents of n-dodecane, kerosene and toluene. The PN ruled nucleation process with thermodynamic factors limited the nucleation rate, which is essential to determine the important parameters. This was achieved using KBHR by applying **Equation (2.26)** to the poly-thermal data with a non-linear plot in  $\ln q - u_c$  co-ordinates. From the best fit, three free parameters were derived ( $a_1$ ,  $a_2$  and  $\ln q_0$ ) with correlation  $R^2$  values given in **Tables 9.2-9.4** for the samples crystallised with PN nucleation in three solvents. Moreover, using the molecular volume and crystallisation enthalpy values (provided in **Chapter 6**) by **Equation (2.27)**, the essential nucleation parameters for PN ruled crystallisation i.e. interfacial tension, nuclei radius and number were calculated and are presented in **Table 9.5**.

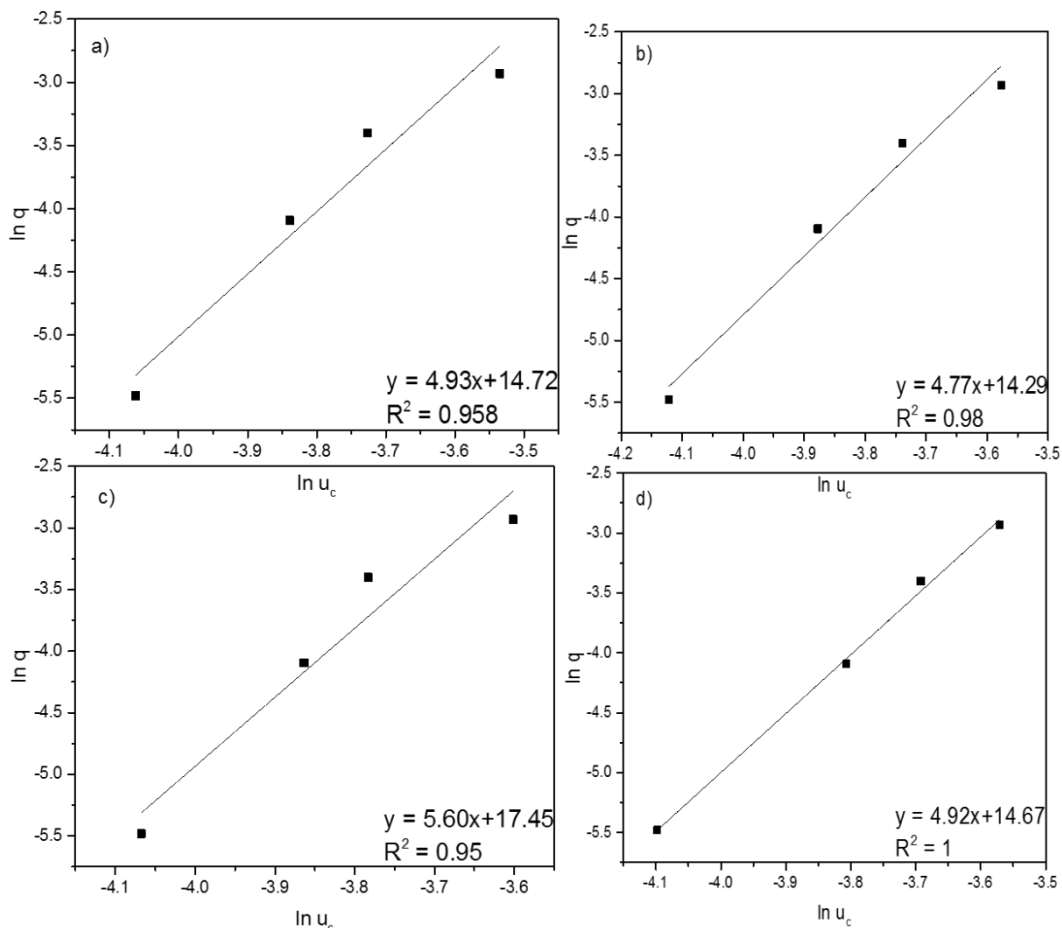


**Figure 9.2: Plots  $\ln q$  vs.  $\ln u_c$  for equi-molar 0.5C18 mixture component in toluene solvent at concentrations of a) 300 g/l. b) 350 g/l. c) 400 g/l. d) 450 g/l. Together with the best linear fit and correlation  $R^2$  values. Data points obtained using the poly-thermal method as provided in Chapter 8.**

As expected from the high fluctuating MSZW behaviour in n-dodecane, the resultant crystallisation was controlled by various nucleation mechanisms that were dependent on chain length, mixture composition and even the concentration of a solution, as seen from **Table 9.2**. The chain length had a dominant effect on this solvent with longer chain length molecules of pure C18 and binary mixtures with major compositions of C18 of  $x=0.8$  and  $0.9$  ruled by an IN mechanism with  $\ln q - \ln u_c$  slope values smaller than three (1.45-2.66) over all four concentrations studied. In contrast, the PN nucleation mechanism was favoured in shorter chain components of C16 and mixtures with a small amount impurity of C18 ( $x=0.1$ ). The associated structural behaviour tended to control from  $x=0.2$  to  $0.7$  as the three transit points respectively for a nucleation mechanism observed at  $0.2\text{C}18$ ,  $0.4\text{C}18$  and  $0.6\text{C}18$  possibility correlated to the phase transition from  $T_{16}\text{-R}_1$ ,  $R_1\text{-O}_p$  and  $O_p\text{-T}_{18}$  respectively. Conclusively, triclinic phase components of pure C18 or C16 together with the mixtures of ( $x=0.1$ ,  $0.8$  and  $0.9$ ) were crystallised with the IN and PN mechanism depending on the effect of the chain length of the solute. Binary mixtures of  $0.4\text{C}18$  and  $0.5\text{C}18$  with  $O_p$  structure were purely ruled by PN. For mixtures involving disordered  $R_1$ , the nucleation mechanisms were mostly IN controlled with variation in lower concentration at  $231$  g/l.

**Table 9.2 Parameters derived from the KBHR approach from C16/C18 mixtures crystallising from a solution of n-dodecane: slope from  $\ln q$  vs.  $\ln u_c$  plots with indicated nucleation mechanism and correlation  $R^2$  values; parameters ( $a_1$ ,  $a_2$  and  $\ln q_0$ ) as obtained from fitting equation of  $\ln q$  vs.  $u_c$  according to Equation (2.26) and correlation  $R^2$  values.**

Con (g/l)	Slope	Nucleation mechanism	$R^2$	$a_1$	$a_2 = b$	$\ln q_0$	$q_0 \left(\frac{K}{S}\right)$	$R^2$
<b>C16</b>								
192	4.15	PN	0.99	3	2.67E-04	7.89	2669.80	1.00
231	4.29	PN	0.96	3	1.93E-04	8.88	7160.75	0.97
269	3.33	PN	0.93	3	4.84E-05	8.74	6270.62	0.91
308	2.99	PN	0.94	3	1.26E-05	8.67	5816.36	0.92
<b>0.1 C18</b>								
192	8.93	PN	0.94	3	1.51E-03	9.86	19172.07	0.89
231	7.09	PN	0.99	3	1.26E-03	8.84	6882.24	0.99
269	6.35	PN	0.85	3	1.01E-03	9.16	9476.40	0.84
308	7.34	PN	0.93	3	1.19E-03	9.59	14624.45	0.94
<b>0.2 C18</b>								
231	3.14	PN	0.99	3	5.58E-06	9.20	9881.01	0.98
269	2.77	IN	0.96					
308	2.33	IN	0.98					
<b>0.3 C18</b>								

<b>231</b>	3.06	PN	0.98	3	9.03E-06	9.51	13557.02	0.97
<b>269</b>	2.16	IN	0.98					
<b>308</b>	1.58	IN	0.98					
<b>0.4C18</b>								
<b>192</b>	5.97	PN	1.00	3	8.46E-04	8.51	4965.90	1.00
<b>231</b>	7.60	PN	0.98	3	1.15E-03	9.41	12227.22	0.97
<b>269</b>	6.48	PN	0.97	3	6.91E-04	9.43	12484.34	0.98
<b>308</b>	6.35	PN	0.98	3	6.51E-04	9.23	10202.83	0.98
<b>0.5C18</b>								
<b>192</b>	4.09	PN	0.95	3	3.24E-04	7.86	2584.77	0.95
<b>231</b>	4.68	PN	0.95	3	4.67E-04	8.13	3383.38	0.95
<b>269</b>	5.31	PN	0.96	3	6.51E-04	8.40	4438.76	0.96
<b>308</b>	6.33	PN	0.99	3	9.21E-04	8.76	6365.89	1.00
<b>0.6C18</b>								
<b>192</b>	2.73	IN	0.93					
<b>231</b>	4.05	PN	0.97		1.41E-04	8.84	6916.60	0.98
<b>269</b>	3.65	PN	0.97		8.52E-05	8.59	5371.70	0.97
<b>308</b>	3.30	PN	0.96		4.96E-05	8.58	5341.86	0.96
<b>0.7C18</b>								
<b>192</b>	2.79	IN	0.93					
<b>231</b>	3.87	PN	0.88		9.99E-05	9.56	14123.99	0.87
<b>269</b>	3.32	PN	0.96		2.60E-05	9.22	10085.26	0.99
<b>308</b>	3.82	PN	0.99		7.07E-05	9.01	8143.70	0.99
<b>0.8C18</b>								
<b>192</b>	1.45	IN	0.99					
<b>231</b>	1.97	IN	0.99					
<b>269</b>	1.60	IN	0.99					
<b>308</b>	2.36	IN	0.99					
<b>0.9C18</b>								
<b>192</b>	1.53	IN	0.98					
<b>231</b>	2.66	IN	0.84					
<b>269</b>	1.82	IN	0.99					
<b>308</b>	2.57	IN	0.97					
<b>C18</b>								
<b>192</b>	1.82	IN	0.99					
<b>231</b>	1.56	IN	0.99					
<b>269</b>	1.75	IN	0.97					
<b>308</b>	1.49	IN	0.99					

In kerosene solutions, consistent mechanism behaviour was obtained as in n-dodecane for a single alkane of C16 was PN controlled and C18 was mainly or nearly IN controlled, as indicated by the slope number, was very close to three indicating thermodynamic factor control in the system became less important whereas the kinetic factors were more controlling. For binary mixtures, most compositions were PN controlled including shorter chain C16 dominant ones ( $x=0.1$  and  $0.2$ ) and close to equal molar compositions of ( $x=0.4, 0.5, 0.6, 0.7$  and  $0.8$ ). Similarly, compositions close to the long-chain component of C18 were mainly or close to IN behaviour for

0.9C18. At last, a composition of 0.3C18 was mostly mediated by IN nucleation in kerosene, the same as in n-dodecane.

Interestingly observation has been found in toluene solution, as shown in **Table 9.4**, both C16 and C18 crystallising by IN mechanism with smaller MSZW than the mixtures. Binary mixtures are mostly ruled by PN crystallisation, especially compositions of x=0.1, 0.2, 0.4 and 0.5C18 having a large number of slope for “rule of three”. It should be noted that 0.3C18 in toluene solution are more likely to be ruled by PN rather than IN as observed in n-dodecane and kerosene solutions, while as increasing the concentration, it is getting closer to being mediated by IN. Not surprisingly, for mixtures with a composition close to C18, the slope is closer to three and controlled by IN mechanism.

**Table 9.3 Parameters derived from the KBHR approach from C16/C18 mixtures crystallising from solution of kerosene: slope from  $\ln q$  vs.  $\ln u_c$  plots with indicated nucleation mechanism and correlation R square values; parameters ( $a_1, a_2$  and  $\ln q_0$ ) as obtained from fitting equation of  $\ln q$  vs.  $u_c$  according to Equation (2.26) and correlation R square values.**

Con (g/l)	Slope	Nucleation mechanism	R <sup>2</sup>	$a_1$	$a_2 = b$	$\ln q_0$	$q_0 \left(\frac{K}{S}\right)$	R <sup>2</sup>
<b>C16</b>								
231	3.52	PN	0.79	3	7.70E-05	9.60	14695.55	0.73
269	3.63	PN	0.49	3	3.49E-05	9.59	14634.25	0.23
308	3.68	PN	0.97	3	4.87E-05	9.59	14575.83	0.97
350	4.70	PN	0.87	3	1.26E-04	10.21	27076.46	0.82
<b>0.1 C18</b>								
231	5.53	PN	0.87	3	8.12E-04	9.86	19172.07	0.89
269	6.03	PN	0.95	3	8.64E-04	8.84	6882.24	0.99
308	4.03	PN	0.83	3	4.06E-04	9.16	9476.40	0.84
350	5.67	PN	0.98	3	6.63E-04	9.59	14624.45	0.94
<b>0.2 C18</b>								
231	6.87	PN	0.92	3	7.13E-04	9.99	21861.67	0.93
269	5.46	PN	0.89	3	5.06E-04	9.28	10743.54	0.89
308	6.22	PN	0.91	3	5.93E-04	9.69	16106.37	0.91
350	5.47	PN	0.95	3	3.75E-04	9.50	13401.34	0.96
<b>0.3 C18</b>								
231	2.90	IN	0.94	3	5.99E-06	9.25	10428.52	0.91
269	2.70	IN	0.96	3				
308	3.11	PN	0.98	3	9.11E-06	9.82	18415.35	0.97
350	2.31	IN	0.99	3				
<b>0.4C18</b>								
231	6.09	PN	0.94	3	9.94E-04	8.69	5944.73	0.94
269	4.46	PN	0.95	3	2.43E-04	8.83	6852.17	0.96
308	5.16	PN	0.97	3	3.92E-04	9.00	8074.61	0.98
350	5.45	PN	0.99	3	4.19E-04	9.07	8703.50	1.00
<b>0.5C18</b>								

231	4.84	PN	0.98	3	5.12E-04	8.12	3345.09	0.99
269	5.30	PN	0.98	3	6.28E-04	8.40	4449.87	0.99
308	5.77	PN	0.98	3	7.77E-04	8.48	4837.24	0.99
350	5.77	PN	0.99	3	8.13E-04	8.38	4341.30	1.00
<b>0.6C18</b>								
231	4.50	PN	0.95	3	3.53E-04	8.37	4308.18	0.95
269	5.07	PN	0.91	3	4.63E-04	8.83	6831.30	0.90
308	5.15	PN	0.95	3	4.45E-04	8.89	7254.45	0.95
350	5.36	PN	0.99	3	4.97E-04	8.71	6063.42	1.00
<b>0.7C18</b>								
231	4.28	PN	0.94	3	2.10E-04	8.86	7054.42	0.95
269	4.22	PN	0.97	3	1.87E-04	8.79	6566.33	0.97
308	4.40	PN	0.91	3	1.92E-03	8.77	6460.49	0.97
350	3.87	PN	0.99	3	1.11E-04	8.70	5996.67	1.00
<b>0.8C18</b>								
231	4.52	PN	0.87	3	1.77E-04	9.78	17668.17	0.87
269	3.10	PN	0.97	3	1.53E-05	9.17	9576.24	0.96
308	4.66	PN	0.95	3	1.34E-04	9.98	21513.16	0.94
350	3.63	PN	0.93	3	6.51E-05	9.31	11099.55	0.91
<b>0.9C18</b>								
231	3.26	PN	0.87	3	3.36E-05	9.65	15595.22	0.82
269	2.81	IN	0.97					
308	2.51	IN	0.89					
350	3.36	PN	0.97	3	2.11E-05	9.96	21113.33	0.97
<b>C18</b>								
231	3.00	PN	0.98	3	4.55E-06	9.67	15874.35	0.97
269	3.75	PN	0.96	3	4.58E-05	10.08	23862.18	0.96
308	2.99	IN	0.98	3	2.97E-06	10.05	23237.21	0.97
350	2.59	IN	0.98					

**Table 9.4 Parameters derived from the KBHR approach from C16/C18 mixtures crystallising from solution of toluene: slope from  $\ln q$  vs.  $\ln u_c$  plots with indicated nucleation mechanism and correlation R square values; parameters ( $a_1$ ,  $a_2$  and  $\ln q_0$ ) as obtained from fitting equation of  $\ln q$  vs.  $u_c$  according to Equation (2.26) and correlation R square values.**

Con (g/l)	Slope	Nucleation mechanism	R <sup>2</sup>	$a_1$	$a_2 = b$	$\ln q_0$	$q_0 \left(\frac{K}{S}\right)$	R <sup>2</sup>
<b>C16</b>								
300	2.52	0.80	IN					
350	2.87	0.79	IN					
400	3.21	0.54	PN	n/a	n/a	n/a	n/a	n/a
450	3.05	0.92	PN	n/a	n/a	n/a	n/a	n/a
<b>0.1 C18</b>								
300	4.54	0.99	PN	3.00	1.5E-04	9.19	9843.93	0.98
350	4.46	0.98	PN	3.00	1.3E-04	9.18	9729.23	0.96
400	5.22	0.99	PN	3.00	2.7E-04	9.23	10148.69	0.98
450	3.87	0.98	PN	3.00	8.5E-05	8.66	5776.19	0.96
<b>0.2 C18</b>								
300	6.43	0.98	PN	3.00	4.1E-04	10.04	22818.57	0.98
350	5.66	0.94	PN	3.00	3.1E-04	9.87	19349.08	0.94
400	6.01	0.99	PN	3.00	3.0E-04	10.18	26444.67	1.00
450	4.71	0.93	PN	3.00	2.3E-04	9.40	12127.13	0.94

0.3 C18								
300	5.37	0.98	PN	3.00	1.5E-04	10.48	35505.75	0.99
350	4.15	0.83	PN	3.00	9.5E-05	10.27	28748.19	0.79
400	3.98	0.99	PN	3.00	4.9E-05	9.84	18697.22	0.97
450	2.93	0.99	IN					
0.4 C18								
300	7.83	0.99	PN	3.00	5.9E-04	9.22	10093.73	0.97
350	6.87	0.93	PN	3.00	5.8E-04	9.50	13353.05	0.97
400	7.13	0.96	PN	3.00	8.4E-04	9.53	13755.86	0.98
450	5.41	0.91	PN	3.00	5.4E-04	9.06	8619.91	0.93
0.5 C18								
300	4.93	0.96	PN	3.00	4.8E-04	8.43	4597.88	0.97
350	5.60	0.95	PN	3.00	3.9E-04	8.42	4522.05	0.99
400	4.77	0.98	PN	3.00	6.0E-04	8.89	7256.70	0.96
450	4.92	1.00	PN	3.00	4.1E-04	8.29	3968.13	0.99
0.6 C18								
300	5.02	0.96	PN	3.00	2.9E-04	9.06	8603.29	0.95
350	5.38	0.99	PN	3.00	3.5E-04	9.23	10160.47	1.00
400	4.41	0.97	PN	3.00	2.1E-04	8.86	7021.98	0.98
450	3.80	0.93	PN	3.00	1.4E-04	8.72	6128.34	0.93
0.7 C18								
300	4.88	1.00	PN	3.00	1.6E-04	9.56	14193.79	0.99
350	3.86	1.00	PN	3.00	7.4E-05	9.02	8246.96	0.99
400	4.18	0.96	PN	3.00	1.4E-04	9.25	10390.11	0.97
450	3.17	1.00	PN	3.00	1.5E-05	8.72	6097.54	1.00
0.8 C18								
300	3.34	0.93	PN	3.00	2.9E-05	9.75	17145.83	0.92
350	3.09	0.94	PN	3.00	1.3E-05	9.72	16729.52	0.92
400	3.50	0.94	PN	3.00	3.2E-05	10.13	25123.53	0.93
450	3.46	0.98	PN	3.00	2.0E-05	9.50	13303.87	0.96
0.9 C18								
300	2.70	0.96	IN					
350	4.43	0.96	PN	3.00	7.1E-05	10.58	39477.26	0.97
400	3.46	0.89	PN	3.00	2.3E-05	10.33	30534.42	0.85
450	3.11	0.96	PN	3.00	1.0E-05	9.98	21696.15	0.95
C18								
300	1.95	0.98	IN					
350	2.92	0.98	IN					
400	2.94	0.91	IN					
450	2.80	0.95	IN					

As shown in **Tables 9.5 to 9.7**, relatively small interfacial tension values were observed, using **Equation (2.27)** with approximation values of molecular volume given in Appendix C, for C16 and C18 alkanes and their mixtures crystallised from three representative solvents: n-dodecane, kerosene and toluene. These parameters (0.27-1.77  $\frac{mJ}{m^2}$ ) using the novel approach of KBHR to study solution phase formation kinetics were quite successful as compared with previous data listed in **Table 9.8**. It was found that the addition of homologue alkane molecules enlarged values of interfacial tension as obtained with 0.1C18 increased approximately double number from pure C18. This

observation is consistent with a previous study by Gerson [119] who studied the composition role in saturation temperature and interfacial tension by the addition of 10% molar ratio of C22 to C20 crystallising in n-dodecane. The resultant saturation temperature decreased by 4.5°C and increased more than double the initial interfacial tension by 0.75 to 1.97  $\frac{mJ}{m^2}$ .

**Table 9.5 Interfacial tension, critical radius and number of molecules for nucleation of C16/C18 mixtures in n-dodecane solution**

Con. (g/L)	$\gamma$ ( $\frac{mJ}{m^2}$ )	$r^*$ (nm)	$i^*$	Con. (g/L)	$\gamma$ ( $\frac{mJ}{m^2}$ )	$r^*$ (nm)	$i^*$
<b>C16</b>				<b>0.1C18</b>			
192	1.28	0.83-0.45	5.97-0.92	192	1.77	1.34-1.03	24.62-11.20
231	1.15	0.95-0.53	9.01-1.51	231	1.67	1.21-0.84	17.89-5.98
269	0.73	0.72-0.36	3.85-0.47	269	1.56	1.21-0.82	18.24-5.60
308	0.47	0.50-0.22	1.28-0.11	308	1.64	1.29-0.91	21.97-7.63
<b>0.2C18</b>				<b>0.3C18</b>			
192	1.13	1.17-0.77	15.07-4.31	192	1.21	1.25-0.82	18.62-5.25
231	0.27	0.55-0.25	1.56-0.15	231	0.31	0.69-0.29	3.04-0.24
<b>0.4C18</b>				<b>0.5C18</b>			
192	1.44	1.15-0.75	14.51-4.00	192	1.03	0.96-0.51	8.26-1.29
231	1.60	1.30-0.95	20.87-8.12	231	1.17	1.04-0.62	10.69-2.30
269	1.35	1.29-0.86	20.45-6.05	269	1.31	1.12-0.71	13.25-3.38
308	1.33	1.27-0.87	19.18-6.15	308	1.47	1.21-0.82	16.86-5.13
<b>0.6C18</b>				<b>0.7C18</b>			
231	0.80	1.04-0.57	10.74-1.71	231	0.80	1.06-0.56	11.23-1.68
269	0.68	0.91-0.46	7.19-0.94	269	0.51	0.80-0.37	4.87-0.49
308	0.57	0.82-0.37	5.15-0.49	308	0.71	0.95-0.48	8.14-1.06

**Table 9.6 Interfacial tension, critical radius and number of molecules for nucleation of C16/C18 mixtures in toluene solution**

Con. (g/L)	$\gamma$ ( $\frac{mJ}{m^2}$ )	$r^*$ (nm)	$i^*$	Con. (g/L)	$\gamma$ ( $\frac{mJ}{m^2}$ )	$r^*$ (nm)	$i^*$
<b>0.1C18</b>				<b>0.2C18</b>			
300	0.78	1.16-0.66	14.89-2.69	300	1.15	1.36-0.94	23.69-7.79
350	0.74	1.14-0.65	14.17-2.62	350	1.05	1.32-0.83	21.49-5.36
400	0.96	1.24-0.77	17.83-4.37	400	1.04	1.38-0.90	24.61-6.78
450	0.65	0.97-0.51	8.55-1.22	450	0.95	1.19-0.69	16.06-3.12
<b>0.3C18</b>				<b>0.4C18</b>			
300	0.81	1.41-0.86	26.30-6.07	300	1.28	1.26-0.84	19.07-5.66
350	0.69	1.23-0.70	17.56-3.26	350	1.27	1.29-0.85	20.42-5.75

400	0.55	1.12-0.59	13.41-1.92	400	1.44	1.30-0.89	20.99-6.72
				450	1.24	1.20-0.75	16.46-4.05
<b>0.5C18</b>				<b>0.6C18</b>			
300	1.16	1.12-0.66	13.28-2.73	300	1.02	1.19-0.70	15.77-3.28
350	1.08	1.11-0.64	12.79-2.50	350	1.09	1.23-0.76	17.66-4.15
400	1.25	1.22-0.76	17.02-4.21	400	0.92	1.10-0.62	12.65-2.26
450	1.10	1.10-0.65	12.62-2.60	450	0.80	1.00-0.51	9.48-1.28
<b>0.7C18</b>				<b>0.8C18</b>			
300	0.94	1.18-0.71	15.48-3.34	300	0.57	0.90-0.41	6.76-0.66
350	0.72	0.96-0.49	8.32-1.12	350	0.43	0.74-0.32	3.81-0.30
400	0.89	1.07-0.58	11.71-1.84	400	0.59	1.00-0.48	9.42-1.04
450	0.43	0.61-0.28	2.15-0.20	450	0.50	0.80-0.39	4.81-0.56
<b>0.9C18</b>							
300	0.37	0.70-0.29	3.24-0.23				
350	0.81	1.21-0.67	16.56-2.86				
400	0.56	0.92-0.50	7.38-1.18				
450	0.42	0.72-0.32	3.55-0.31				

**Table 9.7 Interfacial tension, critical radius and number of molecules for nucleation of C16/C18 mixtures in kerosene solution**

Con. (g/L)	$\gamma \left(\frac{mJ}{m^2}\right)$	$r^* (nm)$	$i^*$	Con. (g/L)	$\gamma \left(\frac{mJ}{m^2}\right)$	$r^* (nm)$	$i^*$
<b>C16</b>				<b>0.1C18</b>			
231	0.85	0.92-0.47	8.17-1.11	231	1.38	1.13-0.74	13.81-3.87
269	0.65	0.65-0.44	2.83-0.87	269	1.41	1.21-0.79	16.74-4.70
308	0.73	0.91-0.47	7.83-1.09	308	1.10	0.97-0.54	8.55-1.46
350	1.00	1.11-0.71	14.29-3.78	350	1.29	0.80-0.50	16.10-4.09
<b>0.2C18</b>				<b>0.3C18</b>			
231	1.38	1.33-0.93	22.29-7.60	231	0.27	0.54-1.53	0.23-0.11
269	1.23	1.21-0.77	16.54-4.26				
308	1.30	1.28-0.87	19.88-6.18	308	0.32	0.76-0.33	4.08-0.33
350	1.12	0.90-0.56	18.58-4.58				
<b>0.4C18</b>				<b>0.5C18</b>			
231	1.52	1.16-0.78	14.82-4.43	231	1.20	1.06-0.62	11.39-2.30
269	0.95	1.10-0.63	12.43-2.37	269	1.29	1.13-0.70	13.51-3.19
308	1.12	1.19-0.72	15.77-3.52	308	1.39	1.16-0.74	14.88-3.80
350	1.14	0.85-0.53	16.98-4.10	350	1.41	0.79-0.50	14.40-3.76
<b>0.6C18</b>				<b>0.7C18</b>			
231	1.09	1.05-0.60	10.89-2.07	231	1.02	1.04-0.57	10.63-1.76
269	1.20	1.14-0.71	13.86-3.40	269	0.98	1.02-0.56	9.95-1.67
308	1.18	1.16-0.72	14.92-3.52	308	2.14	1.14-0.81	13.87-5.07
350	1.23	0.83-0.51	14.95-3.55	350	0.83	0.78-0.40	8.00-1.10
<b>0.8C18</b>				<b>0.9C18</b>			
231	1.04	1.13-0.66	13.77-2.70	231	0.63	0.83-0.40	5.44-0.61
269	0.46	0.66-0.29	2.72-0.22				

308	0.95	1.17-0.70	15.00-3.25					
350	0.75	0.85-0.44	7.41-1.02	350	0.54	0.87-0.41	6.16-0.64	
<b>C18</b>								
231	0.34	0.51-0.22	1.25-0.10					
269	0.74	1.00-0.51	9.22-1.22					
308	0.30	0.51-0.22	1.23-0.10					

**Table 9.8 Previous studied data of interfacial tension of normal alkanes and their mixtures**

Compounds	Reported $\gamma$ ( $\frac{mJ}{m^2}$ )
<u>C20 in n-dodecane [120]</u>	0.389
C22 in <u>n-dodecane</u>	0.217-0.493
<u>C20/C18 in n-dodecane</u>	0.389
<u>C20/C19 in n-dodecane</u>	0.775
<u>C20/C21 in n-dodecane [80]</u>	1.713
<u>C20/C22 in n-dodecane</u>	1.170

## 9.4 Discussion

The nucleation mechanism represented by the slope of  $\ln q$  vs.  $\ln u_c$  according to the “rule of three”, is further plotted as a function of mixture composition, as shown in **Figure 9.3** for C18/C16 mixtures in three solvents of n-dodecane (308 g/l), kerosene (308 g/l) and toluene (350 g/l). The following discussion was built up at the representative concentration of the mixture solutes for each solvent, hence variations might exist for the full set of data in four concentrations.

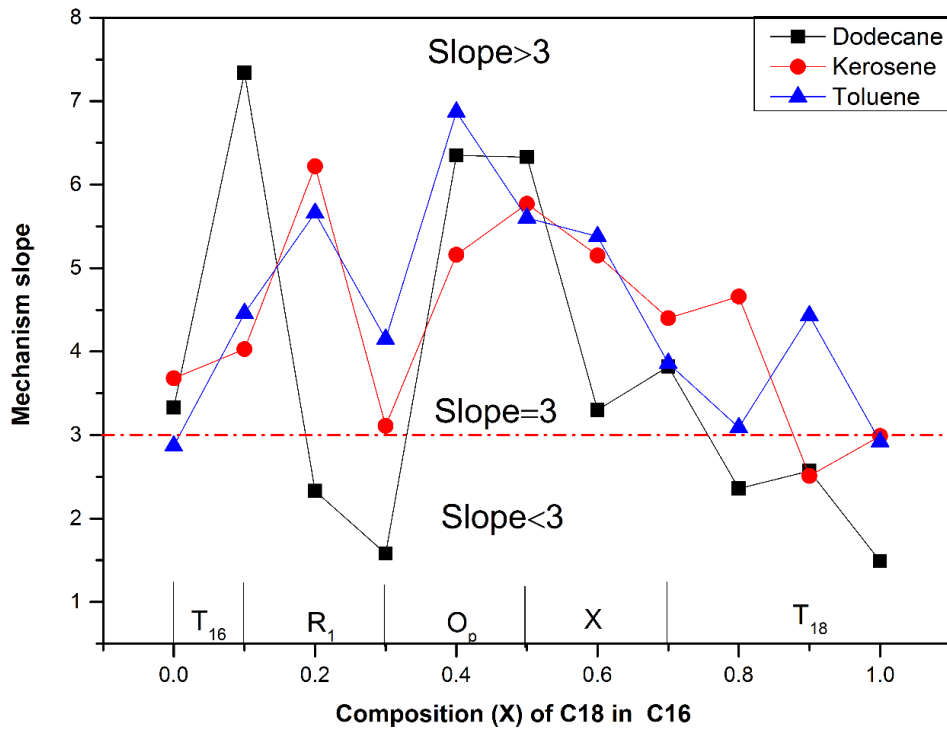


**Figure 9.3: Nucleation mechanism, represented by the slope of  $\ln q$  vs.  $\ln u_c$  according to the “rule of three”, for C18/C16 mixtures in three solvents of n-dodecane (308 g/l), kerosene (308 g/l) and toluene (350 g/l).**

Crystallisation of large proportions of binary mixture samples in three solvents was mediated by the PN nucleation mechanism with a slope larger than three which was more limited by the thermodynamic factor with respect to the associated interfacial tension. Nucleation kinetic behaviour as a function of solution environment and solute composition can be correlated to solution meta-stability (**Figure 9.1**), where the larger slope of nucleation mechanism which was PN rules crystallisation with a resultant large value of MSZW i.e. 0.1C18, 0.2C18, 0.4C18 and 0.5C18 mixture samples. In contrast, smaller MSZW components of C18, C16 having a slope smaller than three or close to three are IN ruled crystallisation as well as the mixtures having dominant compositions of long-chain alkane C18 i.e. 0.8C18 and 0.9C18 or disordered phase of 0.3C18. The nucleation will be more kinetically controlled, behaving like a heterogeneous nucleation mechanism.

Alternatively, from the structural point of view, a composition of  $x=0.1$  to  $0.5$  C18 crystallised by a disordering rotator phase, the resultant interfacial tension of this phase changes as a function phase composition. This can be related to the disorder extent of the mixture rotator phase due to the 0.3C18 having the highest level of

disordering with the least interfacial tension. As a result, it is likely to be heterogeneous nucleation with an IN mechanism. Thus increasing disorder in the solid solution would result in a low saturation temperature and lower interfacial tension which will even alter the nucleation mechanism from PN to IN.

**Table 9.9 Interfacial tension values with mixture compositions are the most PN controlled components (large slope number from the rule of three fitting) in three model solvents. Unit of  $\Upsilon$  is  $\frac{mJ}{m^2}$ .**

Sample	$\Upsilon$ (n-Dodecane)	$\Upsilon$ (Kerosene)	$\Upsilon$ (Toluene)
0.1C18	1.64	1.10	0.74
0.4C18	1.33	1.12	1.27
0.5C18	1.47	1.39	1.08

The most thermodynamically controlled mixtures of the three solvents are compared in terms of interfacial tension values at representative concentrations i.e. 308 g/l of n-dodecane and kerosene, 350 g/l of kerosene as illustrated in **Table 9.9**. The interfacial tension is generally found with smaller values in toluene and greater values in solutions of n-dodecane and kerosene which is similar to these two solvents. This means mixtures with these compositions are easier to crystallise in toluene than the other two solvents. In other words, the solute will be more kinetically controlling as the solvent solubility decreases, which can be illustrated by the observation of C16 with nucleation mechanism transferred to IN in toluene from PN ruled in n-dodecane and kerosene.

It seems that PN ruled samples are more thermodynamically controlled in n-dodecane with a large slope and interfacial tension while if IN controlled it is more kinetic also in n-dodecane with the smallest slope number. This can be explained by IN nucleation being highly kinetically limited controlling the concentration of available nuclei sites ( $C_0$ ), low solubility with resultant low concentration of nuclei sites will inhibit the onset of nucleation. For a PN nucleation, thermodynamic factors in the nucleation rate classical equation are limited by interfacial tension which is  $g$  smaller in lower solubility solvent.

## 9.5 Conclusions

The meta-stability of solution crystallisation is dominantly controlled by nucleation kinetics, i.e. PN ruled nucleation results in larger MSZW, thermodynamically controlled with larger values of interfacial tension. Whereas smaller MSZW is normally mediated by an IN mechanism.

While the nucleation behaviour has a lot of controlling factors from chain length (surface and volume), structural stability and solvent interaction. This can be delivered from the following observations. Interfacial tension of solutes with a triclinic molecular structure is found to decrease as the chain length is increased. Increasing disorder in the solid solution would result in a low saturation temperature and lower interfacial tension which can even alter the nucleation mechanism from PN to IN. When a heterogeneous type nucleation (IN) is formed, the high solubility solvent will accelerate the process by increasing the effective concentration of homologue molecules. However, if there is homogeneous nucleation with high PN slopes, a lower solubility would result in lower interfacial tension from less interaction between solute and solvent.

## **Chapter 10      Conclusions and Future Work**

*Summary:*

*This chapter will conclude the outcomes from this work, reassessment of the aims and objectives of the thesis and suggestions for future work.*

## 10.1 Conclusions of this Study

This work has provided a fundamental study on the binary mixtures of octadecane (C18) and hexadecane (C16) homologues regarding their crystallisation behaviour as a function of mixture composition. This is examined by the influence of crystallisation environment, i.e. in melt phase and in three representative model fuels of n-dodecane, kerosene and toluene.

The structure and morphology of a single component were initially determined in Chapter 5. The structure of C18 crystallised in the melt phase at a low temperature of - 40°C using computational systematic search modelling in combination with high resolution synchrotron powder diffraction data was confirmed to be reliable in determining the structure as indicated by a good agreement with the structure determined by the single crystal method from Nyburg [60] but with the benefit of simpler sample preparation methodologies.

The existence of pre-ordering clusters prior to the solid formation due to the methylene group interaction between interchain molecules was detected by time-resolved synchrotron X-ray diffraction. Thermal expansion coefficients regarding the lattice volume of C18 ( $4.17 \pm 2.48 \times 10^{-4} \text{ }^\circ\text{C}^{-1}$ ) and C16 ( $4.39 \pm 1.94 \times 10^{-4} \text{ }^\circ\text{C}^{-1}$ ) crystals with close values determined from unit cell parameters from the time-resolved XRD. Also, the anisotropic character of crystals was shown with variable thermal expansion behaviour from different axial directions and angles.

Crystal growth studies of C18 carried out in three supersaturations ( $\sigma = 0.036, 0.045$  and  $0.08$ ) in n-dodecane solution revealed a plate-like morphology dominated by the {001} habit plane with smaller side faces changing with supersaturations. Morphological indexation of the observed crystals are predicted using BFDH in combination with the zone axis method with the observed smaller faces (010) (321) (2-10) for  $\sigma = 0.036$ , (1-20) (230) (100) for  $\sigma = 0.045$ , (-110) (130) for  $\sigma = 0.08$ .

Hexadecane presented consistency with homologue molecules of C18 in association with polymorphic behaviour and thermal expansion properties except for the reduced disordering effect in the c-axis. The structure determined using only Rietveld refinement shows good simulation with values of  $R_{wp}$  (0.01) and goodness of fit (2.16). However, as the hydrogen positions could not be recognised in Rietveld refinement

this is the same issue as in the previous study by Me´tivaud [100], lattice energy calculations need to be taken into account for future work by systematic search.

Chapter 6 studied the C18/C16 mixtures in the melt phase in terms of thermodynamic properties and crystallisation kinetics. The binary phase diagram of C18/C16 was revealed using combination techniques of differential scanning calorimetry and powder X-ray diffraction. In between the phase diagram, five monophasic solid phases existed, i.e. the  $R_1$ ,  $T_{16}$ ,  $M_{dcp}$ ,  $O_p$  and  $T_{18}$ . In total five three-phase-equilibrium invariants are revealed including eutectic and peritectic at high temperature regions and eutectoid and peritectoid transitions at low temperature regions.

Kinetic studies using DSC, for the first time, observed the crossover behaviour of the  $R_1$  which existed in a transient to metastable to stable phase, the stability of the  $R_1$  phase was affected by both the composition and alkane chain length. Alternatively, by crash cooling crystallisation, a binary mixture of  $R_1$  solid solution had difficulty to form in the high dense packing triclinic structure, which was rather transformed to the similarly packed intermediate phases of  $M_p$  and  $O_p$ .

Chapter 7 characterised the structure of the C18/C16 mixtures that crystallised from kerosene which was found to have a variety of structural behaviour of mixed samples as a function of compositions. At the limited temperature of  $-40^\circ\text{C}$ , compositions (C16, 0.1C18, 0.7C18 0.9C18 and C18) close to pure components of C18 and C16 on both sides formed solid solutions in triclinic structure with respect to the chain length of the dominant homologue. 0.3C18, 0.4C18 and 0.5C18 were multiple phases with the inherent triclinic structure and two high symmetry structures which were indicated as  $M_{dcp}$  and  $O_p$  with respect to the melt phase solid solution mixtures.

The structure of C18 or C16 crystallising from kerosene solution was refined with the melt structure and had consistency with the melt phase. It also presented with an is polymorphism nature in solution crystallisation of C18 or C16 by in-situ cooling from liquid to  $-40^\circ\text{C}$ . However, the thermal expansion of the molecular volume of the triclinic cell in solution phases of these two components had shown some disordering as the non-ideal linear trend and larger deviation.

The rotator induced crystallisation observed in melt phase alkanes was also found in solution crystallisation. However, it only existed for the mixtures with the longer chain compositions smaller than the equimolar ( $x=0.1, 0.3, 0.4, 0.5\text{C18}$ ). The metastability

of this induced rotator phase was dependent on the mixture compositions which were reduced as the composition of the long chain homologue increased.

Chapters 8 and 9 introduced a poly-thermal method to detect the crystallisation and dissolution temperatures for the C18/C16 mixtures in three model solvents of n-dodecane, kerosene and toluene. In Chapter 8, solubility is determined and assessed with saturation temperature and Van't Hoff analysis. It was found that solubility is in good agreement with the activity coefficient with higher solubility in n-dodecane and the closest to an ideal condition was followed by kerosene and toluene. The saturation temperature reveals the structural transition behaviour as a function of mixture solubility with consistent behaviour in all three solvents. The activity coefficient is found to reflect the non-identical phase formation in solution crystallisation as the high deviation value observed from the C18 molar composition of  $x=0.1, 0.5-0.7$  in all three solvents. Dissolution enthalpy has some inconsistent behaviour in three solvents especially for the mixtures crystallised in disordered structures from  $x=0.2-0.4$ .

Conclusively, the nature of solvents within this study has no major effect on the structural behaviour of C18/C16 mixtures. However, dissolution enthalpy could give more information than the saturation temperatures in the case where mixture samples are formed continuously which is non-distinguishable from transmission detection, i.e. effects from disordering structures or multiple phase formations.

A comprehensive nucleation kinetics study using the KBHR approach based on the poly-thermal data was presented in Chapter 9. The meta-stability of solution crystallisation is dominantly controlled by nucleation kinetics, i.e. PN ruled nucleation resulting in larger MSZW, thermodynamically controlled with larger values of interfacial tension. Whereas smaller MSZW is normally mediated by the IN mechanism.

Crystallisation of most binary mixture samples in three solvents was found to be mediated by the PN nucleation mechanism, which was more limited by the thermodynamic factor and associated interfacial tension. Cases of instantaneous nucleation were also seen in particular compositions with higher C18 concentration i.e. 0.8C18 and 0.9C18 or a disordered phase of 0.3C18. Relatively small interfacial tension values were observed for C16 and C18 alkanes and their mixtures crystallised from three representative solvents n-dodecane, kerosene and toluene. These

parameters ( $0.27-1.77 \frac{mJ}{m^2}$ ) using the novel approach of KBHR to study solution phase formation kinetics were rather successful as compared with previous data.

Nucleation behaviour was found to be affected by chain length (surface and volume), structural stability and solvent interaction. This can be delivered from the following observations. Interfacial tension of solutes with triclinic molecular structure was found to decrease with increasing the chain length. Increasing disorder in the solid solution would result in a low saturation temperature and lower interfacial tension which can also alter the nucleation review of aims and objectives. Higher solubility is found to accelerate the instantaneous nucleation by increasing effective solute concentration, whilst inhibiting the progressive nucleation by causing larger interfacial tension.

## 10.2 Review of Aims and Objectives

- Objective 1: the crystal structure determined by high resolution synchrotron powder data and computational modelling on single alkane of C18 which need to extend to C16 and binary mixture samples.
- Objective 2: has been fully accomplished with a three solvent system.
- Objective 3: nucleation and growth kinetics were achieved using a poly-thermal crystallisation method and application of the KBHR approach. Further calculations of nucleation rate can be carried out by known mass balances from the composition of crystallised solid and the solute composition in solution.
- Objective 4: morphology and growth work was carried out with single alkane C18 in one representative solvent due to the time scale of these experiments and lack of metastability. This work can be extended to the mixture of solid solutions and other solvents.
- Objective 5 has not been able to achieve in the limited time scale of the PhD.

## 10.3 Suggestions for Future Work

This work has concentrated on the understanding of crystal structures, solubility and associated nucleation kinetics with C18/C16 model components as a function of crystallisation environment. To accomplish all the objectives, it is important to apply the computational modelling of a systematic search of C16 and C18/C16 mixtures to confirm the structural behaviour which is certainly not sufficient as defined just by unit

cell parameters. The influence on crystal morphology will be extended from n-dodecane to kerosene and toluene using in-situ growth cell and phase contrast microscopy. Meanwhile, the mixture structures in the different aromatic solvent of toluene essentially need to be determined.

Crystallisation via a rotation phase from the high temperature region was found in the melt and solution phase in this thesis. Future work will be needed for a better understanding of nucleation with insight into structure behaviour in a liquid state. Expected results will reveal the early stages of molecular aggregation prior to the formation of nucleation clusters and how they assemble during nucleation and subsequent growth aiming to build up a structural picture of a nucleation event. Small angle X-ray scattering (SAXS) has been performed on cooled binary mixtures on the X27C beamline at the NSLS using a Q-range of  $0.065 - 0.2 \text{ \AA}^{-1}$ . Scattering from samples (of C18) was weak and hence necessitated a 180 s exposure time. Two size regimes were observed: small structures (in the high Q region), and more extended structures in the low Q region (**Figure 10.1**). The increase in slope of scattering intensity as a function of the Q range from 0.06-0.1  $\text{A}^{-1}$  is consistent with a change in molecular ordering prior to crystallisation (A) followed by a much more abrupt change at the onset of crystallisation (B). Structures in the high-Q region provide some evidence of the presence of pre-nucleation clustering (initiated from dimers). However, the data in this region was limited by resolution and did not yield structure of such intermediates. SANS experiment will complement the previous x-ray studies and will not only utilise the lower Q-range accessible at ILL (to  $10^{-4} \text{ \AA}^{-1}$ ), but will use contrast variation (e.g. between h-C16/ C18 alkane ( $-0.43 \times 10^{-6}/\text{\AA}^2$ ) and d-dodecane ( $\sim 6.7 \times 10^{-6}/\text{\AA}^2$ )) in order to allow accurate determination of form factors in both low and high Q-regions and allow characterisation of pre-nucleation structures.

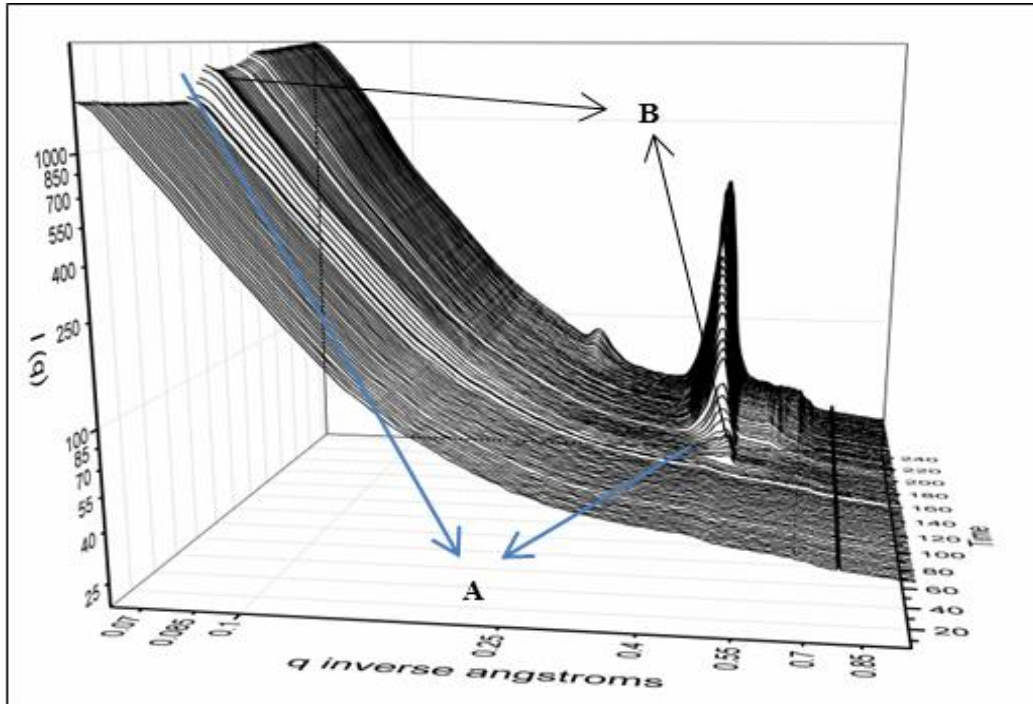


**Figure 10.1: The integrated SAXS raw data for pure C18 during a poly-thermal cooling crystallisation process at a  $0.1^\circ\text{C}/\text{min}$  cooling rate, the figure is plotted in scattering counts as a function of  $q$  range ( $\text{\AA}^{-1}$ ) and cooling time (mins).**

Techniques developed from this model system could be extended to the real HVO fuels and the blended mixture of HVO in diesel fuel to fulfil the practical application.

## List of References

1. Kamm, B., P.R. Gruber, and M. Kamm, *Biorefineries—industrial processes and products*. Vol. 1-2. 2006: Wiley Online Library.
2. Stevens, C. and R. Verhé, *Renewable bioresources: scope and modification for non-food applications*. 2004: John Wiley & Sons.
3. Knothe, G., *Dependence of biodiesel fuel properties on the structure of fatty acid alkyl esters*. Fuel processing technology, 2005. **86**(10): p. 1059-1070.
4. ; Available from: [https://en.wikipedia.org/wiki/Fatty\\_acid\\_methyl\\_ester](https://en.wikipedia.org/wiki/Fatty_acid_methyl_ester).
5. Schenk, P.M., et al., *Second generation biofuels: high-efficiency microalgae for biodiesel production*. Bioenergy research, 2008. **1**(1): p. 20-43.
6. Huber, G.W. and A. Corma, *Synergies between Bio-and Oil Refineries for the Production of Fuels from Biomass*. Angewandte Chemie International Edition, 2007. **46**(38): p. 7184-7201.
7. Derr, D.L., et al., *Method of manufacturing a catalyst and method for preparing fuel from renewable sources using the catalyst*, 2012, Google Patents.
8. Gürü, M., et al., *Improvement of Diesel fuel properties by using additives*. Energy Conversion and Management, 2002. **43**(8): p. 1021-1025.
9. Dunn, R.O., M.W. Shockley, and M.O. Bagby, *Improving the low-temperature properties of alternative diesel fuels: Vegetable oil-derived methyl esters*. Journal of the American Oil Chemists' Society, 1996. **73**(12): p. 1719-1728.
10. Roberts, K.J., *Diesel cold flow additive design 2009b.ppt*, 2009.
11. Mc Kie, D. and C. Mc Kie, *Essentials of crystallography*. 1986.
12. Klug, H.P. and L.E. Alexander, *X-ray diffraction procedures: for polycrystalline and amorphous materials*. X-Ray Diffraction Procedures: For Polycrystalline and Amorphous Materials, 2nd Edition, by Harold P. Klug, Leroy E. Alexander, pp. 992. ISBN 0-471-49369-4. Wiley-VCH, May 1974., 1974. **1**.
13. Mullin, J.W., *Crystallization*. 4 ed. 2001: Butterworth-Heinemann.
14. Tilley, R.J., *Crystals and crystal structures*. Vol. 2. 2006: John Wiley & Sons. 24.
15. Cullity, B.D., *Elements of X-ray Diffraction*. American Journal of Physics, 1957. **25**: p. 394-395.
16. Sangwal, K., *Additives and crystallization processes: from fundamentals to applications*. 2007: John Wiley & Sons.
17. Shinoda, K. and P. Becher, *Principles of solution and solubility*. Vol. 5. 1978: M. Dekker.
18. Ostwald, W., *Studies on formation and transformation of solid materials*. Z. Phys. Chem, 1897. **22**: p. 289-330.
19. Zhang, Y. and Z. Li, *Effects of Cooling Rate, Saturation Temperature, and Solvent on the Metastable Zone Width of Triethanolamine Hydrochloride*. Industrial & Engineering Chemistry Research, 2011. **50**(10): p. 6375-6381.
20. KLEIN, J.-P., R. BOISTELLE, and J. DUGUA, *Cristallisation industrielle. aspects pratiques*. Techniques de l'ingénieur. Génie des procédés, 1994. **3**(J2788): p. J2788. 1-J2788. 31.
21. Zhu, Y., et al., *Influence of calcium ions on the crystallization of sodium bicarbonate*. Journal of crystal growth, 2005. **275**(1): p. e1333-e1339.
22. Shi, R., Y. Huang, and L. Jiao, *Crystallization kinetics of 2-chloro-4, 6-dinitroresorcinol by batch cooling crystallization method*. Chemical Engineering Communications, 2007. **194**(9): p. 1176-1186.

23. Bonnin-Paris, J., et al., *Determination of the metastable zone width of glycine aqueous solutions for batch crystallizations*. Chemical Engineering Communications, 2011. **198**(8): p. 1004-1017.
24. Nývlt, J., *Kinetics of nucleation in solutions*. Journal of Crystal Growth, 1968. **3**: p. 377-383.
25. Nielsen, A.E., *Kinetics of precipitation*. 1964: Pergamon Press;[distributed in the Western Hemisphere by Macmillan, New York].
26. Kubota, N., *A new interpretation of metastable zone widths measured for unseeded solutions*. Journal of Crystal Growth, 2008. **310**(3): p. 629-634.
27. Sangwal, K., *A novel self-consistent Nývlt-like equation for metastable zone width determined by the polythermal method*. Crystal Research and Technology, 2009. **44**(3): p. 231-247.
28. Kashchiev, D. and A. Firoozabadi, *Induction time in crystallization of gas hydrates*. Journal of crystal growth, 2003. **250**(3): p. 499-515.
29. Kashchiev, D., et al., *Effect of cooling rate on the critical undercooling for crystallization*. Journal of Crystal Growth, 2010. **312**(5): p. 698-704.
30. Kashchiev, D., et al., *Dependence of the critical undercooling for crystallization on the cooling rate*. The Journal of Physical Chemistry B, 2010. **114**(16): p. 5441-5446.
31. Corzo, D.M.C., et al., *Nucleation mechanism and kinetics from the analysis of polythermal crystallisation data: methyl stearate from kerosene solutions*. CrystEngComm, 2014. **16**(6): p. 974-991.
32. Kodre, K., et al., *Research and Reviews: Journal of Pharmaceutical Analysis*.
33. Simmons, A.n.d. x-ray\_tube. Available from: [http://www.genesis.net.au/~ajs/projects/medical\\_physics/graphics/x-ray\\_tube.jpg](http://www.genesis.net.au/~ajs/projects/medical_physics/graphics/x-ray_tube.jpg).
34. Suryanarayana, C. and M.G. Norton, *X-ray diffraction: a practical approach*. 1998: Springer.
35. Stock, S. and B. Cullity, *Elements of X-ray diffraction*. Prentice Hall, Upper Saddle River, NJ, 2001.
36. Mnyukh, Y.V., *The structure of normal paraffins and of their solid solutions*. Journal of Structural Chemistry, 1960. **1**(3): p. 346-365.
37. Turner, W.R., *Normal alkanes*. Industrial & Engineering Chemistry Product Research and Development, 1971. **10**(3): p. 238-260.
38. Dirand, M., et al., *Normal Alkanes, Multialkane Synthetic Model Mixtures, and Real Petroleum Waxes: Crystallographic Structures, Thermodynamic Properties, and Crystallization*. Journal of Chemical & Engineering Data, 2002. **47**(2): p. 115-143.
39. Ubbelohde, A.R., *Structure and thermodynamic properties of long-chain compounds*. Transactions of the Faraday Society, 1938. **34**(0): p. 282-299.
40. Müller, A. and K. Lonsdale, *The low-temperature form of C<sub>18</sub>H<sub>38</sub>*. Acta Crystallographica, 1948. **1**(3): p. 129-131.
41. Broadhurst, M.G., *An analysis of the solid phase behavior of the normal paraffins*. J. Res. Natl. Bur. Stand. A, 1962. **66**: p. 241-249.
42. Craig, S.R., et al., *Investigation into the structures of some normal alkanes within the homologous series C<sub>13</sub>H<sub>28</sub> to C<sub>60</sub>H<sub>122</sub> using high-resolution synchrotron X-ray powder diffraction*. Journal of Materials Chemistry, 1994. **4**(6): p. 977-981.

43. Roblès, L., et al., *Mise au point sur le comportement énergétique et cristallographique des n-alcane. II. Série de C<sub>22</sub>H<sub>46</sub> à C<sub>27</sub>H<sub>56</sub>*. J. Chim. Phys., 1998. **95**(1): p. 92-111.
44. Maroncelli, M., et al., *Nonplanar conformers and the phase behavior of solid n-alkanes*. Journal of the American Chemical Society, 1982. **104**(23): p. 6237-6247.
45. Piesczek, W., G. Strobl, and K. Malzahn, *Packing of paraffin chains in the four stable modifications of n-tritriacontane*. Acta Crystallographica Section B: Structural Crystallography and Crystal Chemistry, 1974. **30**(5): p. 1278-1288.
46. Snyder, R.G., et al., *Phase transitions and nonplanar conformers in crystalline n-alkanes*. Science, 1981. **214**(4517): p. 188-190.
47. Craig, S.R., *Synchrotron Radiation Studies of the Structure of n-Alkanes and Homologous Mixtures*, in *Department of Pure and Applied Chemistry 1995*, University of Strathclyde.
48. Sirota, E., et al., *Rotator phases of the normal alkanes: An x-ray scattering study*. The Journal of chemical physics, 1993. **98**(7): p. 5809-5824.
49. Ungar, G., *Structure of rotator phases in n-alkanes*. The Journal of Physical Chemistry, 1983. **87**(4): p. 689-695.
50. Denicolò, I., J. Doucet, and A.F. Craievich, *X-ray study of the rotator phase of paraffins (III): Even-numbered paraffins C<sub>18</sub>H<sub>38</sub>, C<sub>20</sub>H<sub>42</sub>, C<sub>22</sub>H<sub>46</sub>, C<sub>24</sub>H<sub>50</sub>, and C<sub>26</sub>H<sub>54</sub>*. The Journal of Chemical Physics, 1983. **78**(3): p. 1465-1469.
51. Ungar, G. and N. Masic, *Order in the rotator phase of n-alkanes*. The Journal of Physical Chemistry, 1985. **89**(6): p. 1036-1042.
52. Sirota, E., et al., *Rotator phases in mixtures of n-alkanes*. The Journal of Physical Chemistry, 1995. **99**(2): p. 798-804.
53. Sirota, E. and A. Herhold, *Transient phase-induced nucleation*. Science, 1999. **283**(5401): p. 529-532.
54. Sirota, E.B. and A.B. Herhold, *Transient rotator phase induced nucleation in n-alkane melts*. Polymer, 2000. **41**(25): p. 8781-8789.
55. Srivastava, S., et al., *Study of the temperature and enthalpy of thermally induced phase-transitions in n-alkanes, their mixtures and Fischer-Tropsch waxes*. Petroleum Science And Technology, 2000. **18**(5-6): p. 493-518.
56. Kravchenko, V., *The eutectics and solid solutions of paraffins*. Acta Physicochim. URSS, 1946. **21**: p. 335-344.
57. Dorset, D.L. and R.G. Snyder, *Crystal structure of modulated n-paraffin binary solids*. The Journal of Physical Chemistry, 1996. **100**(23): p. 9848-9853.
58. Dorset, D.L., *Crystal structure of an n-paraffin binary eutectic solid. An electron diffraction determination*. The Journal of Physical Chemistry B, 1997. **101**(25): p. 4870-4874.
59. Mazee, W., *Thermal analysis of normal alkanes*. Analytica Chimica Acta, 1957. **17**: p. 97-106.
60. Nyburg, S. and H. Lüth, *n-Octadecane: A correction and refinement of the structure given by Hayashida*. Acta Crystallographica Section B: Structural Crystallography and Crystal Chemistry, 1972. **28**(10): p. 2992-2995.
61. Gerson, A.R. and S. Nyburg, *Structures of two binary n-alkane solid solutions*. Acta Crystallographica Section B: Structural Science, 1994. **50**(2): p. 252-256.
62. Metivaud, V., et al., *Complete determination of the solid (RI)-liquid equilibria of four consecutive n-alkane ternary systems in the range C<sub>14</sub>H<sub>30</sub>-C<sub>21</sub>H<sub>44</sub> using only binary data*. Canadian journal of chemistry, 1999. **77**(3): p. 332-339.

63. Metivaud, V., et al., *Solid-solid and solid-liquid equilibria in the heneicosane-docosane binary system*. Chemistry of materials, 1999. **11**(1): p. 117-122.
64. Achour-Boudjema, Z., M. Bouroukba, and M. Dirand, *Binary phase diagram of molecular alloys of the consecutive even-numbered n-alkanes n-tetracosane (n-C 24 H 50) and n-hexacosane (n-C 26 H 54)*. Thermochimica acta, 1996. **276**: p. 243-256.
65. Rajabalee, F., et al., *New insights on the crystalline forms in binary systems of n-alkanes: Characterization of the solid ordered phases in the phase diagram tricosane+ pentacosane*. Journal of Materials Research, 1999. **14**(06): p. 2644-2654.
66. Nozaki, K., et al., *Solid-solid phase transitions in n-alkanes C<sub>23</sub>H<sub>48</sub> and C<sub>25</sub>H<sub>52</sub>: X-ray power diffraction study on new layer stacking in phase V*. The Journal of Chemical Physics, 1995. **103**(13): p. 5762-5766.
67. Rajabalee, F., et al., *Ordered Phases in n-Heptacosane (C<sub>27</sub>H<sub>56</sub>). Structure Determination of the Mdc1 Phase*. Chemistry of Materials, 2002. **14**(10): p. 4081-4087.
68. Rajabalee, F., et al., *Perfect families of mixed crystals: the "ordered" crystalline forms of n-alkanes*. Physical Chemistry Chemical Physics, 2000. **2**(6): p. 1345-1350.
69. Teare, P., *The crystal structure of orthorhombic hexatriacontane, C<sub>36</sub>H<sub>74</sub>*. Acta Crystallographica, 1959. **12**(4): p. 294-300.
70. Domańska, U. and J. Rolińska, *Correlation of the solubility of even-numbered paraffins C<sub>20</sub>H<sub>42</sub>, C<sub>24</sub>H<sub>50</sub>, C<sub>26</sub>H<sub>54</sub>, C<sub>28</sub>H<sub>58</sub> in pure hydrocarbons*. Fluid Phase Equilibria, 1989. **45**(1): p. 25-38.
71. Ruffier-Meray, V., et al., *Experimental determination and representation of binary and ternary diagrams of n-hexacosane, n-octacosane and n-heptane*. Revue de l'Institut français du pétrole, 1998. **53**(1): p. 27-33.
72. Gerson, A.R., et al., *The role of growth environment on the crystallization of normal alkanes in the homologous series from C<sub>18</sub>H<sub>38</sub> to C<sub>29</sub>H<sub>60</sub>*. Journal of crystal growth, 1993. **128**(1-4): p. 1176-1181.
73. Craig, S., et al., *Investigation into the structures of binary-, tertiary-and quaternary-mixtures of n-alkanes and real diesel waxes using high-resolution synchrotron X-ray powder diffraction*. Journal of Materials Chemistry, 1998. **8**(4): p. 859-869.
74. Flöter, E., et al., *The ternary system (n-heptane+ docosane+ tetracosane): the solubility of mixtures of docosane and tetracosane in heptane and data on solid-liquid and solid-solid equilibria in the binary subsystem (docosane+ tetracosane)*. Journal of Chemical & Engineering Data, 1997. **42**(3): p. 562-565.
75. Turnbull, D. and R.L. Cormia, *Kinetics of Crystal Nucleation in Some Normal Alkane Liquids*. The Journal of Chemical Physics, 1961. **34**(3): p. 820-831.
76. Oliver, M.J. and P.D. Calvert, *Homogeneous nucleation of n-alkanes measured by differential scanning calorimetry*. Journal of Crystal Growth, 1975. **30**(3): p. 343-351.
77. Taggart, A., et al., *An examination of the nucleation kinetics of n-alkanes in the homologous series C<sub>13</sub>H<sub>28</sub> to C<sub>32</sub>H<sub>66</sub>, and their relationship to structural type, associated with crystallization from stagnant melts*. Langmuir, 1996. **12**(23): p. 5722-5728.
78. Turnbull, D. and F. Spaepen, *Crystal nucleation and the crystal-melt interfacial tension in linear hydrocarbons*. Journal of Polymer Science: Polymer Symposia, 1978. **63**(1): p. 237-243.

79. Roberts, K.J., J.N. Sherwood, and A. Stewart, *The nucleation of n-eicosane crystals from solution in n-dodecane in the presence of homologous impurities*. Journal of Crystal Growth, 1990. **102**(3): p. 419-426.
80. Gerson, A.R., K.J. Roberts, and J.N. Sherwood, *An instrument for the examination of nucleation from solution and its application to the study of precipitation from diesel fuels and solutions of n-alkanes*. Powder Technology, 1991. **65**(1): p. 243-249.
81. Chen, B., L. Brecevic, and J. Garside. *Nucleation of tetracosane in hydrocarbon solvents*. in *12th symposium on industrial crystallisation*. 1993.
82. Wu, X.Z., et al., *Surface Freezing in Binary Mixtures of Alkanes: New Phases and Phase Transitions*. Physical Review Letters, 1995. **75**(7): p. 1332-1335.
83. Wu, X.Z., et al., *Surface crystallization of liquid normal-alkanes*. Physical Review Letters, 1993. **70**(7): p. 958-961.
84. Bennema, P., et al., *Morphology of orthorhombic long chain normal alkanes: theory and observations*. Journal of Crystal Growth, 1992. **121**(4): p. 679-696.
85. Liu, X.-Y. and P. Bennema, *On the morphology of crystals of triclinic even normal alkanes: theory and observation*. Journal of Crystal Growth, 1994. **135**(1): p. 209-223.
86. Thompson, S., et al., *Beamline I11 at Diamond: A new instrument for high resolution powder diffraction*. Review of scientific instruments, 2009. **80**(7): p. 075107.
87. Coelho, A., *TOPAS Academic: General Profile and Structure Analysis Software for Powder Diffraction Data*. Bruker AXS, Karlsruhe, Germany, 2007.
88. Coelho, A., *Indexing of powder diffraction patterns by iterative use of singular value decomposition*. Journal of Applied Crystallography, 2003. **36**(1): p. 86-95.
89. Pawley, G., *Unit-cell refinement from powder diffraction scans*. Journal of Applied Crystallography, 1981. **14**(6): p. 357-361.
90. Macrae, C.F., et al., *Mercury: visualization and analysis of crystal structures*. Journal of Applied Crystallography, 2006. **39**(3): p. 453-457.
91. Hammond, R.B., et al., *X-form metal-free phthalocyanine: Crystal structure determination using a combination of high-resolution X-ray powder diffraction and molecular modelling techniques*. Journal of the Chemical Society, Perkin Transactions 2, 1996(8): p. 1527-1528.
92. Hammond, R.B., et al., *Computationally assisted structure determination for molecular materials from X-ray powder diffraction data*. The Journal of Physical Chemistry B, 1997. **101**(33): p. 6532-6536.
93. Kutzke, H., et al., *Metastable  $\beta$ -phase of benzophenone: independent structure determinations via X-ray powder diffraction and single crystal studies*. Acta Crystallographica Section B: Structural Science, 2000. **56**(3): p. 486-496.
94. Harris, R.K., et al., *Structural studies of the polymorphs of carbamazepine, its dihydrate, and two solvates*. Organic process research & development, 2005. **9**(6): p. 902-910.
95. Bentler, P.M. and D.G. Bonett, *Significance tests and goodness of fit in the analysis of covariance structures*. Psychological bulletin, 1980. **88**(3): p. 588.
96. Mayo, S.L., B.D. Olafson, and W.A. Goddard, *DREIDING: a generic force field for molecular simulations*. Journal of Physical chemistry, 1990. **94**(26): p. 8897-8909.

97. Okada, Y. and Y. Tokumaru, *Precise determination of lattice parameter and thermal expansion coefficient of silicon between 300 and 1500 K*. Journal of applied physics, 1984. **56**(2): p. 314-320.
98. Donnay, J.D.H. and D. Harker, *A new law of crystal morphology extending the law of Bravais*. Am. Mineral, 1937. **22**(5): p. 446-467.
99. Hayashida, T., *Crystal Structure of Triclinic Form of n-Octadecane*. Journal of the Physical Society of Japan, 1962. **17**(2): p. 306-315.
100. Métivaud, V., et al., *Hexadecane (C<sub>16</sub>H<sub>34</sub>) + 1-hexadecanol (C<sub>16</sub>H<sub>33</sub>OH) binary system: crystal structures of the components and experimental phase diagram. Application to thermal protection of liquids*. Chemistry of materials, 2005. **17**(12): p. 3302-3310.
101. Rietveld, H., *A profile refinement method for nuclear and magnetic structures*. Journal of applied Crystallography, 1969. **2**(2): p. 65-71.
102. Sun, H., *COMPASS: an ab initio force-field optimized for condensed-phase applications overview with details on alkane and benzene compounds*. The Journal of Physical Chemistry B, 1998. **102**(38): p. 7338-7364.
103. Clydesdale, G., R. Docherty, and K. Roberts, *HABIT-a program for predicting the morphology of molecular crystals*. Computer Physics Communications, 1991. **64**(2): p. 311-328.
104. Cornell, W.D., et al., *A second generation force field for the simulation of proteins, nucleic acids, and organic molecules*. Journal of the American Chemical Society, 1995. **117**(19): p. 5179-5197.
105. Santoro, A.t. and A. Mighell, *Determination of reduced cells*. Acta Crystallographica Section A: Crystal Physics, Diffraction, Theoretical and General Crystallography, 1970. **26**(1): p. 124-127.
106. Niggli, P., *Krystallographische und strukturtheoretische Grundbegriffe*. Handbuch der Experimentalphysik. Vol. 7. 1928: Akademische verlagsgesellschaft, Leipzig.
107. Hanwell, M.D., et al., *Avogadro: an advanced semantic chemical editor, visualization, and analysis platform*. Journal of Cheminformatics, 2012. **4**(1): p. 17.
108. Bennema, P., et al., *Morphology of orthorhombic long chain normal alkanes: theory and observations*. Journal of Crystal Growth, 1992. **121**(4): p. 679-696.
109. Camacho, D.M., et al., *The crystal morphology and growth rates of triclinic N-docosane crystallising from N-dodecane solutions*. Journal of Crystal Growth, 2015. **416**: p. 47-56.
110. Toby, B.H., *EXPGUI, a graphical user interface for GSAS*. Journal of applied crystallography, 2001. **34**(2): p. 210-213.
111. Kousksou, T., et al., *Paraffin wax mixtures as phase change materials*. Solar Energy Materials and Solar Cells, 2010. **94**(12): p. 2158-2165.
112. Courchinoux, R., et al., *Use of the "shape factors" as an empirical method to determine the actual characteristic temperatures of binary phase diagrams by differential scanning calorimetry*. Thermochemica Acta, 1988. **128**: p. 45-53.
113. Mondieig, D., et al., *n-Alkane Binary Molecular Alloys*. Chemistry of Materials, 2004. **16**(5): p. 786-798.
114. Wang, L.P., et al., *Size-Dependent Phase Behavior of the Hexadecane–Octadecane System Confined in Nanoporous Glass*. The Journal of Physical Chemistry C, 2014. **118**(31): p. 18177-18186.

115. Lüth, H., et al., *Crystallographic and calorimetric phase studies of the n-eicosane, C<sub>20</sub>H<sub>42</sub>: n-docosane, C<sub>22</sub>H<sub>46</sub> system*. Molecular Crystals and Liquid Crystals, 1974. **27**(3-4): p. 337-357.
116. Matsuoka, M., et al., *Purification of organic solid solutions by melt crystallization: comparison between layer and suspension crystallization*. Journal of crystal growth, 1996. **166**(1): p. 1035-1039.
117. Gerson, A.R., K. Roberts, and J.N. Sherwood, *X-ray diffraction studies of single and mixed n-alkanes in the homologous series C<sub>18</sub>H<sub>38</sub> to C<sub>28</sub>H<sub>58</sub>*. 1990: Daresbury Laboratory.
118. Provost, E., et al., *Solubility of Some n-Alkanes (C<sub>23</sub>, C<sub>25</sub>, C<sub>26</sub>, C<sub>28</sub>) in Heptane, Methylcyclohexane, and Toluene*. Journal of Chemical & Engineering Data, 1998. **43**(5): p. 745-749.
119. Gerson, A.R., et al., *Novel kinetic and structural studies of wax crystallisation*. Journal of Crystal Growth, 1990. **99**(1): p. 145-149.
120. Roberts, K., J. Sherwood, and A. Stewart, *The nucleation of n-eicosane crystals from solution in n-dodecane in the presence of homologous impurities*. Journal of Crystal Growth, 1990. **102**(3): p. 419-426.

## List of Symbols

a Dimensionless molecular latent heat of crystallisation

b Dimensionless thermodynamic parameter

$C_0$  Concentration of nucleation sites and/or instantaneously nucleated crystallites ( $m^{-3}$ )

C16 Hexadecane

C18 Octadecane

$E_{att}$  Attachment energy

$\Delta H_f$  enthalpy of fusion ( $Jmol^{-1}$ )

$\Delta C_{max}$  Maximum concentration difference ( $m^{-3}$ )

$i^*$  Number of molecules in critical nucleus

$J$  Nucleation rate ( $m^{-3}s^{-1}$ )

$k$  Boltzmann constant ( $JK^{-1}$ )

$k_j$  Empirical parameter of nucleation rate ( $m^{3(m_0-1)}s^{-1}$ )

$k_J$  Nucleation rate constant ( $m^{-3}s^{-1}$ )

$N_a$  Avogadro's number

$N_{det}$  Detectable number of crystallites

$q$  Cooling rate ( $K s^{-1}$ )

$q_0$  Parameter in the ( $q$ ) dependence for both  $PN$  and  $IN$  ( $K s^{-1}$ )

$r$  Nucleus radius ( $m$ )

$r^*$  Critical nucleus radius ( $m$ )

$S$  Supersaturation ratio

$S$  Entropy ( $Jmol^{-1}K^{-1}$ )

$T_c$  Crystallisation temperature ( $K$ )

$T_{diss}$  Dissolution temperature ( $K$ )

$T_e$  Solution saturation (or equilibrium) temperature ( $K$ )

$\Delta T$  Undercooling ( $K$ )

$\Delta T_c$  Critical undercooling for crystallisation ( $K$ )

$u$  Relative undercooling

*uc* Relative critical undercooling for crystallisation

*x* Mole fraction of C18 in C18/C16 mixtures

*x<sub>ideal</sub>* Mole fraction of solute in ideal state

*x<sub>real</sub>* Mole fraction of solute at equilibrium

$\gamma$  Interfacial tension ( $Jm^{-2}$ )

$\gamma_{eff}$  Effective interfacial tension of crystal nucleus in 3D HEN ( $Jm^{-2}$ )

$\gamma$  Activity coefficient

$\lambda$  Molecular latent heat of crystallisation ( $J$ )

$\lambda$  Wavelength (angstrom)

$\sigma$  Relative supersaturation

$\theta$  Bragg angle

$\Delta G_E$  Total excess Gibbs free energy ( $Jmol^{-1}$ )

$\Delta G_v$  Free energy change per unit volume ( $Jm^3$ )

$\Delta H_f$  Molar enthalpy of fusion ( $Jmol^{-1}$ )

$\Delta S_f$  Molar entropy of fusion ( $Jmol^{-1}K^{-1}$ )

$\Delta H_m$  Molar enthalpy of melting ( $Jmol^{-1}$ )

$\Delta S_m$  Molar entropy of melting ( $Jmol^{-1}K^{-1}$ )

$\Delta H_{diss}$  Molar enthalpy of dissolution ( $Jmol^{-1}$ )

$\Delta H_{mix}$  Molar enthalpy of mixing ( $Jmol^{-1}$ )

$\Delta S_{diss}$  Molar entropy of dissolution ( $Jmol^{-1}K^{-1}$ )

$\Delta S_{mix}$  Molar entropy of mixing ( $Jmol^{-1}K^{-1}$ )

## List of Abbreviation

BFDH= Bravais-Friedel-Donnay-Harker model

*CNT*=Classical Nucleation Theory

DLS= Diamond light source

*DIC*=Differential Interference Contrast

DSC=Differential Scanning Calorimetry

FAME=Fatty Acid Methyl Ester

HVO=Hydrogenated vegetable oil

*HEN*=Heterogeneous nucleation

*HON*=Homogeneous nucleation

HT=High temperature

*IN*=Instantaneous nucleation

KBHR=Kashchiev-Borissova-Hammond-Roberts approach

*KJMA*=Kolmogorov-Johnson-Mehl-Avrami approach

LT= Low temperature

MSZW=Metastable Zone Width

MPD=Multipurpose Diffractometer

MAC= Multi-Analysing Crystal

RT=Room temperature

*PN*=Progressive nucleation

PXRD=Powder X-ray diffraction

PSD= Position sensitive detectors

SPXD=Synchrotron powder X-ray diffraction

SAXS=Small angle x-ray scattering

SANS=Small angle neutron scattering

RT= Room Temperature

## Appendix A

The full set of planes obtained from BFDH prediction using Material studio which are grouped according to the zone axis analysis method.

Group 1			
hkl	Mult	dhkl	distance
{ 0 1 0}	2	4.60	21.73026
{ 0 1 -1}	2	4.54	22.0289
{ 0 1 1}	2	4.49	22.28928
{ 0 1 -2}	2	4.32	23.15203
{ 0 1 2}	2	4.23	23.64521
{ 0 1 -3}	2	4.00	24.98874
{ 0 1 3}	2	3.90	25.67209
{ 0 2 -1}	2	2.30	43.5444
{ 0 2 1}	2	2.28	43.80861
{ 0 2 -3}	2	2.22	44.986
{ 0 2 3}	2	2.19	45.74908
{ 0 3 -1}	2	1.53	65.2025
{ 0 3 1}	2	1.53	65.46743
{ 0 3 -2}	2	1.53	65.50244
{ 0 3 2}	2	1.51	66.02885
Group 2			
hkl	Mult	dhkl	distance
{ 1 0 2}	2	4.09	24.45061
{ 1 0 3}	2	4.06	24.64951
{ 1 0 1}	2	4.00	25.01485
{ 1 0 0}	2	3.80	26.29313
{ 1 0 -1}	2	3.55	28.1885
{ 1 0 -2}	2	3.27	30.58643
{ 1 0 -3}	2	3.00	33.3788
{ 2 0 3}	2	2.03	49.27791
{ 2 0 1}	2	1.96	51.14005
{ 2 0 -1}	2	1.84	54.34153
{ 2 0 -3}	2	1.70	58.66348
{ 3 0 2}	2	1.31	76.09709
Group 3			
hkl	Mult	dhkl	distance
{ 1 1 2}	2	3.65	27.39809
{ 1 1 3}	2	3.61	27.68016
{ 1 1 1}	2	3.60	27.7992
{ 1 1 0}	2	3.47	28.85502
{ 1 1 -1}	2	3.28	30.49762
{ 1 1 -2}	2	3.06	32.63853
{ 1 1 -3}	2	2.84	35.1869
{ 2 2 3}	2	1.82	55.02785
{ 2 2 1}	2	1.77	56.49759
{ 2 2 -1}	2	1.69	59.21652
{ 2 2 -3}	2	1.59	63.02316
Group 4			
hkl	Mult	dhkl	distance
{ 1 -1 2}	2	2.68	37.27489
{ 1 -1 3}	2	2.68	37.32846
{ 1 -1 1}	2	2.65	37.72397

{ 1 -1 0}	2	2.59	38.65817
{ 1 -1 -1}	2	2.50	40.04355
{ 1 -1 -2}	2	2.39	41.83533
{ 1 -1 -3}	2	2.27	43.98385
Group 5			
hkl	Mult	dhkl	distance
{ 1 2 2}	2	2.33	42.98705
{ 1 2 1}	2	2.32	43.17704
{ 1 2 3}	2	2.31	43.23416
{ 1 2 0}	2	2.28	43.79844
{ 1 2 -1}	2	2.23	44.83332
{ 1 2 -3}	2	2.08	48.02604
Group 6			
hkl	Mult	dhkl	distance
{ 2 1 3}	2	2.11	47.4972
{ 2 1 2}	2	2.07	48.21693
{ 2 1 1}	2	2.03	49.30961
{ 2 1 0}	2	1.97	50.75114
{ 2 1 -1}	2	1.90	52.51281
{ 2 1 -2}	2	1.83	54.56361
{ 2 1 -3}	2	1.76	56.87229
Group 7			
hkl	Mult	dhkl	distance
{ 1 -2 3}	2	1.79	55.88951
{ 1 -2 2}	2	1.79	55.90538
{ 1 -2 1}	2	1.78	56.2571
{ 1 -2 0}	2	1.76	56.93845
{ 1 -2 -1}	2	1.73	57.9378
{ 1 -2 -2}	2	1.69	59.23907
{ 1 -2 -3}	2	1.64	60.82287
Group 8			
hkl	Mult	dhkl	distance
{ 2 -1 3}	2	1.68	59.54031
{ 2 -1 2}	2	1.66	60.21193
{ 2 -1 1}	2	1.63	61.18481
{ 2 -1 0}	2	1.60	62.44487
{ 2 -1 -1}	2	1.56	63.97514
{ 2 -1 -2}	2	1.52	65.75675
{ 2 -1 -3}	2	1.48	67.7699
Group 9			
hkl	Mult	dhkl	distance
{ 1 3 2}	2	1.603436	62.36607
{ 1 3 1}	2	1.601256	62.45099
{ 1 3 3}	2	1.597884	62.58276
{ 1 3 0}	2	1.591436	62.83632
{ 1 3 -1}	2	1.574392	63.51658
{ 1 3 -2}	2	1.55081	64.48244
{ 1 3 -3}	2	1.521577	65.72131
Group 10			
hkl	Mult	dhkl	distance
{ 2 3 3}	2	1.451785	68.88072
{ 2 3 2}	2	1.44309	69.29576
{ 2 3 1}	2	1.42902	69.97804

{ 2 3 0}	2	1.410042	70.91987
{ 2 3 -1}	2	1.38675	72.11106
{ 2 3 -2}	2	1.359813	73.5395
{ 2 3 -3}	2	1.329935	75.19167

## Appendix B

Table of phase transition temperatures and corresponding heat enthalpy of C18 by five cooling/heating rates from multiple experimental repeats.

Cooling rate (C_min)	Crystallisation				Melting			
	Onset (C)	Peak (C)	End (C)	$\Delta H$ (j_g)	Onset (C)	Peak (C)	End (C)	$\Delta H$ (j_g)
0.25	26.66	26.92	26.29	198.23	27.57	28.45	28.68	-198.24
	26.59	26.86	26.20	179.91	27.51	28.36	28.71	-198.67
	26.61	27.10	26.29	211.98	27.58	28.19	28.86	-213.41
	26.65	27.01	26.35	214.69	27.51	28.18	28.58	-212.98
	26.67	26.99	26.37	213.62	27.52	28.28	28.52	-215.51
	26.64	27.07	26.37	211.73	27.57	28.17	28.53	-214.06
	26.66	26.97	26.34	208.85	27.54	28.27	28.65	-208.81
	0.01	0.05	0.04	9.21	0.03	0.11	0.13	8.07
0.5	26.50	26.83	26.12	192.18	27.58	28.36	28.74	-190.65
	26.64	26.93	26.12	191.71	27.54	28.40	28.76	-191.40
	26.71	26.94	26.25	201.64	27.60	28.32	28.71	-205.05
	26.64	27.01	26.29	193.63	27.59	28.34	28.67	-197.53
	26.65	27.05	26.19	216.88	27.54	28.34	28.80	-218.47
	26.67	26.42	25.70	140.54	27.54	28.30	28.80	-214.62
	<b>Average</b>	<u>26.64</u>	<u>26.95</u>	<u>26.19</u>	<u>199.21</u>	<u>27.57</u>	<u>28.34</u>	<u>28.75</u>
<b>Std</b>	0.07	0.08	0.08	10.66	0.03	0.03	0.05	11.79
1	26.60	26.63	25.67	169.39	27.52	28.74	29.43	-171.08
	26.64	26.03	25.18	112.70	27.56	28.68	29.40	-170.69
	26.63	25.93	24.65	86.93	27.66	28.88	29.48	-165.26
					27.62	28.86	29.52	-167.29
	26.37	26.52	25.47	166.71				
	26.58	26.12	25.28	132.66	27.50	28.56	29.21	-192.79
					27.50	28.56	29.21	-193.41
	26.41	26.72	25.68	193.08				
<b>Average</b>	<u>26.52</u>	<u>26.40</u>	<u>25.46</u>	<u>176.39</u>	<u>27.56</u>	<u>28.71</u>	<u>29.38</u>	<u>-176.75</u>
<b>Std</b>	0.12	0.31	0.23	31.95	0.07	0.14	0.13	12.85
3.2	26.42	26.17	24.36	214.99	27.45	29.30	30.76	-216.23
	26.48	25.38	21.99	117.32	27.48	29.20	30.74	-216.23
	26.40	26.07	24.37	237.86	27.49	29.35	30.75	-238.51
	26.39	26.12	24.39	234.09	27.48	29.40	30.76	-237.34
	26.48	25.43	25.22	108.66	27.52	29.20	30.66	-240.16
	26.47	25.42	25.09	121.08	27.52	29.21	30.65	-240.20
	<b>Average</b>	<u>26.44</u>	<u>25.77</u>	<u>24.24</u>	<u>228.98</u>	<u>27.49</u>	<u>29.28</u>	<u>30.72</u>
<b>Std</b>	0.04	0.39	1.17	12.26	0.03	0.09	0.05	11.83
5	26.36	25.19	24.95	94.15	27.42	29.37	31.29	-213.50
					27.38	29.63	31.41	-213.62
	26.39	26.00	23.87	213.62				
	26.09				27.46	29.83	31.98	-217.41
	26.00	25.58	23.08	215.80	27.46	29.82	31.99	-217.85
	<b>Average</b>	<u>26.21</u>	<u>25.53</u>	<u>23.75</u>	<u>215.00</u>	<u>27.43</u>	<u>29.66</u>	<u>31.67</u>
<b>Std</b>	0.19	0.35	0.88	1.20	0.04	0.22	0.37	2.36

### Appendix C

Table of the approximation values of molecular volume used in KBHR analysis

Composition (x) of C18 in C16/C18	Molecular volume V( $\text{\AA}^3$ )
0	403.365
0.1-0.6	443.455
0.7	443.712
0.8	444.283
0.9	448.036
1.0	448.036